The effect of molecular architecture on the deformation behaviour of drawn bimodal polyethylene

Winke Heidi Werner Van den fonteyne

School of Physics and Astronomy

University of Leeds

Submitted in accordance with the requirements for the degree of

Doctor of Philosophy

August 2016

The candidate confirms that the work submitted is her own and that appropriate credit has been given where reference has been made to the work of others.

This copy has been supplied on the understanding that it is copyright material and that no quotation from the thesis may be published without proper acknowledgement.

© 2016 The University of Leeds and Winke Heidi Werner Van den fonteyne.

The right of Winke Heidi Werner Van den fonteyne to be identified as Author of this work has been asserted by her in accordance with the Copyright, Designs and Patents Act 1988.

Acknowledgements

If it weren't for a great number of people, or, more accurately, a number of great people, this thesis would still be enjoying a happy life as a tree. First of all, I would like to thank my supervisors at the University of Leeds; Prof. Ian Ward and Dr. Peter Hine, and my supervisors at SABIC; Dr. Rudy Deblieck, Dr. Klaas Remerie and Dr. Mark Boerakker. You have given me invaluable guidance and advice throughout these 3.5 years and your passion for polymers has been an inspiration and a much needed motivation in the hectic last months of thesis writing. Thanks to Dr. Daniel Read for useful discussions along the way, and to Dr. Mark Bonner and Prof. Peter Olmsted for their help and insights during the first half of the PhD. Furthermore, I am very grateful to Victor Litvinov, Erik Janssen, Priya Garg, Ralf Kleppinger and everyone else at SABIC and DSM for sharing their impressive pool of knowledge with me. From the Leeds side, Dr. Daniel Baker and Glenys Bowles cannot be excluded from this list, the former for keeping the labs functioning and the latter for keeping me functioning.

I would also like to thank my office mates Edgar, Deev, Outi, Helen, Ben, Steve, Guanghui, Shaj and Sophie for making work a surprisingly enjoyable place. I owe you all a Come Dine With Me! Thanks to maman and papa for supporting me even though you'd rather I had chosen a sunnier place for my PhD, and finally to Robin for providing me with a reference for insanity against which thesis madness pales in comparison.

The funding for this work was provided by SABIC, to whom I am very grateful for keeping me and the Instron alive.

Abstract

The most common failure mode for polyolefin pipes is slow crack growth. A crack is preceded by a craze, a voided wedge of material bridged by highly deformed fibrils. Upon failure of the fibrils, the crack propagates. Both the tendency of the material to form voids and the strength of the fibril at the craze - crack interface are governed by the effective entanglement network. The effective entanglement network comprises all the intermolecular junctions in the material that can effectively transfer load at the time scale of the experiment. In this work, the effective entanglement network of bimodal polyethylene is probed through tensile and creep measurements. Bimodal polyethylene is the industrial standard material for polyethylene pressure pipes, and consists of a high molecular mass, branched fraction and a low molecular mass, linear fraction. The former is responsible for the resistance to slow crack growth, the latter for enabling processing. In the first part of the work, the influence of molecular mass and branch content of the high molecular mass fraction on the effective molecular network is studied. It is found that only a combination of high molecular mass and high branch content increases the resistance of the network. In the second part of the work, the high molecular mass fraction of the bimodal polyethylenes is isolated. Again, a combination of high molecular mass with high branch content results in a higher effective entanglement network, and overall the resistance to deformation is higher in these materials than in the bimodal materials. It is concluded that the resilience of the network depends on the available network density and the friction caused by side chain branches. Independently of the morphological origin of this friction in the solid material, it can be expected to vary with the monomeric friction in the melt.

Abbreviations

^{1}H NMR	Proton nuclear magnetic resonance
A	Cross section
$A(0)^{am}$	Mass fraction of hydrogen atoms in the amorphous phase
$A(0)^{hm}$	Mass fraction of hydrogen atoms in the highly mobile fraction of the amorphous phase
$A(0)^{cr}$	Mass fraction of hydrogen atoms in the crystalline phase
$A(t)$	T_2 relaxation signal from ^{1}H NMR
AFM	Atomic force microscopy
b	Burgers vector
biEH	Bimodal ethylene-hexene
C_4H_8/C_2H_4	Butene pressure to ethylene pressure ratio
CRDF	Creep rate deceleration factor
d	End-to-end distance between effective entanglements
D	Craze fibril diameter
d_p	Distance between the protons in a CH_2 group
DSC	Differential scanning calorimetry
ESC	Environmental stress cracking
ESCR	Environmental stress crack resistance
FID	Free induction decay
f_s	Force needed to break a covalent chain
FNCT	Full notch creep test
G_c	Fracture toughness
G_{HT}	Strain hardening modulus, calculated from the fit of the stress - draw ratio curve to the Haward - Thackray model
G_K	Strain hardening modulus, calculated from the average slope of the stress - draw ratio curve
G_{NHSM}	Strain hardening modulus, calculated from the slope of the stress - Neo-Hookean strain measure curve

h	Planck constant
H_2/C_2H_4	Hydrogen pressure to ethylene pressure ratio
HAADF-STEM	High angle annular dark field scanning transmission electron microscopy
HBEH	High branched ethylene-hexene
HDPE	High density polyethylene
HT-SEC	High temperature size exclusion chromatography
k	Boltzmann constant
K	$\lambda^{-\frac{3}{2}}$
l	Length
l_{cm}	Length of the comonomer in number of carbons
L	$2L_c + L_a$
L_a	Thickness of amorphous layer
LBEH	Low branched ethylene-hexene
L_c	Crystal thickness
LDPE	Low density polyethylene
LLDPE	Linear low density polyethylene
m_b	Molecular mass per backbone bond
$m_{catalyst}$	Catalyst mass
M_0	Molecular mass of a CH_2 group
M_e	Molecular mass between entanglements
M_i	Molecular mass of chain i
M_n	Number average molecular mass
M_w	Weight average molecular mass
$M_{w,e}$	Molar mass of ethylene
$M_{w,mono}$	Molar mass of the comonomer
n_c	Comonomer content in molar fraction
N	Number of Kuhn segments
N_a	Avogadro's number
NHSM	Neo-Hookean strain measure
N_i	Number of chains of molecular mass i
P	Probability of forming a tie molecule
$P_{C_2H_4}$	Ethylene pressure
PE	Polyethylene
PENT	Pennsylvania notch test

r	End-to-end distance of the random coil in the melt
$\bar{r}$	Root mean square of the end-to-end distance of the random coil in the melt
R	Raman depolarisation ratio
R2	Reactor 2
R_g	Radius of gyration
R_u	Universal gas constant
SAXS	Small angle X-ray scattering
SEM	Scanning electron microscopy
t	Time
T	Temperature
T_2	Transverse magnetisation relaxation time
T_2^{am}	Effective transverse magnetisation relaxation time for the amorphous phase
T_2^{hm}	Effective transverse magnetisation relaxation time for the highly mobile fraction of the amorphous phase
T_2^{cr}	Effective transverse magnetisation relaxation time for the crystalline phase
T_m	Melting temperature
T_m^0	Equilibrium melting temperature of a lamella of infinite thickness
T_α	α relaxation temperature
TEM	Transmission electron microscopy
U	Energy needed for the fracture of a covalent chain
UHMWPE	Ultra high molecular weight polyethylene
v_e	Effective entanglement density
WAXS	Wide angle X-ray scattering
w_c	Mass fraction of butene
X_c	Crystallinity
$X_{c,d}$	Crystallinity calculated from density
$X_{c,h}$	Crystallinity calculated from heat of fusion
β	Branch content
γ	Surface energy
Γ	Energy needed to create new surface
γ_{pgr}	Proton gyromagnetic ratio
ΔH_f^0	Enthalpy of fusion of the crystalline phase

Δn	Birefringence
Δn_{max}	Birefringence of a perfectly oriented sample
$\dot{\epsilon}$	True strain rate
θ	Angle
κ	Rescaling constant
λ	Draw ratio
λ_n	Natural draw ratio
μ_0	Permeability of free space
ρ	Density
ρ_a	Density of the amorphous phase
ρ_c	Density of the crystalline phase
σ	True stress
σ_{cr}	Craze stress
σ_e	Interfacial free energy over the basal surface of the lamellae
σ_R	Recovery true stress
σ_T	Total true stress
σ_v	Viscous true stress
σ_y	Yield stress
Σ_e	Number of effective load bearing chains per unit volume
τ	Shear stress

Contents

List of Figures

LIST OF FIGURES

Chapter 1

Context: the role of the molecular entanglement network in the slow crack growth of polyethylene

This chapter explains the motivation for this work and introduces the concepts that need to be understood to interpret its results. It finishes with defining the scope of the work.

1.1 Motivation for the work: polymer pipes and slow crack growth

This work was sponsored by SABIC Petrochemicals, and was carried out with support of their Materials Development for Pipe Technology team. To evaluate and certify the life span of polyolefin pressure pipes used for water and gas distribution, manufacturers like SABIC perform internal pressure tests. The pipe is subjected to a specific pressure resulting in a circumferential stress, at room temperature or a specific elevated temperatures until failure. This circumferential stress, also called hoop stress, is the force exerted on the material in the cylinder wall that is perpendicular to the pipe axis and the pipe radius, divided by the surface on which it acts, the axial cross section of the pipe. Elevated temperatures are used to accelerate the

tests. The time to failure and the failure mode are observed. Depending on the applied (hoop) stress, four failure modes can be identified. Rapid crack growth can occur immediately after the application of the stress, even at stresses of only half the yield stress. This failure mode occurs very rarely but has dramatic consequences [1]. The next three failure modes are drawn schematically in figure 1.1. In stage 1, the applied stress is a large fraction of the yield stress of the material which results in plastic instability and ductile failure [2]. This can take from hours up to a 100 years for the materials currently used by industry. In stage 2, the pipe fails by the growth of small cracks up until a critical point, at which rapid crack growth sets in. The applied stresses are relatively low fractions of the yield stress. The cracks typically develop over 50 years or more, based on predictions from accelerated methods [2]. Stage 3 occurs when chemical degradation of the material sets in due to depletion of the stabilisers in the polymer. It is almost independent of applied stress. One strategy to enlarge the ensured lifetime area under the curve in figure 1.1 is to design materials for which stage 2 failure occurs as late as possible at as high a stress as possible, with the chemical lifetime as the ultimate limit [2–4].

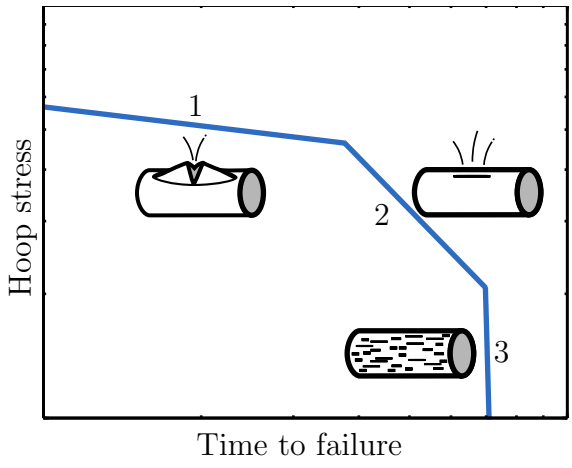

Figure 1.1: The different stages of pipe failure during an internal pressure test. stage 1: ductile failure, stage 2: slow crack growth, stage 3: chemical degradation

Brown and co-workers identified slow crack growth as the dominant mechanism for stage 2 failure and were the first to describe the mechanism behind it [5–9]. The different stages in slow crack growth are craze

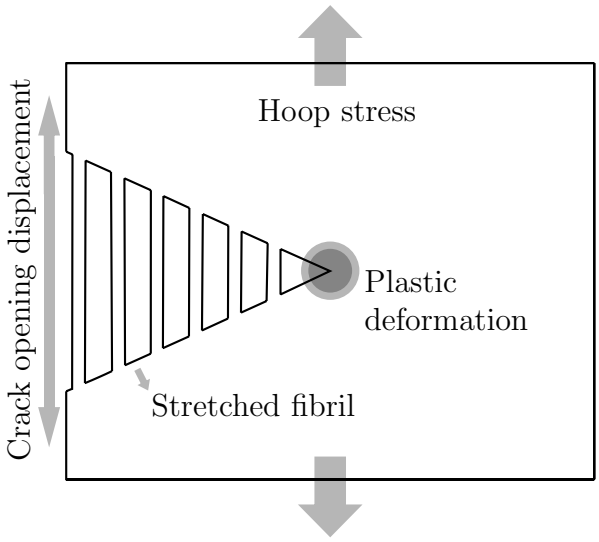

Figure 1.2: Craze mechanism represented schematically. The growth goes from left to right, reproduced from [11]

initiation, followed by craze propagation, followed by termination with a craze - crack transition. A craze is a wedge of material preceding a crack, bridged by fibrils. The three stages of slow crack growth are represented on figure 1.2. In the plastic deformation zone, the craze is initiated. It propagates, forming fibrils bridging and temporarily stabilising the craze. Where the fibrils fail, a crack is formed. Figure 1.3 shows a scanning electron micrograph (SEM) of a craze in medium density polyethylene (PE) [10].

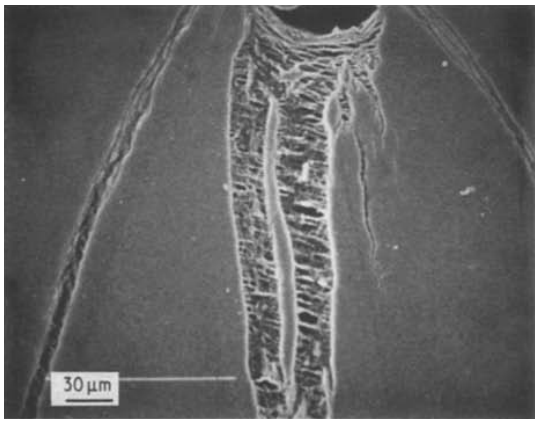

Figure 1.3: Scanning electron micrograph of a craze near a crack tip in medium density polyethylene [10]

1.2 Structure and morphology of polyethylene

To be able to interpret previous research on the slow crack growth of PE, it is important to understand the molecular and crystalline structure of this material and how it changes under the influence of stress. Chemically, PE is a very simple polymer, built up of ethylene monomers, as shown in figure 1.4. The molecular architecture of PE, however, can vary widely, resulting in materials with very different macroscopic properties.

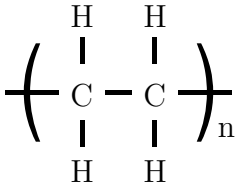

Figure 1.4: Chemical structure of polyethylene

The first commercial PE, low density PE (LDPE), was discovered in 1933 by Imperial Chemical Industries during high pressure tests on ethylene and benzaldehyde mixtures [12]. LDPE is synthesised through addition polymerization in a high pressure process, without catalyst (though an initiator is added, for example peroxide) [13]. It contains randomly dispersed short and long chain branches, about 60 branch points per 1000 carbon atoms. A branch point occurs when a a carbon atom bonds three carbon atoms and one hydrogen atom, rather than two carbon atoms and two hydrogen atoms. A new chain can then form starting from this third carbon atom. The number of long chain branches is significantly lower than the number of short chain branches. In 1953 Karl Ziegler discovered organometallic mixed catalysts which made it possible to synthesise high density PE (HDPE). This work was continued by Giulio Natta, and both chemists received the Nobel Prize in Chemistry for their work in 1963 [12, 14]. HDPE has fewer than 7 branches per 1000 carbon atoms and a relatively high molecular mass [13]. Ultra high molecular weight PE (UHMWPE) is HDPE with extremely long backbone chains. Linear low density PE (LLDPE) was developed to replace LDPE, and bridges the density gap between HDPE and LDPE. It contains short chain branches but no long chain branches. LLDPE is produced by introducing α-olefins during the polymerisation. α-olefins are

alkenes containing one double bond, at one end of the chain. In the context of polymer production, these are referred to as comonomers. When they are incorporated into the main chain, side branches are formed. The nature and ratio of the α-olefin added controls the number and length of the short chain branches [13].

All these variations influence the macroscopic properties of PE. This makes the mechanical behaviour of PE complex to describe, but when understood, these variations also make it possible to tailor the properties of PE very precisely. The links between the molecular architecture and the macroscopic properties are described in the next section.

1.2.1 From microscopic to macroscopic properties

The molecular architecture of PE impacts its macroscopic properties in various ways. It determines the properties of the material in the melt state. The properties in the melt as well as the desired design of the final product decide which manufacturing process is possible and suitable. Then, the molecular architecture together with the processing conditions, both in the melt and in the solid state, determine the properties of the final product. This section therefore explains the influence of the molecular architecture on the melt and the solid state separately.

Properties in the melt

To obtain a viable finished product made out of any PE, the properties in the melt must be suitable for the desired form of processing, for example, injection moulding. Chain length and chain length distribution are important parameters influencing the properties in the melt. This is due to the existence of a critical molecular mass, around 4000 for PE, above which chains intertwine with each other. The mobility of the chains is reduced by the need for coordinated flow through the entanglements [15, 16]. The chain length of a polymer and its distribution can be expressed by the moments of the molecular mass distribution. This can be a number average molecular

mass (M_n), expressing the average chain length:

$$M_n = \frac{\Sigma M_i N_i}{\Sigma N_i}, \tag{1.1}$$

with M_i the molecular mass of chain i and N_i the number of chains of mass M_i, or the weight average molecular mass (M_w):

$$M_w = \frac{\Sigma M_i^2 N_i}{\Sigma M_i N_i}. \tag{1.2}$$

The ratio between these two parameters is a measure for the width of the molecular mass distribution. Long chain lengths result in highly entangled melts, with a high viscosity (melt strength) at low shear rates. At high shear rates, the chains disentangle. Short chain lengths result in a melt with a low viscosity at high shear rates. The dependence of the viscosity on the shear rate is therefore influenced by the molecular mass distribution. A polymer with a broad molecular mass distribution will have a high viscosity at low shear rates, due to the long chains, and a low viscosity at high shear rates, due to the short chains. The long chains disentangle at high shear rates. A polymer with a narrow molecular mass distribution will have a more constant viscosity with shear rate [17]. Chain irregularities and bulky or long chain branches also increase the viscosity by increasing the number of chain entanglements at a given time scale [18]. Extensional flow (flow in one direction) in particular is influenced by long chain branches. This shows the advantage of LLDPE over LDPE. In LDPE, which has both short and long chain branches, the long chain branches are entangled, which causes the stress to increase during melt extension (this effect is called strain hardening). The strain hardening is dependent on the strain rate, with higher strain hardening with increasing strain rate, as the chains have less time to slip. In LLDPE, which only has short chain branches, the chains can slide past each other, avoiding strain hardening [19]. The monomeric friction, representing the energy needed for one monomer in a chain to make one step in a dynamic process, however, is higher in a polymer with short branches than in a linear polymer and goes up with the branch content [20].

Solid state properties

Upon solidifying, PE crystallises partially; it is a semi-crystalline polymer. Due to the regularity of a linear PE chain, it achieves its lowest free energy by ordering itself into a crystal structure. It will fold up to form a lamella, multiple lamellae will pack together to form a crystal. Chain irregularities, bulky chain branches and chain entanglements will significantly influence both the ability to crystallise and the speed of crystallisation as they cannot be fully incorporated in the crystal [21–25]. Very long chains also inhibit crystallisation as they have more chance of being entangled, and have slower crystallisation kinetics [26–28]. The region in between the crystals is referred to as the amorphous phase. The main industrially relevant properties for a polymer are stiffness, failure stress, failure strain and toughness. Figure 1.5 represents the result of a uniaxial tensile test on a polymer test bar. During this test, a constant deformation rate is applied to the sample and the resulting load is recorded. The load is then divided by the sample cross section perpendicular to the application direction of the deformation to obtain stress. Using stress rather than load has the advantage that different samples can be compared without knowledge of their dimensions. The industrially relevant properties can be defined using this figure. Stiffness is expressed by the Young's modulus, the slope of the initial linear part of the stress - deformation curve (denoted with a in figure 1.5). A higher slope indicates that the material is more resistant to deformation, or stiffer. The failure stress and strain are denoted in figure 1.5 as b and c respectively. The toughness of a material is the energy absorbed by a material during deformation, before failure. This can be calculated using the stress - deformation curve, by calculating the area under the curve. It is denoted as d in figure 1.5. The stiffness of a semi-crystalline polymer is proportional to its degree of crystallinity (X_c), while the failure stress is governed by how well the crystals are connected to each other, which in turn is governed by the length of the chains and their orientation [13, 29]. A long chain has more chance of passing through more than one crystal. Such a chain is referred to as a tie molecule. Crystals are neatly ordered and hence use space more efficiently than does amorphous phase. This results in a difference in density between the two phases. The density (ρ) of a perfect PE crystal is always the same. Hence the density of a polymer is a

measure of its crystallinity [23]. Chain irregularities, bulky chain branches and chain entanglements, while reducing the crystallinity, also enhance the connection between crystals. The dynamics of the intercrystalline molecular connections are of major importance in understanding the mechanical properties of the finished product. At certain temperatures (below the melting temperature) and strain rates, chains connecting different crystals can diffuse through those crystals, altering the intercrystalline connectivity. Chain branches influence the ability of the links to move by pinning them. They also influence the dynamics through their effect on crystallisation, causing less and/or smaller crystals for the links to move through.

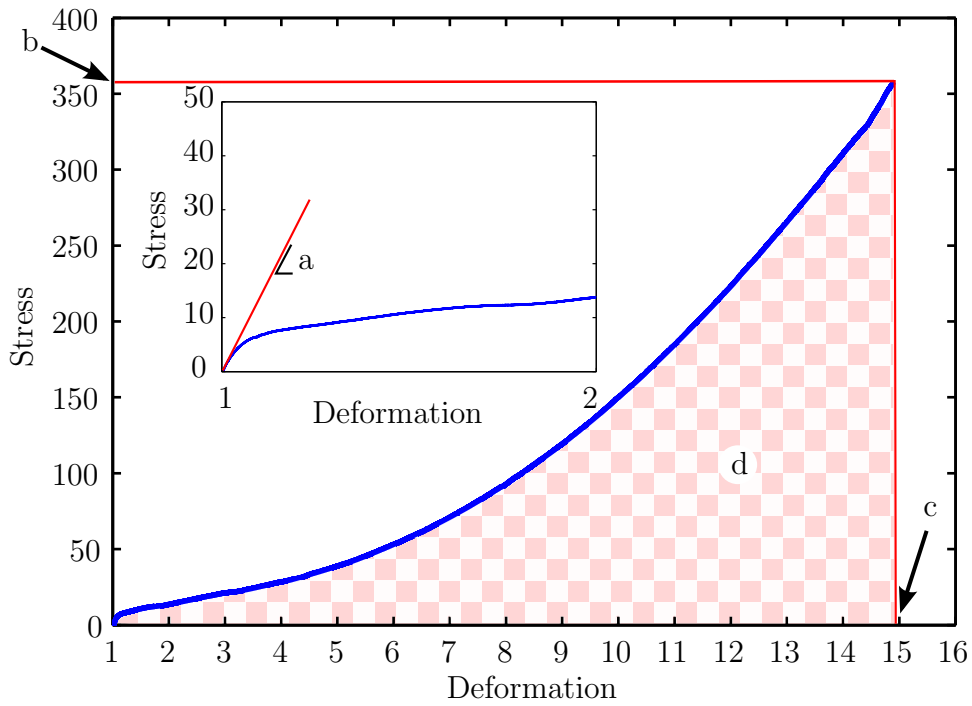

Figure 1.5: Stress - deformation curve resulting from a uniaxial tensile test on polyethylene, with (a) stiffness, (b) failure stress, (c) failure strain and (d) toughness

After or even during crystallisation, other processing steps can be applied to obtain the desired material characteristics. Chain orientation influences both stiffness and strength. Different processing techniques make use of drawing (extending the polymer uni-axially, either in the melt or of the solid material) to line up the molecular chains (both in the crystalline

and the amorphous phase) so polymer fibres with exceptional mechanical properties in the drawing direction are obtained. The optimal speed and temperature of the drawing and the maximum achievable draw ratio depend on the molecular weight and possible side chain branching of the polymer [27, 30, 31].

Properties of common types of polyethylene

Now the four common types of PE as mentioned above (LDPE, HDPE, UHMWPE and LLDPE) can be discussed in terms of their properties. Their typical density, molecular mass and crystallinity are given in table 1.1. LDPE has a low crystallinity and hence a low density, due to the presence of short and long chain branches. This results in a material with low indentation hardness but high toughness [32, 33]. HDPE has fewer than 7 branches per 1000 carbon atoms and a relatively high molecular mass [13]. This results in high crystallinity and hence high stiffness and a high failure stress, but a low failure strain [33]. Ultra high molecular weight PE (UHMWPE) has a very high molecular mass, resulting in a material with low friction, high resistance to wear and high toughness [33]. Linear low density PE (LLDPE) contains short side chains but no long side chains. This results in a material which has a higher failure stress, but also more expensive to produce than LDPE. It is used in packaging where the higher production cost is balanced by material savings [33].

	ρ [kg/m^3]	M_w [kg/mol]	X_c [%]
LDPE	910-925	25000-160000	50-60
HDPE	940-970	100000-500000	>90
UHMWPE	Similar to HDPE	3000000-6000000	Similar to HDPE
LLDPE	920-940	25000-160000	Between LDPE and HDPE

Table 1.1: Properties of common types of polyethylene. ρ is density, M_w is weight average molecular mass and X_c is crystallinity [12, 13, 33]

1.2.2 From isotropic to oriented polyethylene

The semi-crystalline structure of isotropic HDPE can be studied using optical microscopy. An example is given in figure 1.6. It can be seen that

the PE chains are arranged in spherical features, reffered to as spherulites, with a diameter up to 100 μm [34]. Small angle X-ray scattering (SAXS) experiments, among others, reveal that the spherulites consist of lamellae embedded in an amorphous matrix. The lamellae grow out of a common central nucleus and can be twisted about the radial direction of the spherulite [35, 36]. Electron diffraction experiments on single crystals reveal that the molecular chains are nearly perpendicular to the flat surface of the lamellae. Because the molecular chains are much longer than the lamellar thickness, this implies chain folding, for which evidence was first shown by Keller in 1957, and/or the presence of one chain in different adjacent lamellae [35, 37–39]. The latter is the definition of a tie molecule, a specific type of intercrystalline molecular connection. A schematic overview of the structure of a PE spherulite is given in figure 1.7. Possibilities for intercrystalline molecular connections can be the aforementioned tie molecules or entangled chain segments partly incorporated in different crystals. These are sketched in figure 1.8, for a HDPE (1.8a) without chain branches and for a LLDPE with chain branches (1.8b). Both chains have the same backbone chain length, and a similar radius of gyration (R_g) in the melt. Upon crystallisation, LLDPE forms thinner crystal lamellae because the chain branches cannot be incorporated in the crystal. Both of the chains are tie molecules, as they traverse more than one crystal lamella, but the LLDPE forms a larger number of intercrystalline bridges. Entanglements are also shown in the figure, with two entanglements for each chain. It has to be noted that this visualisation of entanglements is qualitative, and the nature of entanglements is not well understood [40, 41]. Experimental indications of the existence of intercrystalline molecular connections can be found in references [5, 10, 42–49].

Applying a tensile stress to spherulitic PE leads to a variety of deformation modes in different regions of the crystals [51, 52]. Three regions are present in a spherulite when subjected to a uniaxial load: the polar, the equatorial and the diagonal domain, given in figure 1.9 as a, b and c respectively. The equatorial domain contains lamellar stacks oriented perpendicularly to the principal tensile axis. SAXS experiments reveal lamellar separation due to deformation of the soft amorphous ligaments in this re-

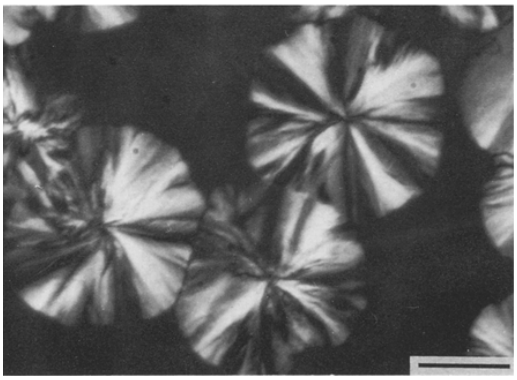

Figure 1.6: Optical micrograph of polycrystalline PE, bar line represents 30 µm [34]

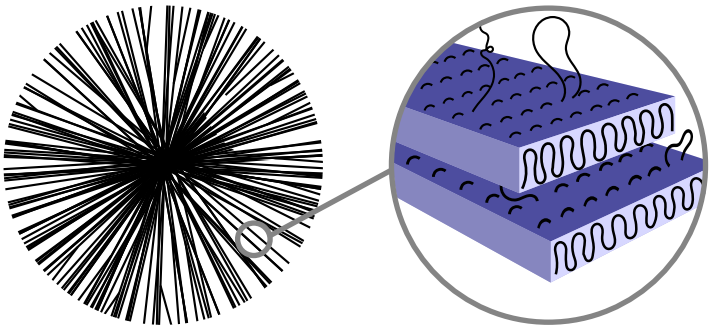

Figure 1.7: Schematic representation of the built-up of a spherulite. Left: spherulitic crystal, every line represent a lamella, right: idealised schematic of two crystal lamellae showing chain folding

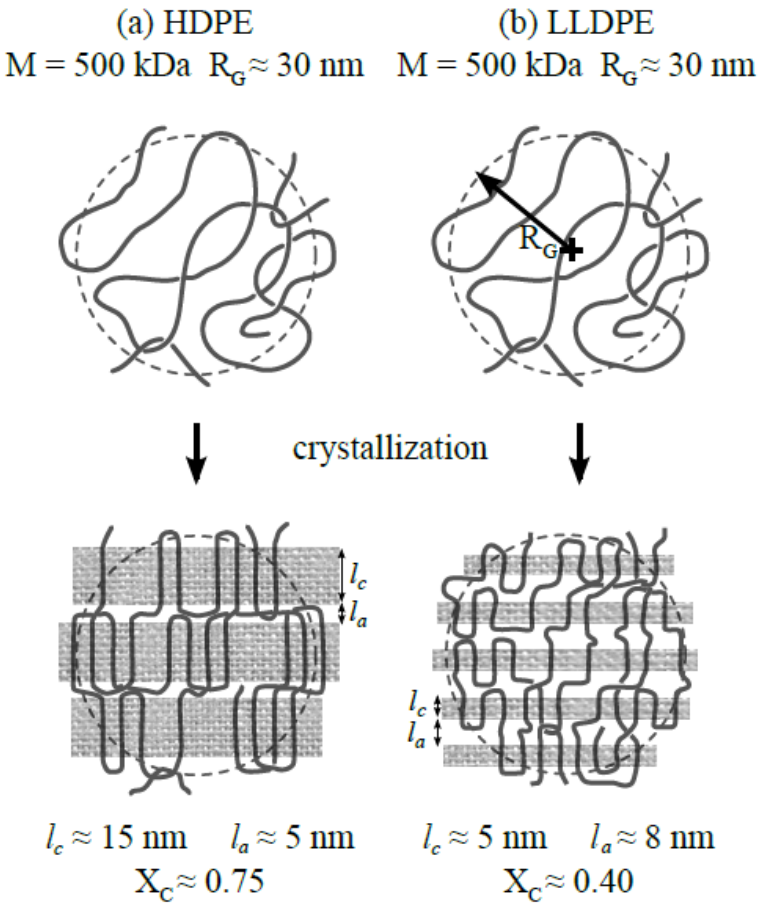

Figure 1.8: Sketch of the different possibilities for the formation of intercrystalline molecular connections: tie molecules and entanglements, for two chains of the same molecules and radius of gyration, but one HDPE (no branches, left) and one LLDPE (branched, right). Reproduced from [50]

gion. This separation is reversible at very small strains, but, above a certain strain, interlamellar voids of several nanometers may be formed [53]. SAXS of HDPE drawn to low strain levels indeed shows the presence of nano-voids in the material [54, 55]. They are oriented perpendicular to the tensile axis [56]. The nano-void volume fraction varies through the different domains. The polar domain contains lamellar stacks oriented along the principal tensile axis which leads to a strong deformation resistance. The diagonal domain contains lamellar stacks that are tilted with respect to the principal tensile axis. These lamellae are subjected to both separation and shear deformation. Interlamellar shearing is the dominant deformation mechanism above the glass transition temperature, but also intralamellar shear will appear locally [57]. The specific critical resolved shear stress can be calculated for a specific crystallographic slip system (a slip system consists of a slip plane and a direction along which the slip occurs). This stress is seen to be much higher in theoretical, perfect crystals than in experiments [35]. This is explained by the presence of dislocations in the crystals. A dislocation is a defect in the crystal lattice. Most commonly observed in PE are screw dislocations. A schematic of a screw dislocation, with its associated Burgers vector (b), is shown in figure 1.10 [58]. A dislocation occurs when part of a crystal plane is missing. Deformation by slip is thus governed by the resistance to dislocation generation and motion on the slip planes. The discussion about the most important factor of these two, generation and motion, is ongoing [59–61]. Two different types of slip are distinguished by the direction of the Burgers vector of the moving dislocation. When the Burgers vector is parallel to the molecular chain axis, this is called chain slip. When the Burgers vector is perpendicular to the molecular chain axis, this is called transverse slip. Both of these can result in fine slip or (less commonly) coarse slip, as depicted in figure 1.11 [60, 62, 63].

As the material deforms further, the crystallographic slip process transfers from a local phenomenon to a collective activity, with intralamellar slip (for example block slip within lamellae) becoming more important than interlamellar slip [57, 64]. Wide angle X-ray ray scattering (WAXS) performed on PE by Hiss *et al.* shows the formation of fibrils a few hundred nanometers thick, caused by crystallite fragmentation, and this finding was confirmed

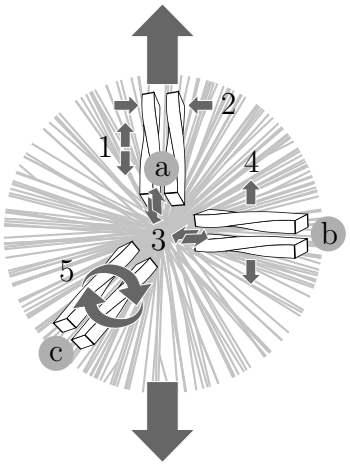

Figure 1.9: Regions in a spherulite during deformation: (a) polar domain, (b) equatorial domain and (c) diagonal domain. Local deformation modes occurring in the different regions: (1) elongation, (2) transverse compression, (3) interlamellar slip, (4) interlamellar separation, (5) rotation. The large arrows indicate the imposed load. Reproduced from [52]

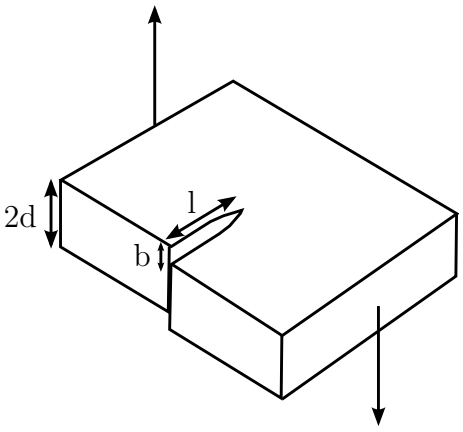

Figure 1.10: Model of a screw dislocation in a crystal lamella, reproduced from [58]. 2d is the lamella thickness, l is the distance from the dislocation to the edge of the crystal and b is the Burgers vector. The arrows indicate the direction of an applied shear stress

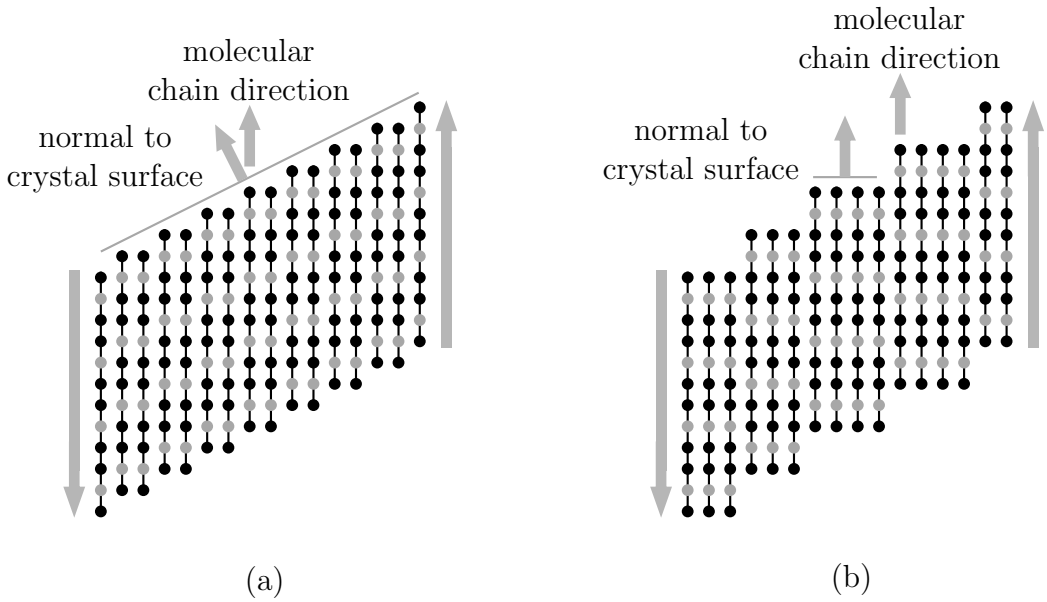

Figure 1.11: Schematic illustration of (a) fine slip and (b) coarser slip, reproduced from [63]

by SAXS, electron microscopy and atomic force microscopy (AFM) studies [56, 65–68]. These fibrils are actually bundles of microfibrils, connected by the former interlamellar links from the spherulitic structure. A microfibril, with a thickness of 0.1 to 30 nm, consists of folded chain blocks (broken off of the lamellae in the spherulitic structure) connected by unfolded chains; the intrafibrillar links. A schematic representation can be seen in figure 1.12. The chains present in the chain blocks are oriented parallel to the drawing direction. Between different chain blocks, amorphous material is present that, due to orientation, is also partly ordered in a pseudo-hexagonal structure [69]. Longitudinal voids can be present between the fibrils [66]. Peterlin states that plastic deformation of this fibrillar structure can only occur by longitudinal sliding of first the fibrils and then the microfibrils past each other [51, 66, 70, 71]. The fibrils start sliding first because they are less tightly interconnected than the microfibrils. This process is hindered by the interfibrillar tie molecules. These molecules undergo stretching and cause unfolding of the chains in the crystal blocks where they are anchored. The interfibrillar tie molecules consequently become more elongated and aligned with the drawing direction. Chain segments of these molecules will therefore be included in the crystal lattice of adjacent crystal blocks. This

leads to a higher density and a higher crystallinity, but, more importantly, to a higher resistance against further drawing. This increase in resistance results in an ever increasing stress. This region in the drawing process is therefore denoted as the strain hardening region. The strain hardening proceeds up to failure [66]. Amornsakchai *et al.* describe this similarly as a fibre composite model [72]. This model is partially confirmed by Tang *et al.*, using SAXS experiments [68]. Tang *et al.* observe additional deformation of the amorphous layers in between the crystalline lamellae at low strains. This happens through the gliding of chain segments along their axes and the slip of planes, comparable to respectively crystallographic chain slip and crystallographic transverse slip [69]. They further alter Peterlin's model by suggesting that the first process to occur at moderate strains is slippage of the microfibrils, and not slippage of the fibrils. The last processes to occur before failure are slippage of the fibrils and chain disentanglement [64].

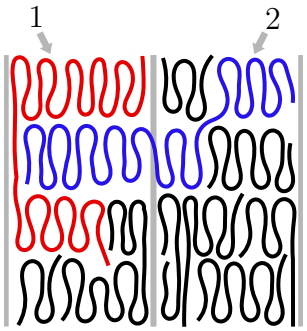

Figure 1.12: Microfibrillar model of the crystal fibril structure: (1) intrafibrillar tie molecule and (2) interfibrillar tie molecule, reproduced from [66]

The transformation of a spherulitic crystal structure into a fibre composite model, followed by failure, results in a stress - deformation curve as shown before in figure 1.13. This is the same curve as figure 1.5, repeated here with the different stages of deformation indicated. Initially, the specimen deforms elastically resulting in a linear relationship between stress and deformation, indicated on figure 1.13 by a. At the yield point, indicated by b, plastic deformation sets in and the spherulitic structure starts transforming as explained above. This leads to a localisation of the deformation, visible in a tensile specimen as the formation of a neck. Further deformation

involves a transition to the fibrillar structure, which involves strain hardening. The yield and strain hardening compete with each other, and the neck propagates through the specimen. This necking region is indicated by c on figure 1.13. The point in the stress - deformation curve where fibrillation becomes the dominant deformation mechanism is called the natural draw ratio (λ_n), indicated by d. Above the natural draw ratio, the fibrils are further untangled and stretched, resulting in strain hardening (indicated by e). Eventually, slippage, chain disentanglement and, dependent on the strain rate, chain fracture, cause the specimen to fail [73–75].

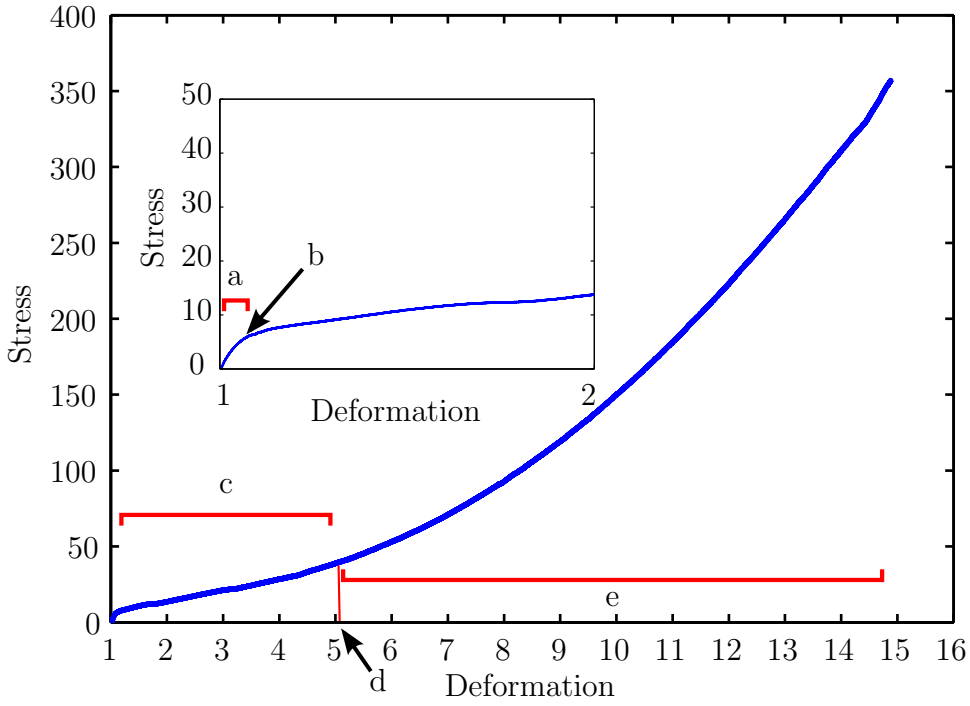

Figure 1.13: Stress - deformation curve resulting from a uniaxial tensile test on polyethylene, with (a) linear elastic region, (b) yield point, (c) necking region, (d) natural draw ratio and (e) strain hardening region

1.3 The mechanisms behind slow crack growth

The concepts introduced in section 1.2 will now be used to explain the mechanisms behind slow crack growth and the influence of molecular architecture on these mechanisms.

1.3.1 Initiation, propagation and termination of a craze

As mentioned in section 1.1, a craze is a wedge of material bridged by fibrils, preceding the crack. Crazing is not the only deformation mode of PE; shear yielding is preferred when the formation of internal surface is inhibited [11, 76]. Shear yielding is plastic deformation without change of volume [11]. From an application point of view, crazing is not the preferred deformation mode as it dissipates less energy than shear deformation [11]. However, as explained in section 1.1, it is the prevalent deformation mechanism in pipe applications at long time scales. At shorter time scales, shear yielding is dominant. Hence the knee point between stage 1 and stage 2 in figure 1.1 represents a transition between these two competing mechanisms, from yield failure at short times and high stresses to brittle failure at long times and low stresses. This explanation largely follows the work of Deblieck *et al.* published in 2011 [11].

Craze initiation

A craze initiates when a void opens up due to a stress concentration. This stress concentration can for example be caused by a defect in the molecular network or catalyst residue [11, 77–81]. As the equatorial region is most sensitive to the axial tensile stress, crazes are more likely to start in this region. Another example of a region more prone to crazing is the amorphous region between neighbouring lamellar stacks having different orientations [80]. Argon and later Kramer studied the craze initiation in amorphous polymers and suggested that it depends on the energy needed to create new surface, Γ [11, 73, 74, 82, 83]:

$$\Gamma = \gamma + \frac{1}{4} v_e U d, \tag{1.3}$$

where γ is the surface energy (the van der Waals cohesive energy between molecules), v_e is the effective entanglement density (effective entanglements are entanglements that can transfer load at the relevant time scale), U is the energy needed for the fracture of a covalent chain and d is the end-to-end distance between effective entanglements. So the second term represents the contribution to the energy by the effective covalent bonds crossing the surface. The $\frac{1}{4}$ is needed as there are two surfaces, and one entanglement

consists of two covalent chains.

Craze propagation

A craze propagates when the macroscopic stress applied reaches a critical value, the craze stress σ_{cr}. The voided regions grow and join to form a fibrillar structure, a craze [29, 84]. The craze propagates perpendicularly to the direction of the applied stress. Kramer and Berger describe the propagation process using a variant of the Taylor meniscus instability process, as originally suggested by Argon [61, 74, 83, 85]. The unstable plastically deformed polymer at the tip of the craze breaks up and transforms into fibrils, as depicted in figure 1.14. The fibrils are highly drawn and have a fibrillar structure as described in section 1.2.2 [86, 87]. A schematic of this process is shown in figure 1.14. The craze-bulk interface can be represented as in figure 1.15. Mathematical treatment of the materials' behaviour leads to

$$\sigma_{cr} \propto \sqrt{\sigma_y \Gamma}, \tag{1.4}$$

with σ_y the yield stress. The fibril diameter D, indicated in figure 1.15, is also related to the surface energy, as

$$D \propto \frac{\Gamma}{\sigma_{cr}}. \tag{1.5}$$

Therefore the fibril diameter varies with the molecular structure of the material and specifically the number of relevant intercrystalline connections at the experimental time scale. For glassy polymers, this was shown through low-angle electron diffraction of a series of polymers with varying molecular entanglement density by Berger [88]. AFM images on polybutene spherulites confirm that semi-crystalline polymers exhibit similar behaviour [80].

At this point it is appropriate to introduce an extra complexity to the craze microstructure. As early as the 1970's, experiments showed that short fibrils connect the fibrils bridging a craze to each other [74]. These fibrils are referred to as cross tie fibrils. They can be observed in transmission electron micrography (TEM), an example of which is shown in figure 1.16,

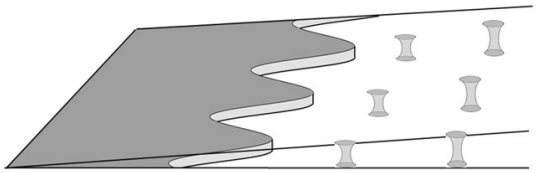

Figure 1.14: Taylor meniscus instability at the tip of the craze, transforming material in fibrils. From [11]

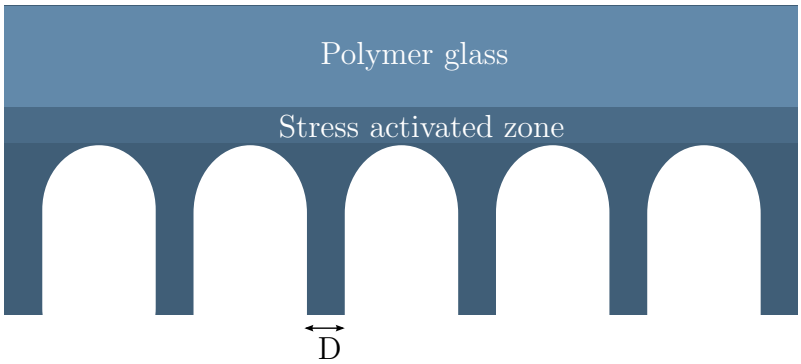

Figure 1.15: Craze-bulk interface, where the fibrils are drawn in from the bulk polymer. D is the fibril diameter, reproduced from [11]

indicated by (a). Fine cross tie fibrils are visible between the coarse fibrils close to the craze-bulk interface. As cross tie fibrils only make up about 15% of the volume of the main fibrils, equation 1.3 remains valid [74].

Craze-crack transition

The fibrils in the craze eventually fail, forming a crack. Brown shows that the cross-tie fibrils have a major effect on the failure of a craze, as they transfer the stress between the primary fibrils, amplifying the stress at the crack tip [90]. He considers the geometry of a crack tip craze as depicted in figure 1.17 and relates the fracture toughness G_c to the strength of the fibril closest to the crack tip. Kramer *et al.* calculated the same relation, though using a slightly different model, but they both conclude that the fracture toughness is proportional to the square of the number of effective load bearing chains per unit volume Σ_e multiplied by the force needed to break one covalent chain f_s in the deformed fibril [90, 91]:

$$G_c \propto (\Sigma_e f_s)^2. \tag{1.6}$$

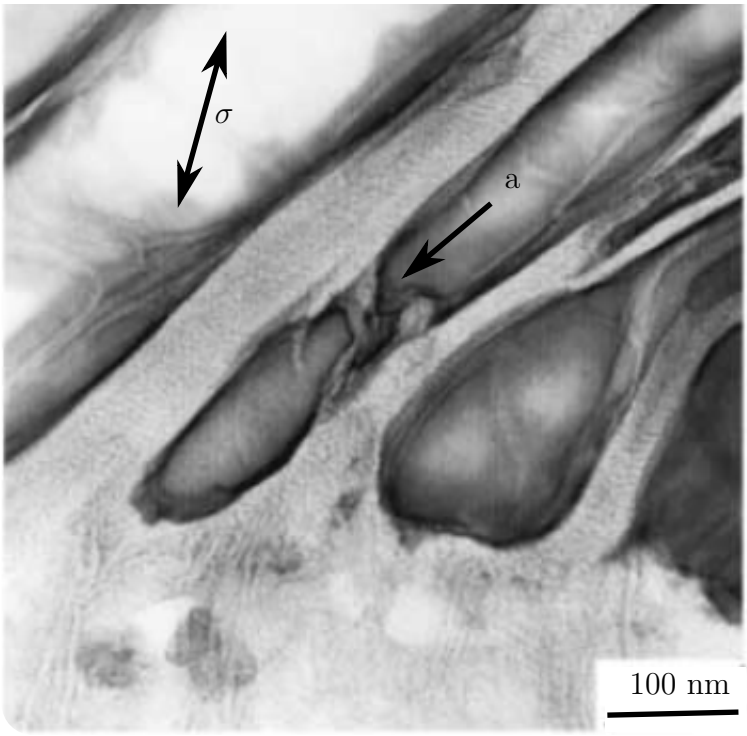

Figure 1.16: Transmission electron micrograph of a section through the fracture surface of a polyethylene-butene copolymer. The direction of the applied stress σ is indicated, and (a) indicates a cross tie fibril. Image reproduced from [89]

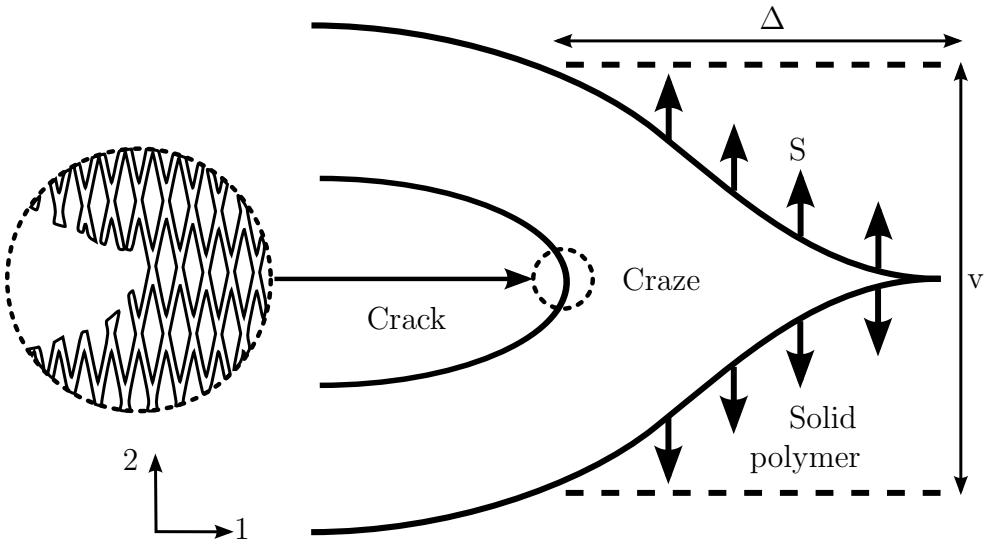

Figure 1.17: The geometry of a crack tip, with Δ the length of the craze, v the width of the craze and S the stress at the craze-bulk interface. Reproduced from [90]

1.3.2 The effective molecular network

In conclusion, the craze stress depends on v_e, the effective entanglement density, and the fracture toughness on Σ_e, the number of effective load bearing chains per unit volume (also referred to as the network density in literature). The network of intercrystalline molecular connections is thus vital in the understanding of slow crack growth and the improvement of the resistance against slow crack growth of materials. The molecular network is made up of different types of intercrystalline molecular connections: tie molecules, molecular chains that are part of more than one crystal, and entanglements, intertwined chains. In literature, the distinction is not always made [50]. It is, however, important to remember that both of these types of connections are transient. There is a time scale at which the chains can disentangle, and a time scale at which the chains can move through the crystals; both entanglements and crystals through friction cause a specific time and temperature dependent resistance against deformation that can be visualised and quantized as a network of effective nodes or effective entanglements. The notion of an 'effective' molecular network is therefore crucial. This network comprises of the connections that can bear load on the time scale of the experiment. The experimental determination of the effective molecular network is not straightforward. The entanglement density in the melt can be measured by rheology measurements, but it is not clear how this correlates with the effective molecular network as present in an oriented fibre at the tip of a crack, and it does not take tie molecules into account. Van Melick however altered the entanglement density to successfully increase the craze-nucleation stress in polystyrene, an amorphous polymer [92]. Raman spectroscopy has been used to assess the number of load bearing chains in drawn fibres. An induced strain will cause peak splitting, and from the intensity of the new peaks the ratio of load bearing chains can be calculated. However, this method does not distinguish between tie molecules and chain entanglements [87, 93–95].

Measurement of the number of effective intercrystalline connections in a solid material is challenging. In the highly drawn fibrils in a craze, a theoretical estimate of the number of tie molecules can be made, based on a model devised by Huang and Brown [96, 97]. The model assumes that if

the end-to-end distance of a molecule in the melt, r, is larger than a critical length, L, the molecule will be a tie molecule. For L they choose

$$L = 2L_c + L_a, \tag{1.7}$$

where L_c is the crystal thickness and L_a is the thickness of the amorphous layer. So the probability of forming a tie molecule depends on the probability of the end-to-end distance to be larger than L. The probability of an end-to-end distance equal to r is:

$$p(r) = ar^2 \exp(-b^2 r^2) \tag{1.8}$$

with a a constant and

$$b^2 = (\frac{3}{2}\bar{r}^2), \tag{1.9}$$

where $\bar{r}$ is the root mean square of the end-to-end distance in the melt. The probability of forming a tie molecule is then:

$$P = \frac{\int_L^\infty r^2 \exp(-b^2 r^2)\mathrm{d}r}{3\int_0^\infty r^2 \exp(-b^2 r^2)\mathrm{d}r}. \tag{1.10}$$

However, studies reveal that the effect on slow crack growth by changing molecular architecture, in particular branch content, is larger than predicted by this model [79, 97–102]. The extra resistance against slow crack growth can originate in a contribution of a different kind of intercrystalline connection, such as entanglements, or an increase in the effectiveness of the tie molecules. It can be imagined that chain branches, not incorporated in the crystals, prevent tie molecules from diffusing through crystal lamellae and so increase the number of effective intercrystalline connections [50]. In the melt, the shear modulus is a measure of the entanglement density, but the question remains if this is representative of the entanglement density in the solid semi-crystalline material. Lamellar folding causes entanglement loss, and the entanglement density in the solid polymer depends strongly on the crystallisation temperature as tie molecules are formed during crystallisation [48]. However, using the shear modulus to calculate the energy needed to create new surface (equation 1.3) results in an acceptable value [11]. Furthermore, the molecular mass between entanglements, M_e, measured from

rheology, correlates well to resistance to slow crack growth [100–102]. Finally, Litvinov *et al.* studied the molecular network in ethylene-propylene rubbers using solid state NMR [103–105]. The interaction strength between nuclear spins is increased by chain entanglements because they increase the anisotropy of chain motions [106]. However, the relationship between the network density as measured from this technique and the effective molecular network density is at present unclear.

1.3.3 The influence of molecular architecture on the effective molecular network and slow crack growth

Much work has been done on the influence of the molecular architecture on the slow crack growth of PE. Slow crack growth failure times are based on tests on notched specimens under tensile load, as originally devised by Brown and co-workers [107]. Because slow crack growth is a slow process, accelerated tests are often used instead. A commonly used accelerated test is environmental stress cracking (ESC). In this test, a notched specimen is pre-soaked in an accelerating agent before being submitted to a tensile load. The accelerating agent enhances the rate of brittle failure without large scale plasticisation, which would cause blunting of the notch [108]. Other common tests are the Pennsylvania notch test (PENT) and the full notch creep test (FNCT). This section summarises the studies correlating aspects of the molecular architecture of PE with slow crack growth resistance, directly or through accelerated tests.

Influence of chain branching

When comparing a HDPE with a copolymer containing butyl branches, Brown and co-workers observed that the slow crack growth rate was 10^2 to 10^3 times lower for the copolymer [7]. Later work confirmed that with increasing branch content, the time to failure in a PENT test increases, but there is a maximum branch density above which no further improvement of the resistance to crack growth is observed [25, 97, 109, 110]. The branches have a twofold effect on the microstructure of PE, as explained in section 1.2.1: they increase monomeric friction and thus decrease the rate of

disentanglement, and they can only be partly incorporated in the crystals, meaning they cause a reduction in crystallinity and reduce the lamellar thickness. The latter also implies that they reduce the yield stress, as it correlates with crystallinity [111]. But due to the structure of the craze, as described in section 1.3.1, this has no influence on slow crack growth. This was confirmed in Brown's work, as the yield stress does not correlate with slow crack growth [7]. So it is the disentanglement rate, influencing v_e and d in equation 1.3, that is lowered by the branches, because a branched molecule is more difficult to disentangle than an unbranched molecule. With v_e and d increasing, the energy needed to create new surface increases. This is reflected in the observation that a higher branch density leads to coarser fibrils in the craze [96]. The maximum branch density can be explained by the influence of the branches on the crystallinity. When the branch density increases, fewer and thinner crystals will be formed. At a certain minimum thickness, the crystals can no longer act as pinning points for the chains and the disentanglement rate (and consequently the slow crack growth rate) increases [96, 109].

Increasing the length of the branches (at low branch contents) has a similar effect to increasing the branch content. For the same number of branches, butyl and hexyl branches suppress crystallinity more effectively and increase monomeric friction more than methyl branches [7, 24, 112]. An increase in branch length from ethyl to butyl and hexyl branching increases the time to failure in environmental stress cracking, by almost 60% and more than 1200% respectively [113].

Influence of molecular mass

The importance of tie molecules has been explained above. As the tie molecule content is expected to increase with increasing molecular mass, when all other parameters are kept constant, increasing the molecular mass should increase the resistance to slow crack growth. This was indeed found by Brown and co-workers, who measured the crack opening displacement rate of PE with different molecular masses, and confirmed in studies on the slow crack resistance of different kinds of PE [110, 114, 115]. An extremely low molecular mass, below 18000, yields PE that does not show crazing,

but fractures suddenly [114]. Below this critical molecular mass, no intercrystalline links can be observed in electron microscopy [42, 116]. Very high molecular mass can also influence crystallinity as increased reptation times slow down the crystallisation and hence very long chains can lead to thinner crystal lamellae [28]. These increase the number of tie molecules as the chance of a chain traversing multiple lamellae (a tie molecule) is higher when the lamellae are thinner [96, 117]. Multiple traversing leads to a higher resistance to slip at longer time scales. Depending on the tractability of the crystals, chains can or cannot slip by crystals at a given time scale [1]. This time scale increases when chains have to pass through multiple lamellae. However, an increasing molecular mass yields an increasing melt viscosity, which limits the processing options for these materials [96, 117].

Influence of molecular mass distribution

As mentioned in the two previous sections, high branch content and high molecular mass impede slow crack growth but also limit processing capabilities. To make industrially relevant materials with high resistance to slow crack growth, blends of PE with different molecular architectures were studied. Blending can be achieved by simply mixing pellets or powder. Huang and co-workers used this method to blend UHMWPE with HDPE, which resulted in UHMWPE particles in a matrix of HDPE. A craze would form in the HDPE and be bridged by the more resistant UHMWPE particle. The counterforce exerted by the particles was proportional to their volume fraction [118]. Another way of blending different polymers is co-extrusion, where pellets of different polymers are heated to above their melting temperature and pushed through a die together.Blends prepared by co-extrusion are generally more homogeneous than powder or pellet blends. Zhou and co-workers co-extrusion blended HDPE with LLDPE in increasing mass fractions of LLDPE. They observed that the composition of the blend is the dominant factor in terms of slow crack growth resistance, over the crystal thickness and the crystal thickness distribution. At 50% or more LLDPE, the slow crack growth resistance increases rapidly. They explain this phenomenon in terms of a molecular network. This is illustrated in figure 1.18. The LLDPE is responsible for the introduction of tie molecules between

the crystals, as the branching inhibits inclusion in the crystals. In this study, the LLDPE also has a higher molecular mass than the HDPE. Long chains have more chance of passing through different crystals and forming a tie molecule. At the point where all the crystals are connected to each other by tie molecules, so that the network becomes continuous, the network strength increases considerably [25, 97].

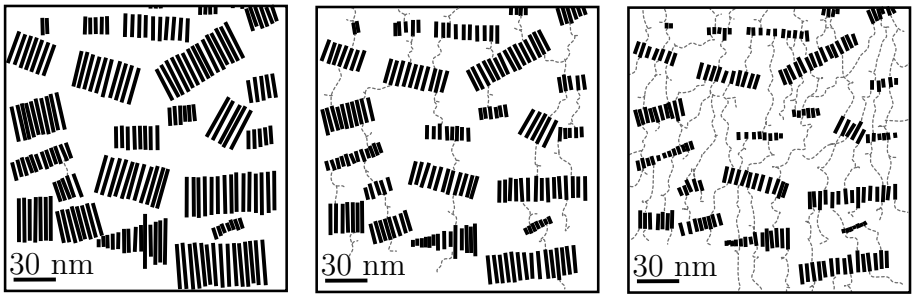

Figure 1.18: Schematic illustration of the crystal-tie molecule network, at 0%, 50% and 100% linear low density ethylene hexene copolymer. Parallel lines represent crystal regions, white space represents amorphous regions, reproduced from [97]

Other studies confirmed that PEs where the branches are predominantly present in the high end of the molecular mass distribution perform better in terms of slow crack growth. Soares and co-workers split different PEs into fractions according to the temperature at which they are soluble in 1,2,4-trichlorobenzene at a certain temperature. A higher temperature implies a higher crystallinity. Tie molecules can be found at intermediate temperatures, as they are partly crystalline and partly amorphous [115]. They found that the material with the best environmental stress crack resistance was that with the highest number of high molecular mass chains in this intermediate fraction [115]. More generally, the fraction of crystals needing larger undercooling to crystallise correlates with the environmental stress crack resistance [119]. These are imperfect crystals, containing more defects, tie molecules and random chain folding. This leads to an entanglement network in the solid state that is closer to that as present in the melt. Krishnaswamy and co-workers studied the influence of the short chain distribution on the slow crack growth of HDPE. It is known that branched PE with a broad

molecular mass distribution as produced with Ziegler-Natta catalysts tends to have the greatest short chain branch content on the shortest chains [28]. When metallocene is used as a catalyst, the short chains are more uniformly distributed over the molecular mass distribution. They found that placing the short chain branches on the longest chains yields a PE with superior resistance to slow crack growth. They ascribed this property to an increase in effective interlamellar connections. This increase in interlamellar connections is partly due to the crystallisation kinetics within the high molecular weight fraction, where the branches slow down the addition of new segments of the chain to an existing crystal front and hence the probability of a different part of the chain being incorporated in a different lamellae or forming an entanglement increases. In the case of a blend with an unbranched fraction of low molecular mass, this easily crystallisable fraction can incorporate parts of the long chains without side branches [28].

To fully exploit the good properties of a PE with short chain branches on the highest molecular mass chains and combine this with good processability, a cascade reactor process was developed and is now commonly used in industry [17]. It is shown schematically in figure 1.19. In the first reactor, low molecular weight HDPE is produced. This is then transferred to a second reactor, where comonomer is added to produce high molecular mass LLDPE, without adding catalyst. The type of comonomer added determines the length of the branches, the amount determines the branch density [11, 17]. A polymer thus produced is said to have a 'bimodal' molecular mass distribution. Lagaron and co-workers compared a bimodal polymer containing butyl branches to a range of homopolymers and copolymers. The bimodal polymer has an outstanding environmental stress crack resistance [87]. UHMWPE also has a superior environmental stress crack resistance, but does not have the benefit of easy processing. From the mechanical properties, Hubert and co-workers derived that bimodal PE has an increased number of chain entanglements and an increased tie molecule density compared to unimodal PE, but its crystallinity has not been reduced because of the contribution of the short, unbranched chains to the crystallinity [120, 121].

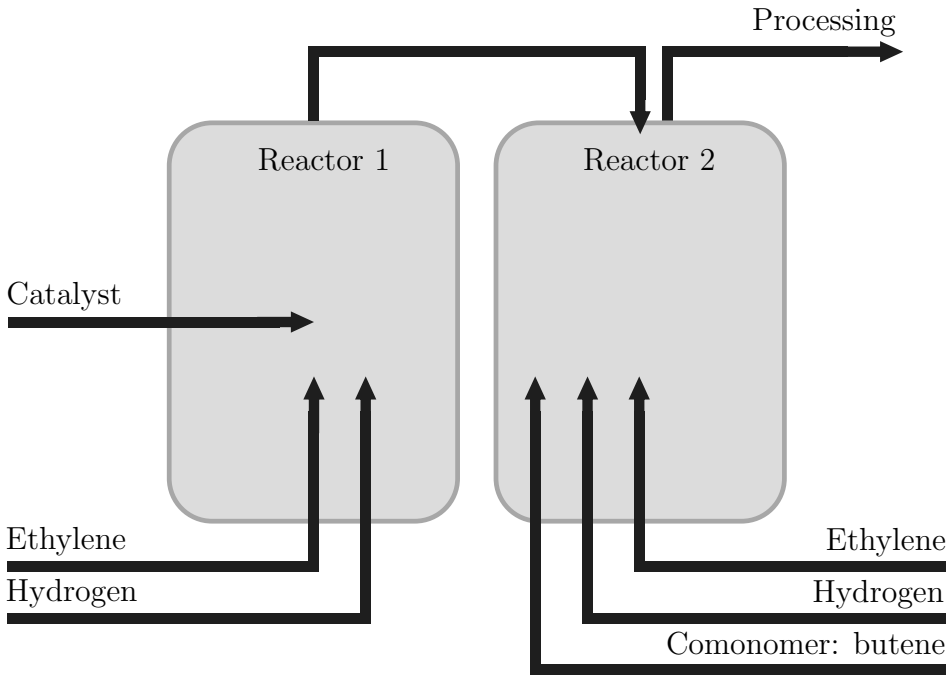

Figure 1.19: Schematic illustration of the bimodal process

The parameters of the reactor process and the catalyst used in it determine the molecular architecture of the polymer, and thus the properties in the melt and the solid state. Continuous efforts are made to improve both the catalyst and the process, in terms of quality of the final product and cost effectiveness of the production process.

1.4 Probing the effective molecular network

The discussion in section 1.3.3 shows that the physical origins of the effective molecular network are still the subject of debate. The contributions of different kinds of intercrystalline connections such as tie molecules and entanglements are not clear, as is the role of the crystal lamellae. Furthermore, the transient nature of the network poses a challenge in morphological studies. It would however be advantageous to devise short term tests on lab scale amounts of material that probe the effective molecular network in a similar way to slow crack growth, so materials can be ranked in terms of their resistance to slow crack growth. This section provides an overview of mechanical properties suggested in literature to correlate to slow crack

growth. Some of these tests are currently used in industry to test new materials on their resistance to slow crack growth.

1.4.1 Strain hardening modulus

Kurelec *et al.* (2005) predicted the resistance to slow crack growth from the average slope of the strain hardening of a material at 80°C, as shown in figure 1.20. This was confirmed in more recent papers. The strain hardening modulus (G_p) is the slope of the stress-draw ratio curve above the natural draw ratio [29, 101, 102, 122, 123]. The connection between the strain hardening response and the slow crack growth is can be understood when considering the structure of a craze. Section 1.3.1 discusses how the craze-crack transition depends on the effective molecular network in the stretched fibril at the tip of the craze. It can be assumed that the response of the bulk material drawn over its natural draw ratio depends on that same network. This was confirmed by Lagaron *et al.*, who used optical microscopy and micro-Raman spectroscopy to show that the molecular orientation of fibrils in a craze is comparable to that of cold-drawn samples. From this they conclude that PE drawn over its natural draw ratio is a good model for a fibril in a craze [124].

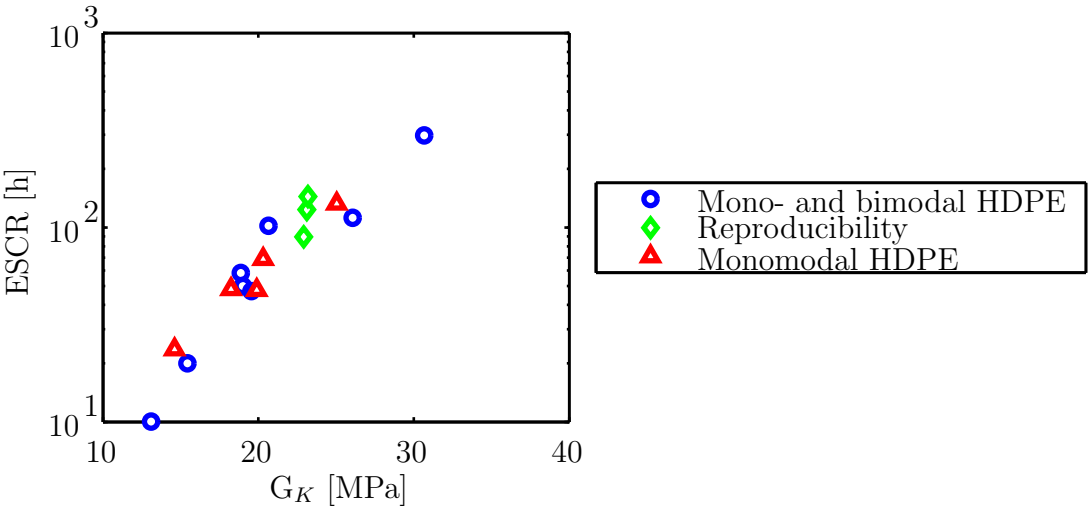

Figure 1.20: Strain hardening modulus as a function of environmental stress crack resistance for different monomodal and bimodal polyethylenes. The reproducibility data points show that the experimental variation in G_K is smaller than in ESCR, data from [122]

If the strain hardening modulus reflects the effective entanglement density of a purely entropic network, it could be described as

$$G_p = v_e R_u T, \tag{1.11}$$

with R_u the universal gas constant and T temperature [11]. It would then follow from equation 1.6 that

$$G_c \propto (G_p(\dot{\epsilon}, M_w, T))^2, \tag{1.12}$$

where $\dot{\epsilon}$ is the strain rate. However, the effective entanglement density as calculated from equation 1.11, using the strain hardening response at room temperature, is far greater than the entanglement density in the melt [11, 92]. Even if the number of effective entanglements increases due to for example tie molecules between crystals, the two entanglement densities should still have the same order of magnitude, and have the same trend as a function of temperature. Kramer pointed out that there is a difference of two orders of magnitude, and that the strain hardening modulus decreases with increasing temperature [125]. If strain hardening is caused by a purely entropic network, the strain hardening modulus should increase with increasing temperature. The network can thus not be purely entropic. Furthermore, the density of the network is time dependent and for a semi-crystalline polymer at room temperature, the strain hardening modulus also includes the time dependent contributions from the crystals, which makes it difficult to interpret the long term differences between materials. Therefore, the industry standard test for measuring the strain hardening modulus is a tensile test at 80°C. This temperature is chosen because it is above the α-relaxation temperature of PE. If polyethylene is cooled from the melting temperature until liquid nitrogen temperature (-196°C), three endo- or exothermic processes are observed. The first process (around 60°) is called the α-relaxation [126]. The α-relaxation is caused by chain motions in the interphase between amorphous and crystalline regions, and requires chain mobility in the crystal [127, 128]. Therefore, it requires pre-melting of imperfect crystals. When the crystal thickness decreases, the α-relaxation moves to lower temperatures [129, 130]. This process is not to be confused with the α-relaxation in glassy polymers, which is also known as the

glass transition and involves an increase in mobility of the chains in the amorphous phase. It has to be emphasized that from molecular dynamics simulations, it is seen that the motion of a chain through a crystal requires the same amount of energy, whether this chain is linear or branched and independently of the crystal thickness. The energy required for chain pull-out is 27 kcal/mol [131]. At the long time scales of slow crack growth, the transient network contributions of the crystals are heavily reduced. Testing the material above its α-relaxation temperature aims to reduce these transient contributions, to make it possible for manufacturers to rank PE in terms of its slow crack resistance at long time scales. However, it is not clear whether all the contributions of the crystalline fraction to the strain hardening modulus are eliminated at 80°C [11]. A possible way of probing this would be to use the transient stress dip test, originally described by Fotheringham and Cherry [132]. Describing the viscoelastic behaviour as a spring and a dashpot in parallel (the Kelvin-Voigt model), the spring represents the elastic and the dashpot the viscous contribution. To determine the stress on the separate arms, a stress dip test is performed. A specimen is extended until a certain total stress (σ_T). At this stress, the cross head is reversed and driven back until a lower stress. The stress is monitored. Three types of behaviour are possible: the stress decays immediately, the stress increases at first to decay afterwards or the stress stays constant at first to decay afterwards. Figure 1.21 shows these possibilities schematically. If the stress decays immediately, there is still stress in the dashpot and it decays over time. If the stress increases at first, the dashpot in under compression and as the dashpot flows, the stress increases. If the stress stays constant, the strain rate is the dashpot is initially zero. This means the stress just after the dip corresponds to the stress σ_R in the spring, or the molecular network. The difference between the total stress and the stress in the spring is the stress in the dashpot before the dip, σ_v [133].

Calculating the strain hardening modulus

As stated above, the strain hardening modulus is calculated from the stress-draw ratio curve above the natural draw ratio. Kurelec *et al.* calculate it

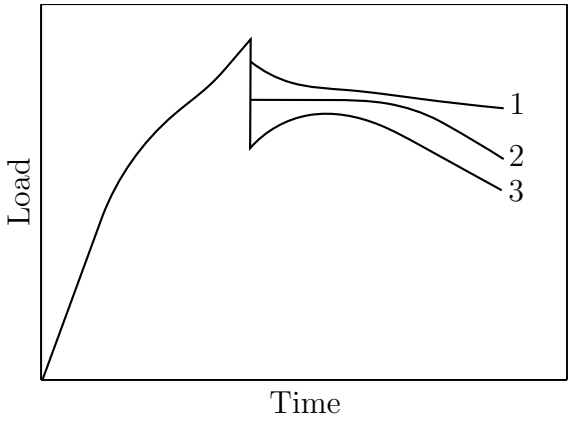

Figure 1.21: Schematic representation of the stress behaviour after the 'dip' during a transient stress dip test: (1) $\sigma_T > \sigma_R$, (2) $\sigma_T = \sigma_R$ and (3) $\sigma_T < \sigma_R$, after [133]

as

$$< G_K >= \frac{1}{N} \sum_{i=1}^{N} \frac{\sigma_{i+1} - \sigma_i}{\lambda_{i+1} - \lambda_i}, \tag{1.13}$$

the average slope of the stress - draw ratio curve, starting above the natural draw ratio until a maximum draw ratio [122]. In this work, when the strain hardening modulus is calculated in this way, it is referred to as $< G_K >$ (from 'Kurelec'). N is the number of difference quotients taken, λ is the draw ratio,

$$\lambda = \frac{\text{extension}_i}{\text{gauge length}}, \tag{1.14}$$

and σ_i is the stress,

$$\sigma_i = \frac{\text{load}_i}{A_i}, \tag{1.15}$$

where A_i is the cross section at time i,

$$A_i = \frac{A_{\text{initial}}}{\lambda_i}. \tag{1.16}$$

To be able to compare materials using this simple definition, the average slope should be taken over the same draw ratio range for every material. To overcome this drawback, McCarthy *et al.* apply a Neo-Hookean constitutive

model instead [123]:

$$\sigma = C + G_{NHSM}(\lambda^2 - \frac{1}{\lambda}), \tag{1.17}$$

where C describes the yield stress, extrapolated to draw ratio 0. This model is based on the Haward-Thackray model for rubber elastic networks and has been successfully applied to both amorphous and semi-crystalline polymers [134–136]. The model was developed for rubber networks with fixed junctions, assuming that the chain segments between the junctions obey Gaussian statistics and that the deformation is affine - the vector length of the chain changes with the same ratio as the corresponding length in the bulk material [29]. The strain hardening modulus calculated in this way will be referred to as G_{NHSM}. The model suggests that the stress at large deformations can be split into a frictional contribution from the yield, and a network contribution. The frictional force can be interpreted as the yield stress and remains constant. The network force is caused by the deformation of the molecular network, described as a rubber elastic network. It has to be noted that for this model to work at high draw ratios ($\lambda > 3$), the studied polymer cannot act as a rubber. A rubber network does not obey equation 1.17 at high draw ratios. So the network involved in strain hardening of semi-crystalline materials must continuously thin during drawing. Equation 1.17 assumes that the individual chains behave in a Gaussian way [136], which is not the case. A correction for this non-Gaussian behaviour is suggested by Haward based on the derivations of Treloar and Cohen [136–138]:

$$\sigma = \sigma_y + \frac{1}{3}G_{HT}\lambda(\lambda\frac{3-\frac{\lambda^2}{N}}{1-\frac{\lambda^2}{N}} - \frac{1}{\lambda^2}\frac{3-\frac{1}{\lambda N}}{1-\frac{1}{\lambda N}}), \tag{1.18}$$

where N is the number of flexible units ('Kuhn segments') between entanglements. Equation 1.18 has also been applied successfully to the stress-strain behaviour of semi-crystalline materials, and will be referred to as the Haward-Thackray model [136]. The strain hardening modulus as calculated using this equation will be referred to as G_{HT}.

1.4.2 Creep of oriented fibrils

A different mechanical test shown to correlate well with resistance to slow crack growth is creep. During a creep test, a material is held at constant stress and its deformation is monitored. Cawood *et al.* (1993) were able to predict the performance of different types of PE in terms of slow crack growth from their resistance to creep beyond the natural draw ratio [139]. Rose *et al.* expanded this work to include a wide range of PE homopolymers and copolymers. They also introduced the concept of the creep rate deceleration factor (CRDF), as the absolute value of the gradient of the linear part of the log(strain rate) - draw ratio curves resulting from creep tests:

$$CRDF = \frac{d[ln(\dot{\epsilon})]}{d\lambda}. \tag{1.19}$$

Figure 1.22 gives an example of a log(strain rate) - draw ratio curve for polyethylene. The linear part of the curve is indicated. This is the part over which the CRDF is calculated. It has to be noted that the definition of the CRDF makes use of the natural logarithm, while the visualisation makes use of the common logarithm. In this work, the visualisation is used to determine from which point the curve becomes linear, but the CRDF is always calculated using equation 1.19. The concept of this visualisation was first introduced by Sherby and Dorn in 1958 [140]. An example of those curves for different kinds of PE is given in figure 1.23 [86]. O'Connell *et al.* (1995) combined data from creep curves and found a reproducible and unique stress-strain-strain rate surface for each material. They also found that there was a limiting draw ratio at which the samples failed. When the surface is known, the time for a sample subjected to a given initial stress and strain to reach this limiting draw ratio can be calculated [84, 141–143]. They noticed that as the draw ratio of a material increases, the strain rate decreases; the material becomes more resistant against creep with increasing draw ratio. Strain hardening lengthens the time for the material to reach its limiting draw ratio. Similarly to the introduction of the CRDF, they introduced a different parameter, $\frac{d[ln(\dot{\epsilon})]}{d(\sigma)}$, where σ is true stress, to rank the materials in terms of creep resistance and consequently slow crack growth resistance. Caution has to be taken when using either of

these parameters. Creep seems to be the dominating factor in slow crack growth, but other material parameters such as yielding, natural draw ratio and failure draw ratio also have an influence. The excellent correlations from both Cawood's work and O'Connell's work however suggest that these other material parameters might somehow be reflected in the creep behaviour [84, 139].

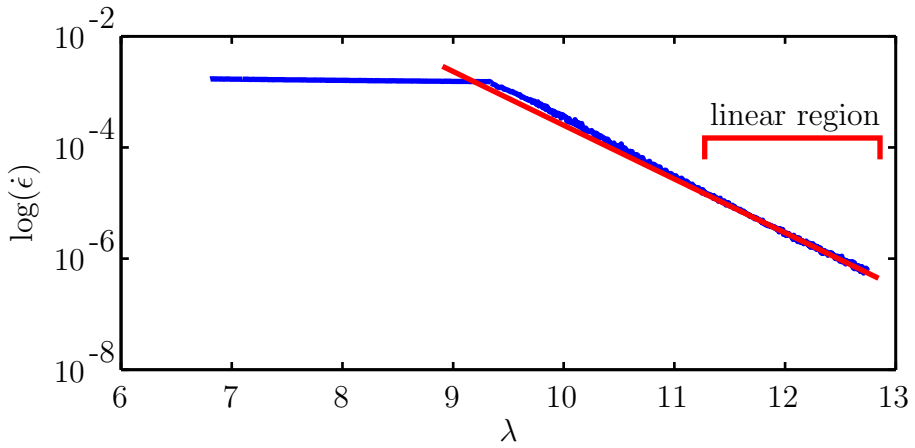

Figure 1.22: Example of a log(strain rate) - draw ratio curve for polyethylene, with the calculation of the creep rate deceleration factor indicated

1.4.3 Natural draw ratio

The natural draw ratio is the draw ratio at which the spherulitic structure of isotropic PE is completely transformed and fibrillation becomes the dominant deformation mechanism [75]. This is reflected by an upswing in the stress-draw ratio curve during tensile drawing. The molecular factors determining the natural draw ratio are widely agreed to be chain entanglements and intercrystalline tie molecules, forming a macromolecular network [66, 75, 144, 145]. As the macromolecular network is also assumed to dominate the slow crack growth behaviour and measurement of the natural draw ratio is fairly straightforward, researchers have tried to use the natural draw ratio to predict the slow crack growth behaviour of materials [28, 119, 146, 147]. Cazenave and co-workers found a good inverse correlation between the natural draw ratio and the environmental stress crack resistance of monomodal and bimodal polymers produced with different catalysts. As can be seen in figure 1.24, materials with a lower natural draw

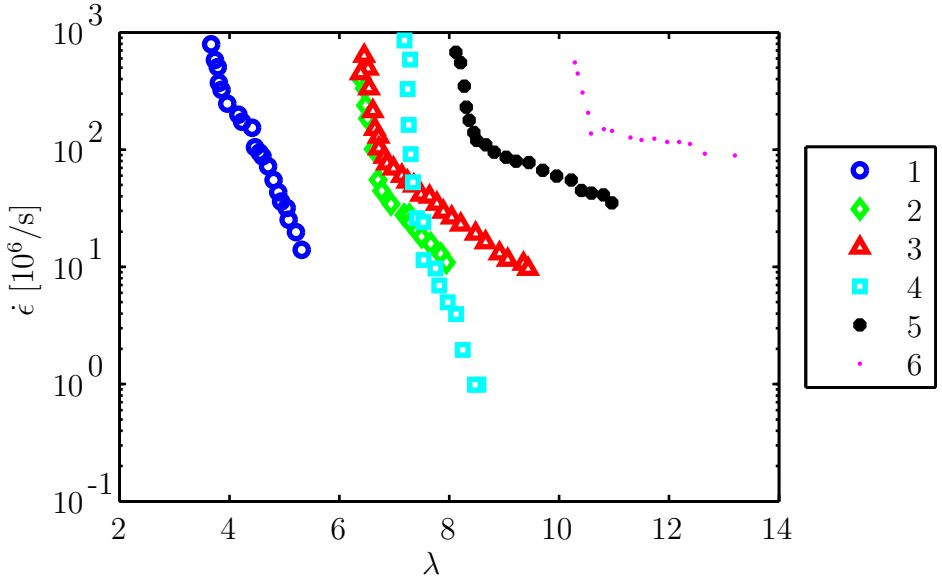

Figure 1.23: Strain rate as a function of draw ratio for selected samples: (1), (2), (3), (5), (6) polyethylene homopolymers with densities between 932 and 960 kg/m^3 and (4) polyethylene copolymer with 1.3/1000C ethyl branches, data from [86]

ratio have a higher environmental stress crack resistance [119, 146]. The density and the ratio of chains that need more undercooling to crystallise do not correlate unequivocally with environmental stress crack resistance. Decreasing natural draw ratio and decreasing density increase the ESC resistance. Ward and Sweeney remark that although the molecular factors determining the natural draw ratio may indeed by similar to those determining the chain disentanglement during slow crack growth, it seems safer to relate slow crack growth to the true stress-true strain-true strain rate surface (as explained in section 1.4.2), because this relates to the material after deformation [29]. Furthermore, time dependent processes that might play a role in the creep of the fibrils at the tip of the crack are not reflected in the natural draw ratio.

1.5 Scope of this work

This work aims to understand the physical phenomena behind creep failure in bimodal PE, as this presents the mechanism behind slow crack growth. The motivation to study slow crack growth is twofold. Firstly, understanding the physical mechanisms behind slow crack growth enables manufac-

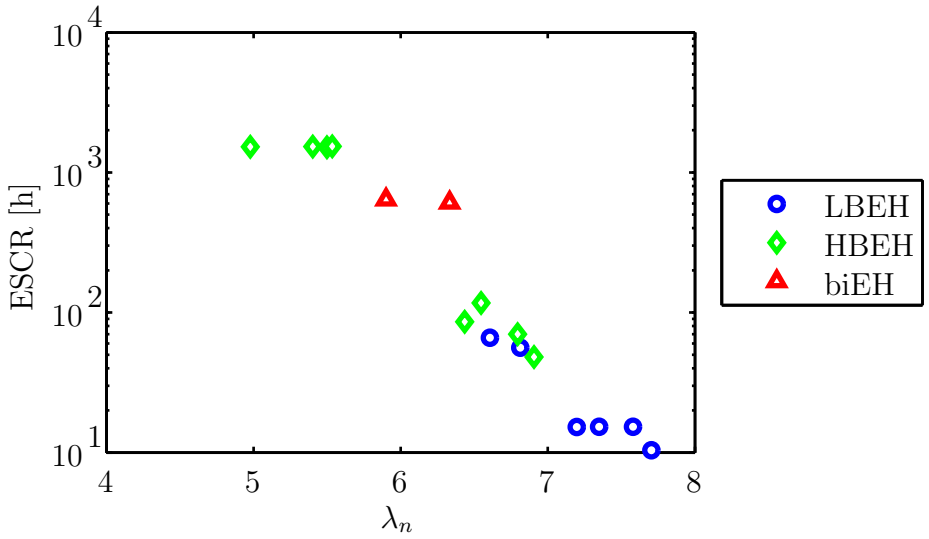

Figure 1.24: Environmental stress crack resistance as a function of natural draw ratio for LBEH: ethylene-hexene with a narrow molecular weight distribution and low comonomer content, HBEH: ethylene-hexene with a broader molecular weight distribution and high comonomer content, biEH: ethylene-hexene with a bimodal molecular weight distribution whereby the side chains are located on the long chains, data from [146]

turers to evaluate, rank and tailor the resistance of materials against it. Secondly, understanding which parameter or combination of parameters are important for slow crack growth is useful in the design of short-term tests to predict failure due to slow crack growth.

In this chapter, it has been shown that the slow crack growth resistance of PE correlates with the strain hardening modulus at 80°C. This correlation can be expected from the interpretation of both slow crack growth and strain hardening as a response of the effective molecular network. The creep behaviour and the natural draw ratio have also been shown to correlate with slow crack growth. PE drawn over its natural draw ratio is a good model for the fibrils as present at the tip of the crack [124]. Remaining questions include the magnitude and the nature of possible friction contributions (e.g. from crystals) to the strain hardening modulus and the effect of the interplay between molecular mass, branch content, entanglements, tie molecules and crystals on the structure property relations of PE. The creep behaviour and the strain hardening behaviour of a set of materials is studied. Do both tests result in the same ranking, as they should both

correlate with the resistance against slow crack growth? And if not, what are the physical mechanisms dominating each deformation mode?

Also as discussed in this chapter, longer chains, increased branch content and branching on the high end of the molecular mass distribution increase the resistance to slow crack growth. The development of new polymers incorporating these features challenges the protocols currently used in industry to rank materials in terms of their slow crack growth resistance. To study how these features interplay with each other to influence the slow crack growth in PE, materials with varying molecular architectures are produced for this work and their creep and strain hardening behaviour is studied. These materials are based on the commercial bimodal PEs currently used by industry in pipe applications. Eight materials are studied in total. A schematic of the materials is given in table 1.2. A detailed description of the materials can be found in the next chapter. Four bimodal PEs are studied, each consisting of a low molecular mass, unbranched fraction and a high molecular mass, branched fraction. The high molecular mass, branched fractions of these four bimodals were also produced and studied separately, to determine the influence of the dilution of the molecular network by the addition of the low molecular mass fraction. The nature of this dilution is studied: are the differences in behaviour the result of a straight mixture or does blending influence the structure of the materials? The high molecular mass, branched fractions are varied in terms of molecular architecture. Two levels of molecular mass (low and high) and two levels of branch content (low and high) are chosen and materials are produced with every combination of these two features:

- low molecular mass and low branch content,
- low molecular mass and high branch content,
- high molecular mass and low branch content and
- high molecular mass and high branch content.

Monomodal polyethylene	High molecular mass, high branch content	
	High molecular mass, low branch content	
	Low molecular mass, high branch content	
	Low molecular mass, low branch content	
Bimodal polyethylene	High molecular mass, high branch content	
	High molecular mass, low branch content	
	Low molecular mass, high branch content	
	Low molecular mass, low branch content	

Table 1.2: Schematic overview of the materials studied in this work

Chapter 2

Experimental methods

This chapter describes the methods used for structural and mechanical characterisation of the materials. The methods for structural characterisation are described in section 2.1. The methods for mechanical characterisation are described in section 2.2. Drawing of the materials and all the mechanical tests are performed at 80 ± 1 °C, the reason for this is explained in section 1.4.1. Molecular characterisation (section 2.1.1) is performed by the sponsor of this work. Transmission electron microscopy (section 2.1.2) is performed in collaboration with the sponsor of this work. The other tests described in this chapter are performed at the University of Leeds.

2.1 Structural methods

This section describes the methods used to study the structure and morphology of the materials used in this work.

2.1.1 Molecular mass distribution and branch content with liquid state proton nuclear magnetic resonance

The molecular structure of the materials is characterised by SABIC (Geleen, Netherlands). To determine end groups and branch content, liquid state proton nuclear magnetic resonance spectroscopy (^{1}H NMR) is performed. Samples are dissolved at 130°C in trichloroethylene stabilised by di-tertbutyl-paracresol. ^{1}H spectra are recorded at 120°C on a 600 MHz spectrometer.

To determine the molecular mass distribution, high temperature size exclusion chromatography (HT-SEC) is applied. Samples are dissolved in trichlorobenzene. A Polymer Laboratories column (13 µm PLgel Olexis, 300 x 7.5 mm) is used for the separation, and detection is done with a Polymer Char IR5 detector. The calibration is performed with linear polyethylene (PE) standards, based on [148].

2.1.2 Morphology with transmission electron microscopy

Transmission electron microscopy (TEM) is done on the compression moulded samples to study their homogeneity and observe potential differences in lamellar thickness between the samples. The samples are prepared by embedding in resin and exposing their internal surface by trimming at -120°C in a Leica Ultracut UCT with a Reichert FC S unit. Then, the samples are stained for 24 hours in a 2% RuO_4 solution. Ultra-thin sections of 70 nm are cut with the Leica Ultracut UCT, using a DiATOME cryo 45° knife. The sections are collected on copper 50 or 100 mesh grids with Formvar film. The samples are then examined in a Philips CM200 transmission electron microscope (using a LaB_6 cathode) at an acceleration voltage of 120 kV. To enhance the contrast between crystalline and amorphous regions, high angle annular dark field scanning TEM (HAADF-STEM) is applied. This allows the detector to detect electrons scattered over very wide angles. When working with heavy atoms, this leads to a higher contrast between light and heavy atoms in the resulting image. As the samples in this work are stained using RuO_4 and this is more absorbed by one of the phases, HAADF-STEM yields an increases contrast between the two phases. The lamellar thickness is calculated using image analysis software ImageJ.

2.1.3 Thermal properties with differential scanning calorimetry

Differential scanning calorimetry (DSC) is performed on a TA DSC Q2000 with DSC Q series software to observe the melting temperature (T_m) and the heat of fusion (ΔH_f), which are used to calculate the lamellar thickness (L_c) and the crystallinity ($X_{c,h}$) respectively. The equipment is calibrated once a month. Firstly, the heat flow is corrected for the thermal capacitance

and thermal resistance of the equipment parts. This is done by first running the DSC without a sample or pans, and then running it with sapphire disks on the sample and reference platforms. Then, the heating curve of indium between 100°C and 180°C is used to calibrate the temperature and the heat flow. However, the temperature behaviour of the calorimeter can become non-linear at low temperatures. Therefore, calibration with adamantane is also performed. Tzero aluminium hermetic pans are used in a nitrogen atmosphere. The measurements are performed following the ASTM standard D7426, under a nitrogen atmosphere. First, the samples are cooled to -10°C and held isothermal for 5 min. Then they are heated to 200°C at a heating rate of 10°C/min and held isotherm for 5 min. Subsequently, the samples are cooled to -10°C at the same rate and held isothermal for 5 min, after which they are heated again to 200°C at the same rate. The peak crystallization temperature is calculated from the cooling curve, the melting enthalpy from the heating curve. Depending on the purpose of the analysis, the first or second cycle are used. The first cycle reflects the state of the material including the thermal history, the second cycle should be the same for a material regardless of its thermal history, as that has been erased during the first cycle. The lamellar thickness is calculated using the Gibbs-Thomson equation:

$$T_m = T_m^0(1 - \frac{2\sigma_e}{\Delta H_f^0 L_c}), \tag{2.1}$$

where T_m^0 is the equilibrium melting temperature of a lamella of infinite thickness (145.5°C), σ_e is the interfacial free energy over the basal surface of the lamellae (associated with the energy of chain folding during crystallisation, 90 mJ/m^2) and ΔH_f^0 is the enthalpy of fusion of the crystalline phase (290 J/cm^3) [149, 150]. The crystallinity can be calculated from DSC by dividing the measured heat of fusion ΔH_f by ΔH_f^0 [151].

2.1.4 Crystallinity with density gradient column

The crystallinity of isotropic and drawn samples is also measured using a density gradient column. The column is built in house and consists of a 1.7 l tube with 2 mm markers inside a water jacket. The water jacket is held at 23.0 ± 0.2°C. The tube is filled with gradient mixtures of degassed iso-

propyl alcohol and degassed distilled H_2O, using a H& D Density Gradient Column Filler. The bottom density and top density of the column are set according to the desired range and precision of the experiment. The column is calibrated with at minimum 10 calibrated density gradient column floats, spread evenly over the density range. The samples are cut into symmetrical specimens, with the largest dimension smaller than 6 mm. The specimens are thoroughly wetted with isopropyl alcohol before being introduced to the column. To make sure air bubbles are not influencing the measurement, multiple specimens are measured for each sample and visual inspection is carried out. The specimens are left to settle for at least 6 hours before their density is measured. The crystallinity ($X_{c,d}$) is then calculated using

$$X_{c,d} = \frac{\frac{1}{\rho} - \frac{1}{\rho_a}}{\frac{1}{\rho_c} - \frac{1}{\rho_a}}, \tag{2.2}$$

where ρ_a is the density of purely amorphous PE (853 kg/m^3) and ρ_c is the density of purely crystalline PE (1004 kg/m^3) [152]. The precision of this method depends on the difference between the top and the bottom density of the column but is never lower than 0.1 kg/m^3 for an individual measurement. Three measurements are done to calculate the standard error.

2.1.5 Orientation with polarised light microscopy

The short range orientation of isotropic samples is measured using a Zeiss Jena polarised light microscope and the Michel-Levy chart. The thickness ($\pm$ 0.001 mm) is measured using a micrometer. Polarised white light is sent through the sample, and the resulting colour is compared with the colours on the Michel-Levy chart at the relevant thickness. The chart then indicates the birefringence of the sample.

For drawn samples, a compensator is used. The specimen is kept under strain after drawing by fitting it in a harness (as seen on figure 2.1), before taking it out of the Instron and mounting it on the microscope stage. A Zeiss Jena compensator with an Ehringhaus composite calcite plate and a function table at 589.3 nm, based on [153], is used to calculate the retardation. The thickness ($\pm$ 0.001 mm) of the specimen at the location of the measurement is measured using a micrometer and hence the birefringence

Δn ($\pm$ 0.001) is calculated. Using the pseudo-affine deformation model, the corresponding draw ratio can be calculated [154, 155]. The pseudo-affine deformation model treats the polymer as an assembly of uni-axial, rod-like units embedded in an elastic matrix, building on the notion that the birefringence is largely due to the geometrical orientation of the crystallites [156]. When a strain is applied to the polymer, the rod-like crystallites rotate towards the drawing direction. It can be calculate that if Θ is the original angle between the symmetry axis of the rod-like unit and the drawing direction, and Θ' is the angle between these two axes after drawing, that

$$tan(\Theta') = \frac{tan(\Theta)}{\lambda^{-3/2}}. \tag{2.3}$$

The relationship between birefringence and draw ratio can then be calculated as

$$\Delta n = \frac{\Delta n_{max}}{2}[\frac{3}{1-K^2} - \frac{3Kcos^{-1}K}{(1-K^2)^{3/2}} - 1], \tag{2.4}$$

with

$$K = \lambda^{-3/2}, \tag{2.5}$$

and Δn_{max} the birefringence of a perfectly oriented crystal [29]. For PE, this is 0.058 [157]. The birefringence was measured in samples just after drawing (standard error $\pm$ 0.001 from multiple measurements on one sample) and after a set time at room temperature. After 24 hours, the birefringence does not change. After eight days, the birefringence increases by 0.006. Therefore, all birefringence measurements were done within 24 hours after drawing.

2.1.6 Orientation with polarised Raman spectroscopy

The bond orientation of isotropic and drawn samples is measured using polarised Raman spectroscopy. A Renishaw RM1000 Raman spectrometer, controlled by GRAMS suite software, is used. A 515.32 nm solid state laser (Spectra-Physics) with a maximum output power of 50 mW is focused on the specimen to a diameter of 5μm, using an Olympus ultra-long working

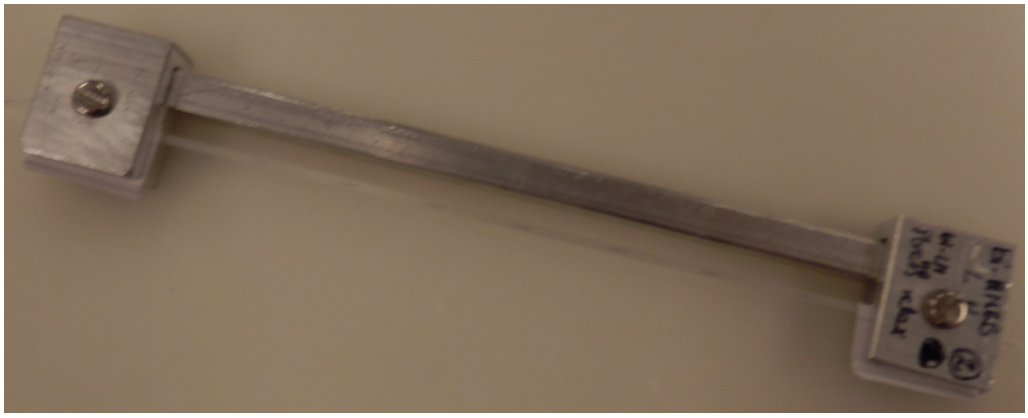

Figure 2.1: Harness used to keep specimens under strain after taking out of the Instron

distance 50x objective lens on a Leica optical polarising microscope. The laser photons interact with molecular vibrations in the specimen, and are excited from the ground state to a virtual energy state. Different interactions are possible, outlined in figure 2.2: Rayleigh scattering, Stokes and anti-Stokes scattering. Stokes and anti-Stokes scattering are inelastic, and the energy difference between the incident and scattered photons is specific for the chemical groups present in the material. Stokes scattering is more intense than anti-Stokes scattering and hence this is the response used for analysis. Furthermore, the polarisation direction of the scattered light depends on the molecular orientation in the material.

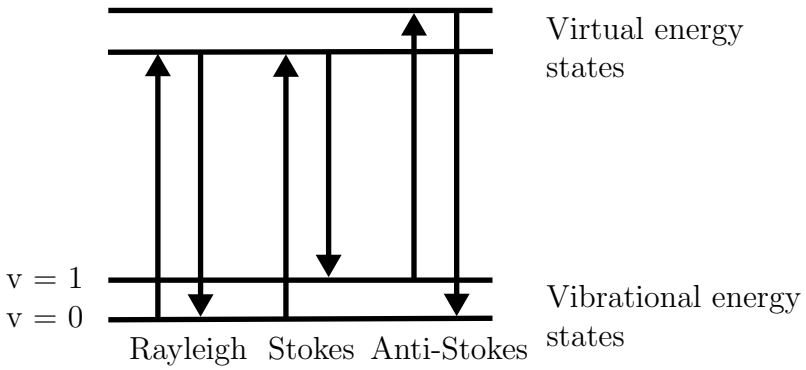

Figure 2.2: Model for the elastic (Rayleigh) and inelastic (Stokes and anti-Stokes) scattering of laser photons by the molecular groups. v is the vibrational quantum number [158]

The scattered photons are detected by the objective in terms of inten-

sity as a function of the Raman wavenumber. The Raman wavenumber is related to the difference between the incident and the scattered frequency [158]. A 1800 lines/mm grating is used in the Raman system to provide a measurement range of the frequency shift from 600 cm^{-1} to 1600 cm^{-1} with a resolution of 0.5 cm^{-1}. The polariser and analyser are arranged so that spectra are collected both in parallel and perpendicular direction, as shown in figure 2.3. The samples are mounted on a rotating stage and spectra are taken every 10 degrees between 0° and 180°. At every angle, the intensity measured with the analyser perpendicular to the incident light (figure 2.3 b) is divided by the intensity measured with the analyser parallel to the incoming light (figure 2.3 a). This is called the depolarisation ratio R. If R is constant as a function of angle, the sample is isotropic.

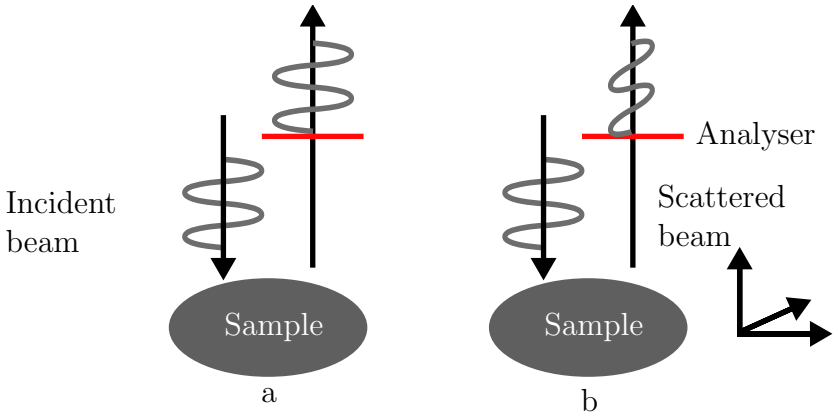

Figure 2.3: Set-up for the measurement of the depolarisation ratio: (a) analyser is parallel to incident light and (b) analyser is perpendicular to incident light

In a cylindrically symmetric system, the degree of orientation of a molecular bond can be described using β, the angle between the bond and a specific axis, for example the drawing axis. To describe the degree of orientation of a system involving many bonds, mean field theory can be applied to find an orientation distribution function [159]. For a uniaxial system with rod-like molecular bonds, Humphries, James and Luckhurst calculated that the pseudo-potential field can be defined as

$$U = \sum_{L}^{n} < u_{LL:n} > P_L(cos\beta) < P_L(cos\beta) >, \tag{2.6}$$

with $< u_{LL:n} >$ the statistical average of the expansion coefficient, $P_L(cos\beta)$ the L^{th} Legendre polynomial and $< P_L(cos\beta) >$ the statistical average of the Legendre polynomials [159]. These last terms are also called the order parameters. Using this definition of the pseudo-potential field, they define the orientation distribution function as

$$f(\beta) = \frac{e^{-\frac{U}{kT}}}{\int e^{-\frac{U}{kt}} sin(\beta) d\beta}, \tag{2.7}$$

with k the Boltzmann constant. After expansion of this equation to the second rank and simplification,

$$f(\beta) = (\frac{1}{8\pi^2})(1 + \frac{5}{2} < P_{200} > (3cos^2\beta - 1), \tag{2.8}$$

with

$$< P_{200} >=< P_2(cos\beta) > \tag{2.9}$$

as mentioned above. Furthermore, for a cylindrically symmetric system Jones *et al.* calculate the depolarisation ratio R as

$$R = \frac{I_\perp}{I_\parallel} \tag{2.10}$$

with

$$I_\perp = \frac{1}{15}(-1 + r^2) + < P_{200} > [\frac{1}{21}(-1 + r^2)] \tag{2.11}$$

and

$$I_\parallel = \frac{1}{5} + \frac{4}{15}r + \frac{8}{15}r^2 + < P_{200} > [\frac{1}{21}(3 + r - 4r^2)(1 + 3cos(2\theta))] \tag{2.12}$$

with r the differential polarisability ratio. Using equation 2.10 to fit the depolarisation ratio as a function of angle θ, $< P_{200} >$ can be found. The degree of orientation of the sample increases with increasing $< P_{200} >$ value.

Background subtraction and fluorescence correction are done using software developed by Wayne State University [160, 161]. The method used is the 'adaptive minmax method', where a polynomial fit is applied to the

background radiation. An example of a Raman spectrum is given on figure 2.4. The assignments of the Raman bands are given in table 2.1, according to references [162–166]. To find the positions of the Raman bands, the spectra are fitted using software developed at the University of Maryland at College Park. Bands a, b, c, d, e and f are fitted with a Gaussian, while bands g, h, i and j are fitted using Lorentzian fits (these two functions result in the lowest least square errors for the respective peaks). An example of the fitting of the Raman bands is given in figure 2.5. Band b, d and f cannot be fitted at every angle due to their low intensity and/or proximity to a different band with stronger intensity. It is difficult to determine the error introduced by the background subtraction and fluorescence correction, but the standard deviation of the order parameters is ± 7% after repeated measurements. This will be taken as the minimum error on the order parameter.

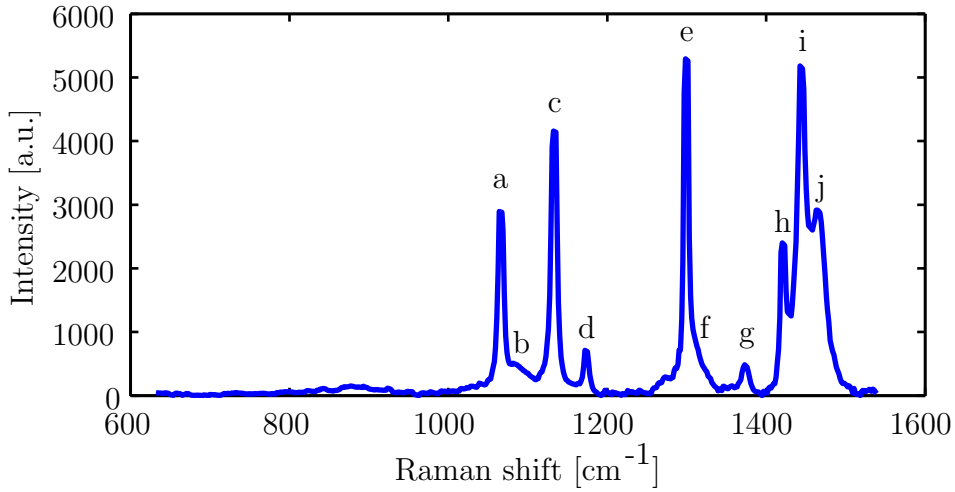

Figure 2.4: Example of a Raman spectrum for polyethylene. The letters indicate the Raman bands corresponding to table 2.1

The band intensities are used to calculate the orientation of the amorphous phase and the crystalline phase in the samples. From table 2.1, it can be seen that the 1080 cm^{-1} (b) Raman band is caused by C-C stretching in the amorphous chains, the 1130 cm^{-1} (c) band is caused by symmetric C-C stretching in the trans chains (both amorphous and crystalline) and the 1420 cm^{-1} (h) band is caused by CH bending in the orthorhombic crystalline chains. The order parameter of these phases can be calculated by fitting the depolarisation ratio as a function of angle. In the case of the

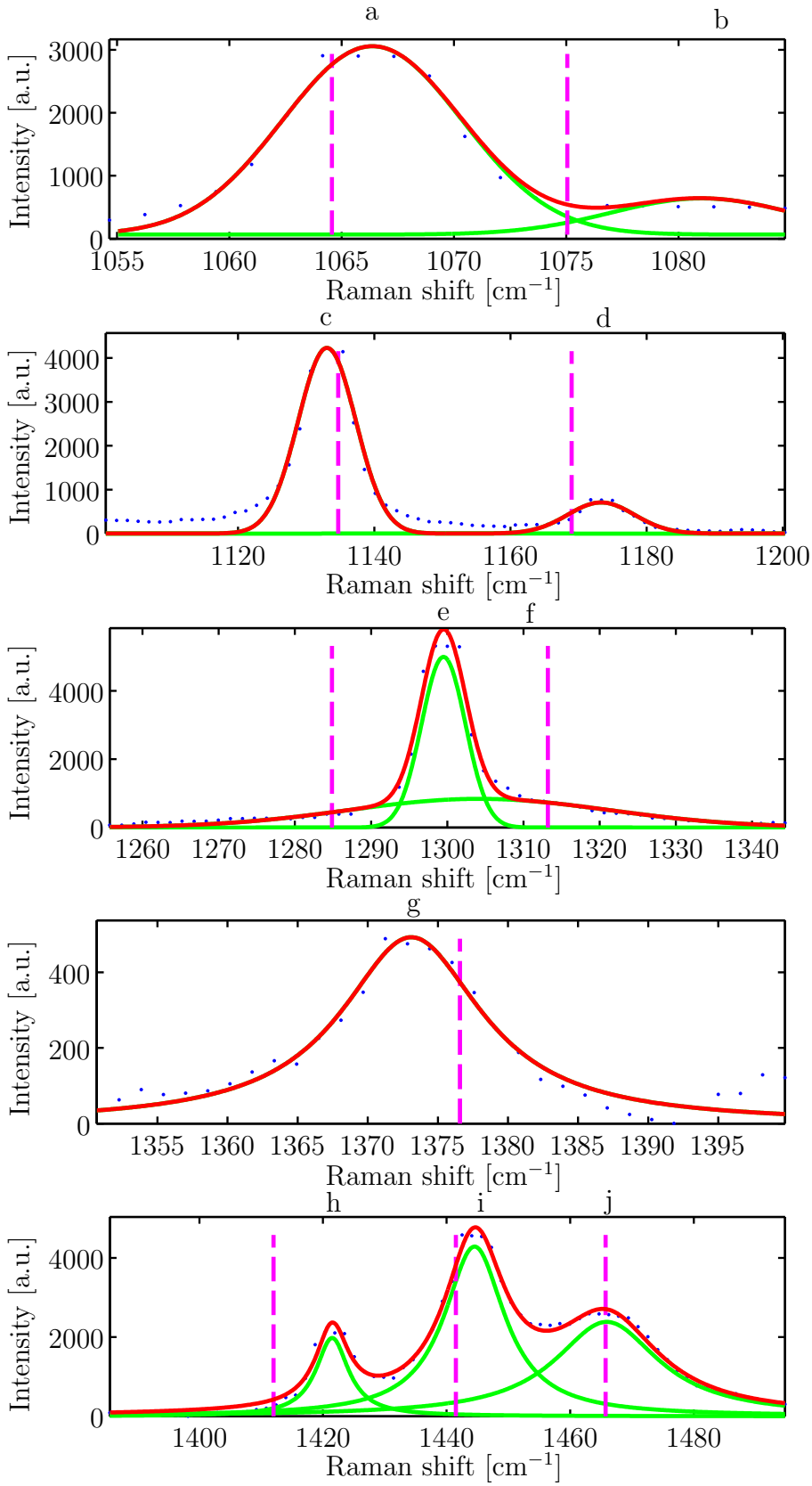

Figure 2.5: Example of the fitting of the Raman bands for bi-HMHB. Blue dots - data, red line - overall fit and green line - peak fits

	Frequency [cm^{-1}]	Phase	Mode
a	1060	Trans chain	Asymmetric C-C stretching
b	1080	Amorphous	C-C stretching
c	1130	Trans chain	Symmetric C-C stretching
d	1170	Crystalline (with amorphous contributions)	CH_2 rocking
e	1296	Crystalline	CH_2 twisting
f	1310	Amorphous	CH_2 twisting
g	1370	Crystalline	CH_2 wagging
h	1420	Crystalline (orthorhombic)	CH_2 bending CH_2 wagging
i	1440	Amorphous trans	CH_2 bending
j	1460	Amorphous melt-like	CH_2 bending

Table 2.1: Assignment of Raman bands for polyethylene, based on [162–166]

bonds in the sample being oriented preferably in the 0° direction, the perpendicular and parallel intensities, and the resulting depolarisation ratio, are shown in figure 2.6. Only fits that result in R-square values over 0.90 are accepted. The fitting error on $< P_{200} >$ is given for all values. The low intensity of band b means that the fitting process cannot be applied to this peak. Therefore, a qualitative parameter reflecting the orientation is given for this peak. This qualitative parameter is 1-I_{yy}/I_{zz}. I_{yy}/I_{zz} is the depolarisation ratio at 0° (or 180°). Errors are introduced because of tilting of the sample, so this parameter is not precise and can only be used to find large differences between materials or draw ratio. A high orientation results in 1-I_{yy}/I_{zz} close to 1. Both the c and the h Raman band are high in intensity and thus return good fitting results. Because the h band gives an indication of crystalline orientation and the c band is a combination of crystalline and amorphous orientation, the combination of these two order parameters gives an indication of the orientation trends in the amorphous phase.

The stability of the Raman orientation at room temperature was checked

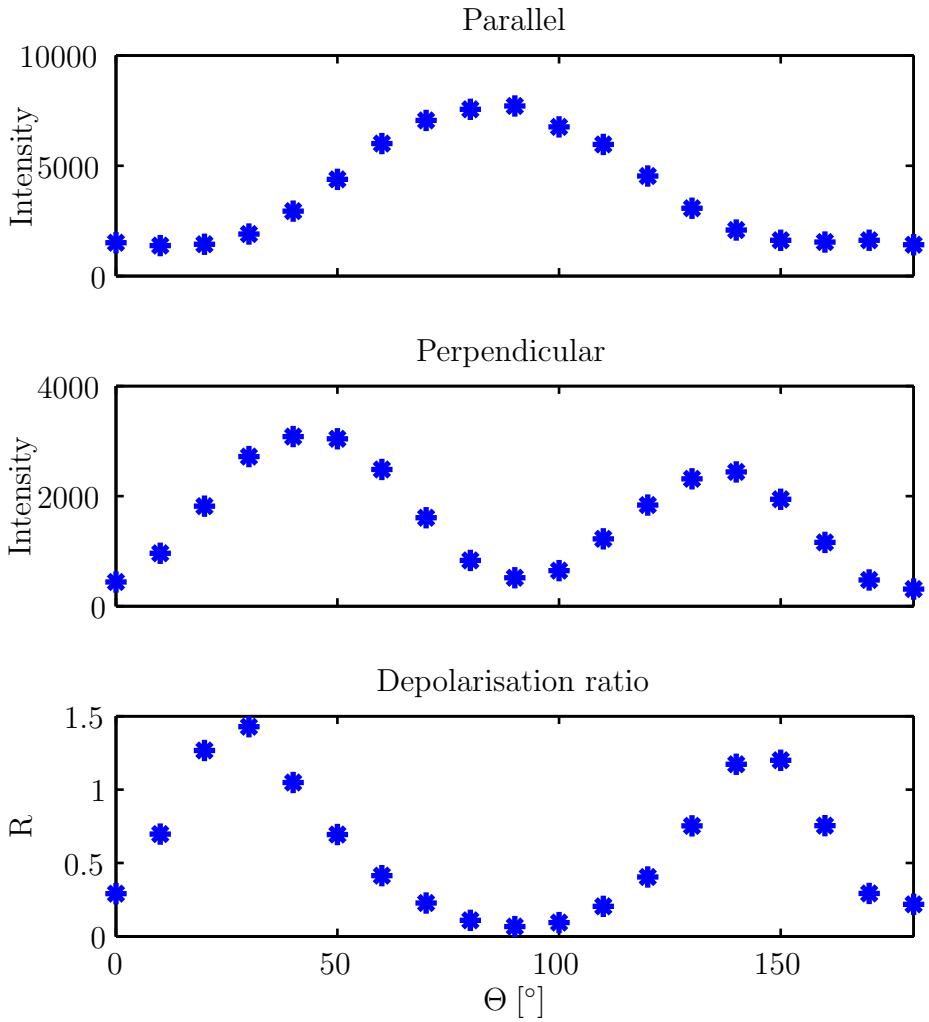

Figure 2.6: Example of the parallel and perpendicular Raman intensity and the depolarisation ratio as a function of rotation angle of the sample

by measuring the Raman orientation parameters just after drawing and after eight days at room temperature. For band b, $< P_{200} >$ is originally 0.17 $\pm$ 0.02, and after eight days 0.23 $\pm$ 0.04. For band c, it is originally 0.57 $\pm$ 0.01 and after eight days 0.60 $\pm$ 0.02. For band h, it is originally 0.71 $\pm$ 0.04 and after eight days 0.76 $\pm$ 0.04. It can be concluded that the orientation parameters do not change significantly. All Raman measurements are done within five days after drawing.

2.2 Mechanical methods

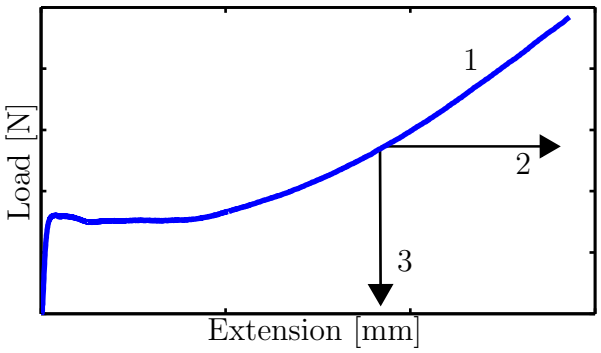

Figure 2.7: Overview of the load - extension conditions applied during the mechanical tests: 1) strain hardening at constant true strain rate, 2) creep at constant load, 3) stress relaxation at constant extension

Mechanical tests are used to probe the constitutive behaviour of the materials studied in this work under different deformation modes. The materials are drawn beyond their natural draw ratio as explained in section 3.3.1 to resemble the fibrils as present at the crack tip. The relationship between stress and draw ratio is tested under different conditions. In figure 2.7 a schematic overview of these conditions is given. When the instantaneous draw ratio increase per time is held constant and the stress is monitored, the resulting path is path 1 (strain hardening). Keeping the draw ratio increase per time constant implies that the cross head speed accelerates during the test. When from a certain stress or draw ratio, the stress is held constant and the draw ratio is monitored, the resulting path is path 2 (tensile creep). When from a certain stress or draw ratio, the draw ratio is held constant and the stress is monitored, the resulting path is path 3 (stress relaxation).

Some of the tests described in this section are combinations of the different paths. All the mechanical tests are performed on pre-drawn samples. The samples are pre-drawn at a temperature of 80°C, a constant true strain rate (see definition in section 2.2.1) of 3 10^{-2}/s, until an extension of 135 mm. A detailed explanation of why these parameters are chosen for pre-drawing can be found in section 3.3.1.

2.2.1 Strain hardening tests

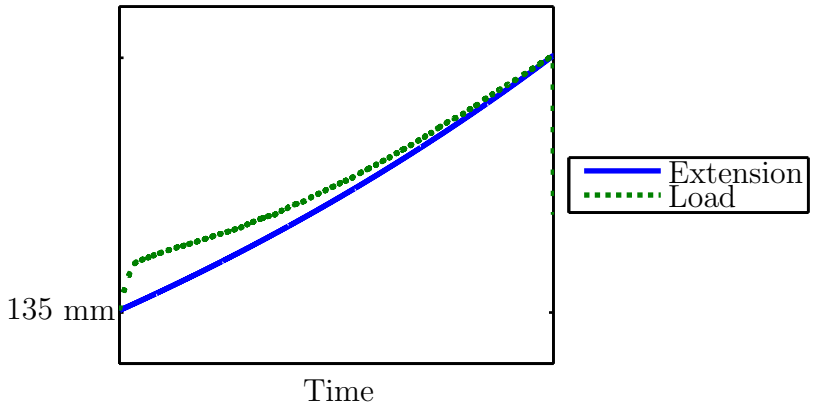

Figure 2.8: Extension and load as a function of time during a strain hardening test. A pre-drawn sample is drawn at constant true strain rate until failure or maximum extension in the equipment. The knee seen at the start of the test occurs at the maximum load reached during pre-drawing. Between pre-drawing and the actual test, some load relaxation takes place. The knee point marks the point in the test were the material reaches the point as before relaxation again

Strain hardening tests are performed on the materials after initial drawing, on an Instron model 5564 using Bluehill software to program the test and output the data. The specimen is pre-drawn as described in section 3.3.1. After measuring the dimensions, the temperature is stabilised at 80°C again and the sample is drawn at a set constant true strain rate until failure or until the maximum possible extension in the Instron (375 mm) is reached (a schematic of this test can be found in figure 2.8). The true strain rate is calculated as

$$\dot{\epsilon} = \frac{ln(\frac{\text{extension}_{t_i}}{\text{extension}_{t_{i-1}}})}{t_i - t_{i-1}}. \tag{2.13}$$

Because extension$_{t_{i-1}}$ increases over time, to keep the strain rate constant, the cross head speed of the Instron will increase. Time (± 0.01s), extension (± 0.1 mm) and load (± 0.04 N) are recorded. From these parameters, draw ratio (± 0.1), true strain rate (± 0.05%) and true stress (± 2 %) are calculated. The draw ratio is calculated using equation 1.14, where the extension is corrected for the compliance of the equipment (measured at the relevant loads using a stiff steel rod) and $\lambda_{\text{after pre-drawing}}$ is the draw ratio measured at the end of pre-drawing. The true stress is calculated using equations 1.15 and 1.16. G_K is calculated by averaging the slope between draw ratio and 7 and draw ratio 11, for every 0.1 draw ratio. G_{NHSM} and G_{HT} are calculated by fitting the stress-strain curves to the equations described in section 1.4.1, using the Levenberg-Marquardt algorithm in Matlab. The strain hardening protocol is tested to check the sensitivity of the strain hardening modulus to changes in the experimental set-up. The results of these tests are described in section 4.2.1.

2.2.2 Tensile creep tests

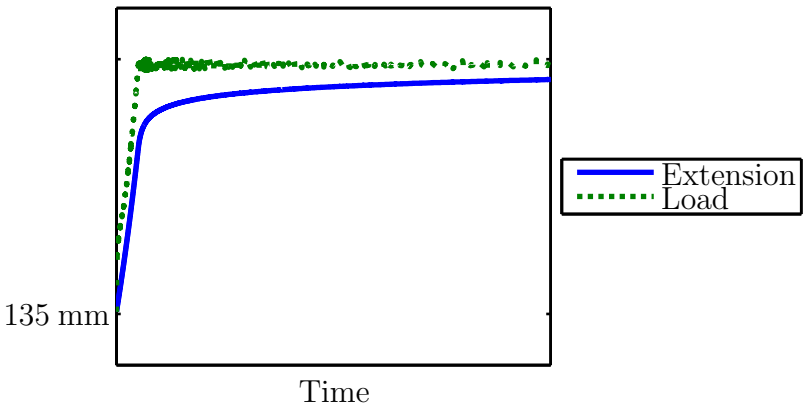

Figure 2.9: Extension and load as a function of time during a tensile creep test. A pre-drawn sample is drawn to a pre-set load. Then the load is held constant for a minimum of 12 hours unless failure occurs earlier

Tensile creep tests are performed on an Instron model 5564 using Bluehill software to program the test and output the data. The specimen is pre-drawn as described in section 3.3.1. After measuring the dimensions, the temperature is stabilised at 80°C again and the sample is drawn at a true strain rate of 1.667 ± 0.001 10^{-3}/s until a set load. Then, the load is held

constant for 12 hours, unless failure or the maximum possible extension in the Instron (375 mm) are reached earlier (a schematic of this test can be found in figure 2.9). Time, extension and load are recorded. From these parameters, draw ratio, true strain rate and true stress are calculated as described in section 2.2.1.

The creep rate deceleration factor (CRDF) ($\pm$ 3%) is calculated by plotting the logarithm of the true strain rate as a function of draw ratio, as explained in section 1.4.2. If a linear region is reached during the creep test, this is isolated and the slope of this region is calculated using fitting tools in Matlab. For each test, an average true stress and draw ratio are calculated over the linear region.

2.2.3 Stress relaxation tests

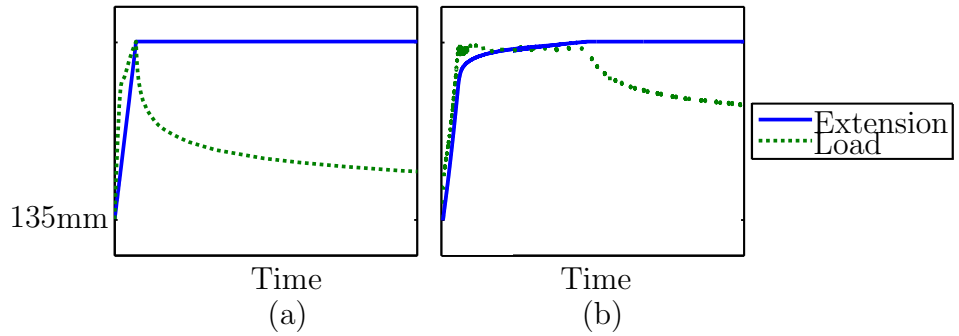

Figure 2.10: Extension and load as a function of time during a stress relaxation test, (a) after strain hardening, (b) after tensile creep. In (a), a pre-drawn sample is drawn at a constant true strain rate until a pre-set load. Then the extension is held constant and the load monitored. In (b), a pre-drawn sample is drawn at a constant true strain rate until a pre-set load. Then the load is held constant for a pre-set time. After this time, the extension is held constant and the load monitored

Stress relaxation tests are performed on an Instron model 5564 using Bluehill software to program the test and output the data. The specimen is pre-drawn as described in section 3.3.1. Stress relaxation is done at different points during the strain hardening. After measuring the dimensions, the temperature is stabilised at 80°C again and the sample is drawn at a set constant true strain rate until a set extension. Then, the extension is held constant for a set time (a schematic of this test can be found in figure 2.10

(a)). Stress relaxation is also done at different points during the creep. For this, after measuring the dimensions, the temperature is stabilised at 80°C again and the sample is drawn at a set constant true strain rate until a set load. The load is held constant for a set time. Then, the extension is held constant for a set time (a schematic of this test can be found in figure 2.10 (b)). For both tests, time, extension and load are recorded. From these parameters, draw ratio, true strain rate and true stress are calculated as explained in section 2.2.1. The fitting of the stress relaxation curves is done using fitting tools in Matlab.

2.2.4 Transient stress dip tests

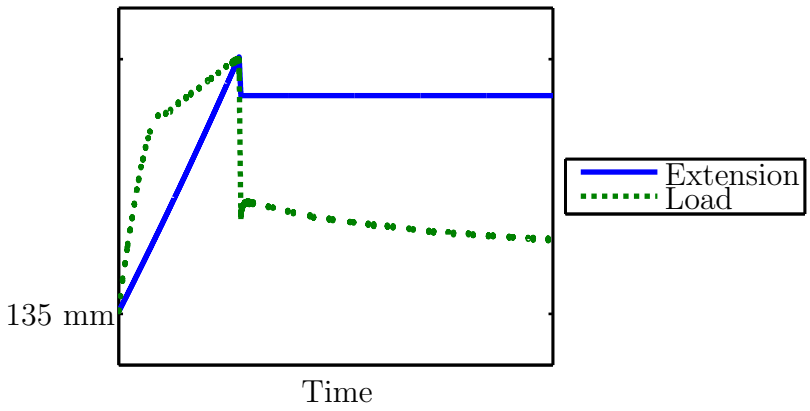

Figure 2.11: Extension and load as a function of time during a transient stress dip test. A pre-drawn sample is drawn until a pre-set load. Then, the extension is decreased until a pre-set extension. Then the extension is held constant and the stress is monitored

Transient stress dip tests are performed on an Instron model 5564 using Bluehill software to program the test and output the data. The specimen is pre-drawn as described in section 3.3.1. A schematic of the test is given in figure 2.11. After measuring the dimensions, the temperature is stabilised at 80°C and the sample is drawn at a true strain rate of 1.667 $\pm$ 0.001 10^{-3}/s until a set extension (this is the first part in figure 2.11, until the maximum for both extension and load). Then, the Instron cross head is driven back at a true strain rate of 5.49 10^{-3}/s until a set extension. This is the maximum true strain rate that can be used to avoid overshooting in terms of extension in the Instron. This part can be seen as the vertical 'dip' in figure 2.11. This extension is held constant for a set time or until it

is clear what behaviour the material is exhibiting (the last part, with constant extension and decreasing load, in figure 2.11). Time, extension and load are recorded. From these parameters, draw ratio, true strain rate and true stress are calculated as explained in section 2.2.1.

As explained in section 1.4.1, to interpret the transient stress dip test, the viscoelastic behaviour of the sample is described by a spring and a dashpot in parallel. If after the dip, a stress plateau is observed (as described in figure 1.21), it can be assumed that the stress in the dashpot is zero, and hence the stress on the plateau equals the stress in the spring. A problem with the application of the transient stress dip tests on the bimodal materials studied in this work however can be seen in figure 2.12. This figure gives an example of the behaviour after the 'dip' for bi-HMLB, after transient stress dip tests at a strain rate of around 10^{-3}/s. The dips are given in draw ratio. A clear difference in behaviour can be seen between the 0.03 dip and the 0.40 dip. An initial stress plateau, however, cannot be detected. This might be obscured by a small 'bump' in the stress just after the dip, probably caused by the Instron adjusting the extension after the dip. The detection of the dip where the total stress after the dip σ_T and the recovery stress σ_R are equal is therefore not reliable, and these tests are not further pursued.

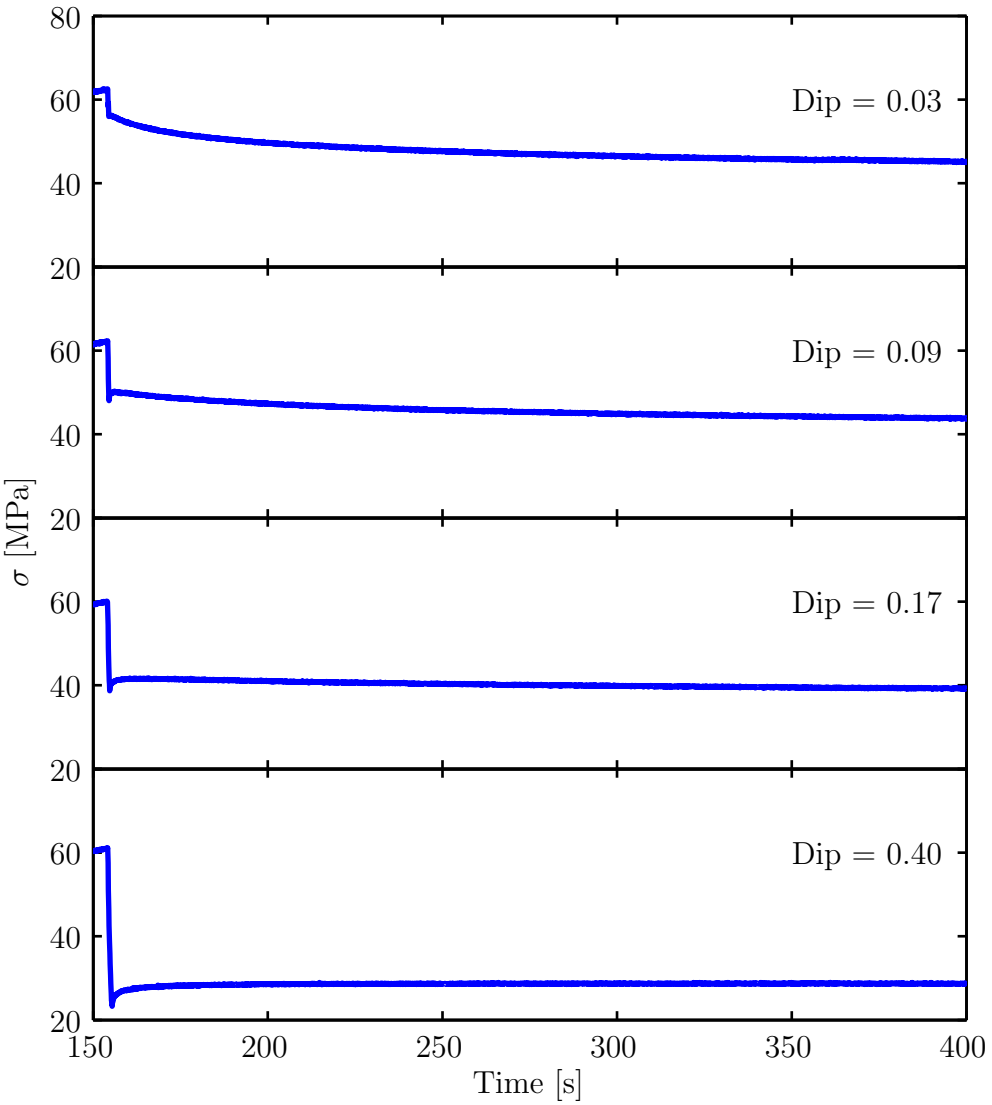

Figure 2.12: The behaviour after a stress dip test for bi-HMLB

Chapter 3

Production and characteristics of the materials

The aim of this work is to understand the deformation behaviour of a polyethylene (PE) fibril at the tip of the crack. As discussed in chapter 1, this material is drawn beyond its natural draw ratio. To mimic this, isotropic samples are also drawn beyond their natural draw ratio before testing. The characteristics of the material up until reaching the natural draw ratio are described in this chapter. It is important to know these so the relevance of the different characteristics for the behaviour of the oriented material can be studied. This chapter is divided into three sections. These correspond to the three stages in the material production. In section 3.1, the production and characteristics of the PE as produced by the reactor are described. In section 3.2, the production and characteristics of the PE after compression moulding are described. In section 3.3, the production and characteristics of the pre-drawn materials are described.

3.1 Production and characteristics of the powder and pellet materials

This section describes the synthesis of the PE materials and their characteristics. Table 1.2 gives a schematic overview of the materials produced for this work. The molecular mass (M) and branch content (β) are varied, and for each combination, a bimodal material is produced as well as its high

molecular mass fraction separately.

3.1.1 Production of the powder and pellet materials

Materials for this work are produced by SABIC (Geleen, Netherlands). Section 1.5 explains how the desired characteristics for the materials were determined. Four types of bimodal PE and five types of monomodal PE are synthesised and in all cases a Ziegler-Natta catalyst is used. For bimodal PE, a two step batch reactor process is used, to replicate the cascade reactor process as shown before in figure 1.19. Instead of two reactors, one reactor is used, but the processing conditions are changed in the same manner as for the cascade process. The settings for the first step are the same for all the bimodals. This means that the low molecular mass fraction in these materials is the same. In the second step, the settings are varied to obtain differences in molecular mass and branch content. To obtain a higher molecular mass, the hydrogen over ethylene pressure ratio is decreased. To obtain a higher branch content, the butene over ethylene pressure ratio is increased. The names used to discuss the properties of the materials is based on their different molecular architectures. The prefix 'bi-' indicates the material is bimodal. In the following code, H stands for high, L for low, M for molecular mass and B for branch content. So bi-HMHB is a bimodal PE, with a high molecular mass and a high branch content in its high molecular mass fraction. This is relative to the other materials produced for this work. The proportion of low molecular mass fraction is 51 % for all materials. For monomodal branched PE, a single reactor process was used. The same settings were used as for the second part of the process. So the monomodal materials are a model for the high molecular mass fraction as present in the bimodal material. The label 'R2-' precedes the names of these materials. For completeness, also the low molecular mass fraction of the bimodal materials is produced separately. This is the same for all the bimodal materials and is named 'R1'. The materials and their production parameters can be found in table 3.1. $m_{catalyst}$ is the amount of catalyst added to the reactor en $P_{C_2H_4}$ the ethylene pressure applied. H_2/C_2H_4 and C_4H_8/C_2H_4 are the ratios of the hydrogen pressure to the ethylene pressure and the butene pressure to the ethylene pressure respectively. For some materials, more than one batch is produced to have an adequate amount of

material. These batches are mixed in powder form before further processing. All materials are stabilised with Irganox 1010, Irgafos 168 and calcium stearate. The bimodal materials are extruded to form pellets. This is not possible for the R2 materials, as their very high molecular mass inhibits the extrusion process.

3.1.2 Characteristics of powder and pellet material

Table 3.3 shows the results of the molecular characterisation, with the methods described in section 2.1.1. Figures 3.1 and 3.2 show the molecular mass distributions. It can be seen from figure 3.2 that the molecular mass of the R1 material indeed corresponds to the low molecular mass fraction in the bimodal materials. The same applies to the R2 materials. There is a distinct difference between the high molecular mass and low molecular mass materials. The results for the bimodal materials in table 3.3 are averages of the low and high molecular mass fractions present in these materials. An indication of the branch content of the high molecular mass fractions present in the bimodal materials can be found by applying a simple rule of mixtures. If the branch content of the high molecular mass fractions present in a bimodal material would be the same as that of the corresponding R2 material, the average branch content can be calculated:

$$\beta_{\text{bimodal}} = 0.51\beta_{\text{R1}} + 0.49\beta_{\text{R2}}. \tag{3.1}$$

The results of this simple calculation can be found in table 3.2. The calculated branch content lies close to the measured branch content, and there is a distinct difference between the HB and LB materials. The branch content for R1 and the bimodal materials is plotted as a function of molecular mass in figure 3.3. For R1, the branch content is so low that it is indistinguishable from random noise. This is expected as no comonomer was added, although a very small amount of branching can be formed due to the catalyst. For R2, branching is present over the whole width of the molecular mass distribution. It is significantly higher for the HB materials than for the LB material. The bimodals have an increasing branch content with molecular mass. This is expected as they are a combination of the unbranched R1 material and the branched R2 material.

		R1					
	Batch code	130110-b2a	130130-b2a				
Step 1	$P_{C_2H_4}$ [10^5 Pa]	2.2	2.2				
	H_2/C_2H_4	4.5	4.7				
		R2-HMHB		R2-HMLB	R2-LMHB	R2-LMLB	
	Batch code	130826-b1b	131004-b2b	130207-b1b	130827-b1b	130910-b1b	130930-b1b
Step 2	$P_{C_2H_4}$ [10^5 Pa]	1.8	1.8	1.5	1.8	1.8	1.8
	H_2/C_2H_4	0.008	0.005	0.016	0.079	0.071	0.073
	C_4H_8/C_2H_4	0.147	0.150	0.051	0.181	0.085	0.090
		Bi-HMHB		Bi-HMLB	Bi-LMHB	Bi-LMLB	
	Batch code	140206-b1		131002-b1	140212-b1	140205-b1	
Step 1	$P_{C_2H_4}$ [10^5 Pa]	2.2		2.2	2.2	2.2	
	H_2/C_2H_4	4.490		4.465	4.533	4.480	
Step 2	$P_{C_2H_4}$ [10^5 Pa]	2.7		2.7	2.7	2.7	
	H_2/C_2H_4	0.006		0.015	0.076	0.080	
	C_4H_8/C_2H_4	0.140		0.051	0.177	0.089	

Table 3.1: Production parameters of the materials used in this study. $m_{catalyst}$ is the amount of catalyst added to the reactor en $P_{C_2H_4}$ the ethylene pressure applied. H_2/C_2H_4 and C_4H_8/C_2H_4 are the ratios of the hydrogen pressure to the ethylene pressure and the butene pressure to the ethylene pressure respectively

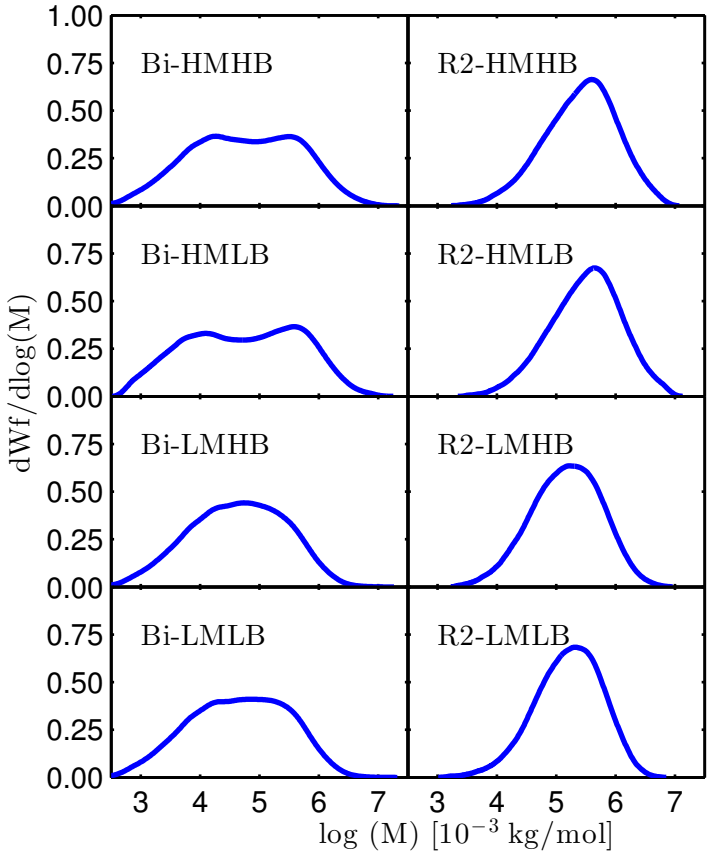

Figure 3.1: Molecular mass distribution of the bimodal and monomodal branched materials, M is molecular mass, W_f is the weight fraction

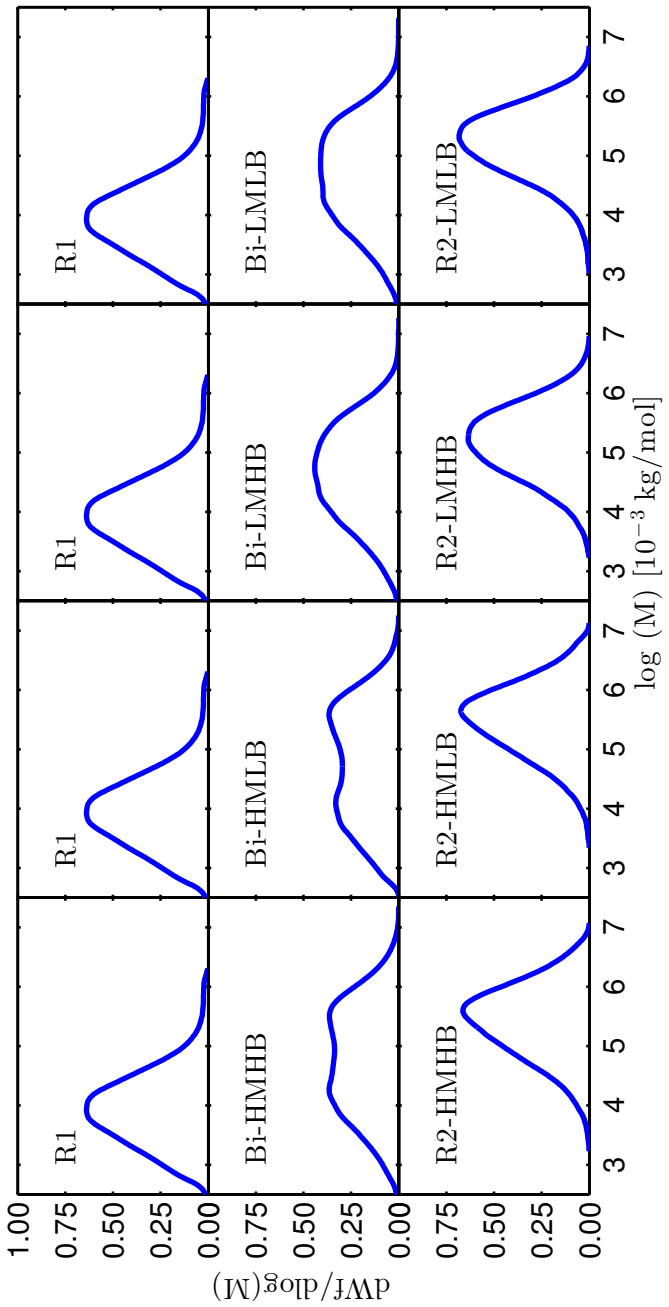

Figure 3.2: Molecular mass distribution of the bimodal and monomodal branched materials, M is molecular mass, W_f is the weight fraction

	β, ethyl [/1000C]	
	Calculated	Measured by ^{1}H NMR
Bi-HMHB	5.7	6.4
Bi-HMLB	2.6	2.4
Bi-LMHB	7.1	8.3
Bi-LMLB	3.9	3.9

Table 3.2: Comparison of the calculated and measured ethyl branch content of the bimodal materials. The calculated branch content was calculated using equation 3.1, with β_{R1} and β_{R2} the measured values as in table 3.3 for the R1 and the R2 materials respectively

The presence of long chain branching in the materials is investigated. The formation of long chain branches can be an undesired side effect of PE synthesis, and influences the flow behaviour of the material. As the mechanical tests will be done on the bimodal and R2 materials, only these materials were investigated. The intrinsic viscosity (η) was plotted as a function of molecular mass and compared to the reference plot for a linear PE, for which the parameters of the work of Scholte *et al.* are used [148]. This is shown on figure 3.4. The plots deviate only slightly from the linear PE reference plot.

The thermal properties for the initial materials are measured from the second melting endotherm of the DSC curves. The results are given in table 3.4. The crystallinity of the bimodal materials is higher than for the R2 materials. This is due to the addition of the easily crystallisable R1 fraction. Calculating the crystallinity of bi-HMHB following a simple rule of mixture using the data for R1 and R2-HMHB, a crystallinity of 62.6 % would be expected. This is close to what is found from DSC, and also holds for the other materials. This implies that the trends within the two families of materials, R2 and bimodal, are the same. The crystallinity is higher for the low branched than for the highly branched materials, in each family. There is a small difference between R2-HMLB and R2-LMLB, which can be ascribed to R2-LMLB having a slightly higher branch content. The difference in branch content between R2-HMHB (11.5/1000C) and R2-LMHB (14.3/1000C) does not result in a difference in crystallinity.

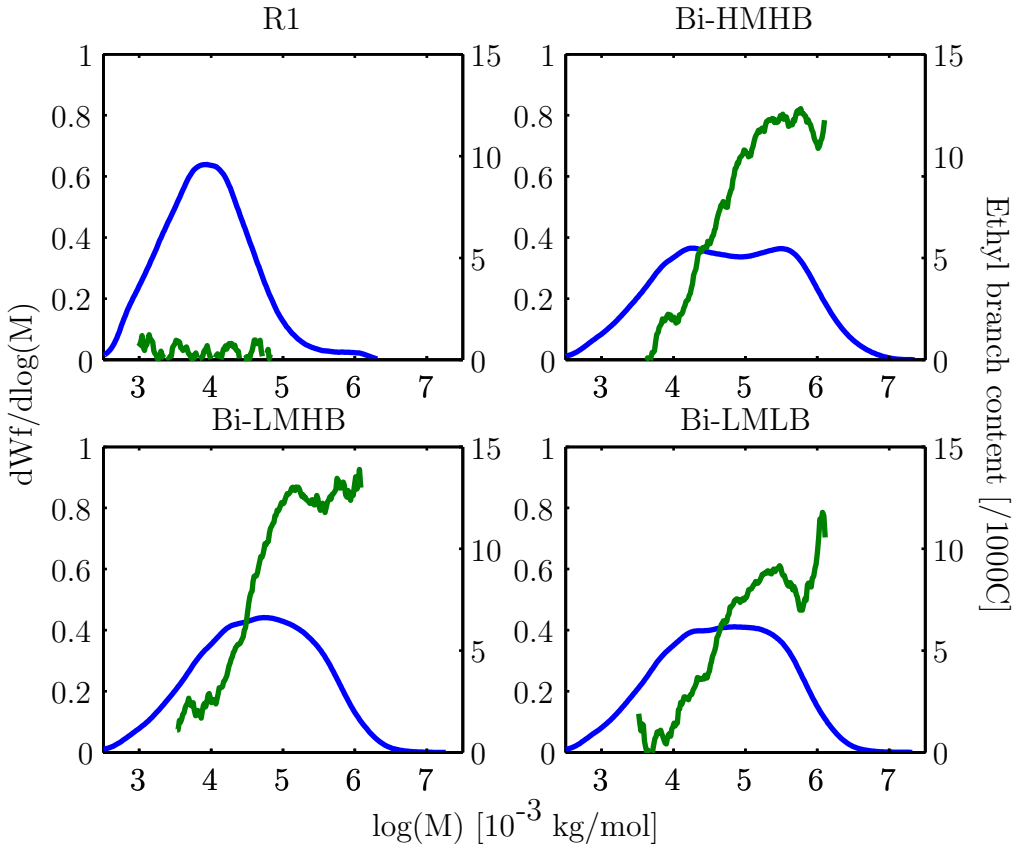

Figure 3.3: Ethyl branch content as a function of molecular mass for R1, bi-HMHB, bi-LMHB and bi-LMLB

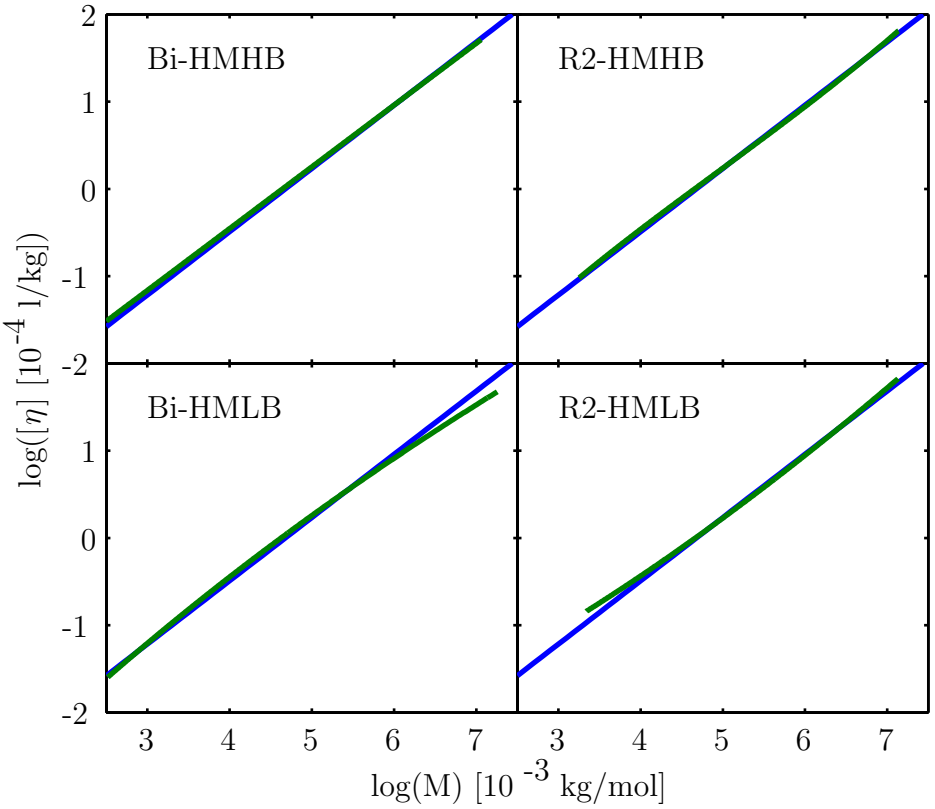

Figure 3.4: Intrinsic viscosity as a function of molecular mass for Bi-HMHB, R2-HMHB, Bi-HMLB and R2-HMLB, with the Mark-Houwink reference for linear polyethylene in blue

	R1	R2-HMHB	R2-HMLB	R2-LMHB	R2-LMLB
ρ [kg/m^3]	not measured	917 ± 1	926 ± 1	917 ± 1	925 ± 1
β, methyl [/1000C]	0.3	undetectable	undetectable	0.1	0.3
β, ethyl [/1000C]	0.2	11.5	5	14.3	7.7
Butene content [w%]	0.1	4.6	2.0	5.7	3.1
M_n [kg/mol]	3.6	89	110	57	61
M_w [kg/mol]	33	610	720	340	330
M_z [kg/mol]	440	2000	2400	1200	960
M_w/M_n	9.2	6.9	6.5	6.0	5.4
M_z/M_w	13.3	3.3	3.3	3.5	2.9
		Bi-HMHB	Bi-HMLB	Bi-LMHB	Bi-LMLB
ρ [kg/m^3]		943 ± 1	951 ± 1	942 ± 1	950 ± 1
β, methyl [/1000C]		0.8	0.2	undetectable	0.3
β, ethyl [/1000C]		6.4	2.4	8.3	3.9
Butene content [w%]		2.6	1.0	3.3	1.6
M_n [kg/mol]		7.8	8.6	7.9	7.7
M_w [kg/mol]		330	335	195	195
M_z [kg/mol]		2200	2000	1200	1200
M_w/M_n		42.3	39.0	24.7	25.3
M_z/M_w		6.7	6.0	6.2	6.2

Table 3.3: Characteristics of the bimodal and monomodal materials in powder and pellet form. The reproducibilities for M_n, M_w and M_z are 10-20%, 10% and 10-20% respectively

	ΔH_f [J/g]	T_m [°C]	$X_{c,h}$ [%]	L_c [m]
R1	250 ± 2	130 ± 1	87 ± 1	$1.77 \pm 0.02\ 10^{-8}$
R2-HMHB	108 ± 2	121 ± 1	37.2 ± 0.7	$1.07 \pm 0.02\ 10^{-8}$
R2-HMLB	143 ± 3	127 ± 1	49 ± 1	$1.40 \pm 0.02\ 10^{-8}$
R2-LMHB	108 ± 2	120 ± 1	37.3 ± 0.7	$1.07 \pm 0.02\ 10^{-8}$
R2-LMLB	130 ± 3	124 ± 1	44.8 ± 0.9	$1.22 \pm 0.02\ 10^{-8}$
Bi-HMHB	176 ± 4	129 ± 1	61 ± 1	$1.57 \pm 0.02\ 10^{-8}$
Bi-HMLB	210 ± 4	130 ± 1	73 ± 1	$1.72 \pm 0.02\ 10^{-8}$
Bi-LMHB	178 ± 4	128 ± 1	61 ± 1	$1.52 \pm 0.02\ 10^{-8}$
Bi-LMLB	189 ± 4	129 ± 1	65 ± 1	$1.64 \pm 0.02\ 10^{-8}$

Table 3.4: Results of thermal analysis at 10°C/min for the powder and pellet materials

In table 3.5, the crystallinity for the powder and pellet materials as measured from the density (see section 2.1.4) is shown. The same trends as for the crystallinity calculated from the heat of fusion are present, but the absolute values are different, and diverge more from the heat of fusion crystallinities with increasing branch content. The crystallinity as measured from density does not make a distinction between the HMLB and LMLB materials within one family, whereas the crystallinities as measured from heat of fusion are still ranked as expected from their branch contents (the branch content of R2-HMLB is 5, while the branch content of R2-LMLB is 7.7). A comparison of the two crystallinities is shown on figure 3.5. In literature, this difference has been attributed to the contribution from the less mobile amorphous layers between crystal lamellae [167]. Between crystal lamellae, there is a fraction of the amorphous phase in which the mobility is higher than for a crystal, but still low because of the constraint of being surrounded by less mobile crystals. This fraction is called the interphase. In materials with a higher branch content (and hence thinner lamellae), this fraction has been found to be higher [168, 169]. The effect of the interphase on DSC crystallinity is small because it only takes into account the crystalline heat of fusion. For the crystallinity as measured from the density column, however, the larger density of the interphase compared to the density of the amorphous phase leads to an overestimate of the crystallinity. To quantify this effect, the thickness and volume fraction of the interphase

would need to be measured. This has been done in the past using Raman (using the longitudinal acoustic modes and the internal modes) and solid state NMR [170, 171]. This does however not fall within the scope of this work. However, the discrepancy between DSC and density results has to be kept in mind when discussing crystallinity in the following chapters.

	$X_{c,d}$ [%]
R2-HMHB	46.5 ± 0.5
R2-HMLB	52.2 ± 0.5
R2-LMHB	46.6 ± 0.5
R2-LMLB	51.8 ± 0.5
Bi-HMHB	63.3 ± 0.6
Bi-HMLB	68.2 ± 0.7
Bi-LMHB	62.9 ± 0.6
Bi-LMLB	67.6 ± 0.7

Table 3.5: Crystallinities based on densities as given in table 3.3 for powder and pellet materials

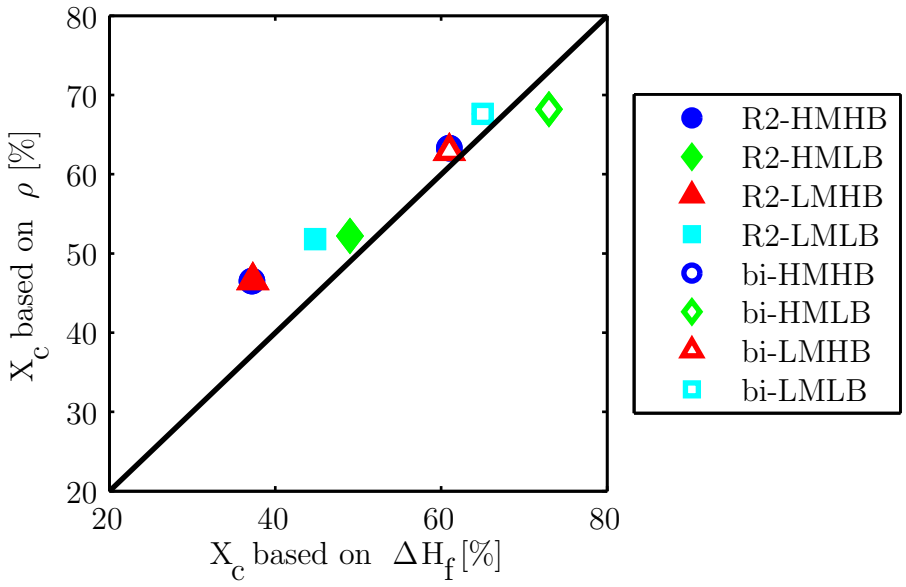

Figure 3.5: Crystallinity based on density as a function of crystallinity based on heat of fusion. Solid line is where the two crystallinities are the same

3.2 Production and characteristics of the compression moulded sheets

This section describes the compression moulding of the R1, R2 and bimodal materials and the characteristics of the resulting sheets. Compression moulding of the R1 material results in very brittle sheets due to the low molecular mass of this material. Therefore characterisation of this sheet is not possible.

3.2.1 Compression moulding

The pellets and powders are compression moulded into sheets at Intertek Chemicals and Pharmaceuticals (Geleen, the Netherlands) on a Fontijne Grotnes hot press. Table 3.6 summarises the details of the moulding procedure. The powders or pellets are spread out evenly over the mould to avoid flow and thickness variations. Melinex flexible film is placed between the material and the press to avoid transcrystallisation - where the spherulites nucleate on the mould sufrace, causing an inhomogeneous surface layer in the sheet - and to facilitate the release of the sheet after moulding. All sheets are pressed at a thickness of 250 μm, however the resulting thickness can vary and is checked for each sample individually prior to pre-drawing.

Time [s]	Temperature [°C]	Pressure [10^3 Pa]
300	180	390
180	180	4710
900	180	80
		Cooling at 1.7°C/s
	Press opens when temperature is below 25°C	

Table 3.6: Summary of ISO1872 moulding procedure as used by Intertek

3.2.2 Characteristics of compression moulded sheets

This section describes the morphology and thermal properties of the compression moulded sheets of bimodal and R2 material.

3.2 Production and characteristics of the compression moulded sheets

Morphology

Examples of transmission electron micrographs (TEM, prepared with the methods described in section 2.1.2) are given in figures 3.6, 3.7, 3.8, 3.9, 3.10, 3.11, 3.12 and 3.13 for R2-HMHB, R2-HMLB, R2-LMHB, R2-LMLB, bi-HMHB, bi-HMLB, bi-LMHB and bi-LMLB respectively. Contrast for the R2 micrographs was not optimal in TEM. This is probably caused by the large amount of amorphous material and free volume. To increase the contrast, high angle annular dark field scanning transmission electron microscopy (HAADF-STEM) is applied. Figures 3.6(top) and 3.10(top) show R2-HMHB and bi-HMHB at a fairly low magnification. It can be seen that in the bimodal material, spherulites - recognisable as fan-like structures - are clearly visible, while for the R2 material, there is no visible structure in the material. This is a general difference between the bimodal materials and the R2 materials, and can also be seen on the figures with a slightly larger magnification: figures 3.6 (bottom left), 3.7 (left), 3.8 (left) and 3.9 (left) for the R2 materials, and figures 3.10 (bottom left), 3.11 (left), 3.12 (left) and 3.13 (left) for the bimodal materials. In all cases, the spherulites are more developed in the bimodal material than in its R2 counterpart. Micrographs were taken over a range of sheets and at different places in the sheets for all materials, and no significant inhomogeneities found. It is thus concluded that the compression moulded sheets are homogeneous. In figures 3.6 (bottom right), 3.7 (right), 3.8 (right), 3.9 (right) for the R2 materials, and 3.10 (bottom right), 3.11 (right), 3.12 (right) and 3.13 (right), at large magnification, worm-like structures can be observed. These are the individual crystal lamellae, seen from the side. They can be seen in all materials. The lamellae thickness, calculated with image analysis using ImageJ, is 10 ± 2 nm for R2-HMLB and 12 ± 2 nm for bi-HMHB. Caution has to be taken with this result as it is a local measurement.

Thermal properties

Thermal analysis is done according to the procedure explained in section 2.1.3. The results can be found in table 3.7. The enthalpy of fusion and the melting temperature are lower for the R2 materials than for the bimodal materials. The addition of a low molecular mass fraction increases the crystallinity and the crystal thickness in the bimodal materials. Within

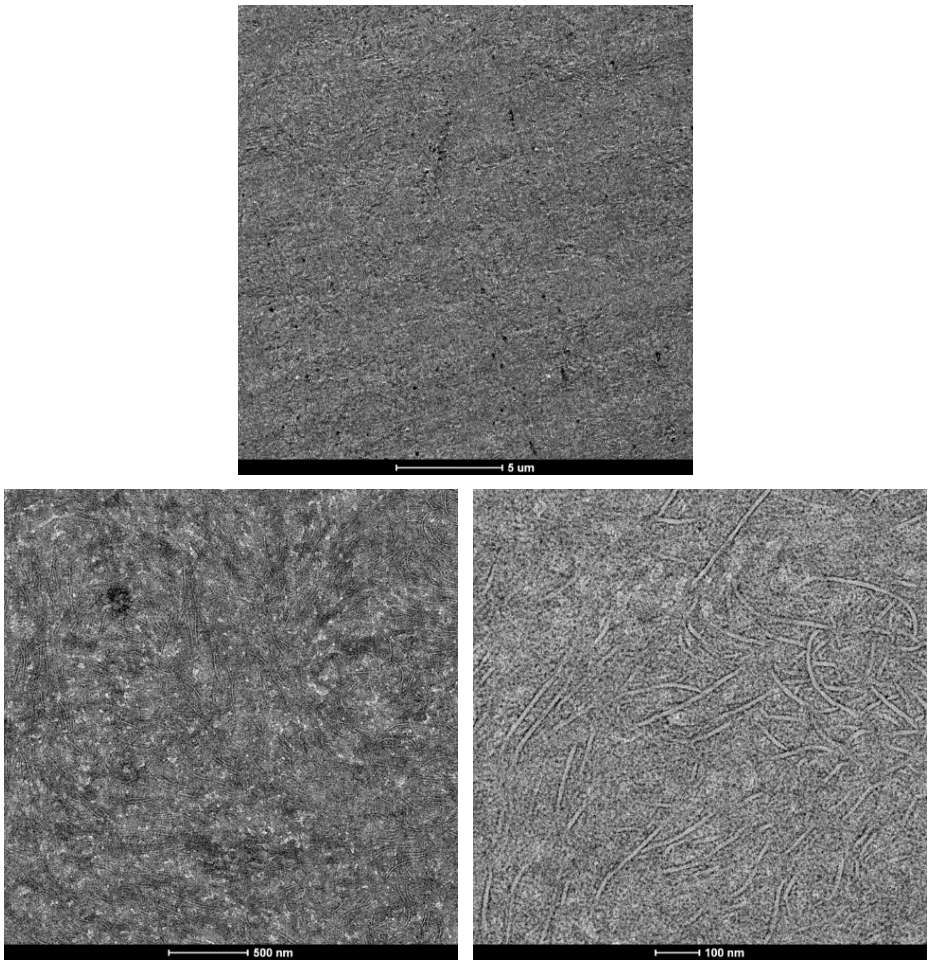

Figure 3.6: High angle annular dark field scanning transmission electron micrograph on R2-HMHB after 24 hours of RuO_4 staining

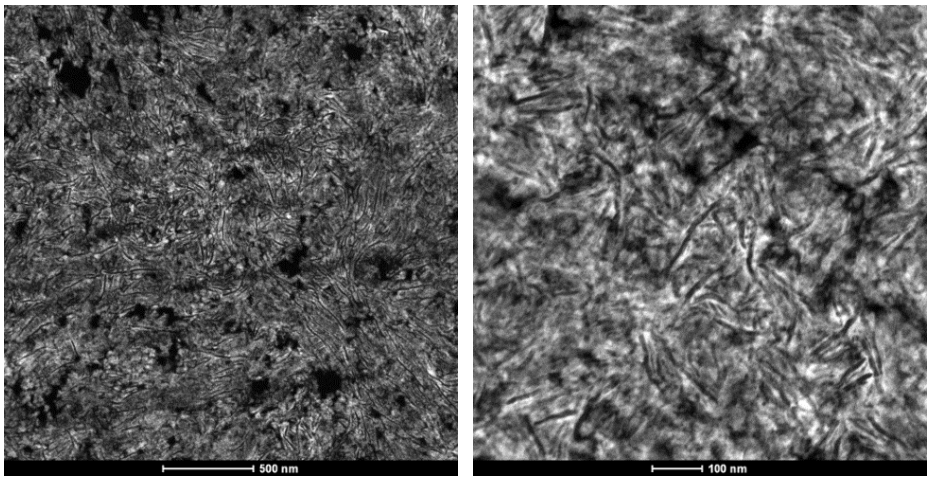

Figure 3.7: High angle annular dark field scanning transmission electron micrograph on R2-HMLB after 24 hours of RuO_4 staining

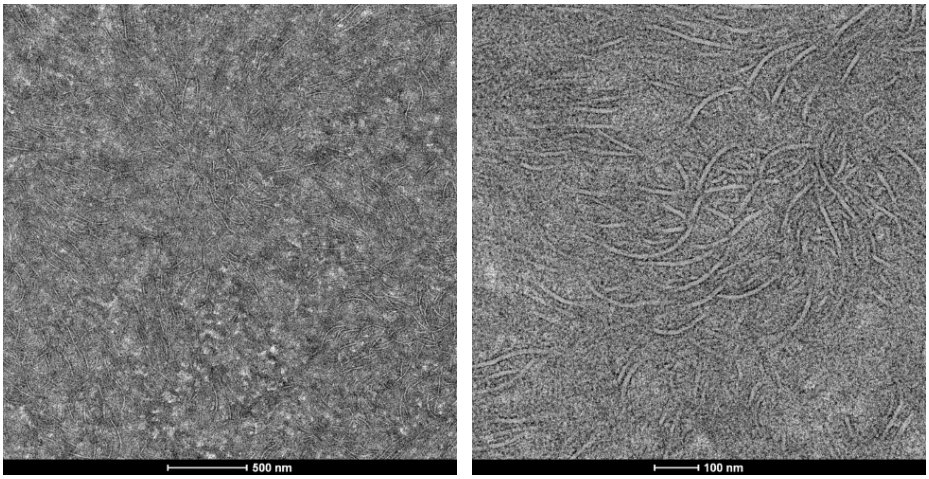

Figure 3.8: High angle annular dark field scanning transmission electron micrograph on R2-LMHB after 24 hours of RuO_4 staining

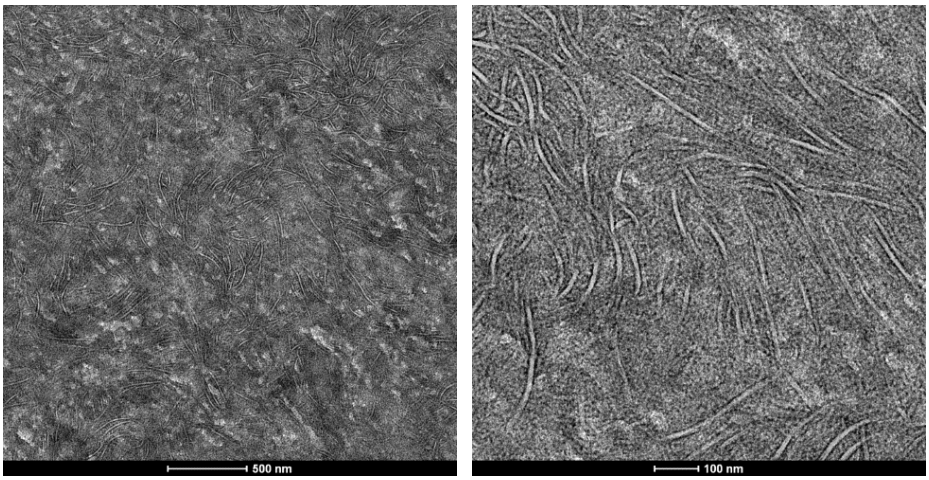

Figure 3.9: High angle annular dark field scanning transmission electron micrograph on R2-LMLB after 24 hours of RuO_4 staining

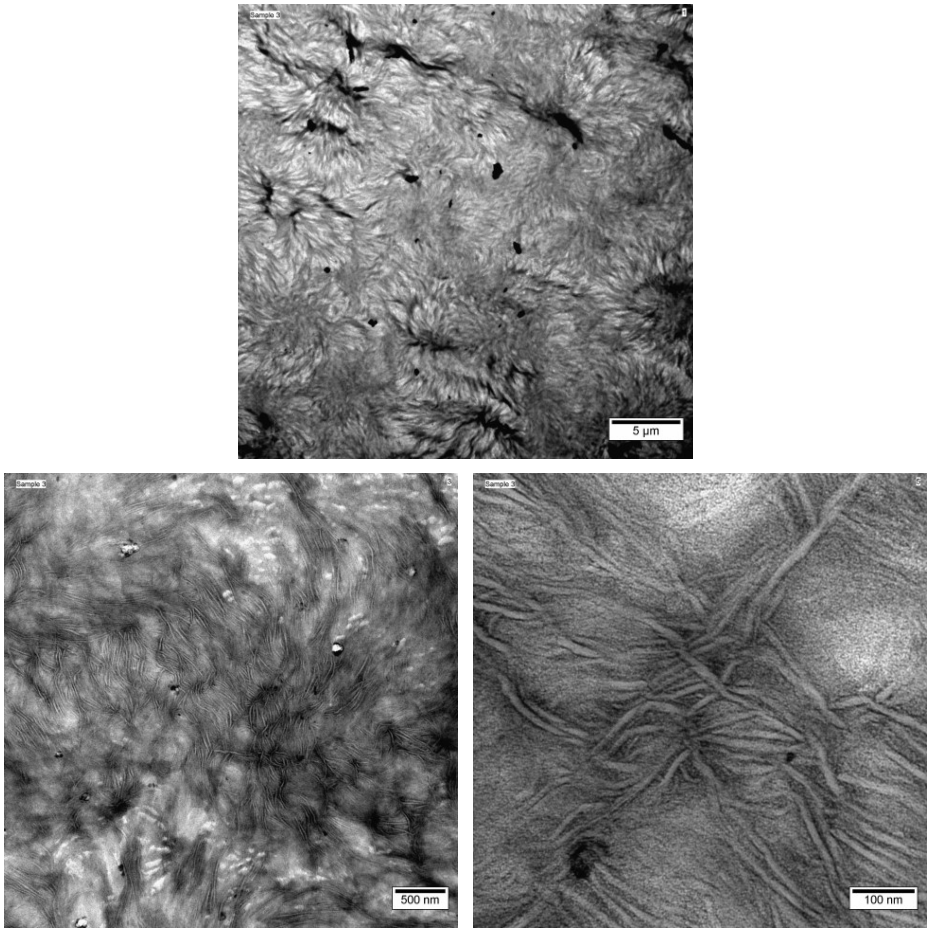

Figure 3.10: Transmission electron micrographs on bi-HMHB after 24 hours of RuO_4 staining

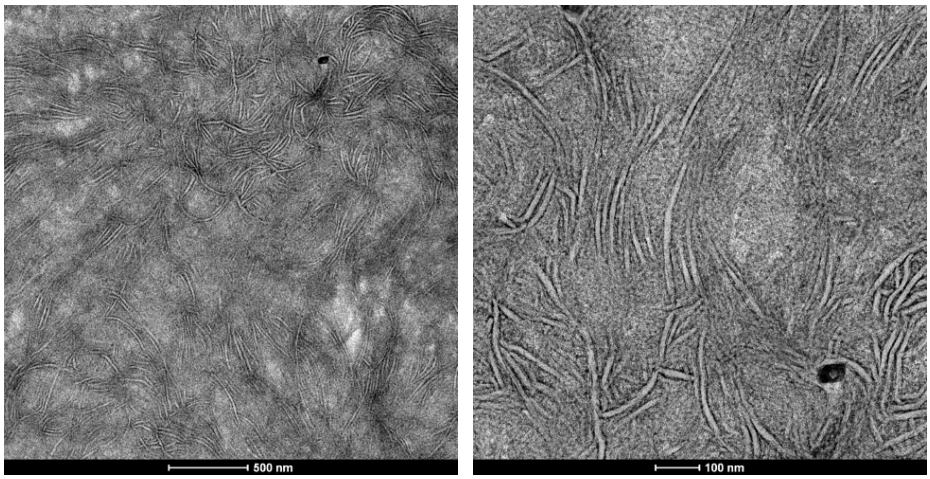

Figure 3.11: Transmission electron micrographs on bi-HMLB after 24 hours of RuO_4 staining

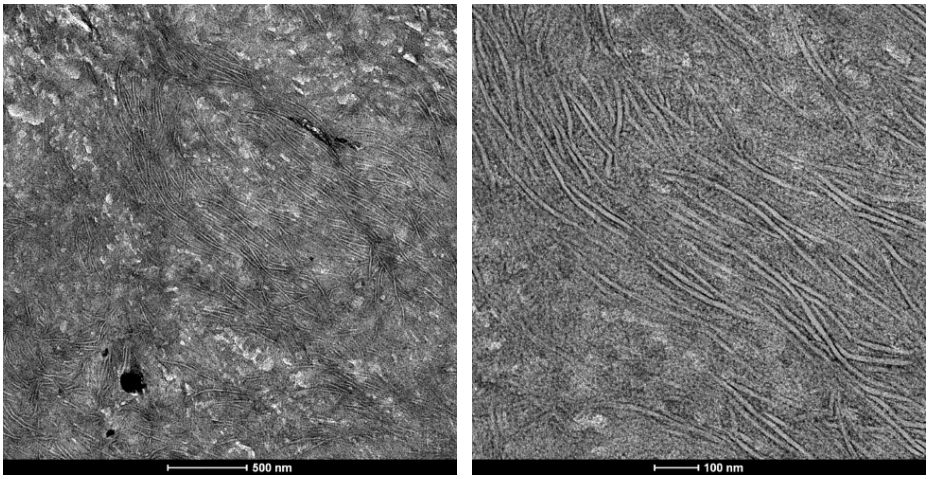

Figure 3.12: Transmission electron micrographs on bi-LMHB after 24 hours of RuO_4 staining

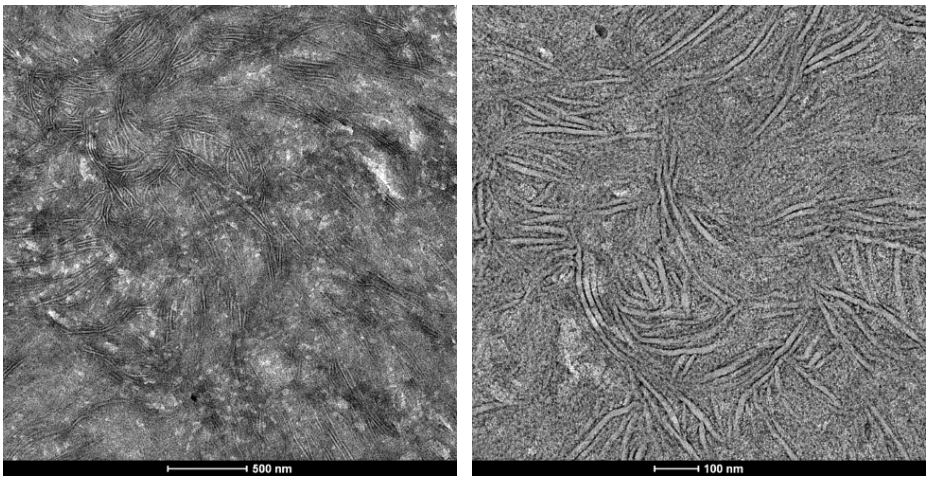

Figure 3.13: Transmission electron micrographs on bi-LMLB after 24 hours of RuO_4 staining

one family of materials (R2 or bimodal), the same trends are present. The highly branched materials have a lower enthalpy of fusion and a lower melting temperature than the low branched materials, again reflecting the influence of the fraction of branches on the crystallisation. As can be seen in table 3.3, the branch content of for example R2-HMHB and R2-LMHB is not exactly the same. Plotting the enthalpy of fusion and the melting temperature as a function of branch content (figures 3.14 and 3.15) shows that these parameters are sensitive to branch content, but more so for the low branched materials than for the highly branched materials. In general, the sensitivity to branch content is lower in the bimodal materials than in the R2 materials. This can be expected as the bimodal materials all contain a large fraction of R1. A quantitative relation between the ΔH_f and the structure of polyethylene has not been proposed in literature. ΔH_f depends on the crystallinity and in the case of small crystals, on the surface energy of the crystals. This makes it difficult to quantify a relationship [172, 173]. Empirical models do exist to predict T_m, based on contributions to the melting temperature from the individual monomers in the main chain and the side chains. However, these models are accurate within around 20°C, so cannot be used to distinguish between the materials used in this work [173]. The α-relaxation temperature also depends on the branch content; it moves to lower temperatures with increasing branch content as it is easier for the chains to move through thin crystal lamellae. The lamellar thickness corresponds to that found from TEM images (see section 3.2.2).

	ΔH_f [J/g]	T_m [°C]	T_α [°C]	$X_{c,h}$ [%]	L_c [10^{-8} m]
R2-HMHB	104 ± 2	121	66	36.1 ± 0.7	1.11 ± 0.02
R2-HMLB	137 ± 6	126	73	48 ± 2	1.36 ± 0.02
R2-LMHB	102 ± 2	121	65	35.3 ± 0.7	1.08 ± 0.03
R2-LMLB	129 ± 3	123	71	45 ± 1	1.21 ± 0.04
Bi-HMHB	169 ± 4	128	72	58 ± 1	1.55 ± 0.03
Bi-HMLB	205 ± 8	130	81	71 ± 3	1.76 ± 0.08
Bi-LMHB	172 ± 3	128	71	59 ± 1	1.54 ± 0.05
Bi-LMLB	178 ± 5	129	78	63 ± 2	1.62 ± 0.09

Table 3.7: Results of thermal analysis at 10°C/min for compression moulded sheets. Precision on temperatures is ± 1 °C

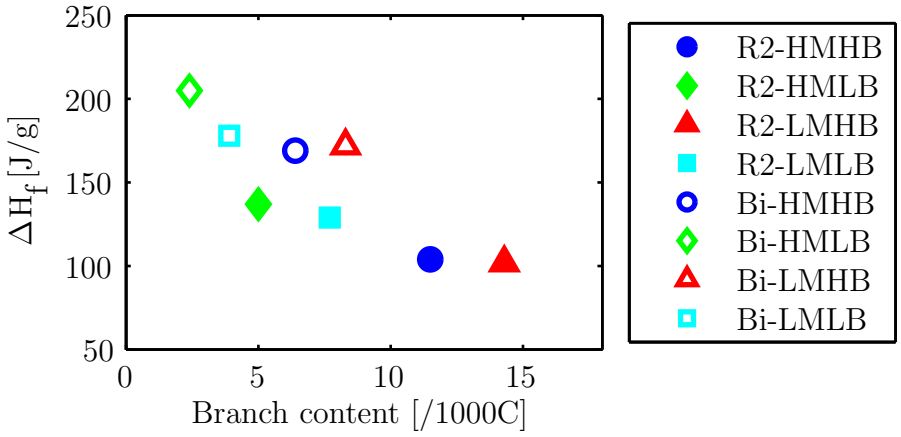

Figure 3.14: Enthalpy of fusion ΔH_f as a function of branch content

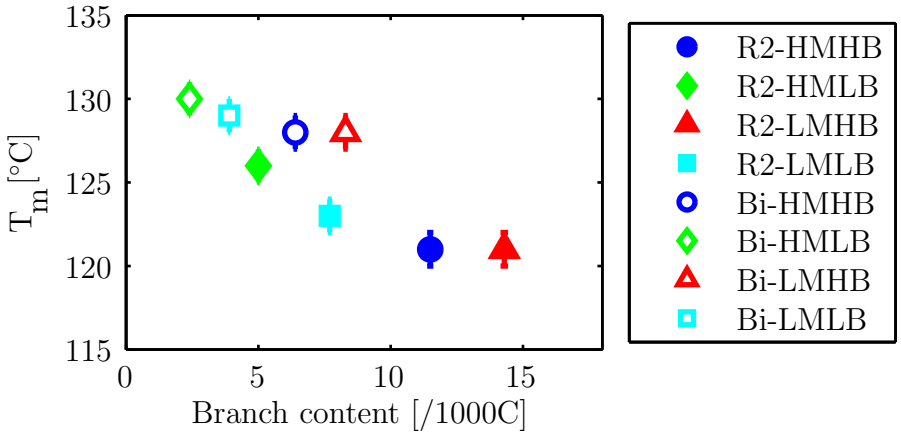

Figure 3.15: Melting temperature T_m as a function of branch content

Crystallinity

The crystallinity as measured from DSC is the crystallinity of the material close to the melting point. The crystallinity at room temperature can be measured using a density gradient column as explained in section 2.1.4. The results are summarised in table 3.8. The trends are the same as for the crystallinity as measured from DSC: the R2 materials have a lower crystallinity, and within one family the crystallinity is lower at high branch contents. At low crystallinities, the density column yields a higher crystallinity than the DSC. At high crystallinities, the density column yields a lower crystallinity than the DSC. These are the materials with the lowest crystallinities overall (and the highest branch contents). The crystallinity is equal or lower than the crystallinity of the powder and pellet materials, due to the melting and recrystallisation of the material during the compression moulding. The crystallinity stays similar for the high branched materials, except for bi-HMHB. As before, it is sensitive to large changes in branch content, but not to small changes (R2-LMHB has a slightly higher crystallinity than R2-HMHB, despite having a higher branch content).

	$X_{c,d}$ [%]
R2-HMHB	46.4 ± 0.5
R2-HMLB	50.8 ± 0.5
R2-LMHB	46.7 ± 0.5
R2-LMLB	51.0 ± 0.5
Bi-HMHB	62.6 ± 0.6
Bi-HMLB	67.4 ± 0.7
Bi-LMHB	62.9 ± 0.6
Bi-LMLB	66.3 ± 0.7

Table 3.8: Crystallinities of the compression moulded sheets, calculated from their density

Orientation

When inspected through cross polarisers, the sheets made from R2 material show cross shaped birefringence, an indication of preferred orientation in the material (see figure 3.16). Modifications of the moulding procedure and additional heat treatments do not visibly change the appearance of the

samples. The birefringence Δn of the sheet was measured using a Zeiss optical microscope and the Michel-Levy chart, and found to be 0.00069. Using the pseudo-affine deformation model (explained in section 2.1.5), the corresponding draw ratio λ can be calculated as 1.02. It will be assumed that this small degree of orientation has no influence on the strain hardening properties on the samples. In the case of nylon fibres, it has been shown that the initial draw ratio does not influence the strain hardening [174]. The sheets produced from bimodal material do not show birefringence.

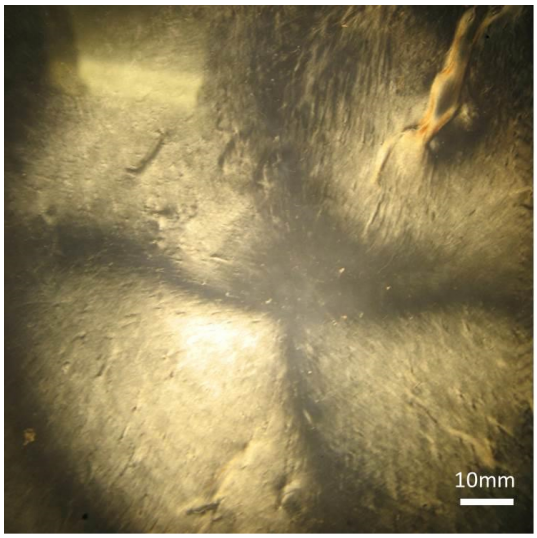

Figure 3.16: Photograph of R2-HMLB compression moulded sheet between cross polarisers

Birefringence gives an average orientation in the specimen (though it is dominated by the crystals), but from polarised Raman spectroscopy (2.1.6), the orientation in the crystalline and amorphous phase can be calculated separately. As explained in table 2.1, the 1080 cm^{-1} Raman band is caused by C-C stretching in the amorphous chains, the 1130 cm^{-1} band is caused by symmetric C-C stretching in the trans chains (both amorphous and crystalline) and the 1420 cm^{-1} band is caused by CH bending in the orthorhombic crystalline chains. Therefore the orientation parameters based on the 1080 cm^{-1} indicate the orientation in the amorphous phase, while the orientation parameters for the 1420 cm^{-1} indicate the orientation in the crystalline phase. The orientation parameters for the 1130 cm^{-1} are used as control, they should lay between the two others. For the isotropic com-

pression moulded materials, the orientation is so low that the $< P_{200} >$ parameter cannot be calculated. A qualitative idea of the orientation can be given by 1-I_{yy}/I_{zz}. This is shown in table 3.9. A high orientation results in 1-I_{yy}/I_{zz} close to 1. As can be seen from the table, the values for 1-I_{yy}/I_{zz} are around 0.2 - 0.3 for all materials, except for bi-LMLB where it is 0.5. This implies that bi-LMLB is slightly oriented even in the isotropic state.

	1-I_{yy}/I_{zz} 1080 cm^{-1}	1130 cm^{-1}	1420 cm^{-1}
R2-HMHB	0.2 ± 0.1	0.2 ± 0.1	0.2 ± 0.1
R2-HMLB	0.2 ± 0.1	0.2 ± 0.1	0.2 ± 0.1
R2-LMHB	0.3 ± 0.1	0.3 ± 0.1	0.3 ± 0.1
R2-LMLB	0.2 ± 0.1	0.2 ± 0.1	0.2 ± 0.1
Bi-HMHB	0.2 ± 0.1	0.3 ± 0.1	0.3 ± 0.1
Bi-HMLB	0.2 ± 0.1	0.2 ± 0.1	0.2 ± 0.1
Bi-LMHB	0.2 ± 0.1	0.3 ± 0.1	0.4 ± 0.1
Bi-LMLB	0.5 ± 0.1	0.5 ± 0.1	0.5 ± 0.1

Table 3.9: Qualitative order parameters for the compression moulded sheets

3.3 Production and characteristics of pre-drawn materials

This section describes the pre-drawing of the R2 and bimodal materials and the characteristics of the resulting fibres.

3.3.1 Cutting and drawing

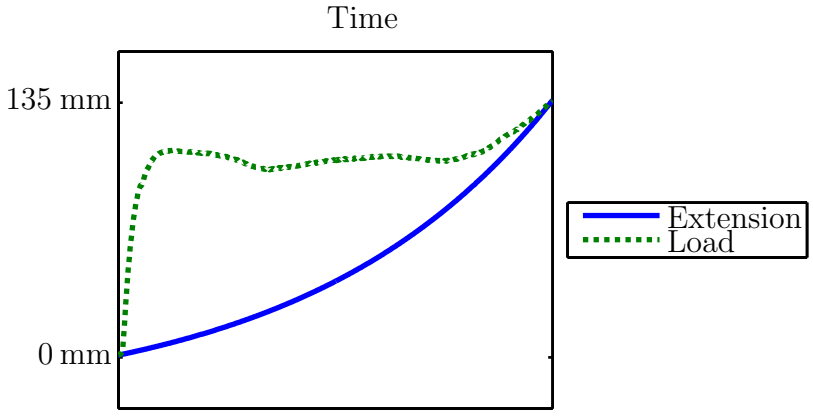

Figure 3.17: Extension and load as a function of time during initial drawing of the materials

After compression moulding, dumbbell shaped samples are cut for the mechanical tests. To make sure all the samples are drawn above their natural draw ratio, the natural draw ratio of the samples at the appropriate temperature and strain rate is measured. Trials reveal that at a strain rate of 3 10^{-2}/s, all materials can be drawn into their strain hardening region. At strain rates above or below this strain rate, some of the materials will fail during necking. The natural draw ratio of the materials is then established at 3 10^{-2}/s and 80°C. For this, ink dots are placed on the dumbbell sample, 2 mm apart from each other. An oven, mounted on an Instron 5564, is heated to 80°C. The dumbbell is placed in the oven for 5 min before being clamped. The gauge length is 27 mm. The sample is then drawn at a constant true strain rate of 3 10^{-2}/s, using Bluehill software to control the test. One or multiple necks develop in the sample. When the neck occupies the full specimen length, the sample is photographed and the draw ratio ($\pm$ 0.1) is calculated from the distance between the dots using image processing in Matlab. This is done thrice for each of the materials. It is established that all materials are fully necked at an extension of 135 mm. Therefore, all materials are pre-drawn at a temperature of 80°C, a strain rate of 3 10^{-2}/s to an extension of 135 mm, using the equipment and protocol described above (a schematic of this test can be found in figure 3.17). At this extension, the thickness ($\pm$ 0.001 mm), width ($\pm$ 0.01 mm) and draw ratio ($\pm$ 0.2) of the specimen are measured, before starting the tests as described in chapter 2.

The yield of the materials at 3 10^{-2}/s is shown in figure 3.18. A double yield point can be observed for all the materials. As explained in section 1.2.2, crystal slip processes are supposed to be the dominant phenomenon for the onset of plastic deformation in semi-crystalline polymers [62]. Ward *et al.* and other researchers ascribe the first yield point to the start of interlamellar shear (sliding of crystal blocks), and the second to intralamellar shear (shearing of crystal blocks) [175, 176]. The existence of the second yield point is contested by Hiss *et al.*, who claim it arises only from the way the draw ratio - stress data is plotted, rather than a physical phenomenon [64]. They however do not provide an explanation for experimental findings from X-ray diffraction and thermal analysis that suggest two competing processes [177–179]. The yield stress and draw ratio for a strain rate of 3 10^{-2}/s are given for the first and second yield point in table 3.10. These are determined by the two intersecting lines method [13]. It can be seen that for the first yield point, the yield draw ratio ($\lambda_{y,1}$) is the same for all the materials. The yield stress ($\sigma_{y,1}$) of the bimodal materials is significantly higher for the bimodal materials than for the R2 materials. In one family of materials, the yield stress is lower for the highly branched materials than for the low branched materials. These results are in line with literature, where it is shown that while the yield draw ratio is independent of crystallinity (and strain rate), the yield stress depends on the lamellar thickness [180, 181]. When comparing the stress at the first yield point with the lamellar thickness as calculated from DSC (table 3.7), it can be seen that also in these materials, thicker lamellae lead to a higher stress. For the second yield point, the draw ratio ($\lambda_{y,2}$) is again similar for all the materials. For all the materials, the stress ($\sigma_{y,2}$) scales with lamellar thickness like the stress at the first yield point, but there is no difference between the R2 and bimodal materials. The ratio $\sigma_{y,1}/\sigma_{y,2}$ is around 0.3 for the R2 materials and around 0.7 for the bimodal materials. The bimodal materials are expected to have more regular chain folded crystals, which makes sliding at the crystal boundaries easier. The chain folding of the R2 materials is perturbed by the branches, as shown in figure 3.19. This promotes homogeneous deformation of the crystal lamellae, as this topology causes the stress to be redistributed over the entire thickness of the lamella [178].

From figure 3.18), it can indeed be seen that the first yield point is less pronounced for the R2 materials than for the bimodal materials, and less for the highly branched materials than the low branched materials.

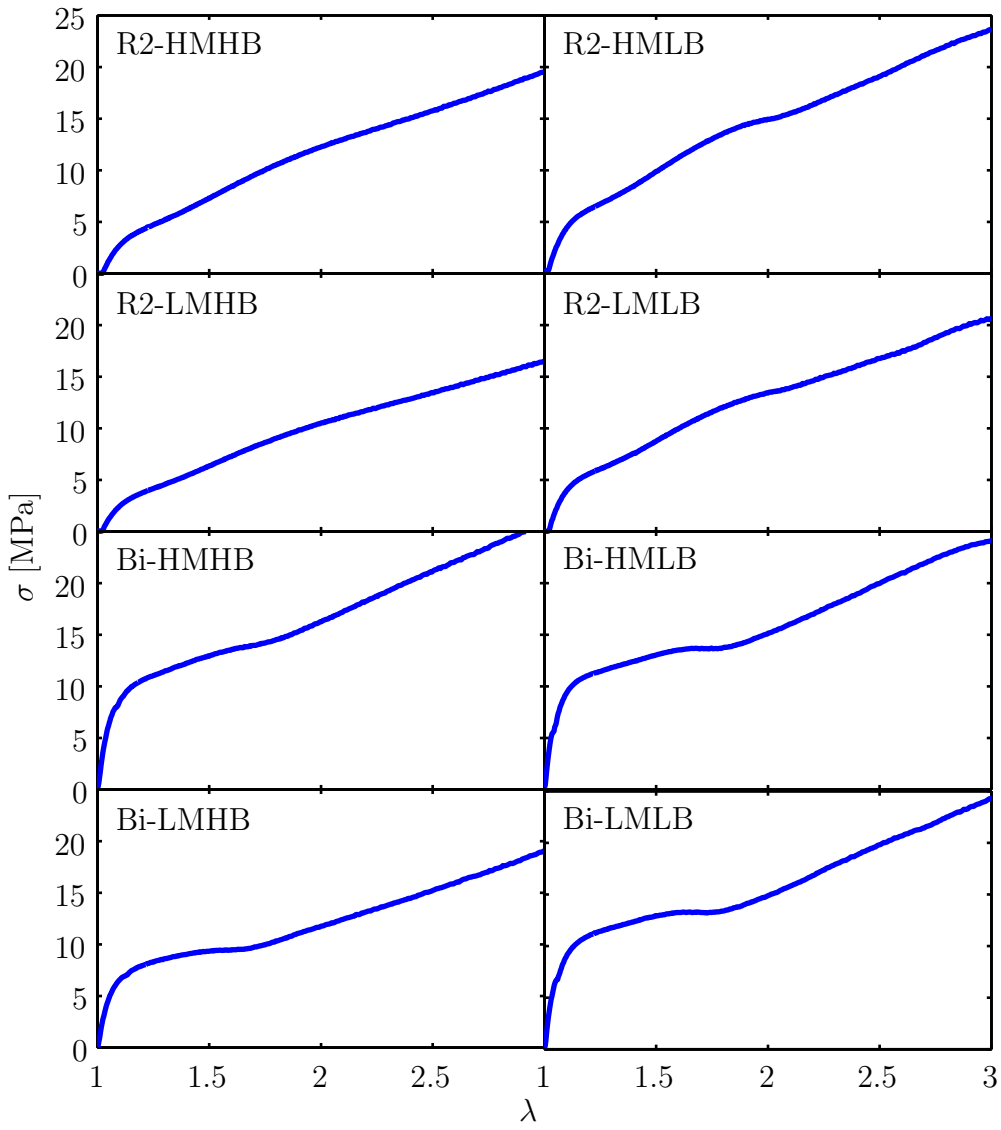

Figure 3.18: True stress as a function of draw ratio during yield at 3 10^{-2}/s

The natural draw ratios of the materials are given in table 3.11. The measurement of the natural draw ratio via the Considère construction ($\lambda_{n,t}$), where the natural draw ratio is defined as the draw ratio at which a line through draw ratio 0 is the lowest tangent to the stress-draw ratio curve of a sample that shows necking. This is illustrated in figure 3.20. However, the

	$\lambda_{y,1}$ †	$\sigma_{y,1}$ [MPa]	$\lambda_{y,2}$	$\sigma_{y,2}$ [MPa]
R2-HMHB	1.1 ± 0.2	3.3 ± 0.2	1.8 ± 0.2	10.8 ± 0.4
R2-HMLB	1.1 ± 0.2	4.9 ± 0.2	1.8 ± 0.2	13.2 ± 0.3
R2-LMHB	1.1 ± 0.2	3.1 ± 0.2	1.9 ± 0.2	10.0 ± 0.2
R2-LMLB	1.1 ± 0.2	4.5 ± 0.2	1.9 ± 0.2	12.7 ± 0.2
Bi-HMHB	1.1 ± 0.2	8.3 ± 0.7	1.5 ± 0.2	11.9 ± 0.6
Bi-HMLB	1.1 ± 0.2	10.2 ± 0.3	1.7 ± 0.2	13.8 ± 0.4
Bi-LMHB	1.1 ± 0.2	7.7 ± 0.5	1.5 ± 0.2	10.4 ± 0.5
Bi-LMLB	1.1 ± 0.2	10.1 ± 0.2	1.5 ± 0.2	11.9 ± 0.8

Table 3.10: Draw ratio ($\lambda_{y,x}$) and stress ($\sigma_{y,x}$) at the first (x=1) and second (x=2) yield point, at 3 10^{-2}/s, from the two intersecting lines method. † note that draw ratio values of less than 1 are unphysical

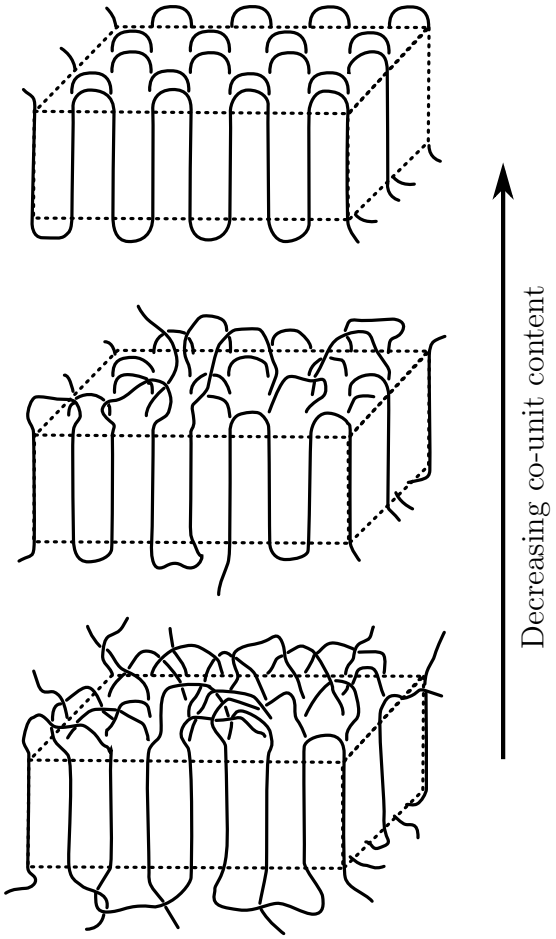

Figure 3.19: Schematic for the influence of branch content on the chain folding topology, as shown in [178]

application of this method does not seem appropriate for the materials used in this study. Especially for the R2 materials, due to the quick propagation of the neck through the sample, the natural draw ratio as measured from the Considère construction occurs later than the end of the propagation of the sample through the neck, essentially in the strain hardening region. A more reliable method seems to be to look at the sample during the test and record the draw ratio at which the neck has fully propagated through the sample and starts deforming homogeneously, $\lambda_{n,o}$ (o for optical) (it has to be noted that Seguélá in his review of the natural draw ratio describes the measurement as 'straightforward', which is clearly not the case with these materials) [75]. Both draw ratios are given in table 3.11. The natural draw ratio is sometimes interpreted as a measure of the density of the entangled network, as Tarin *et al.* have shown that slowly crystallised HDPE, assumed to have a lower tie molecule content than fast crystallised material, has an increased natural draw ratio [75, 144]. The inverse correlation found by Cazenave *et al.* between the natural draw ratio and the resistance to environmental stress cracking (ESC, see section 1.3.3) seems to confirm this [119]. From the natural draw ratio from the optical measurement, it would therefore be expected that the high molecular mass R2 materials perform better than their low molecular mass counterparts, and that bi-HMHB performs better than the other bimodals, in fact, bi-HMHB should perform as good as R2-HMHB. These results will be compared in the next two chapters to the mechanical properties of the materials.

	$\lambda_{n,o}$	$\lambda_{n,t}$	$\sigma_{n,o}$ [MPa]	$\sigma_{n,t}$ [MPa]
R2-HMHB	3.6 ± 0.2	4.7 ± 0.2	36 ± 6	38.4 ± 0.8
R2-HMLB	3.5 ± 0.2	4.2 ± 0.2	42 ± 2	37 ± 1
R2-LMHB	4.1 ± 0.2		36 ± 3	
R2-LMLB	3.9 ± 0.2	4.6 ± 0.4	39 ± 7	37 ± 6
Bi-HMHB	3.5 ± 0.2	5.6 ± 0.4	19 ± 3	51 ± 9
Bi-HMLB	4.7 ± 0.2	5.5 ± 0.2	32.4 ± 0.6	48 ± 4
Bi-LMHB	4.4 ± 0.3	5.7 ± 0.2	21 ± 3	43 ± 6
Bi-LMLB	5.0 ± 0.2	5.4 ± 0.2	31 ± 3	42.9 ± 0.9

Table 3.11: Natural draw ratio and stress at natural draw ratio from optical measurement ($\lambda_{n,o}$, $\sigma_{n,o}$) and the Considère tangent construction ($\lambda_{t,o}$, $\sigma_{t,o}$) from tensile measurements at 3 10^{-2}/s, 80°C

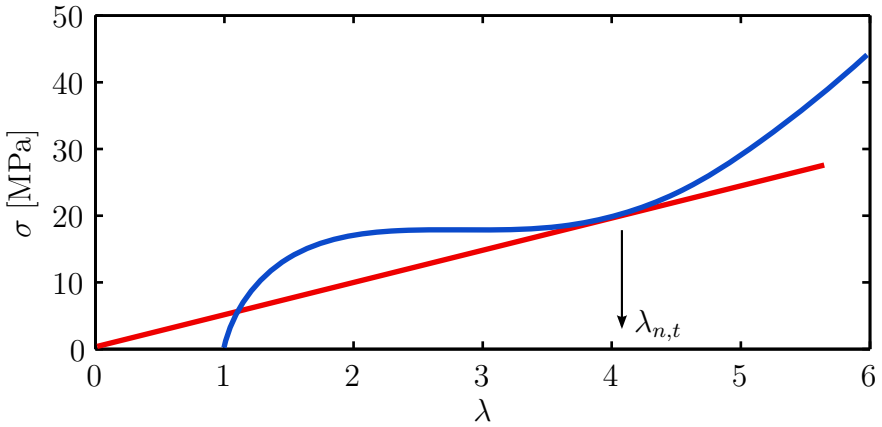

Figure 3.20: Considère tangent construction to find the natural draw ratio

3.3.2 Characteristics of pre-drawn materials

In the following chapters, the structural changes in the materials such as crystallinity and orientation during strain hardening and creep will be discussed. To make a comparison possible of the trends in the different materials, the structure of the pre-drawn materials is studied. Firstly, the draw ratio and stress after pre-drawing are measured and given in table 3.12. At 135 mm extension, one would expect a draw ratio of 6. However, the actual draw ratio, as measured from ink dots placed on the samples, is lower. For the R2 materials, it is around 4.5. For the bimodal materials, it is higher, and it reaches the expected value of 6 for bi-LMLB. This is interesting as the R2 materials are expected to have a higher effective network density, and bi-LMLB is the material that is expected to have the lowest effective network density. The stress after pre-drawing is generally higher for the low branched materials.

Thermal analysis on the pre-drawn samples shows that the crystallinity according to DSC stays very similar in most cases (see table 3.13). The trends seen for the crystallinity of the powder and sheet materials are the same for the pre-drawn materials (a higher branch content means a lower crystallinity). The same can be seen for the lamellar thickness.

The crystallinity was also checked using the density gradient column (table 3.14). It has decreased slightly compared to the compression moulded

	λ	σ [MPa]
R2-HMHB	4.5 ± 0.2	49 ± 2
R2-HMLB	4.7 ± 0.2	58 ± 1
R2-LMHB	4.6 ± 0.2	40 ± 3
R2-LMLB	4.6 ± 0.2	46.5 ± 0.9
bi-HMHB	5.0 ± 0.2	44.5 ± 0.9
bi-HMLB	5.3 ± 0.2	51 ± 1
bi-LMHB	5.4 ± 0.2	41.0 ± 0.8
bi-LMLB	6.0 ± 0.2	52 ± 1

Table 3.12: Draw ratio and stress of the materials after pre-drawing

	ΔH_f [J/g]	T_m [°C]	T_α [°C]	$X_{c,h}$ [%]	L_c [10^{-8} m]
R2-HMHB	111 ± 2	120	65	38.4 ± 0.8	1.05 ± 0.02
R2-HMLB	135 ± 3	126	71	47 ± 1	1.34 ± 0.02
R2-LMHB	111 ± 2	121	64	38.4 ± 0.8	1.07 ± 0.02
R2-LMLB	138 ± 3	124	71	48 ± 1	1.23 ± 0.02
bi-HMHB	169 ± 3	128	71	58 ± 1	1.48 ± 0.02
bi-HMLB	195 ± 4	131	80	67 ± 1	1.85 ± 0.02
bi-LMHB	171 ± 3	127	70	59 ± 1	1.48 ± 0.02
bi-LMLB	185 ± 4	130	76	64 ± 1	1.76 ± 0.02

Table 3.13: Results of thermal analysis at 10°C/min for pre-drawn materials. Precision on the temperatures in ± 1 °C

materials and the powder materials. This decrease is stronger for the low branched bimodal materials. Table 3.12 also shows the birefringence after pre-drawing for the materials. The birefringence is higher in low branched materials, and similar for corresponding bimodal and R2 materials. The overall orientation appears to be dependent on the branch content of the high molecular mass, branched fraction, independently of whether a low molecular mass, linear fraction is present.

	$X_{c,d}$ [%]	Δ n
R2-HMHB		0.041 ± 0.001
R2-HMLB		0.024 ± 0.001
R2-LMHB		0.039 ± 0.001
R2-LMLB		0.043 ± 0.001
bi-HMHB	60.4 ± 0.1	0.043 ± 0.001
bi-HMLB	64.0 ± 0.1	0.046 ± 0.001
bi-LMHB	61.3 ± 0.1	0.042 ± 0.001
bi-LMLB	63.5 ± 0.1	0.044 ± 0.001

Table 3.14: Crystallinity from density and birefringence of the materials after pre-drawing

After pre-drawing, the Raman orientation is measured again. The results are given in table 3.15 and table 3.16. Table 3.15 summarises the qualitative Raman parameters to allow for comparison with the compression moulded sheets, table 3.9. 1-I_{yy}/I_{zz} has increased in the amorphous phase after pre-drawing compared to the compression moulded sheets, except for bi-LMLB, where it has stayed constant. In the crystalline phase, it has increased for all the bimodal materials to the same amount, very close to 1. The $< P_{200} >$ order parameters cannot be calculated for the amorphous phase, because the intensity of the 1080 cm^{-1} peak is too low. $< P_{200} >$ is the same for all the bimodal materials, both for 1130 cm^{-1} and 1420 cm^{-1}. This implies that the orientation in the amorphous phase is also similar in all bimodal materials, even though the draw ratio after pre-drawing is lower for bi-HMHB and higher for bi-LMLB.

	1-Iyy/Izz 1080 cm^{-1}	1130 cm^{-1}	1420 cm^{-1}
bi-HMHB	0.60 ± 0.04	0.86 ± 0.06	0.93 ± 0.06
bi-HMLB	0.6 ± 0.1	0.85 ± 0.06	0.93 ± 0.07
bi-LMHB	0.6 ± 0.1	0.85 ± 0.06	0.92 ± 0.06
bi-LMLB	0.5 ± 0.1	0.84 ± 0.06	0.92 ± 0.06

Table 3.15: Qualitative orientation parameters from Raman for the pre-drawn bimodal materials

	$< P_{200} >$ 1130 cm^{-1}	1420 cm^{-1}
bi-HMHB	0.47 ± 0.07	0.66 ± 0.05
bi-HMLB	0.51 ± 0.04	0.69 ± 0.05
bi-LMHB	0.55 ± 0.04	0.71 ± 0.05
bi-LMLB	0.46 ± 0.05	0.66 ± 0.07

Table 3.16: Order parameters of the bimodal materials after pre-drawing

3.4 Molecular mass between entanglements

The molecular mass between entanglements in the melt can be predicted from the characteristics of the polymers, based on the work of Larson *et al.* and Fetters *et al.* [182–184]. Their model is optimised for branched polymers, so it will only be applied to the R2 materials. The input parameters for the model are the molar mass of the comonomer $M_{w,mono}$ (for butene this is 56.11 g/mol), the molar mass of ethylene $M_{w,e}$ (28 g/mol), the universal gas constant R_u (8.314 J/(mol K)), the temperature T in K (taken as 423 K), the length of the comonomer in number of carbons l_{cm} (4 in the case of butene) and finally the mass fraction of butene in the polymer w_c and the density in the melt. Knowing these parameters, the molecular mass between entanglements M_e can be calculated as

$$M_e = \frac{4}{5}\frac{\rho R_u T}{G_N^0}, \tag{3.2}$$

with

$$G_N^0 = 24820 m_b^{-3.49}, \tag{3.3}$$

for m_b, the molecular mass per backbone bond, between 14 and 28 g/mol.

Equation 3.3 is an empirical correlation based on experimental results listed in literature [184]. Equation 3.2 is based on the tube model. In this model, the molecules surrounding a chain in a highly entangled melt confine the chain so it can only move in a tube-like region [185]. m_b can be calculated using

$$m_b = \frac{n_c M_{w,mono} + M_{w,e}(1 - n_c)}{2}, \tag{3.4}$$

with n_c the comonomer content in molar fraction, calculated from the mass fraction of butene:

$$n_c = \frac{-2w_c}{w_c(l-2) - l_{cm}}. \tag{3.5}$$

The results for n_c and m_b are given in table 3.17. Assuming a melt density for polyethylene melts is around 780 kg/m^3 at 150°C [186], the molecular mass between entanglements can be calculated to be 9 ± 2 10^2 g/mol for all the R2 materials. The reference value for HDPE is 1250 g/mol [106]. The model used, however, does not take into account the chain stiffness, as this only contributes to a lesser extent to the entanglement density [11]. With increased branch content, the average thickness of the chain also increases. The contour length density $\frac{L}{V}$, the chain contour length per unit volume, can be calculated as

$$\frac{L}{V} = \frac{M_w^2 l_0}{N_a \rho m_0}, \tag{3.6}$$

where l_0 is the bond length and N_a Avogadro's number [187]. This is expected to be highest for the HMHB materials, and lowest for the LMLB materials.

	w_c %	n_c %	m_b g/mol
R2-HMHB	4.60	2.30	14.33
R2-HMLB	2.00	1.00	14.14
R2-LMHB	5.70	2.86	14.41
R2-LMLB	3.10	1.54	14.22

Table 3.17: Mass fraction of butene, comonomer content and molecular mass per backbone bond, calculated from the polymer characteristics

3.4 Molecular mass between entanglements

To find an experimental value for the molecular mass between entanglements, Litvinov *et al.* use melt state proton NMR, and specifically the T_2 relaxation signal [106]. In NMR, the T_2 relaxation is the transverse magnetisation relaxation. If the magnetic field applied is oriented in the z direction, the T_2 relaxation is the relaxation of the component of the resulting nuclear spin magnetisation in the xy plane. This relaxation is more efficient when the strength of the nuclear spin interactions is higher. An increase in the interaction strength can be caused by anisotropic chain motions, due to the topological constraints imposed on a molecular chain by an entanglement [188]. Hence the efficiency of the T_2 relaxation is a measure of the number of entanglements. In the case of infinitely long chains, the molecular mass between entanglements is found to be 1760 $\pm$ 80 g/mol using this technique [106]. PEs with different molecular masses were tested and M_e was extrapolated to infinitely long chains because only for that situation one can assume that all the network junctions will persist throughout the duration of the experiment.

In the framework of this PhD, a similar technique was applied to find M_e. This work was done by Victor Litvinov at SABIC (Geleen, Netherlands). In this case solid state NMR was used. In the solid state, the topological constraints determining the T_2 relaxation include crystals. When the temperature approaches the melting temperature, this crystal contribution decreases. Therefore, to find the network junctions originating purely from entanglements, the T_2 relaxation is studied as a function of crystallinity, and M_e in the amorphous phase is calculated from the extrapolation to zero crystallinity. The results for the R2 and bimodal materials studied in this work are given in table 3.18. $1/T_2^{am}$, the inverse of the T_2 relaxation time for the amorphous phase as a whole, is higher for the R2 materials than for the bimodal materials. So T_2 is shorter for the R2 materials. A low T_2 implies a high M_e; the molecular mass between entanglements is lower for the R2 materials. The mass fraction of network chains in the amorphous phase is higher for the R2 materials than for the bimodal materials. Within the network chains, M_e is nearly 50 % smaller than in the amorphous phase as a whole for the bimodal materials, taking it closer to the values for R2. By taking into account the crystallinity of the materials, $1/2M_e^{total}$, the to-

tal network density, can be calculated. This makes the difference between the bimodal materials and the R2 materials larger. The available network density is 3 to 4 times higher in the R2 materials than in the bimodal materials. This illustrates clearly how the low molecular mass fraction in the bimodal materials acts to thin the entanglement network.

	Amorphous phase		Network chains in amorphous phase			
	$1/T_2^{am}$	Fraction	$1/T_2^{net}$	M_e	$1/2M_e^{am}$	$1/2M_e^{total}$
	[ms^{-1}]	[wt%]	[ms^{-1}]	[g/mol]	[mmol/kg]	[mmol/kg]
R2-HMHB	0.68	89 ± 3	0.70	2060	237	127 ± 5
R2-HMLB	0.68	90 ± 3	0.70	2060	237	117 ± 5
R2-LMHB	0.59	82 ± 3	0.70	2060	205	109 ± 5
R2-LMLB	0.65	83 ± 3	0.73	1970	226	111 ± 5
bi-HMHB	0.29	54 ± 3	0.52	2760	101	38 ± 2
bi-HMLB	0.31	55 ± 3	0.53	2710	108	35 ± 2
bi-LMHB	0.24	50 ± 3	0.45	3190	84	31 ± 2
bi-LMLB	0.26	51 ± 3	0.48	2990	91	31 ± 2

Table 3.18: T_2 relaxation parameters for the amorphous phase (^{am}) and the network chains (^{net}), with an error of approximately 10%, mass fraction of the network chains in the amorphous phase, molecular mass between entanglements M_e (with an error of approximately 5%) and average density of chain entanglements, supposing a functionality of chain entanglements of four $1/2M_e$, for the amorphous phase and, taking into account the crystallinity as measured from the density of the sheets, in total. Data from unpublished work by Litvinov *et al.*

It has to be stressed that these results only describe the *available* network density, and caution has to be taken when drawing conclusions about the *effective* network density from this. To translate the available network density to effective network density, the stability of the entanglements over time needs to be studied. This stability is governed by the friction between chains. The melt friction has been found to increase with branch content [20]. Hence in the solid state amorphous phase, the highly branched materials are expected to have a higher friction between chains than the low branched materials. This also indicates that the friction between tie chains and crystals in the solidified, crystallised material will be higher for a high branched material than for a low branched material. Hence a high branch

content and a high number of tie chains make the available network more stable over time, and hence increase the effective network density. It is thus expected that within one family of materials, the HMHB materials will have the highest effective network density. Because the difference in available network density is so high between the R2 materials and the bimodal materials, it is also expected that the effective network density is higher in the R2 materials than in the bimodal materials.

3.5 Summary

In summary, the materials behave as expected from the literature and the mechanisms explained in chapter 1. The crystallinity and lamellar thickness rank with branch content and are higher in the bimodals, which contain 51% low branched fraction. Higher crystallinity leads to a higher stress at the first yield point. The natural draw ratio is challenging to measure for these materials. In the bimodal materials, it is lower for the highly branched materials. The stress at the natural draw ratio is higher for the bimodal materials, and decreases with increasing strain rate. The materials are highly oriented after drawing, which can be seen both from the birefringence and the Raman response. The orientation in the different phases as measured by Raman is similar for all bimodals. The available entanglement density is nearly three times higher for the reactor 2 materials than for the bimodal materials, but friction needs to be taken into account when making conclusions about the effective entanglement density.

Chapter 4

Results I: Bimodal polyethylene

Bimodal polyethylenes are the current industry standard for pipe applications. A bimodal polyethylene is a reactor blend of a low molecular mass, linear polyethylene and a high molecular mass, short chain branched polyethylene. The low molecular mass fraction reduces the melt viscosity, which enhances processing capabilities. The high molecular mass fraction increases the resistance to creep and hence slow crack growth. For industrial purposes, the goal is to optimise fractions of these two components, along with the moelcular architecture of the high molecular mass fraction. In this chapter, the influence of varying the branch content and the molecular mass in the high molecular mass fraction of the bimodal polyethylenes on their deformation behaviour is studied. Firstly, their creep behaviour is described and discussed. Secondly, their strain hardening behaviour is described and discussed. Finally, a comparison is made between the two types of deformation modes.

4.1 Creep behaviour

A material held at a fixed stress undergoes creep deformation. One can imagine this to be similar to the situation of a fibril at the tip of the crack in a pipe segment. The pipe is under constant internal pressure, creating a hoop stress in the pipe walls that causes the fibril to deform. The rate of deformation is stress and material dependent. Rose *et al.* suggested to

use the creep rate deceleration factor (CRDF) as a measure for slow crack growth, as discussed in section 1.4.2 [86]. The creep rate deceleration factor is a measure of how fast the deformation rate decreases with increasing draw ratio. The more the deformation rate decreases (so the more negative the creep rate deceleration factor), the more resistant to slow crack growth a material is. To enable comparison with the strain hardening tests and to be above the α-relaxation temperature, the tests are done at 80°C.

4.1.1 The influence of stress on the shape of the creep curves

Figure 4.1 gives the load as a function of time during a creep test for bi-HMHB. The first part of the test is always the same, as the material is extended until the starting creep stress (given in the legend). From the point this stress is reached, the Instron keeps the load constant. Figure 4.2 shows the extension as a function of time. After the starting creep stress is reached, the material extends more for higher starting creep stresses.

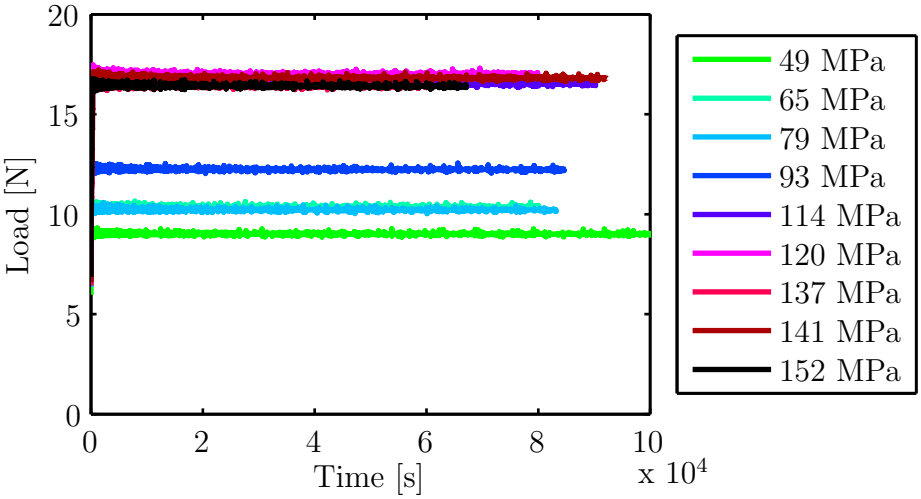

Figure 4.1: Load as a function of time during creep tests starting at a given stress for bi-HMHB

Normalising the results to take into account sample dimensions results in figures 4.3 and 4.4. The draw ratio displays the same trends as the extension. The stress increases during the test as it depends on the load (held constant) and the cross section (decreasing due to increasing draw ratio).

The stress chosen to characterise the creep test is the stress at the start of the creep. Figure 4.5 shows the strain rate decay as a function of time.

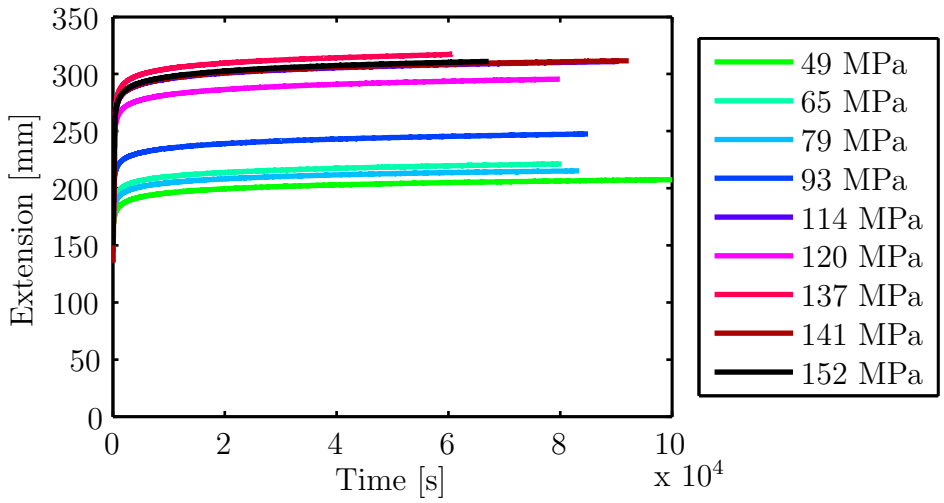

Figure 4.2: Extension as a function of time during creep tests starting at a given stress for bi-HMHB

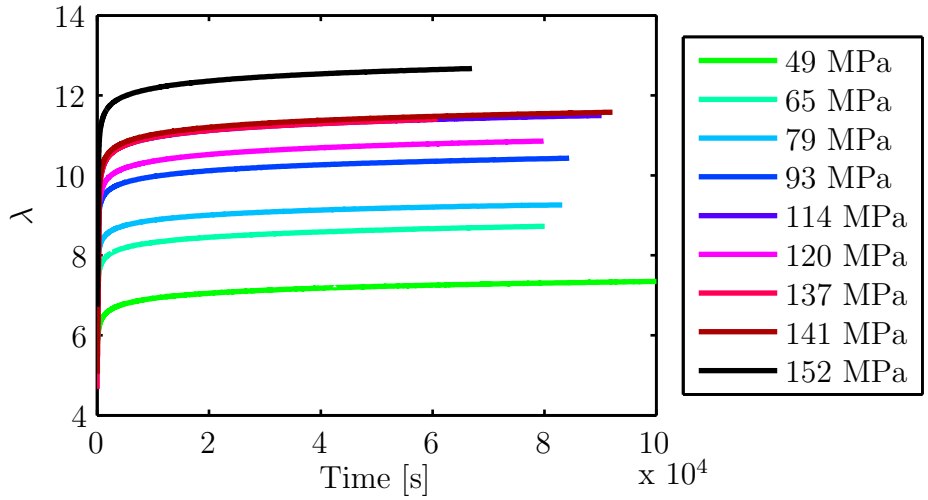

Figure 4.3: Draw ratio as a function of time during creep tests starting at a given stress for bi-HMHB

To compare different materials using one parameter - the creep rate deceleration factor - the strain rate is plotted as a function of draw ratio. This is called a Sherby-Dorn curve. The strain rate decay over time is similar for the materials, but the draw ratio depends on the starting creep stress.

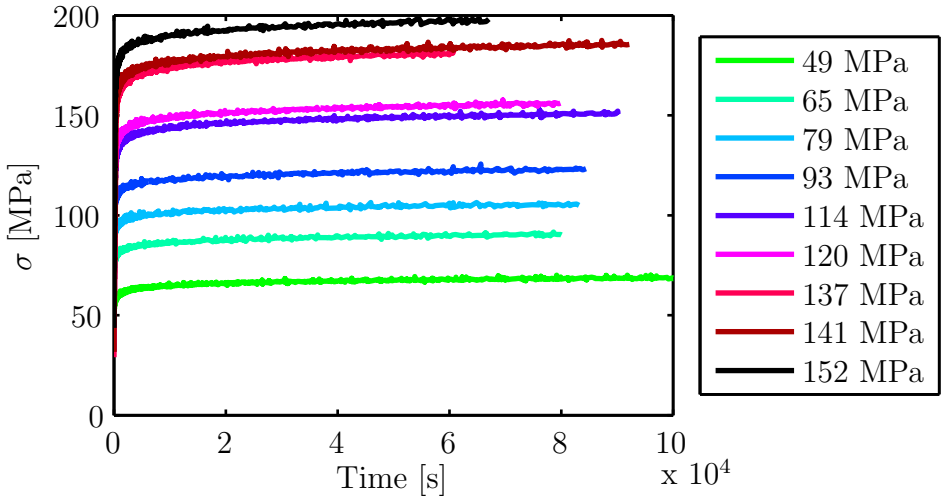

Figure 4.4: Stress as a function of time during creep tests starting at a given stress for bi-HMHB

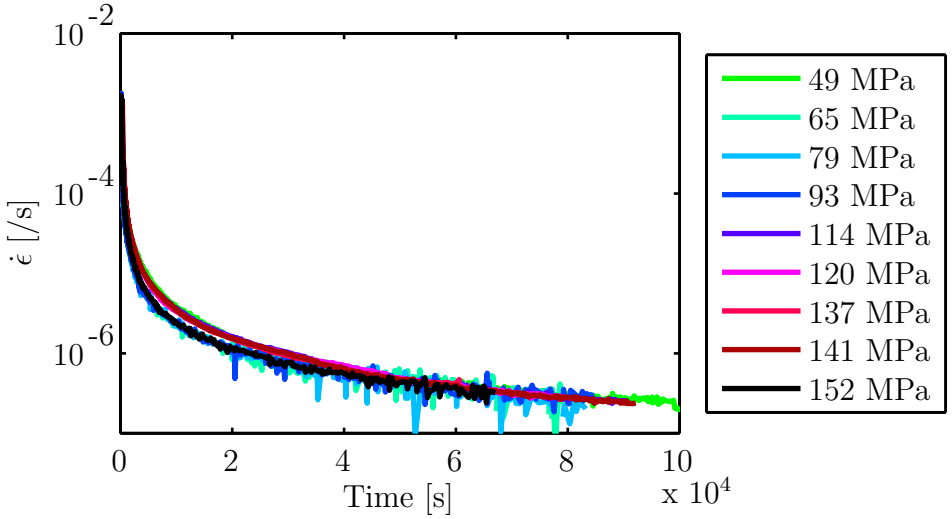

Figure 4.5: Strain rate as a function of time during creep tests starting at a given stress for bi-HMHB

The Sherby-Dorn curves at different starting creep stresses are given in figures 4.6, 4.7, 4.8 and 4.9 for bi-HMHB, bi-HMLB, bi-LMHB and bi-LMLB respectively. At low stresses, after the initial strain hardening at 10^{-3}/s, there is an almost instantaneous drop in strain rate with draw ratio (e.g., creep at 29 MPa for bi-LMHB and creep at 53 and 54 MPa for bi-LMLB). Then, the strain rate decreases with draw ratio linearly (the noise at the low strain rate end of the curves signals the region where the experimental equipment is not longer able to distinguish between extension data points). For higher stresses, the strain rate decreases with draw ratio more or less linearly from the start of the creep test. The creep rate deceleration factor is calculated from the high stress, linear part of the curves. To find the linear part, a linear least square fitting is applied to the data from the start of constant load. Then, the first data points are taken away and the rest of the data is fitted again until the fit visually matches the data. Due to the equipment used, data points taken at strain rates under 10^{-7}/s are less reliable so small variations from linearity can be visible in some of this data, and hence this data is ignored when doing the linear fitting. The CRDF is then calculated using equation 1.19 over this range of data.

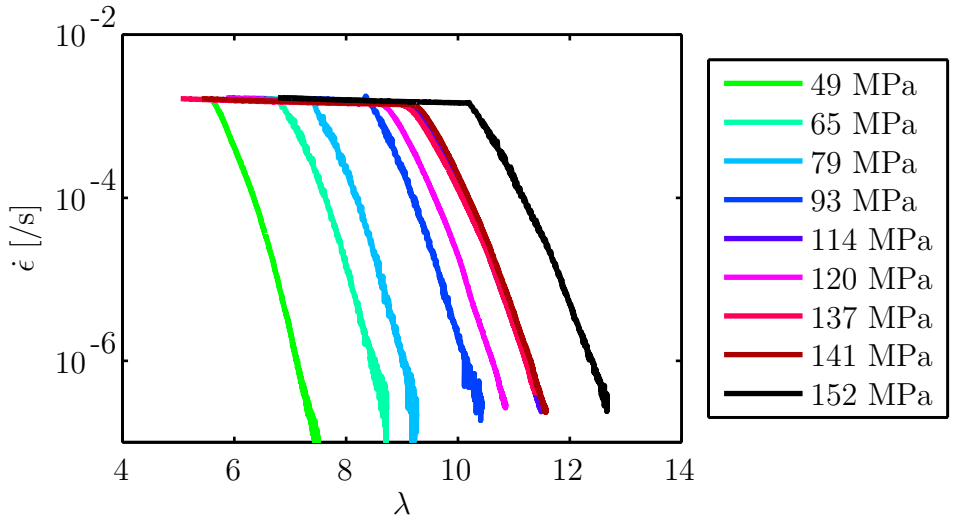

Figure 4.6: Strain rate as a function of draw ratio for bi-HMHB

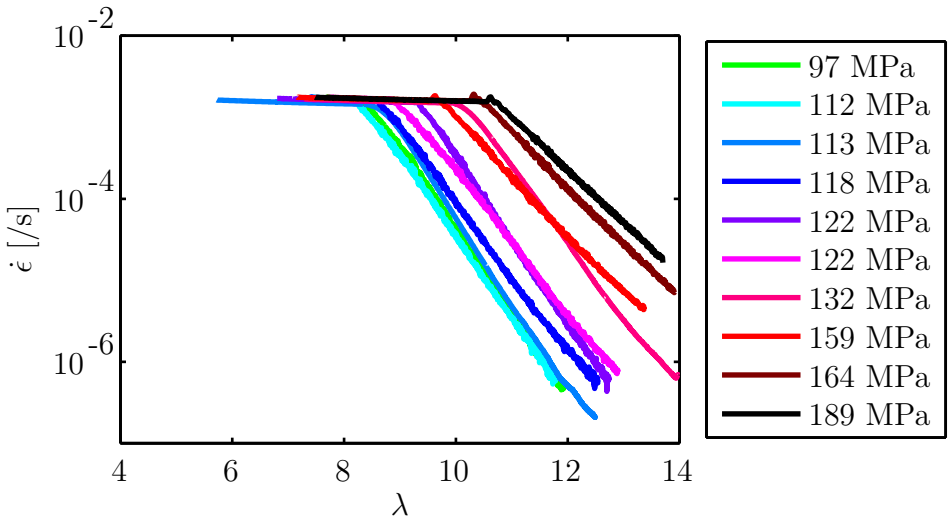

Figure 4.7: Strain rate as a function of draw ratio for bi-HMLB

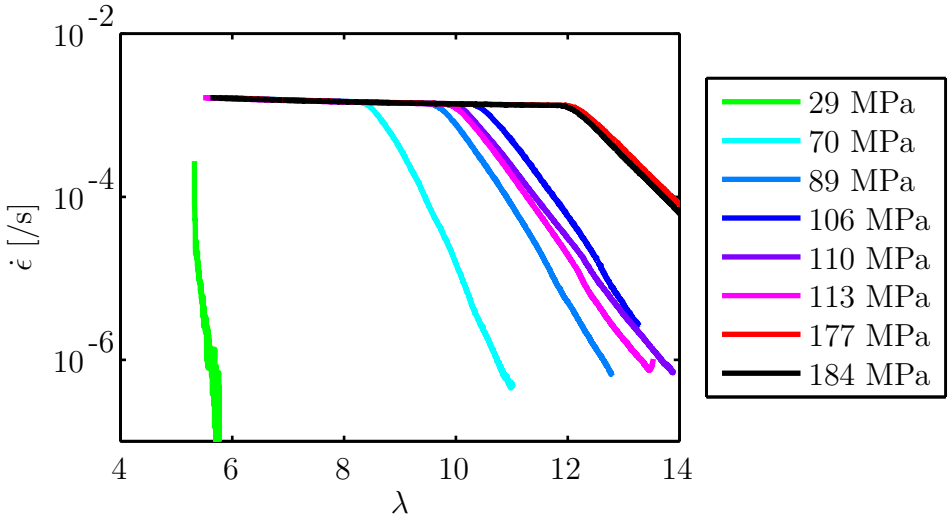

Figure 4.8: Strain rate as a function of draw ratio for bi-LMHB

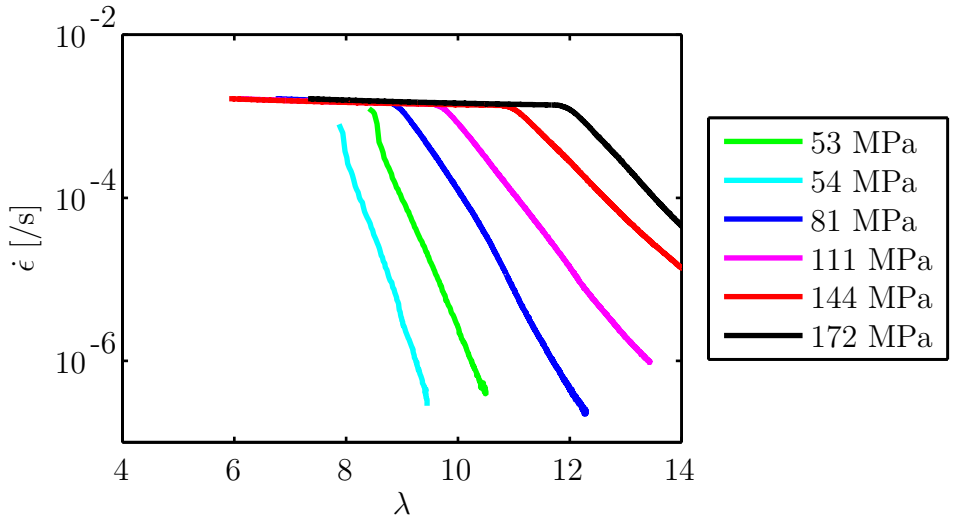

Figure 4.9: Strain rate as a function of draw ratio for bi-LMLB

4.1.2 The influence of starting strain rate on the creep behaviour

The sensitivity of the Sherby-Dorn curves to the starting strain rate of the creep test is studied. To achieve the starting creep stress, the specimen is extended at a constant strain rate of 10^{-3}/s. This strain rate is chosen because it is in the middle of the strain rate range accessible for these materials (as explained in section 4.2). The influence of this choice on the resulting creep rate deceleration factor is studied. Lowering the initial strain rate to 10^{-4}/s leads to a negligible change in creep rate deceleration factor for bi-HMLB. Figure 4.10 shows the Sherby-Dorn curves for three bi-HMLB specimens at similar starting creep stress. The red and the green curve start at a lower strain rate than the blue curve. The curves are shifted compared to each other in terms of draw ratio. At a lower strain rate, a higher draw ratio is needed to reach the same stress. However, between 10^{-3}/s and 10^{-4}/s, it seems that this effect is not distinguishable due to the variation in draw ratio after pre-drawing between the samples at one strain rate. The Sherby-Dorn curves are shifted but have the same slope.

This is confirmed for bi-HMLB at a stress of around 170 MPa (see figure 4.11) and for bi-LMHB at a stress of around 60 MPa (see figure 4.12) and 115 MPa (see figure 4.13). In figure 4.13 a strain rate of 10^{-3}/s is compared to a starting strain rate of 10^{-5}/s, and the same conclusions are reached. It

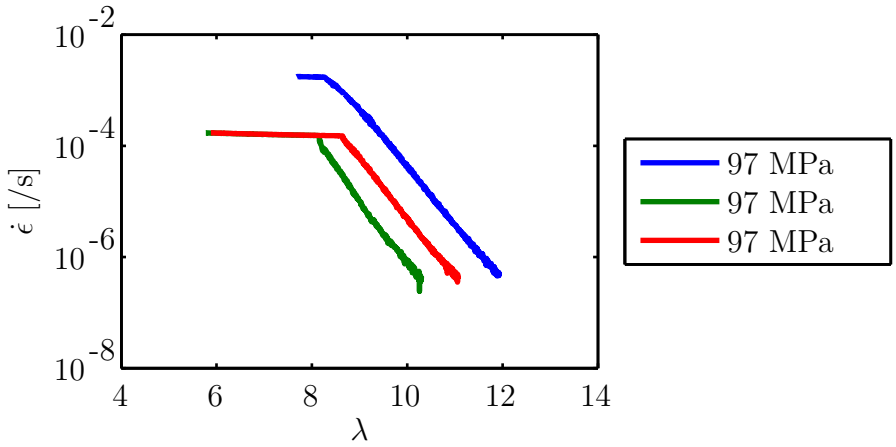

Figure 4.10: Sherby-Dorn plots for bi-HMLB at similar stresses, starting at different strain rates

can be concluded that a variation in starting strain rate, which also influences the time at elevated temperature, does not influence the shape of the Sherby-Dorn curves significantly.

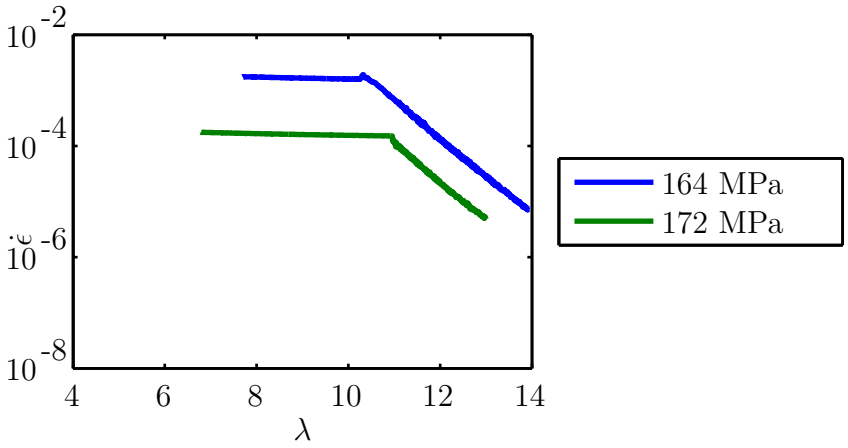

Figure 4.11: Sherby-Dorn plots for bi-HMLB at similar stresses, starting at different strain rates

4.1.3 Influence of stress history on the creep behaviour

Creep tests are performed from different starting stresses. Before the test can start, the material is drawn at a constant strain rate until the starting stress is reached. This implies that for creep tests with different starting stresses, the starting draw ratio is also different. The starting orientation of the material is different, depending on the starting draw ratio and thus

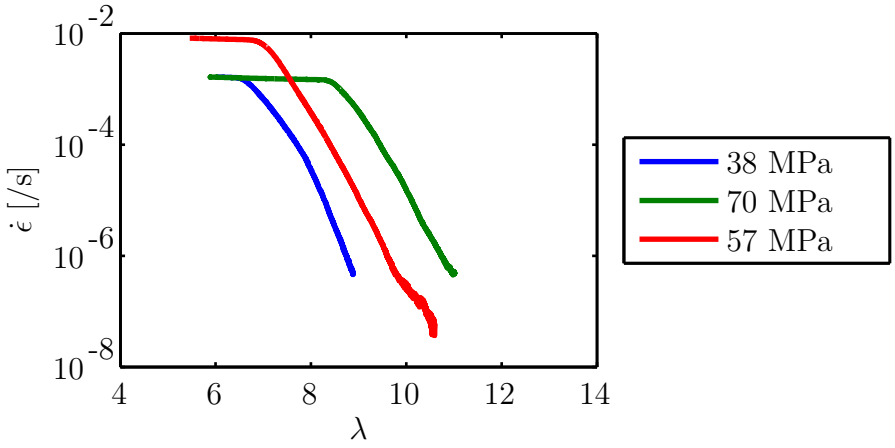

Figure 4.12: Sherby-Dorn plots for bi-LMHB at similar stresses, starting at different strain rates

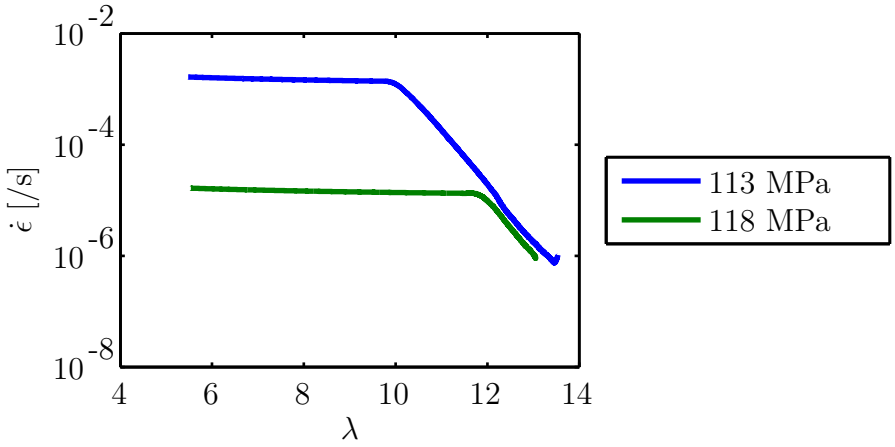

Figure 4.13: Sherby-Dorn plots for bi-LMHB at similar stresses, starting at different strain rates

the starting stress of the creep test. At high stresses, the material is highly drawn before the creep test starts. The influence of the structure evolution during strain hardening on the CRDF is studied by doing creep tests, at the same starting draw ratio but a different starting stress. A way to reach the same stress for different draw ratios is stress relaxation. Bi-HMLB samples are drawn until a certain draw ratio, then stress relaxed, and finally subjected to creep at a stress between the maximum stress previously reached and the stress after stress relaxation. The creep stress at which the pre-stressed sample can be tested depends on the maximum stress reached during strain hardening, time constraints and the speed of stress relaxation. Ideally, one would draw a sample until the maximum draw ratio and then test it at lower and lower creep stresses. However, stress relaxation until a very low stress from the high stress developed after pre-stressing is not practically possible. Therefore, samples are stretched to different draw ratios and tested at stresses equal to or higher than the stress reached after around 70 10^3s.

A schematic of such a test is shown on figure 4.14. For this test, the draw ratio changes by 0.04 over a creep test with a duration of 10^5s. The resulting CRDF is too low to calculate reliably. In figure 4.15, a repeat of this test is shown, with a similar result (a draw ratio change of 0.02 over 10^3s, CRDF again too low to calculate reliably). Comparing this to creep tests done on samples that were not pre-stressed shows that the creep behaviour is different (see figure 4.16). The CRDF of these samples is -5.0 $\pm$ 0.1 for 50 MPa and -2.03 $\pm$ 0.06 for 84 MPa. The draw ratio reached in the 84 MPa test is similar to the draw ratio of the pre-stressed samples.

Figure 4.17 describes another creep test on pre-stressed material, at a stress of 118 MPa. The draw ratio changes by 0.03 over 10^5s and the CRDF is again too small to calculate reliably. Comparing this result to creep on samples that are not pre-stressed, shown in figure 4.18, leads to the same conclusions. The CRDF for these tests is -0.92 $\pm$ 0.03 for creep at 113 MPa and -0.89 $\pm$ 0.03 for creep at 118 MPa. The creep rate of the pre-stressed sample is again lower. The draw ratio in the pre-stressed creep test is similar to the draw ratio reached in these tests.

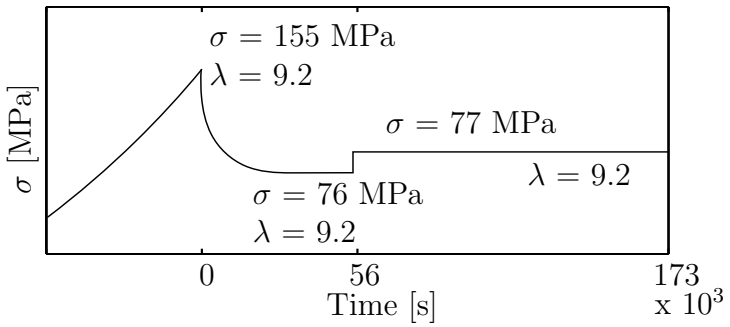

Figure 4.14: Schematic of creep of a high draw ratio specimen ($\lambda = 9.2$) at low stress ($\sigma = 69$ MPa)

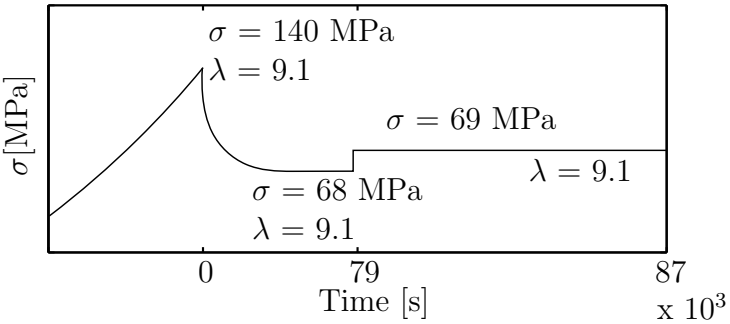

Figure 4.15: Schematic of creep of a high draw ratio specimen ($\lambda = 9.1$) at low stress ($\sigma = 77$ MPa)

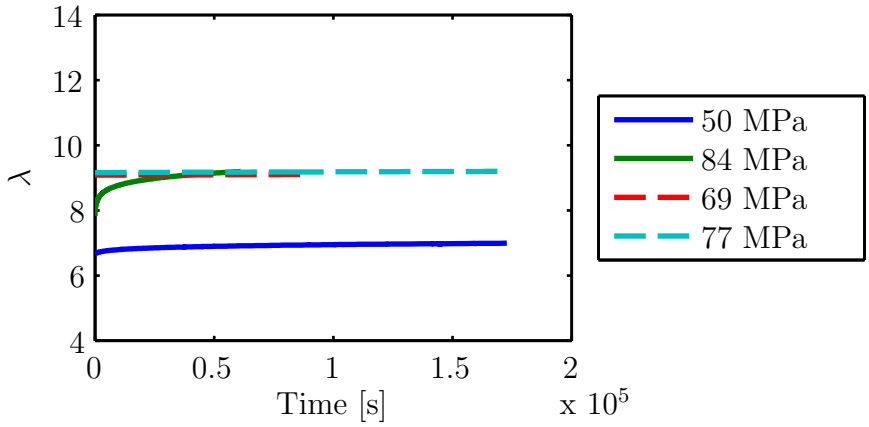

Figure 4.16: Comparison of creep for samples at low (solid) and high (dashed line) draw ratio, for stresses around 70 MPa

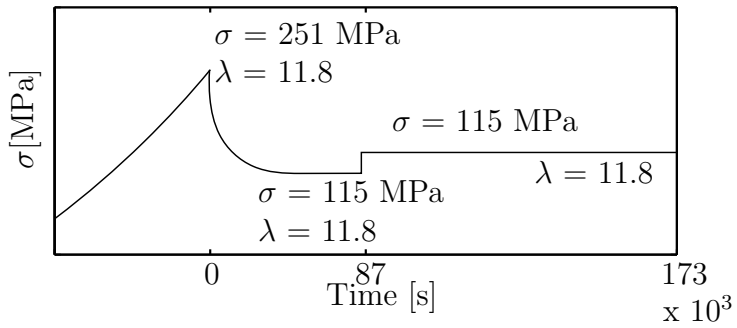

Figure 4.17: Schematic of creep of a high draw ratio specimen ($\lambda = 11.8$) at low stress ($\sigma = 117$ MPa)

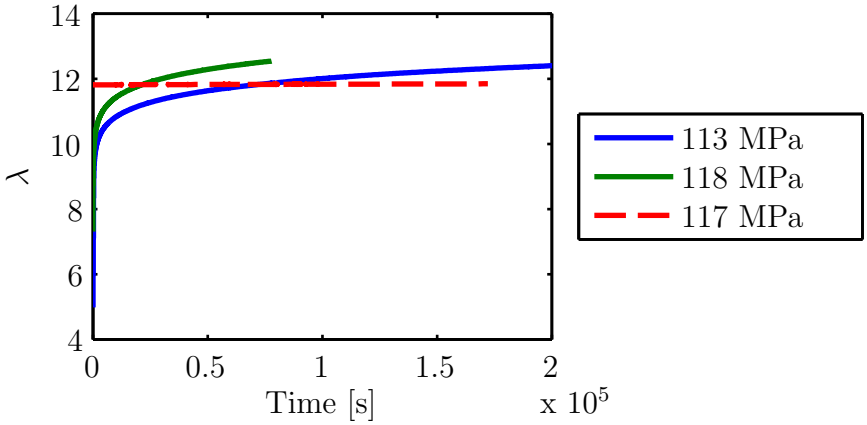

Figure 4.18: Comparison of creep for samples at low (solid) and high (dashed line) draw ratio, for stresses around 120 MPa

Finally, a pre-stressed creep test was performed at a draw ratio close to the maximum draw ratio that can be reached in the experimental set up for bi-HMLB. The description of the test is given in figure 4.19. The draw ratio changes by 0.4 over 5 10^4s. The CRDF is -2.35 $\pm$ 0.07. From a comparison with classic creep tests at similar stresses (see figure 4.20) it can be seen that the draw ratio is similar to the draw ratios reached in the classic tests.

Pre-stressed samples follow the same trend as 'classic' samples (increasing CRDF with increasing stress), but their resistance to creep is higher than the 'classic' samples. They are not on the same stress-strain-strain rate surface as the 'classic' materials, as they do not reach the same strain rate at a similar stress and draw ratio. The difference between a pre-stressed sample

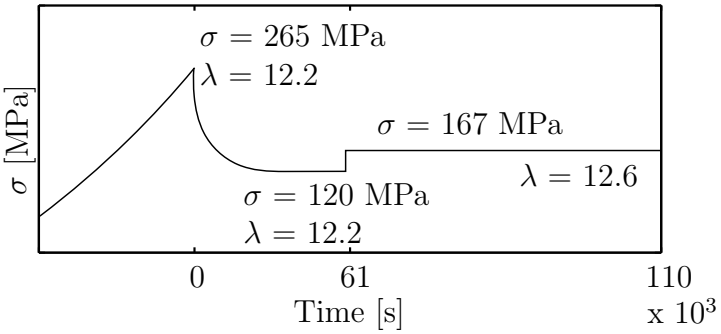

Figure 4.19: Schematic of creep of a high draw ratio specimen ($\lambda = 12.2$) at low stress ($\sigma = 171$ MPa)

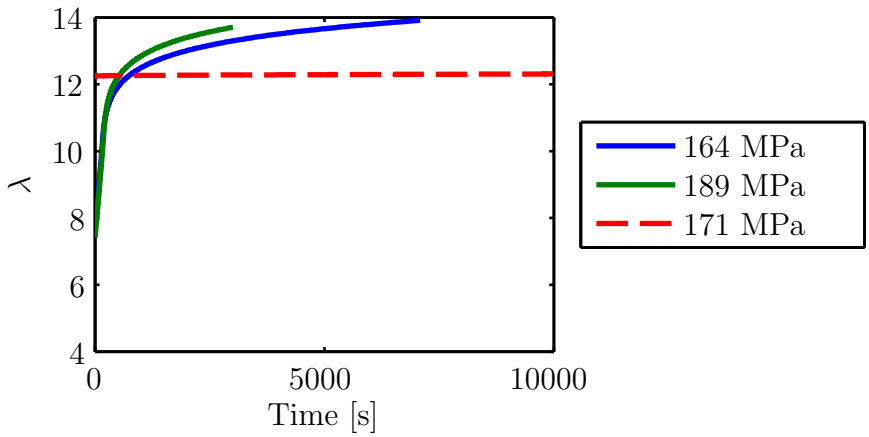

Figure 4.20: Comparison of creep for samples at low (solid) and high (dashed line) draw ratio, for stresses around 170 MPa

before and after stress relaxation is studied to understand this behaviour. The results are given in table 4.1. The birefringence and the crystallinity are not significantly different before and after stress relaxation, but the lamellar thickness increases. To study whether this is an effect of the stress relaxation, creep tests are performed before and after stress relaxation, but this time, after the stress relaxation, they are drawn to a higher draw ratio than the previous maximum draw ratio reached before creep. Sherby-Dorn curves for bi-HMHB subjected to creep at similar stress, with and without stress relaxation, are shown in figures 4.21 and 4.22. The resulting Sherby-Dorn curves are very similar. The stress relaxation has no influence on the creep. This is also reflected in the creep rate deceleration factor. For creep starting at 118 MPa, the CRDF is -1.87 ± 0.06 without stress relaxation and -1.93 ± 0.06 with stress relaxation. For creep starting around 122 MPa, the CRDF is -2.06 ± 0.06 without stress relaxation and -1.95 ± 0.06 with stress relaxation.

Δn	$X_{c,h}$ [%]	L_c [mm]
Before stress relaxation		
0.050 ± 0.001	71 ± 1	2.17 ± 0.02 10^{-8}
After stress relaxation		
0.053 ± 0.001	73 ± 1	2.42 ± 0.02 10^{-8}

Table 4.1: Birefringence, crystallinity and crystal thickness before and after stress relaxation at a draw ratio of around 9. Before stress relaxation: bi-HMLB drawn at 1.45 10^{-3}/s until 241 ± 5 MPa and a draw ratio of 9.2 ± 0.2. After stress relaxation: bi-HMLB drawn at 1.45 10^{-3}/s until 260 ± 5 MPa and a draw ratio of 8.0 ± 0.5, then stress relaxed for 61000s until 126 ± 3 MPa

Sherby-Dorn curves for bi-HMLB subjected to creep at similar stress, with and without stress relaxation, are shown in figure 4.23. The same conclusion follows as for bi-HMHB; the stress relaxation does not influence the creep. Again, this is reflected in the CRDF. For creep starting between 97 MPa and 112 MPa, the CRDF is around -1.0 ± 0.1 without stress relaxation. After 5 hours of stress relaxation and creep at 103.9 MPa, the CRDF is -0.93 ± 0.03. After 50 hours of stress relaxation and creep at 110 MPa, the CRDF is -0.89 ± 0.03. No significant difference in CRDF can be found

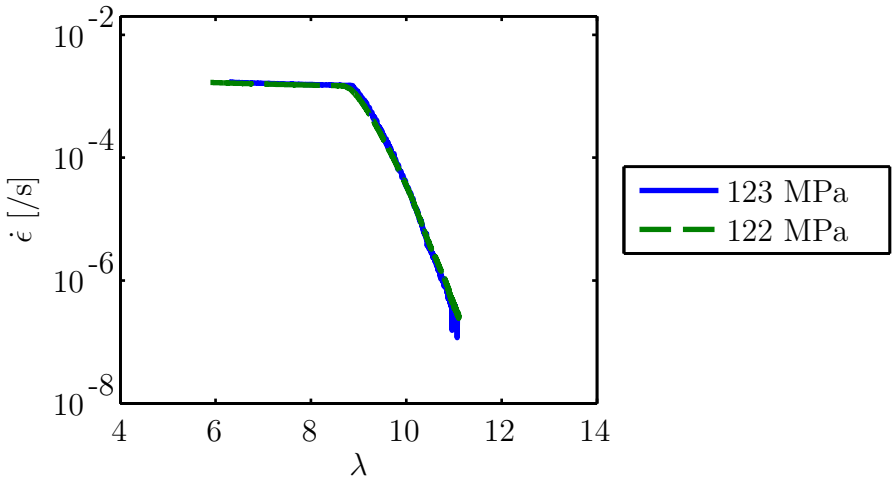

Figure 4.21: Sherby-Dorn curves for bi-HMHB, dashed line after stress relaxation for 17 hours

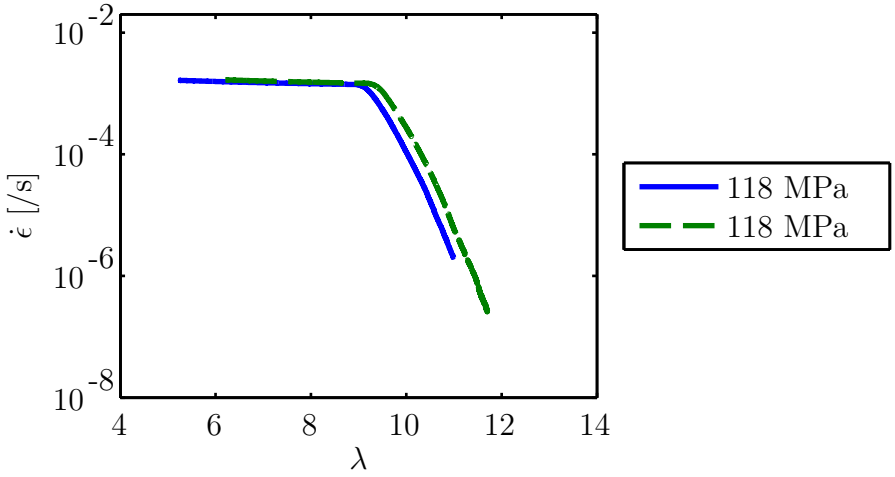

Figure 4.22: Sherby-Dorn curves for bi-HMHB, dashed line after stress relaxation for 121 hours

before and after stress relaxation.

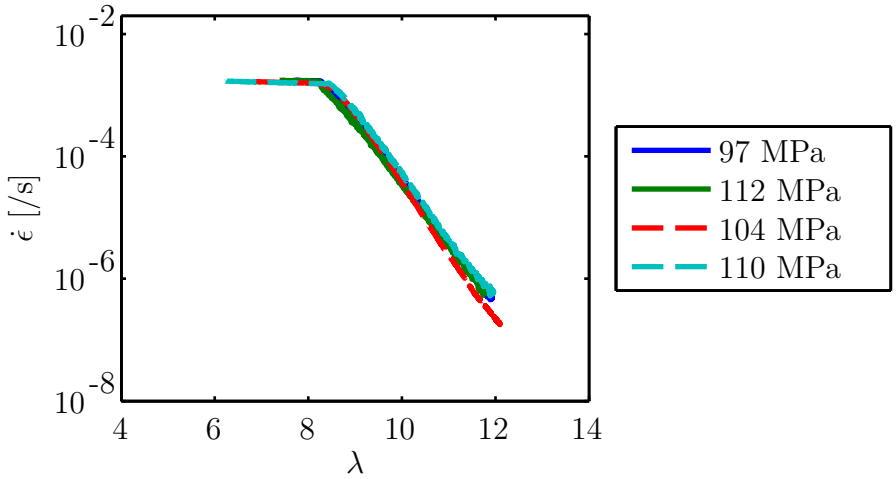

Figure 4.23: Sherby-Dorn curves for bi-HMLB, dashed line after stress relaxation for 5 hours (103.9 MPa) and 50 hours (110.4 MPa)

From these results, it is clear that it is not the stress relaxation, but the pre-stress that has a positive effect on the resistance to creep. A material subjected to creep at a lower stress than the maximum stress it has been drawn to is more resistant to creep than a material subjected to creep at a higher stress than the maximum stress is has been drawn to. The structure developed at high stress is more resistance to creep, and is stable during stress relaxation. In section 4.2.6, it will be seen that after strain hardening until a higher stress, the material retains a larger proportion of that stress. In section 4.2.5, it will be seen that the birefringence increases with draw ratio. Hence the better resistance to creep at a higher starting draw ratio can be ascribed to the formation and development of chain extended crystals. These are more able to retain the stress and hence provide a better resistance to creep.

4.1.4 Influence of stress on the creep rate deceleration factor

The creep rate deceleration factor, calculated from the linear part of the Sherby-Dorn curves, as a function of stress is given for the four bimodal materials in figure 4.24. Overall, the creep resistance decreases with increasing starting creep stress. Bi-HMHB has a lower creep rate deceleration

factor (and hence a better resistance to creep) than the other three bimodal materials, which have the same creep rate deceleration factor. It appears that only a combination of high molecular mass and high branching increases the resistance to creep. At stresses close to the final stress after pre-drawing (see table 3.12), the creep rate deceleration factor drops dramatically, as can be seen for bi-LMHB and bi-LMLB.

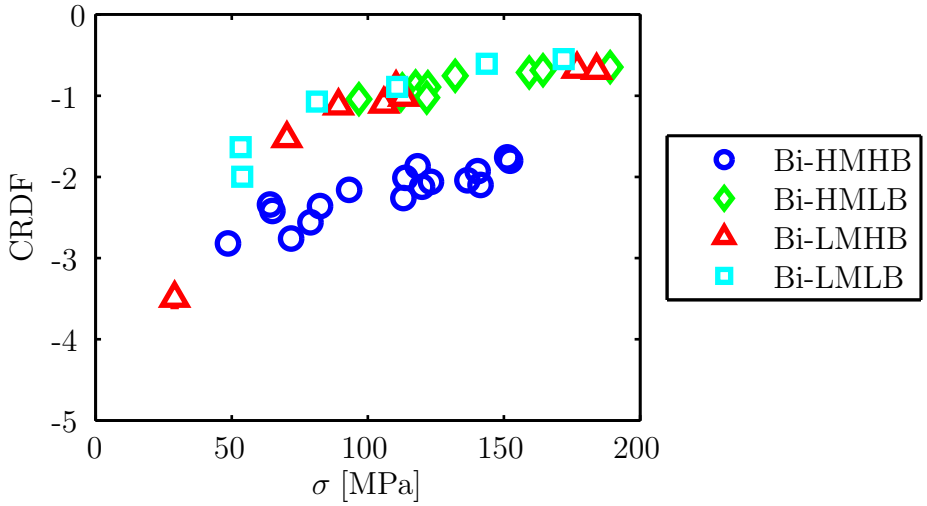

Figure 4.24: Creep rate deceleration factor as a function of stress for the bimodal materials

Limits to the stress range for the calculation of the creep rate deceleration factor

Figure 4.25 shows the draw ratio as a function of time for bi-HMHB at high (starting) creep stresses. If failure occurs before the Sherby-Dorn curve reaches the linear part, the creep rate deceleration factor cannot be calculated. For bi-HMHB, failure occurs after creep at an average strain rate of $1.9 \pm 0.7\ 10^{-4}$, an average draw ratio of 12.1 ± 0.2 and an average stress of 223 ± 10 MPa. The highest stress at which the creep rate deceleration factor can be measured is thus when the material fails during the linear part of the Sherby-Dorn curve. The lowest stress at which the creep rate deceleration factor can be measured is in theory the stress after pre-drawing, if the accuracy of the testing equipment allows to determine the extension difference over time.

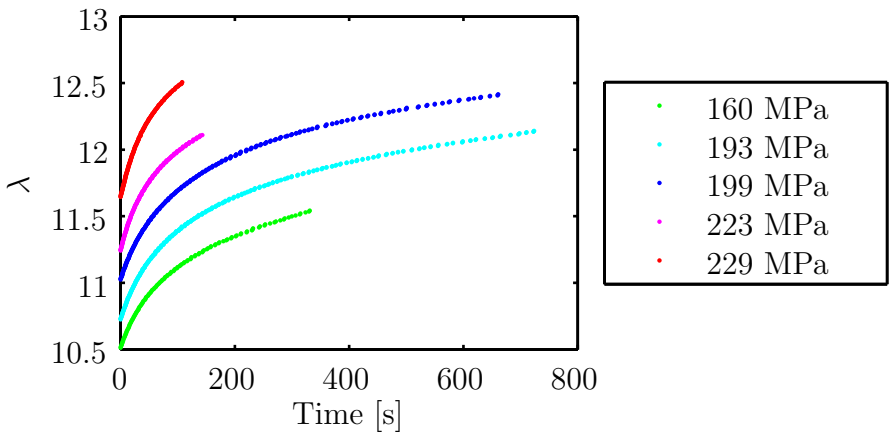

Figure 4.25: Draw ratio as a function of time for bi-HMHB, during creep at high stress

4.1.5 Stress relaxation after creep

Stress relaxation is done after creep. Figure 4.26 gives a schematic of this test. The results are given in table 4.2. The stress retention after 1000s is similar for all the materials at all stresses. The same can be concluded for the stress retention after 10000s. Section 4.2.6 will identify the determining factor for stress relaxation.

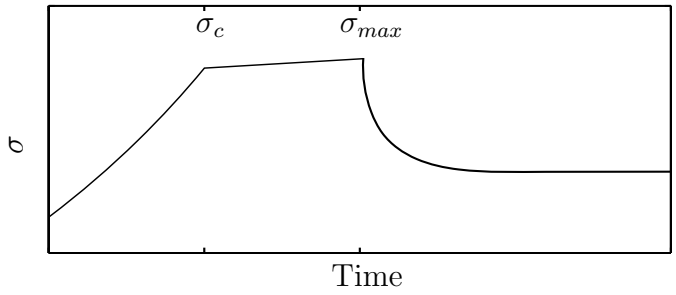

Figure 4.26: Schematic of the creep followed by stress relaxation test

4.1.6 Influence of temperature on creep

The influence of temperature on creep behaviour is studied for bi-HMHB and bi-HMLB. For bi-HMHB, creep behaviour is compared at 70°C, 80°C and 90°C. The creep behaviour at 70°C and 80°C at similar starting creep stresses is compared in figure 4.27. The CRDF at 80°C at 93 and 113 MPa is -2.16 ± 0.06 and -2.26 ± 0.07 respectively. The CRDF at 70°C, for a

	σ_c [MPa]	λ_c	σ_{max} [MPa]	λ_{max}	$\dot{\epsilon}_{max}$ [/s]	$\frac{\sigma_{1000s}}{\sigma_{max}}$	$\frac{\sigma_{10000s}}{\sigma_{max}}$
bi-HMHB	51	5.6	72	7.6	$2.63\ 10^{-7}$	0.99	0.96
	114	8.5	147	10.7	$2.99\ 10^{-7}$	0.99	0.95
bi-HMLB	58	5.9	85	8.3	$5.51\ 10^{-7}$	0.98	0.93
	132	9.3	186	12.8	$5.96\ 10^{-7}$	0.98	0.91
bi-LMHB	59	6.8	86	9.5	$4.26\ 10^{-7}$	0.99	0.94
bi-LMLB	46	5.4	72	8.1	$4.25\ 10^{-7}$	0.99	0.94
	59	6.5	86	9.3	$4.35\ 10^{-7}$	0.99	0.94

Table 4.2: Parameters of stress relaxation after creep tests. The standard error on the stresses is 2%, the standard error on the draw ratios 0.2 and the error on the stress ratios is 0.03

stress in between - 107 MPa, is -2.24 ± 0.07. So the behaviour at 70°C is not significantly different for this material and stress level.

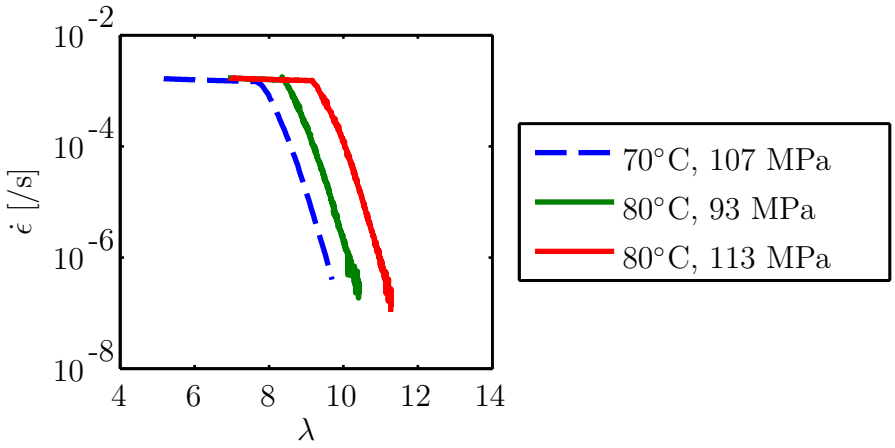

Figure 4.27: Sherby-Dorn curves at 70°C (dashed line) and 80°C (solid line) for bi-HMHB

For bi-HMHB at 90°C, two stress levels are studied, the first one around 40 MPa (figure 4.28) and the second one around 130 MPa (figure 4.29). For the low stress level, the CRDF is expected to be between -5.0 ± 0.1 and -3.12 ± 0.09 based on the 80°C tests. For 90°C, the CRDF is -2.21 ± 0.07 at a stress of 46 MPa. For the high stress level, the CRDF is expected to be between -2.06 ± 0.06 and -2.04 ± 0.06 based on the 80°C tests. For 90°C, the CRDF is -1.52 ± 0.05 at a stress of 130 MPa. In both cases, the creep resistance is significantly lower at this temperature and stress level.

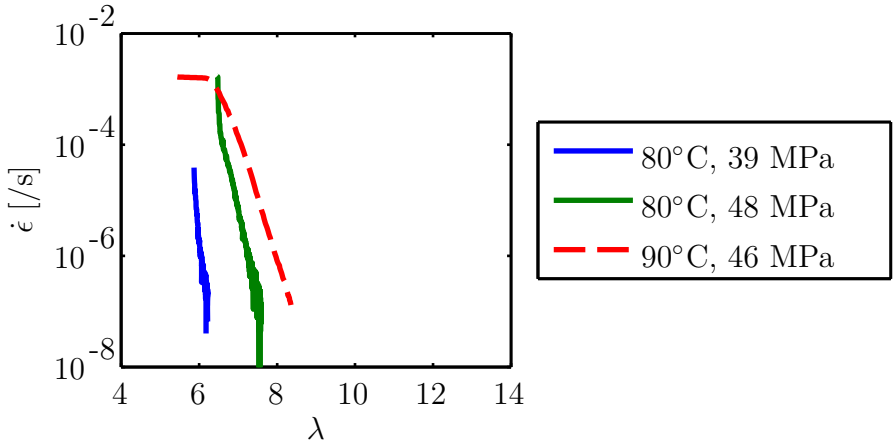

Figure 4.28: Sherby-Dorn curves at 80°C (solid line) and 90°C (dashed line) for bi-HMHB

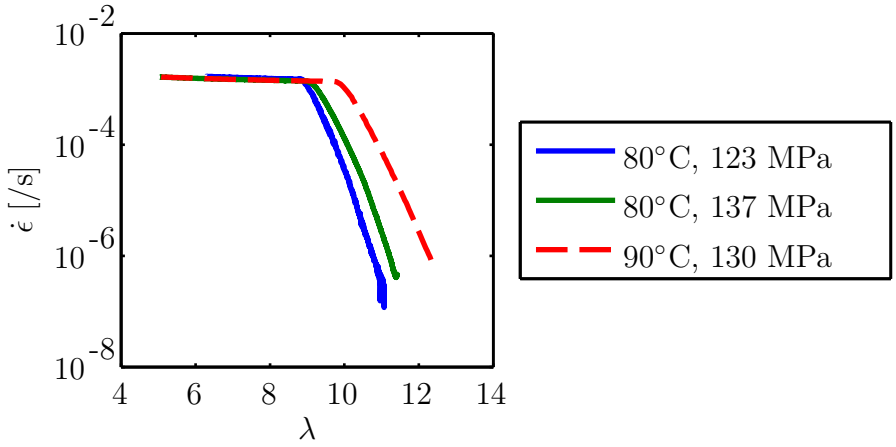

Figure 4.29: Sherby-Dorn curves at 80°C (solid line) and 90°C (dashed line) for bi-HMHB

The creep behaviour of bi-HMLB is compared at 25°C, 70°C, 80°C and 90°C. A comparison of creep at 25°C and 80°C for different stresses is shown in figures 4.30 and 4.31. Around 115 MPa, room temperature creep is lower than creep at 80°C creep, but does not result in a linear region where the CRDF can be calculated (the same is observed for a stress of around 160 MPa). At a higher stress, the CRDF can be calculated, which results in a CRDF of -1.06 ± 0.03 for creep starting at 226 MPa for 25°C. For comparison, at 80°C, a stress of 187 MPa results in a CRDF of -0.65 ± 0.02. The creep resistance at 25°C is higher than at 80°C.

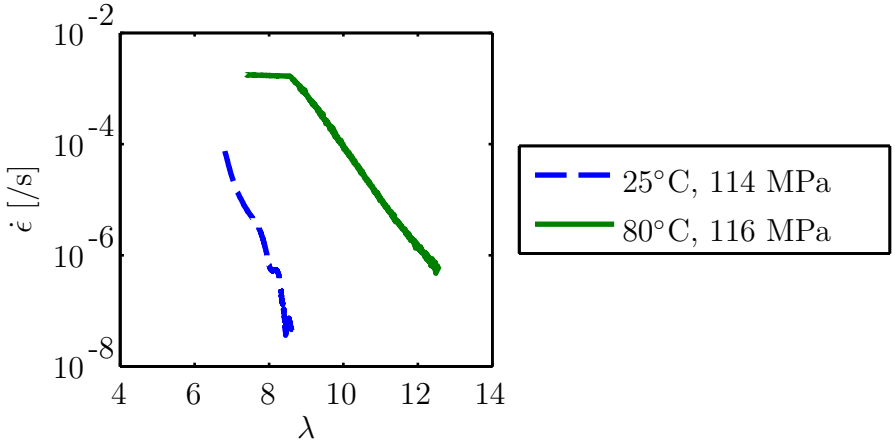

Figure 4.30: Sherby-Dorn curves at 25°C (dashed line) and 80°C (solid line) for bi-HMLB

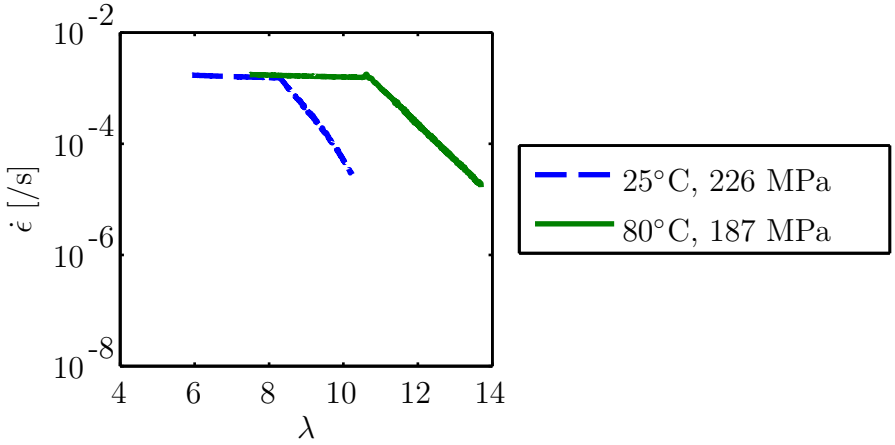

Figure 4.31: Sherby-Dorn curves at 25°C (dashed line) and 80°C (solid line) for bi-HMLB

The same trend can be seen for tests at 70°C. Figure 4.32 shows a com-

parison of creep tests at 70°C and 80°C. No significant difference is seen between the test at 70°C and the tests at 80°C.

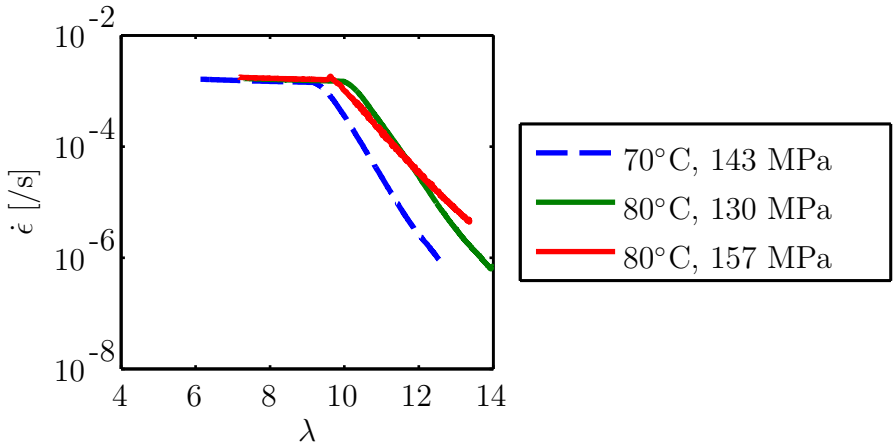

Figure 4.32: Sherby-Dorn curves at 70°C (dashed line) and 80°C (solid line) for bi-HMLB

Finally, tests were done at 90°C and compared to the creep behaviour at 80°C. This is shown in figure 4.33. The lowest measurable CRDF at 80°C is -5.4 ± 0.2, for a stress of 38 MPa. At a stress of 30 MPa, the CRDF can still be measured a creep test at 90°C, with a result of -1.98 ± 0.06. In conclusion, for both bi-HMHB and bi-HMLB, there is no significant difference between the creep behaviour at 70°C and at 80°C, but the resistance to creep drops significantly above 90°C. The mobility of the chains increases with increasing temperature, which explains the lower resistance to creep at 90°C. However, why the creep resistance does not change between 70°C and 80°C is not clear. As will be seen in section 4.2.7, the sensitivity to temperature of the strain hardening modulus between 70°C and 90°C is approximately linear.We suggest more measurements over a wider range of temperature should be taken to explore the temperature sensitivity of both modes of deformation.

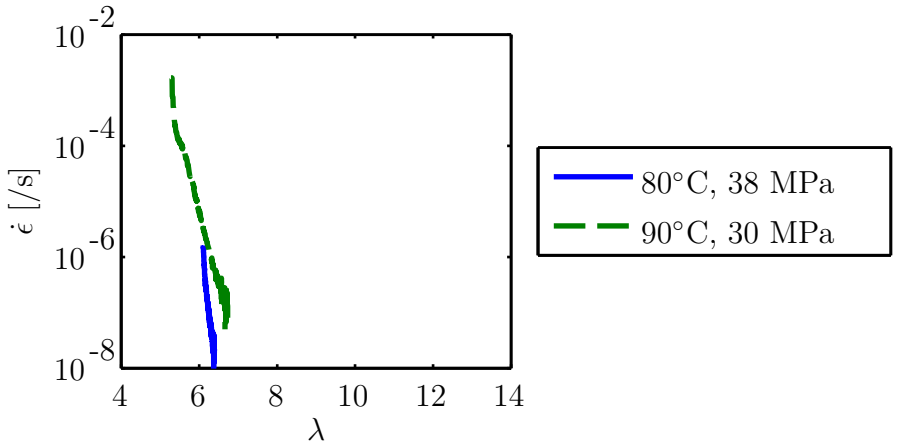

Figure 4.33: Sherby-Dorn curves at 80°C (solid line) and 90°C (dashed line) for bi-HMLB

4.1.7 Discussion: influence of molecular mass and branch content on the creep behaviour of bimodal polyethylene

The resistance to creep decreases with increasing stress for all materials. At stresses below and very close to the maximum stress reached during pre-drawing, there is a dramatic decrease of resistance with stress. At higher stresses, the slope of the CRDF versus stress curve is much shallower. In this region, the slope is similar for all the bimodal materials, but bi-HMHB has a lower CRDF than bi-HMLB, bi-LMHB and bi-LMLB. It appears that only a combination of high branch content and high molecular mass reduces the CRDF in this region. Bi-HMHB is expected to have the highest number of tie molecules out of the four materials. It has a high molecular mass, making it more likely for the chains to cross multiple lamellae, and due to the high branch content is has a lower lamellar thickness. The number of intercrystalline bridges is thus expected to be highest. On top of that, the friction, whether originating from a branch being pulled over an entanglement or into a crystal, can be expected to be high in this material due to the branch content. As could be seen in table 3.18, the available molecular network is similar for all the bimodals (there is a small increase for bi-HMHB, but not enough to explain the difference in creep resistance), but the high number of tie chains combined with high friction leads to a higher effective network density for bi-HMHB.

4.2 Strain hardening behaviour

The significance of the strain hardening modulus and its relation to the effective entanglement network are described in section 1.4.1. The strain hardening modulus can be obtained using a simple tensile measurement at constant strain rate and high temperature and has been shown to correlate with slow crack growth in semi-crystalline polymers [122, 123]. In this section, the strain hardening behaviour of the bimodal materials is described and discussed.

4.2.1 Optimisation of the test protocol

Strain hardening measurements are performed by pre-drawing the samples at a strain rate of 3 $10^{-}2$/s as described in section 3.3.1, measuring sample dimensions, setting the strain rate to the desired value and drawing until failure or until the equipment extension limit. The variation in the resulting strain hardening curve is discussed and it is checked whether the details of the protocol have an influence on the resulting strain hardening behaviour.

Variability

The variation in strain hardening behaviour is studied for all the materials at a strain rate of around 1.45 10^{-3}/s. Repeated tests are shown on figures 4.34, 4.35, 4.36 and 4.37 for bi-HMHB, bi-HMLB, bi-LMHB and bi-LMLB respectively. A variation of 10% in stress can be expected due to thickness variations throughout the dumbbell samples, which are maximum 30 µm. As can be seen on figure 4.34, the difference between samples can be larger than the expected 10%, sometimes up to 30%, especially at higher strain rates. To reduce the standard error, up to 7 repeated measurements were performed.

Influence of opening the oven

To be able to check the specimen dimensions after pre-drawing, the oven needs to be opened. The influence of this (short) temperature shock is studied. Figure 4.38 shows the comparison between bi-HMLB samples drawn following the 'classic' protocol and samples pre-drawn at 3 10^{-2}/s, then

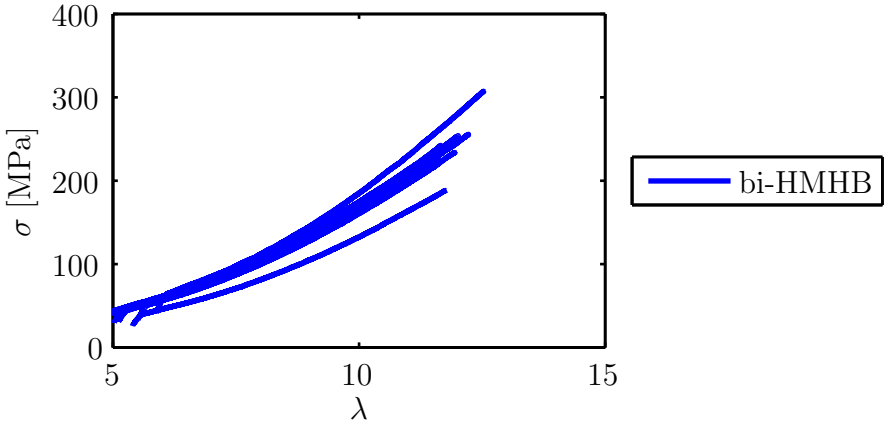

Figure 4.34: Variability of the strain hardening at a strain rate of approximately 1.45 10^{-3}/s for bi-HMHB

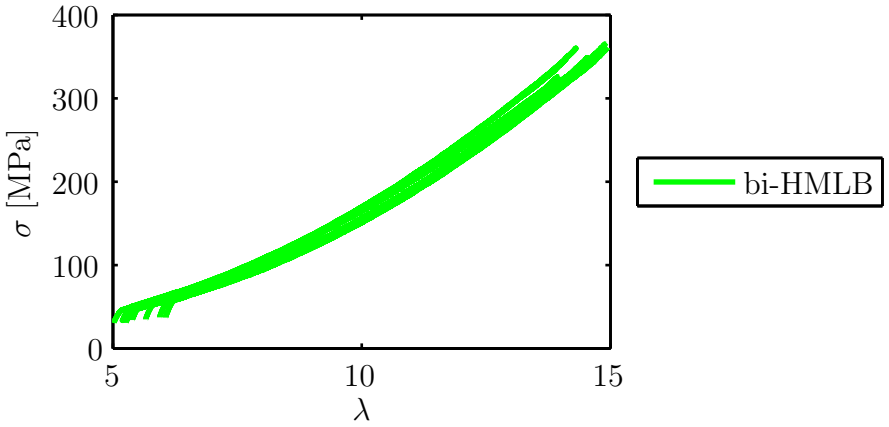

Figure 4.35: Variability of the strain hardening at a strain rate of approximately 1.45 10^{-3}/s for bi-HMLB

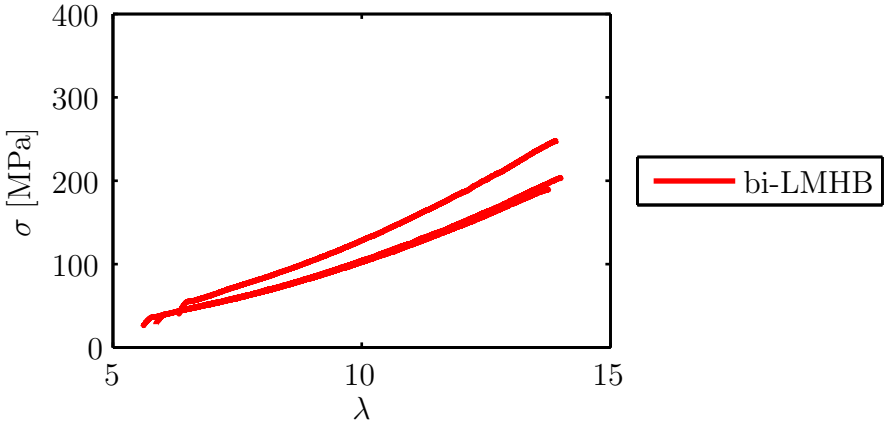

Figure 4.36: Variability of the strain hardening at a strain rate of approximately 1.45 10^{-3}/s for bi-LMHB

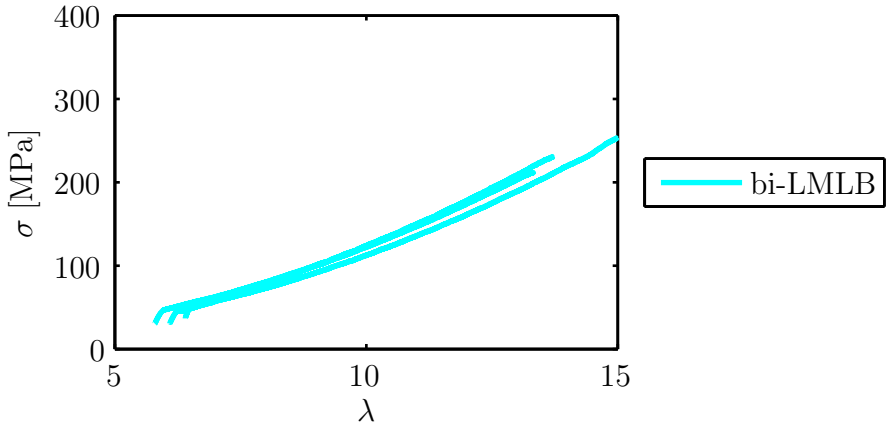

Figure 4.37: Variability of the strain hardening at a strain rate of approximately 1.45 10^{-3}/s for bi-LMLB

drawn at approximately 1.45 10^{-3}/s but without opening the oven to check sample dimensions in between. The strain hardening behaviour agrees. It is concluded that there is no significant influence of opening the oven.

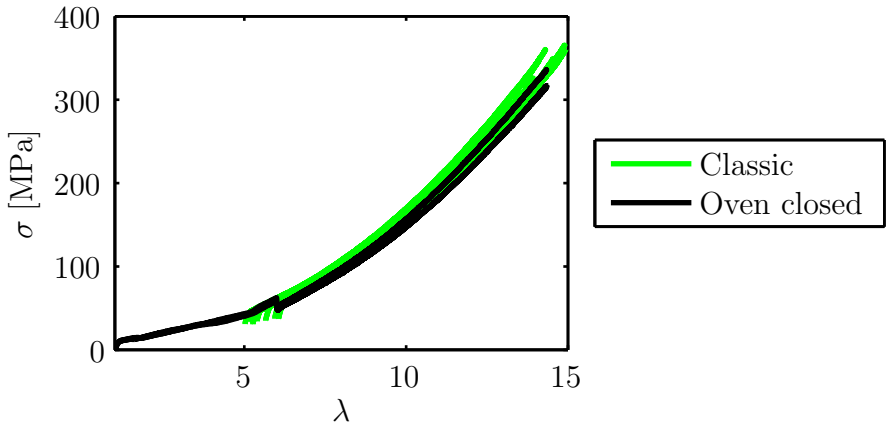

Figure 4.38: 'Classic' strain hardening protocol versus strain hardening without opening the oven for bi-HMLB

Influence of stress relaxation during dimension check

To be able to check the specimen dimensions after pre-drawing, the oven needs to be opened and the specimen stress relaxes for a couple of minutes during which the dimensions are checked. The influence of this stress relaxation is studied. Figure 4.39 shows the comparison between bi-HMLB samples drawn following the 'classic' protocol and samples pre-drawn at 3 10^{-2}/s, drawn at approximately 1.45 10^{-3}/s, without opening the oven to

check sample dimensions in between, but with stress relaxation for 7 minutes. The strain hardening behaviour agrees. It is concluded that there is no significant influence of the stress relaxation during the dimension check.

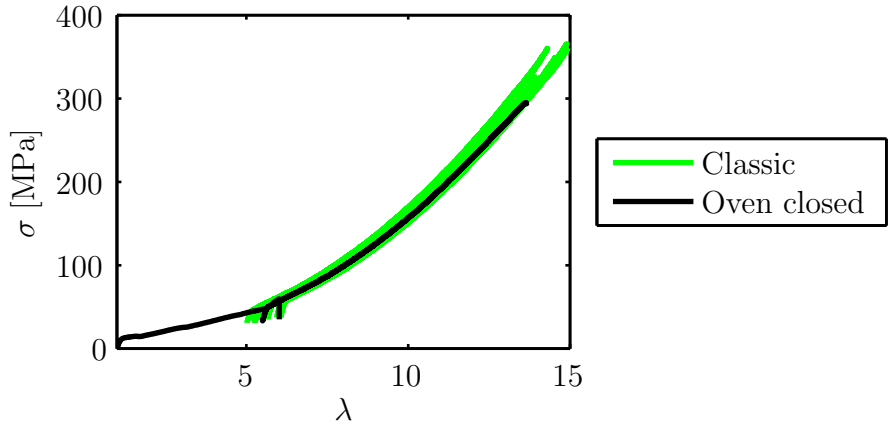

Figure 4.39: 'Classic' strain hardening protocol versus strain hardening without opening the oven, with stress relaxation, for bi-HMLB

Influence of pre-drawing strain rate

All materials can be drawn from isotropic into the strain hardening region at a strain rate of around 3 10^{-2}/s. For lower strain rates (and sometimes higher strain rates, depending on the material), some of the materials fail during the necking process. Therefore it is decided to pre-draw all materials at a strain rate of 3 10^{-2}/s. The effect of this pre-drawing is studied in the bimodal materials, which can also all be drawn through the neck at a strain rate of around 1 10^{-3}/s. A comparison is made between the strain hardening behaviour of the 'classic' tests (pre-drawing at 3 10^{-2}/s, dimension check, drawing at 1 10^{-3}/s) and drawing from isotropic (pre-drawing and drawing at 1 10^{-3}/s without dimension check in between). The results are shown in figures 4.40, 4.41, 4.42 and 4.43 for bi-HMHB, bi-HMLB, bi-LMHB and bi-LMLB respectively. It can be seen that the variation within the isotropic protocol is slightly smaller except for bi-LMLB, but overall the strain hardening behaviour is the same as for the classic protocol.

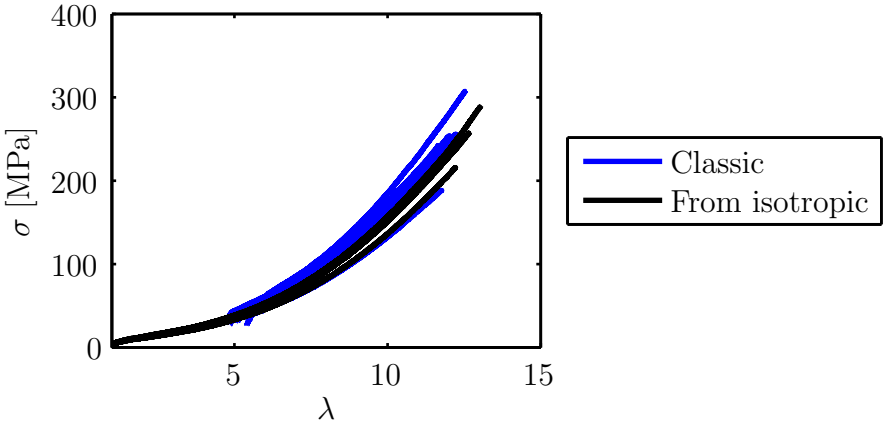

Figure 4.40: 'Classic' strain hardening protocol versus strain hardening from isotropic for bi-HMHB

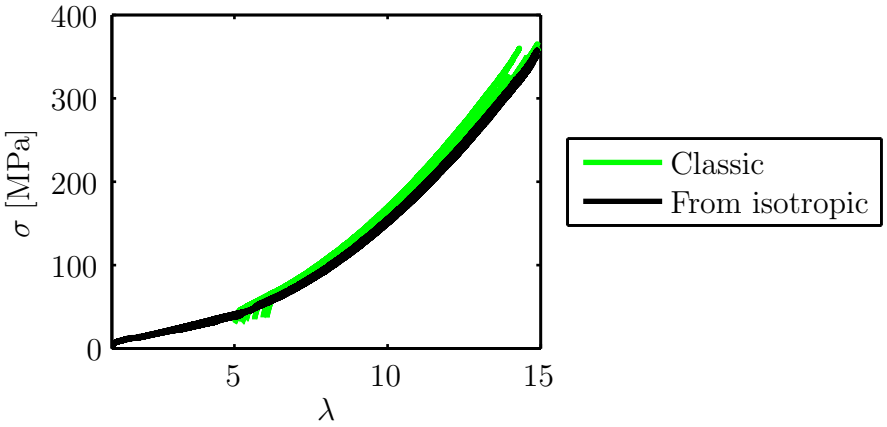

Figure 4.41: 'Classic' strain hardening protocol versus strain hardening from isotropic for bi-HMLB

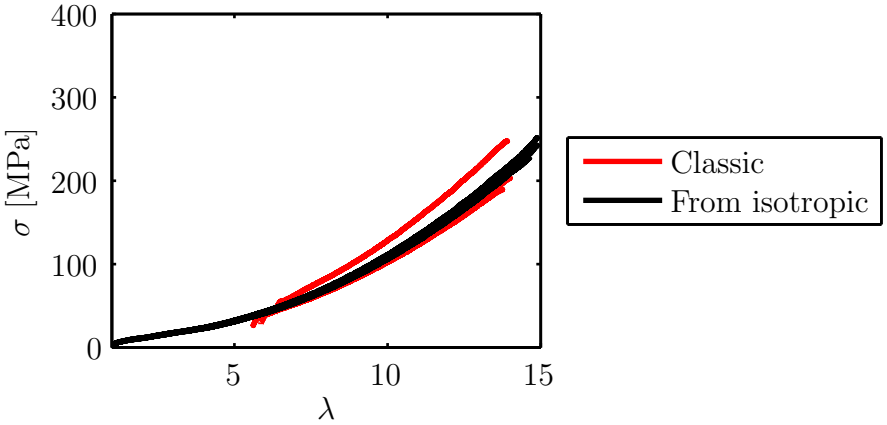

Figure 4.42: 'Classic' strain hardening protocol versus strain hardening from isotropic for bi-LMHB

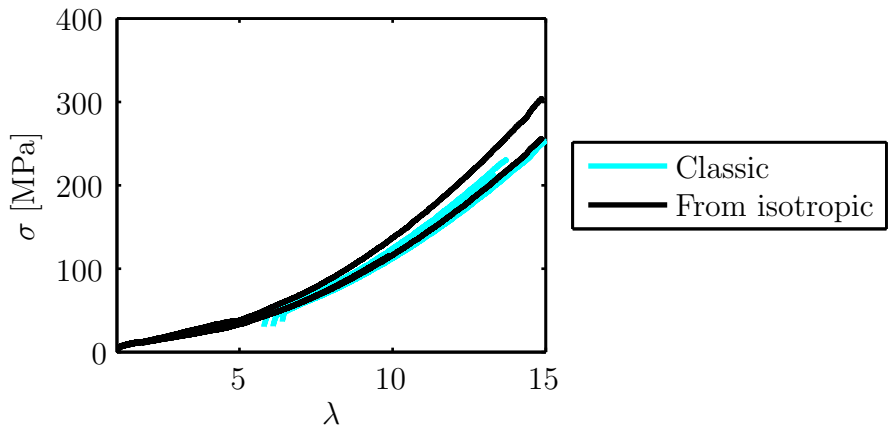

Figure 4.43: 'Classic' strain hardening protocol versus strain hardening from isotropic for bi-LMLB

Influence of test duration

The time duration of the tests for bi-HMLB is given per material in table 4.3. For the other materials, the test durations are similar. For one strain rate, there is no correlation between measuring time and resulting strain hardening curve.

$\dot{\epsilon}$ [/s]	Test duration [s]
$1.50\ 10^{-7} \pm 8\ 10^{-11}$	$1.45\ 10^{6}$
$1.60\ 10^{-6} \pm 8\ 10^{-10}$	$7.58\ 10^{4} \pm 6\ 10^{2}$
$7.00\ 10^{-6} \pm 1\ 10^{-7}$	$9.43\ 10^{4} \pm 6\ 10^{3}$
$1.40\ 10^{-5} \pm 4\ 10^{-7}$	$5.14\ 10^{4} \pm 1\ 10^{4}$
$7.30\ 10^{-5} \pm 2\ 10^{-6}$	$8.10\ 10^{3} \pm 2\ 10^{3}$
$1.38\ 10^{-4} \pm 2\ 10^{-6}$	$6.21\ 10^{3} \pm 1\ 10^{2}$
$6.83\ 10^{-4} \pm 7\ 10^{-6}$	$1.27\ 10^{3} \pm 4\ 10^{-3}$
$1.30\ 10^{-3} \pm 9\ 10^{-20}$	$6.38\ 10^{2} \pm 6\ 10^{-1}$
$6.30\ 10^{-2} \pm 2\ 10^{-4}$	$1.26\ 10^{2} \pm 1\ 10^{0}$
$1.35\ 10^{-2} \pm 3\ 10^{-4}$	$6.24\ 10^{1} \pm 1\ 10^{0}$
$3.20\ 10^{-2} \pm 2\ 10^{-5}$	$2.35\ 10^{1} \pm 2\ 10^{-1}$

Table 4.3: Average test duration of the strain hardening test (excluding pre-drawing time) per strain rate for bi-HMLB

4.2.2 Influence of strain rate on the shape of the strain hardening curves

The influence of strain rate on the strain hardening of the bimodal materials is studied. Slow crack growth is a process that takes place over several decades. Hence the strain rates involved are very low and the time scales very long. The strain hardening tests are accelerated by performing them at elevated temperature, but the precise time - temperature superposition parameters are not known. Therefore it is important to understand what happens to the strain hardening behaviour when the strain rate is lowered, and whether the ranking of the materials using the strain hardening modulus changes with strain rate. Industrial tests are performed at constant cross head speed rather than constant true strain rate, but the corresponding true strain rate lies between 10^{-2}/s at the start of the test and 10^{-3}/s at the end. In this work, the materials fail quickly after the start of the test at high strain rates. The limiting upper strain rate at which the behaviour of the materials can still be assessed is 1.5 10^{-1}/s. At low strain rates, the tests take over 48 hours, longer than practically possible. The lowest strain rate used is 1.5 10^{-6}/s, though the occasional test is done at 1.5 10^{-7}/s.

Extension as a function of load for the bimodal materials for different strain rates is given in figure 4.44. The shape of the curves is different at different strain rates. At high strain rates, the curves curve upwards. For low strain rates, load relaxation is observed at the start of the curves. For all the materials, this relaxation can be observed until a strain rate of around 1.43 10^{-5}/s. Normalising the results over sample dimension as described in section 1.4.1 results in stress - draw ratio curves, given in figure 4.45. At strain rates below 1.44 10^{-5}/s, the low molecular mass materials display a nearly linear stress increase with draw ratio. At higher strain rates, the upswing in stress is clear and becomes stronger with increasing strain rate.

4.2.3 Calculating the strain hardening modulus

The three strategies described in section 1.4.1; the average slope, the Neo-Hookean strain measure and the Haward-Thackray model, are used to calcu-

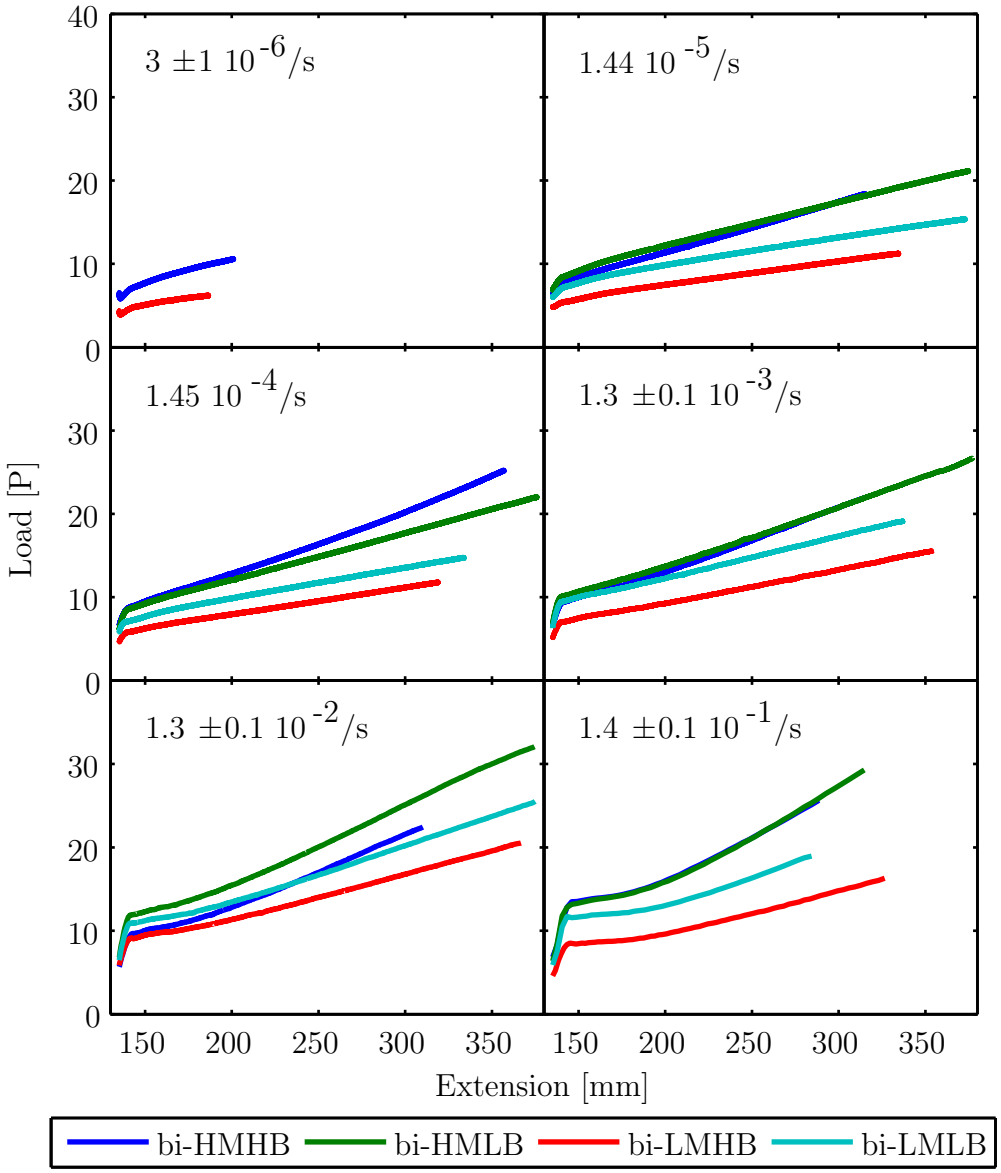

Figure 4.44: Load as a function of extension for different strain rates for the bimodals

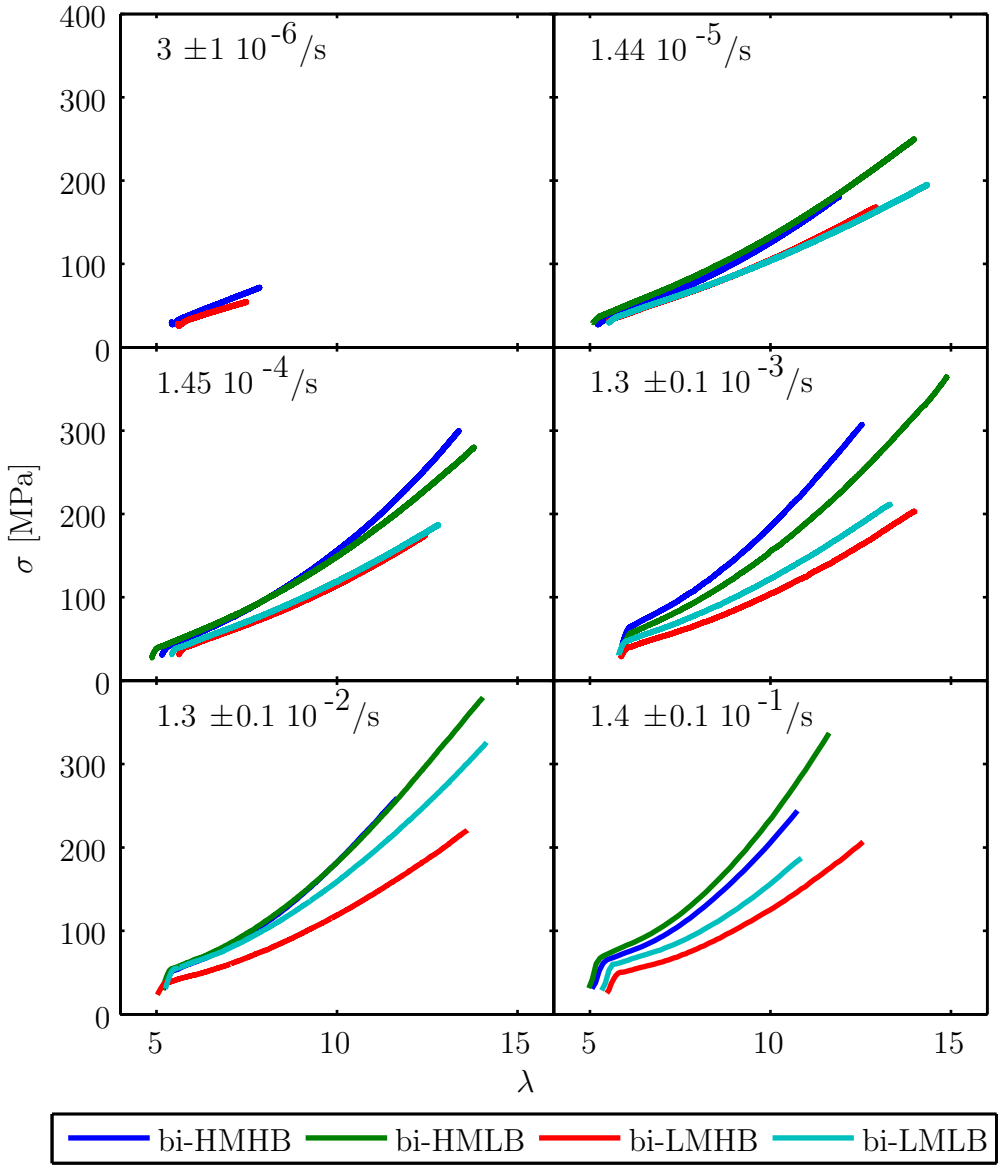

Figure 4.45: Stress as a function of draw ratio for different strain rates for the bimodals

late the strain hardening modulus G_p. It is shown that there is no significant difference between the calculations, but the bimodal materials do not fit a Neo-Hookean model over the entire strain rate range studied.

Average slope

Firstly, the average slope $< G_K >$ is calculated for the curves, between draw ratio 7 and draw ratio 11. This excludes the curves at strain rates below 5 10^{-6}/s, as tests at this strain rate cannot be performed over this draw ratio range within a practical time scale, and for bi-HMHB, curves above 10^{-1}/s, as the failure draw ratio at this strain rate and higher is below draw ratio 11. The result is given in figure 4.46. The standard errors over different tests are too small to be visible on the figure. To show the upswing of the curves, the average error on individual tests is set out as a function of strain rate in figure 4.47. For this, the standard error on the average slope of tests at the same strain rate was averaged. This is essentially a measure of how linear the stress - draw ratio curves are. It can be seen that the standard error increases with increasing strain rate, reflecting the higher upswing at higher strain rates seen in figure 4.45. For the highly branched materials, the error as a function of strain rate increases approximately linearly. For the low branched materials, the increase happens more rapidly, suggesting the upswing in the stress - draw ratio curves with strain rate is more pronounced for these materials.

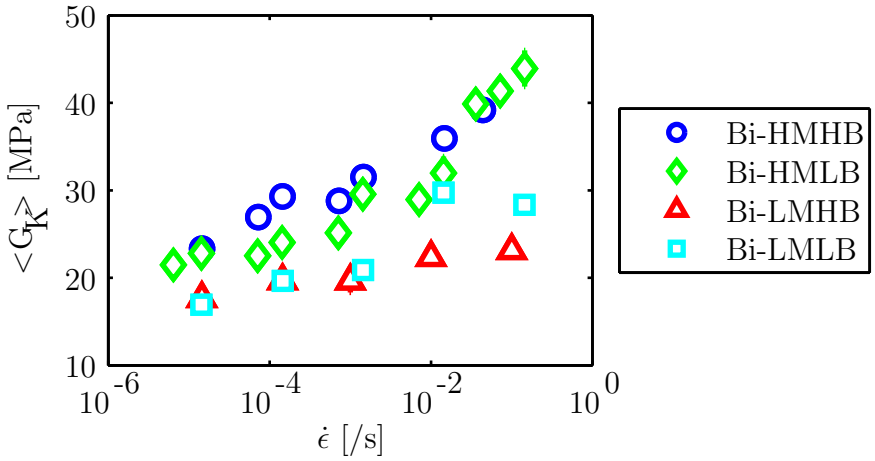

Figure 4.46: Average strain hardening modulus as a function of strain rate for the bimodal materials

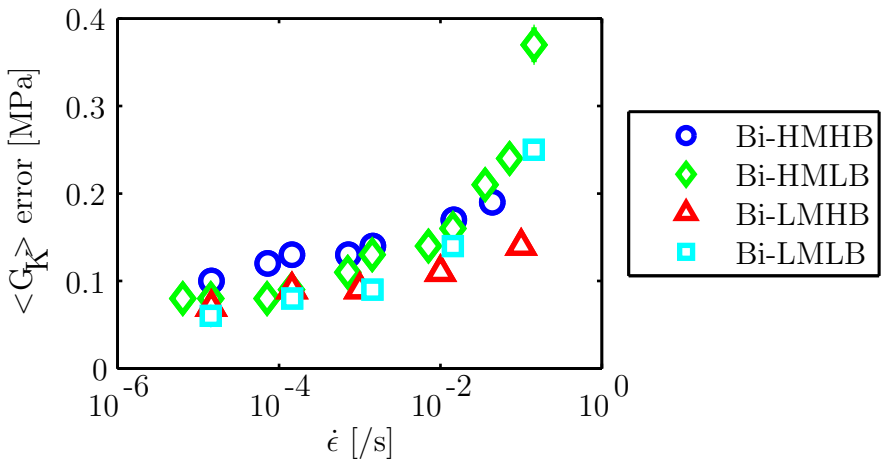

Figure 4.47: Average standard error on average strain hardening modulus as a function of strain rate

Neo-Hookean strain measure

To calculate the strain hardening modulus using the Neo-Hookean strain measure (NHSM), the stress is plotted as a function of $\lambda^2 - 1/\lambda$. The result can be seen in figure 4.48. The linearity of the curves varies with strain rate. An example is given in figures 4.49, 4.50 and 4.51, where the local slope of the stress - NHSM curve is given for strain rates of around 5.5 10^{-6}/s, 7 10^{-4}/s and 1.5 10^{-1}/s respectively. It can be seen that the slope increases at a strain rate of around 1.5 10^{-1}/s. This is reflected in the R^2 squared values for the curves, shown in figure 4.52 as a function of strain rate for the different materials. The R^2 squared value drops from a strain rate of around 10^{-2}/s for all materials. It drops less for the highly branched materials than for the low branched materials (this can easily be seen when comparing the R^2 squared value around 10^{-1}/s), but the onset of the drop is not distinguishably different for the materials. For this reason, the strain hardening modulus based on the Neo-Hookean strain measure is only calculated at strain rates below 10^{-2}/s for the bimodal materials.

From the definitions of $< G_K >$ and G_{NHSM} as given in equations 1.13 and 1.17 respectively, it can be derived that

$$< G_K >= G_{NHSM}(\lambda_{min} + \lambda_{max}), \tag{4.1}$$

with $\lambda_{min} = 7$ and $\lambda_{max} = 11$, the limits used for the calculation of

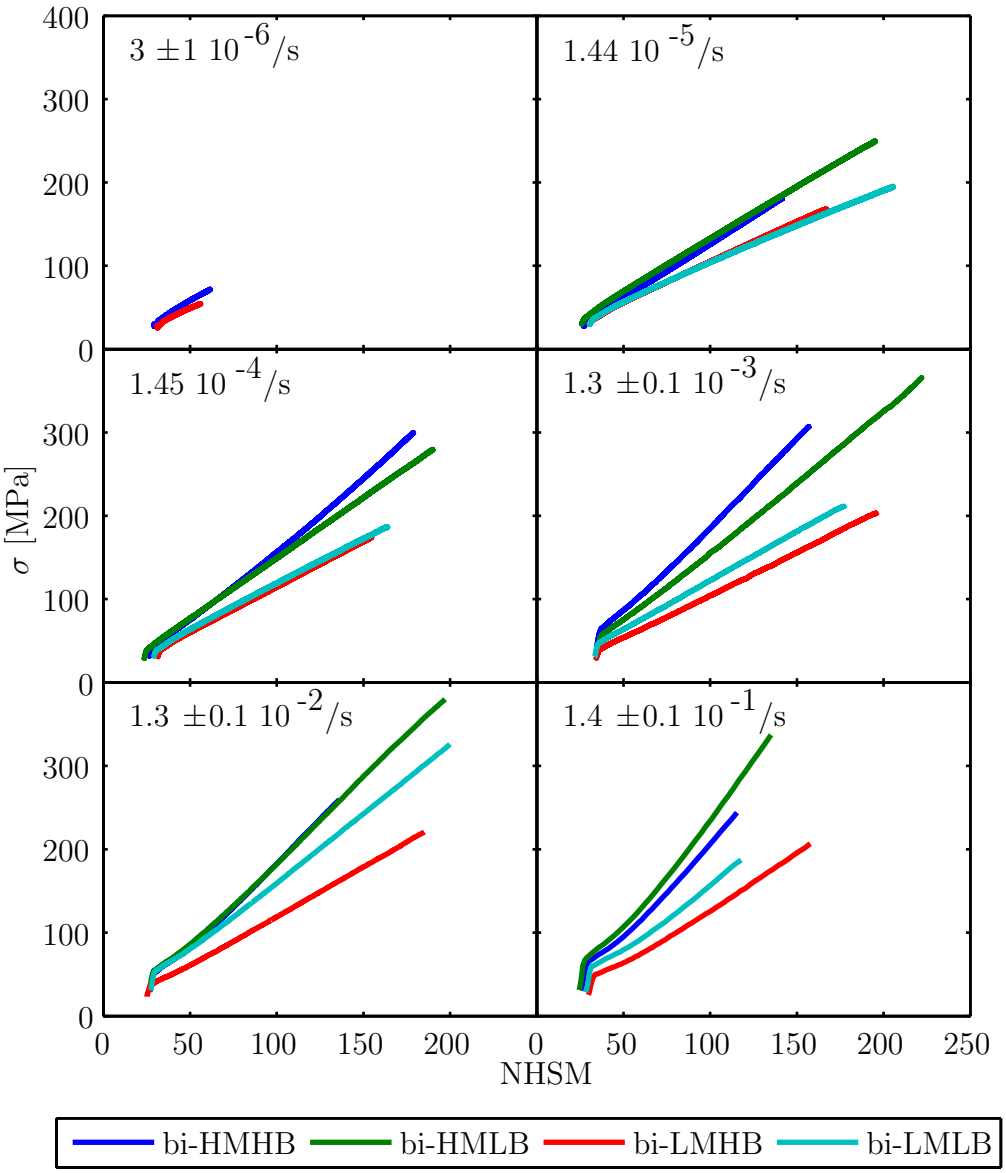

Figure 4.48: Comparison of strain hardening curves at similar strain rates for the bimodal materials

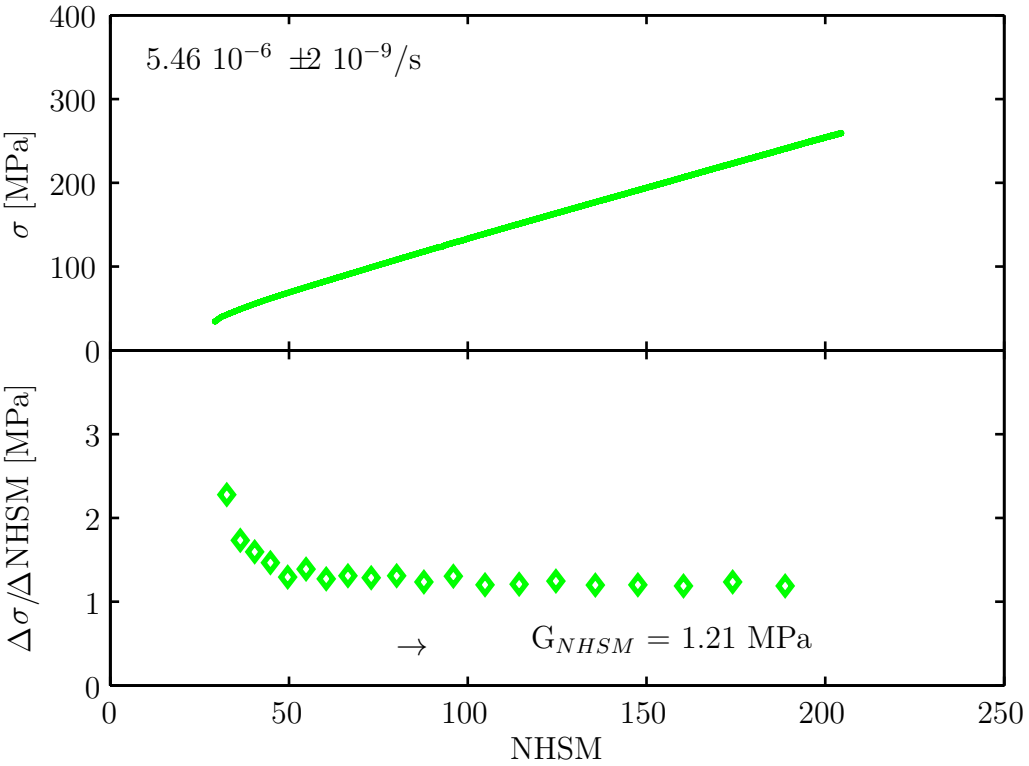

Figure 4.49: Local slope over the NHSM range for bi-HMLB at a low strain rate

$< G_K >$ above. Figure 4.53 shows $< G_{NHSM} >$, calculated using equation 4.1 and G_{NHSM}, as a function of strain rate. Comparison with figure 4.46 shows that there is no significant difference; the trends are the same.

Haward-Thackray model

Finally, the strain hardening modulus was calculated using equation 1.18. This takes into account the non-Gaussian character of the network chains under deformation. The Haward-Thackray model fits the strain hardening behaviour well at every strain rate. An example at low strain rate and high strain rate is given for bi-HMLB in figures 4.54 and 4.55 respectively. As expected, the number of Kuhn segments increases at lower strain rates, where equation 1.18 essentially collapses to equation 1.17. This is the region where the behaviour could be adequately described by the Neo-Hookean strain measure (assuming the chains to be Gaussian). In order to compare G_{HT} as measured from the Haward-Thackray model with $< G_K >$, the average slope is calculated as

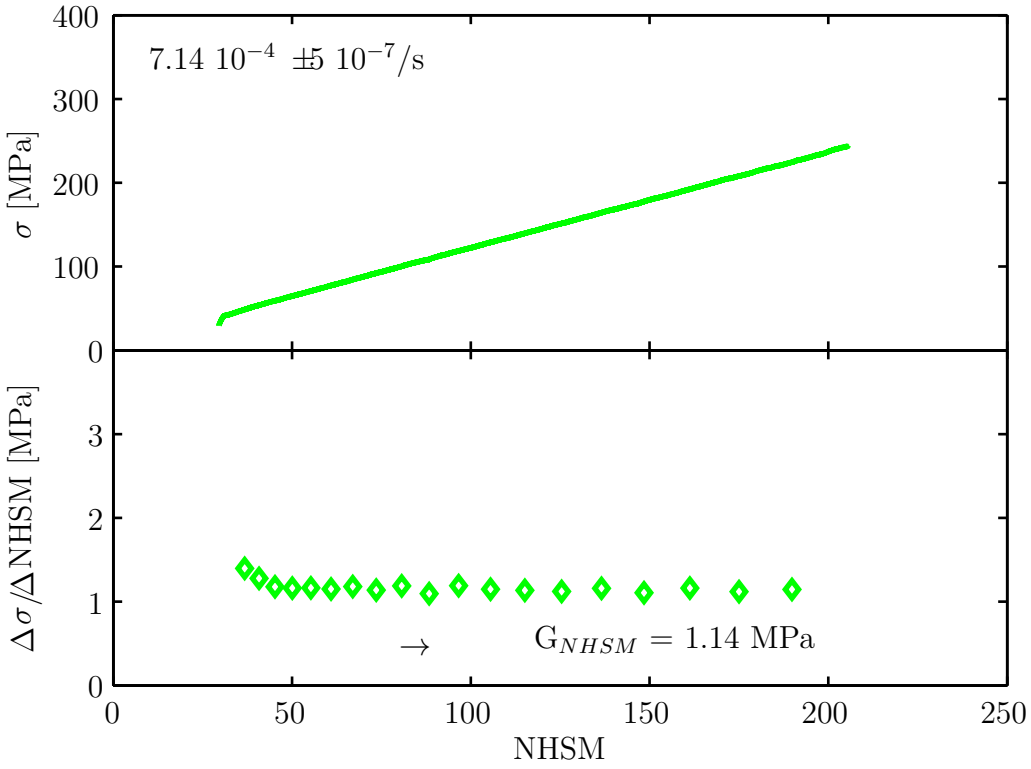

Figure 4.50: Local slope over the NHSM range for bi-HMLB at an intermediate strain rate. The arrow indicates from where the overall strain hardening modulus is calculated

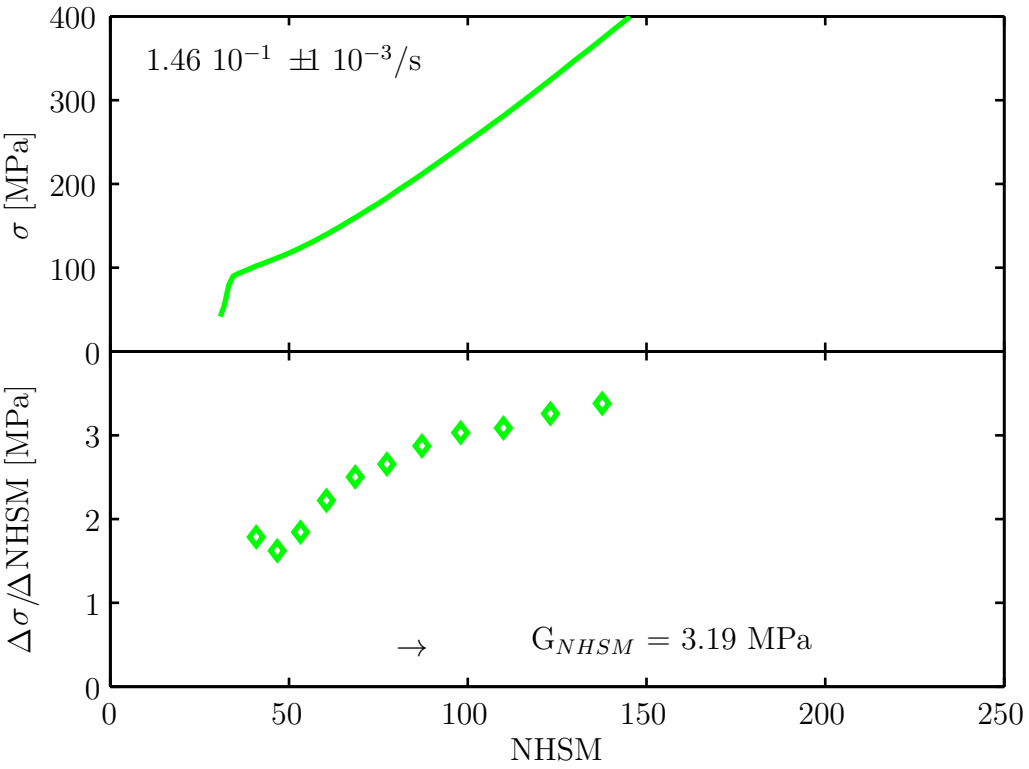

Figure 4.51: Local slope over the NHSM range for bi-HMLB at a high strain rate. The arrow indicates from where the overall strain hardening modulus is calculated

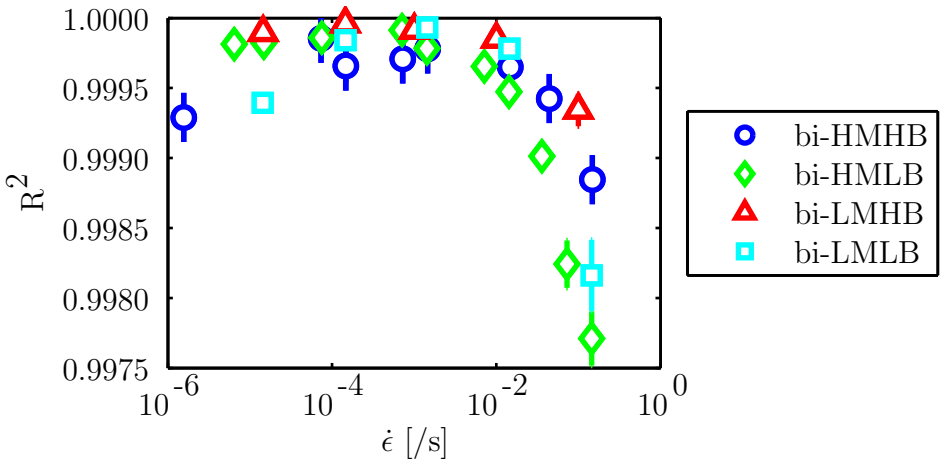

Figure 4.52: R squared value for the least-squares linear fit, calculated on the data starting from NHSM = 50

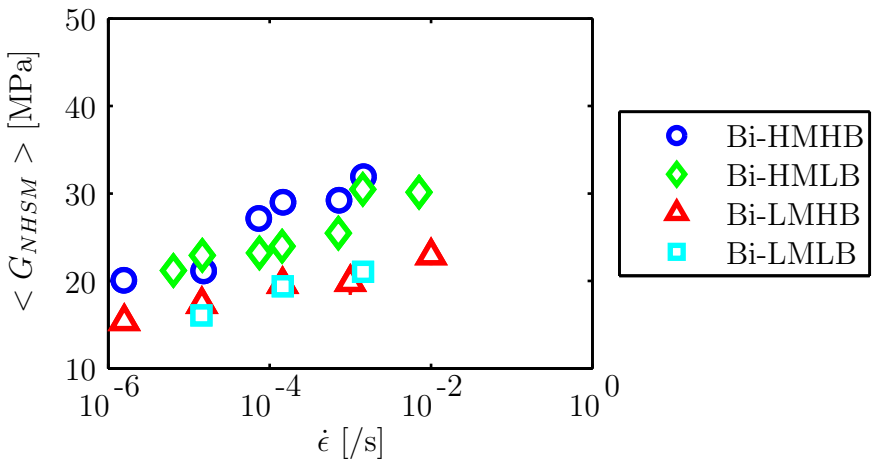

Figure 4.53: $< G_{NHSM} >$ calculated from G_{NHSM} as a function of strain rate for the bimodal materials

$$< G_K >= \frac{1}{6} G_{HT} \Big(\frac{(6\lambda_{min} - 4\frac{\lambda_{min}^3}{N})(1 - \frac{\lambda_{min}^2}{N}) + (\frac{\lambda_{min}}{N})(3\lambda_{min}^2 - \frac{\lambda_{min}^4}{N})}{(1 - \frac{\lambda_{min}^2}{N})^2} + \frac{(6\lambda_{max}^2 - 4\frac{\lambda_{max}^3}{N})(1 - \frac{\lambda_{max}^2}{N}) + (\frac{\lambda_{max}}{N})(3\lambda_{max}^2 - \frac{\lambda_{max}^4}{N})}{1 - \frac{\lambda_{max}^2}{N})^2} - \frac{(\frac{1}{\lambda_{min}^2 N})(\lambda_{min} - \frac{1}{N}) - (3 - \frac{1}{\lambda_{min} N})}{(\lambda_{min} - \frac{1}{N})^2} - \frac{(\frac{1}{\lambda_{max}^2 N})(\lambda_{max} - \frac{1}{N}) - (3 - \frac{1}{\lambda_{max} N})}{(\lambda_{max} - \frac{1}{N})^2} \Big), \quad (4.2)$$

with λ_{min} and λ_{max} 7 and 11 respectively, as before. This results in figure 4.56. It can be seen that the results are very close to those for the average slope and the Neo-Hookean strain measure.

The strain hardening behaviour at every strain rate and for every bimodal material can be approximated using the Haward-Thackray model. This implies that the dynamics of the system are essentially the same over the range of strain rates and materials studied.

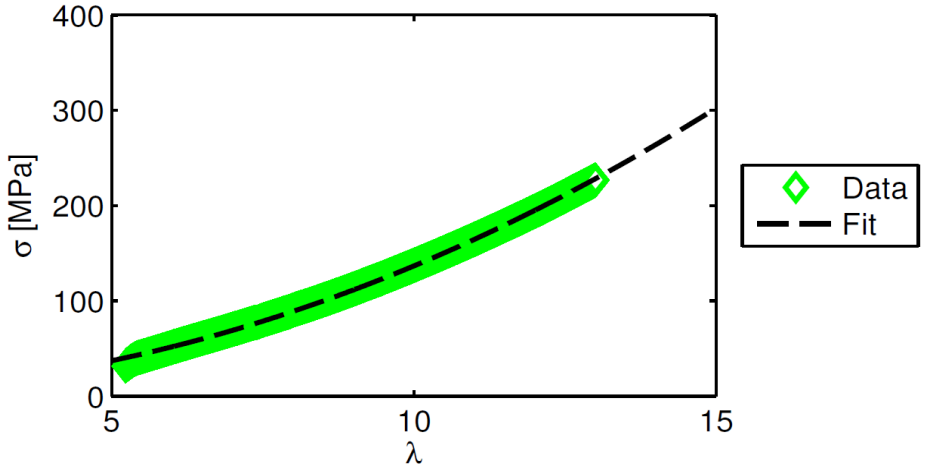

Figure 4.54: Strain hardening fitted using the Haward-Thackray model for bi-HMLB of a strain rate of approximately 8 10^{-5}/s

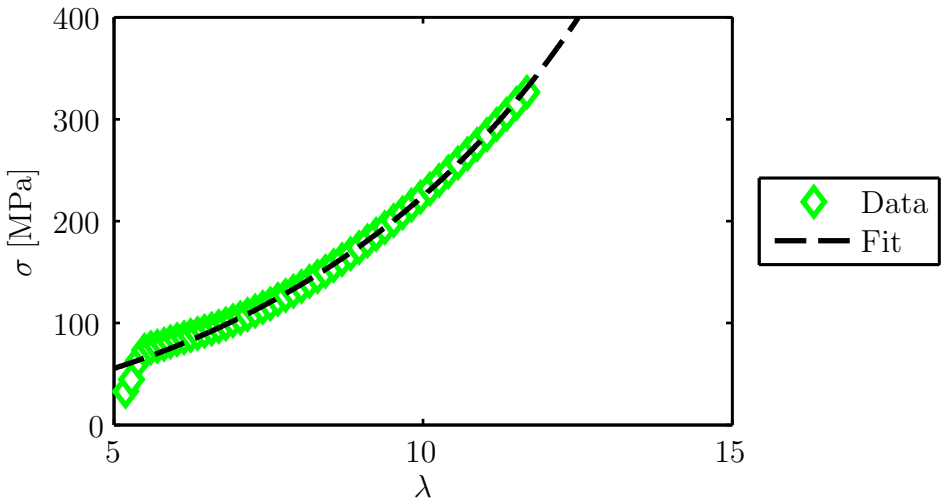

Figure 4.55: Strain hardening fitted using the Haward-Thackray model for bi-HMLB of a strain rate of approximately 7 10^{-2}/s

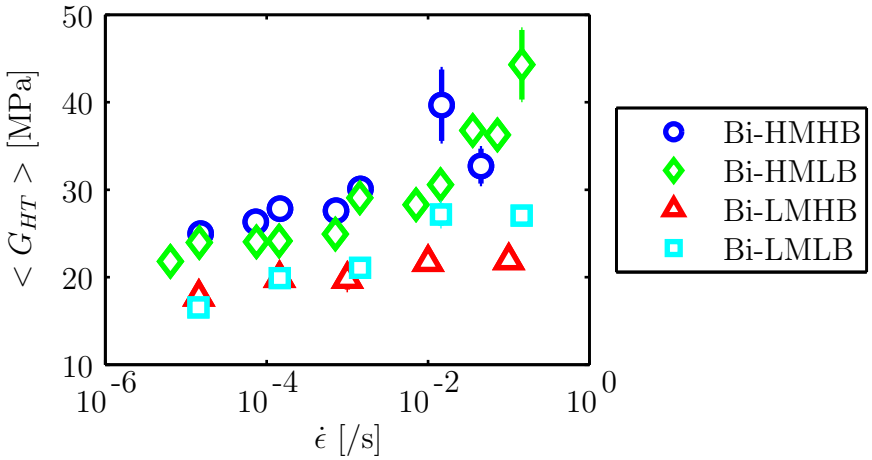

Figure 4.56: $< G_{HT} >$ calculated from G_{HT} calculated using the Haward-Thackray model as a function of strain rate for the bimodal materials

4.2.4 Failure after strain hardening for bi-HMHB

For bi-HMLB, bi-LMHB and bi-LMLB, failure does not occur during the strain hardening within the extension limits of the Instron (maximum draw ratio of 15). For bi-HMHB, at higher strain rates, failure occurs consistently. The failure draw ratio and failure stress are shown in figures 4.57 and 4.58 respectively. They both decrease with increasing strain rate. The results are in line with the results for failure after creep (see section 4.1.4), though the limited data for failure after creep would prevent detecting subtle differences. Failure is dictated by the number of effective chains crossing the surface and the force needed to fracture one covalent chain [29]. This is hence lower for bi-HMHB than for the other materials. From equation 3.6, it can be expected that the chain contour length is higher for this material, and hence the effective crossing density is lower, as the chains cannot be packed together as closely as in the other materials.

The other bimodal materials do not reach failure within the limits of the experimental set-up, so the stress at a certain draw ratio was compared instead. A good material in terms of slow crack growth has a high strain hardening modulus, but also a high stress at natural draw ratio. After predrawing, the low branched materials have the highest stress, but this is at a specific strain rate of 3 10^{-2}/s. Figures 4.59 and 4.60 compare the stress of

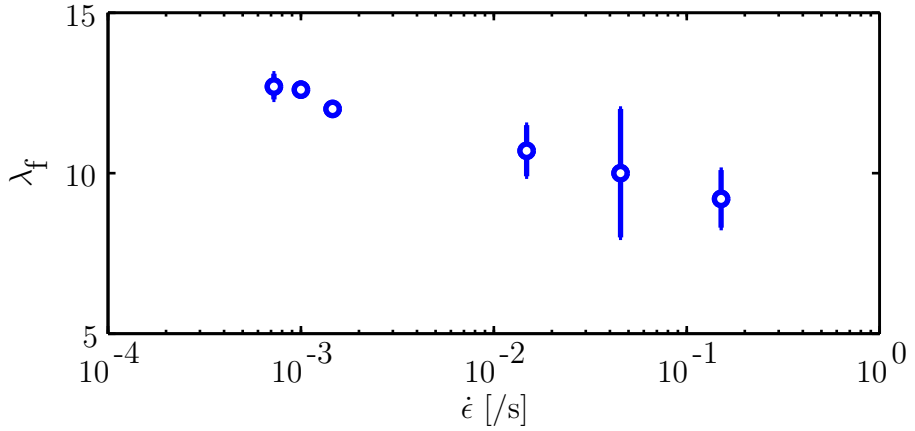

Figure 4.57: Failure draw ratio as a function of strain rate for bi-HMHB

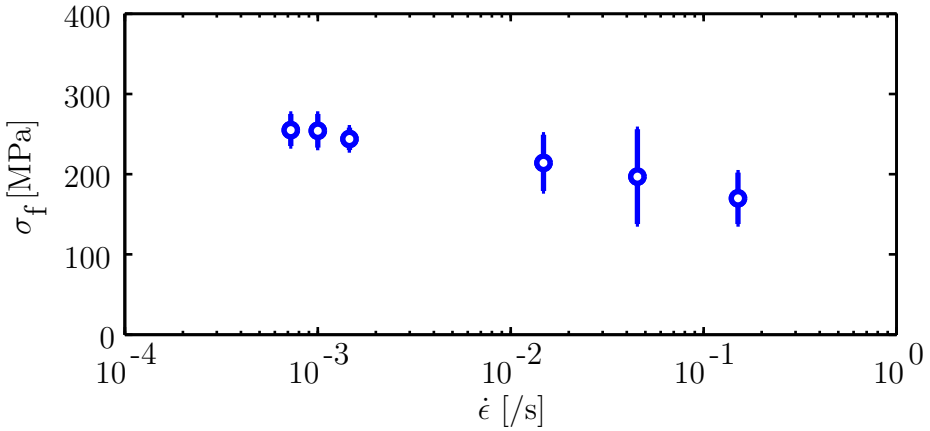

Figure 4.58: Failure stress as a function of strain rate for bi-HMHB

the bimodal materials at a draw ratio of 6 and 9 respectively. Similar trends as for the strain hardening modulus can be seen, where the high branched materials are outperformed by the low branched materials at high strain rates. While the stress at draw ratio 9 for bi-HMLB continually increases with increasing strain rate, the stress for bi-HMHB and bi-LMHB seem to plateau. The behaviour for bi-LMLB is not clear.

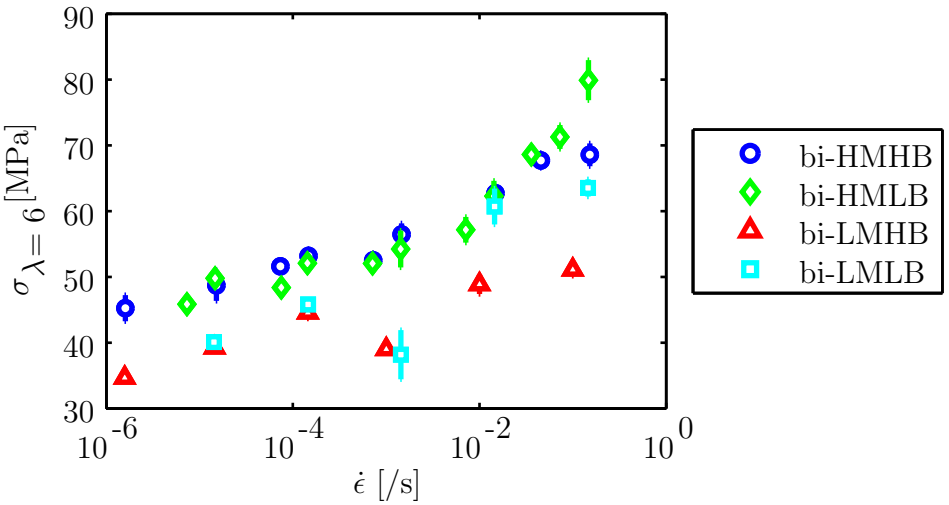

Figure 4.59: Stress at draw ratio 6 as a function of strain rate for the bimodal materials

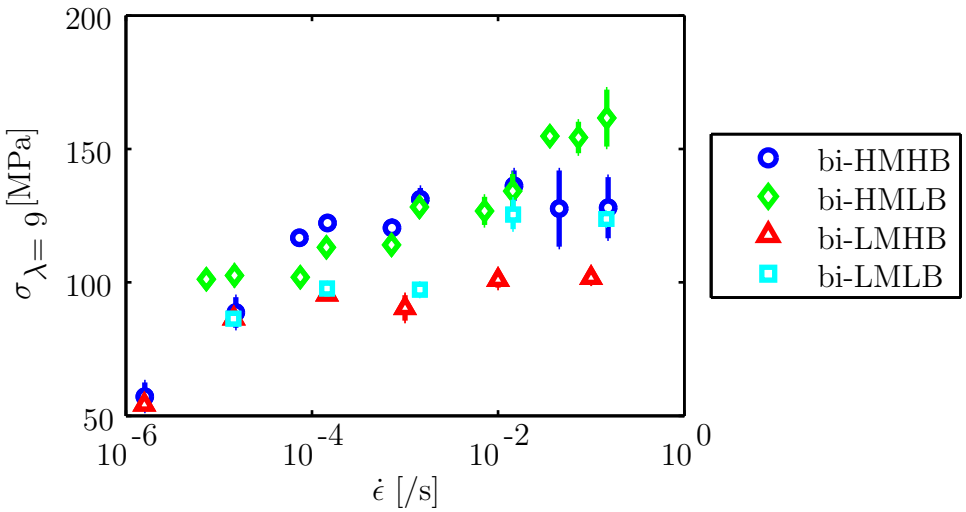

Figure 4.60: Stress at draw ratio 9 as a function of strain rate for the bimodal materials

4.2.5 Structure changes during strain hardening

The crystallinity of the samples is measured after the strain hardening test. The results are given in table 4.4. This crystallinity was measured for the samples after strain hardening, after the strain was released. This has to be kept in mind when discussing these results. Comparing the materials after strain hardening at 10^{-5}/s, at a draw ratio of around 6, the influence of the branch content can be seen: materials with a low branch content have a high crystallinity. The crystallinity of the bimodal materials slightly increases compared to the pre-drawn materials (and decreases compared to the compression moulded material). For bi-HMLB, there is an exception after strain hardening at 10^{-7}/s. In this case, the crystallinity increases until the level of the compression moulded material. These results suggest that after the spherulitic breakdown during the fibrillation, strain induced crystallisation causes an increase in crystallinity during strain hardening. The test duration for the test at 10^{-7}/s is 1.45 10^6s, or 400 hours, and this long time at high temperature promotes crystal growth.

	SH parameters	$X_{c,d}$ [%]
bi-HMHB	10^{-3}/s, 7.4	62.0 ± 0.1
	10^{-5}/s, 5.8	61.6 ± 0.1
bi-HMLB	10^{-5}/s, 6.1	66.48 ± 0.08
	10^{-7}/s, 6.7	67.7 ± 0.2
bi-LMHB	10^{-5}/s, 6.1	62.41 ± 0.02
bi-LMLB	10^{-5}/s, 6.2	65.80 ± 0.05

Table 4.4: Crystallinity evolution with strain hardening. The standard error on the draw ratio after strain hardening varies between 0.06 and 0.3

The birefringence of the samples is measured after strain hardening, according to the procedure explained in section 2.1.5. The results are given in table 4.5 and on figure 4.61. The birefringence is measured on the sample under strain. In general, the birefringence increases with increasing draw ratio. For 10^{-3}/s, the birefringence increases faster with draw ratio for the low branched materials compared to the highly branched materials. The highly branched materials reach a plateau birefringence around draw ratio 8. This suggests that the maximum attainable orientation has been reached

for these materials. The low branched materials almost reach perfect crystallinity at high draw ratios.

	SH parameters	Δn
bi-HMHB	10^{-3}/s, 7.4 ± 0.2	0.045 ± 0.001
	10^{-3}/s, 8.3 ± 0.2	0.049 ± 0.002
	10^{-3}/s, 10.2 ± 0.2	0.050 ± 0.001
bi-HMLB	10^{-3}/s, 8.9 ± 0.2	0.048 ± 0.001
	10^{-3}/s, 10.5 ± 0.2	0.057 ± 0.001
bi-LMHB	10^{-3}/s, 8.8 ± 0.2	0.047 ± 0.001
	10^{-3}/s, 9.1 ± 0.2	0.047 ± 0.001
	10^{-3}/s, 9.7 ± 0.2	0.047 ± 0.001
bi-LMLB	10^{-3}/s, 9.1 ± 0.2	0.048 ± 0.001
	10^{-3}/s, 11.1 ± 0.2	0.054 ± 0.001

Table 4.5: Birefringence evolution with strain hardening

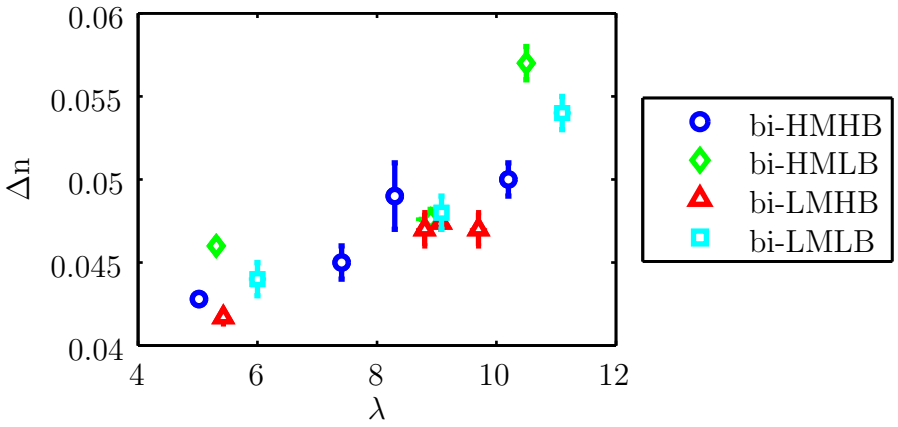

Figure 4.61: Birefringence as a function of draw ratio after strain hardening at 10^{-3}/s

Table 4.6 shows the orientation in the amorphous phase after strain hardening, measured from Raman spectroscopy using the procedure explained in section 2.1.6. When compared to table 3.9, the amorphous orientation in the isotropic material, it can be seen that the orientation has increased significantly, except for bi-LMLB. When comparing the bimodal results to table 3.15, the amorphous orientation after pre-drawing, it can be seen that the orientation does not change significantly. No significant difference can be seen between the materials after strain hardening.

	SH parameters	1-I_{yy}/I_{zz}
bi-HMHB	10^{-3}/s, 7.4 ± 0.1	0.7 ± 0.1
	10^{-5}/s, 5.8 ± 0.1	0.6 ± 0.1
	10^{-5}/s, 7.0 ± 0.2	0.7 ± 0.1
bi-HMLB	10^{-5}/s, 6.1 ± 0.1	0.5 ± 0.1
	10^{-7}/s, 6.7 ± 0.2	0.6 ± 0.1
bi-LMHB	10^{-5}/s, 6.1 ± 0.1	0.7 ± 0.1
bi-LMLB	10^{-5}/s, 6.2 ± 0.1	0.6 ± 0.1

Table 4.6: Qualitative orientation parameters and order parameters at 1080 cm^{-1} from Raman after strain hardening

Table 4.7 shows the orientation in the crystalline phase after strain hardening. The $< P_{200} >$ order parameter increases in every material with draw ratio, except for bi-HMLB, where it stays similar after strain hardening at 10^{-7}/s until a draw ratio of 6.7 ± 0.2, until a lower value even than the value after pre-drawing. For a draw ratio of around 6 after strain hardening at 10^{-5}/s, the orientation is higher in bi-LMLB compared to the rest of the bimodals.

	SH parameters	$< P_{200} >$
bi-HMHB	10^{-3}/s, 7.4 ± 0.1	0.68 ± 0.05
	10^{-5}/s, 5.8 ± 0.1	0.57 ± 0.04
	10^{-5}/s, 7.0 ± 0.2	0.61 ± 0.04
bi-HMLB	10^{-5}/s, 6.1 ± 0.1	0.63 ± 0.05
	10^{-7}/s, 6.7 ± 0.2	0.58 ± 0.04
bi-LMHB	10^{-5}/s, 6.1 ± 0.1	0.69 ± 0.05
bi-LMLB	10^{-5}/s, 6.2 ± 0.1	0.86 ± 0.06

Table 4.7: Order parameters at 1420 cm^{-1} from Raman after strain hardening

Table 4.8 shows the overall orientation after strain hardening. Comparing the bimodal materials after strain hardening at 10^{-5}/s until a draw ratio of around 6, the overall orientation is similar. Comparing the values for the bimodal materials with the values after pre-drawing, from table 3.15, it can be seen that the values have not changed significantly with strain hardening. Keeping in mind that the $< P_{200} >$ value for 1420 cm^{-1} increases from pre-drawing to strain hardening, this implies that orientation in crystalline

phase is more sensitive to strain hardening than orientation in the amorphous phase, especially for bi-LMLB.

	SH parameters	$< P_{200} >$
bi-HMHB	10^{-3}/s, 7.4 ± 0.1	0.43 ± 0.03
	10^{-5}/s, 5.8 ± 0.1	0.39 ± 0.06
	10^{-5}/s, 7.0 ± 0.2	0.50 ± 0.04
bi-HMLB	10^{-5}/s, 6.1 ± 0.1	0.52 ± 0.05
	10^{-7}/s, 6.7 ± 0.2	0.48 ± 0.04
bi-LMHB	10^{-5}/s, 6.1 ± 0.1	0.50 ± 0.04
bi-LMLB	10^{-5}/s, 6.2 ± 0.1	0.47 ± 0.06

Table 4.8: Order parameters at 1130 cm^{-1} from Raman after strain hardening

Both crystallinity and birefringence increase during strain hardening. The birefringence reaches a plateau around draw ratio 8 for the highly branched materials, suggesting that their maximum orientation has been reached. From Raman orientation parameters it can be seen that the orientation contribution of the crystals is larger than that of the amorphous phase.

4.2.6 Stress relaxation after strain hardening

Stress relaxation tests were performed on the strain hardened materials. After strain hardening at a strain rate of around 1.67 10^{-5}/s until a stress of around 40 MPa, followed by stress relaxation, the stress in the bimodal materials is compared. From table 4.9, it can be seen that the stress drops by a similar ratio for all the materials after 1000s and 10000s of stress relaxation ($\sigma_{1000s}/\sigma_{max}$ and $\sigma_{10000s}/\sigma_{max}$ are the same for all the materials).

Stress relaxation behaviour after strain hardening at different strain rates is compared for bi-HMHB. The results are shown in table 4.10. The strain rate of the strain hardening part of the test has a major influence on the ratio of the stress after 1000s of stress relaxation to the stress before relaxation. The correlation is shown in figure 4.62.

	bi-HMHB	bi-HMLB	bi-LMHB	bi-LMLB
σ_{max} [MPa]	38.2 ± 0.8	44.6 ± 0.9	34.4 ± 0.7	38.5 ± 0.8
λ_{max}	5.1 ± 0.2	5.6 ± 0.2	5.5 ± 0.2	5.8 ± 0.2
σ_{1000s} [MPa]	35.0 ± 0.7	40.5 ± 0.8	32.5 ± 0.6	35.1 ± 0.7
σ_{10000s} [MPa]	31.3 ± 0.6	35.4 ± 0.7	28.6 ± 0.6	30.7 ± 0.6
$\sigma_{1000s}/\sigma_{max}$	0.92 ± 0.03	0.91 ± 0.03	0.94 ± 0.03	0.91 ± 0.03
$\sigma_{10000s}/\sigma_{max}$	0.82 ± 0.02	0.79 ± 0.02	0.83 ± 0.03	0.80 ± 0.02

Table 4.9: Parameters of the stress relaxation tests for the bimodal materials, at a strain rate of approximately 1.67 10^{-5}/s

$\dot{\epsilon}$ [/s]	σ_{max} [MPa]	λ_{max}	σ_{1000s} [MPa]	$\frac{\sigma_{1000s}}{\sigma_{max}}$ [%]
3.39 10^{-2}	86 ± 2	7.1 ± 0.2	50 ± 1	58 ± 2
1.70 10^{-2}	81 ± 2	7.2 ± 0.2	48 ± 1	59 ± 2
1.70 10^{-2}	80 ± 2	6.9 ± 0.2	47.3 ± 0.9	60 ± 2
1.17 10^{-2}	76 ± 2	7.1 ± 0.2	46.1 ± 0.9	61 ± 2
8.35 10^{-3}	91 ± 2	7.9 ± 0.2	58 ± 1	63 ± 2
6.71 10^{-3}	84 ± 2	7.9 ± 0.2	53 ± 1	63 ± 2
5.05 10^{-3}	63 ± 1	7.9 ± 0.2	39.8 ± 0.8	64 ± 2
1.69 10^{-3}	70 ± 1	7.2 ± 0.2	48 ± 1	69 ± 2
1.18 10^{-3}	69 ± 1	7.5 ± 0.2	48 ± 1	69 ± 2
1.18 10^{-3}	75 ± 1	8.0 ± 0.2	53 ± 1	71 ± 2

Table 4.10: Parameters of the stress relaxation tests for bi-HMHB, at different strain rates

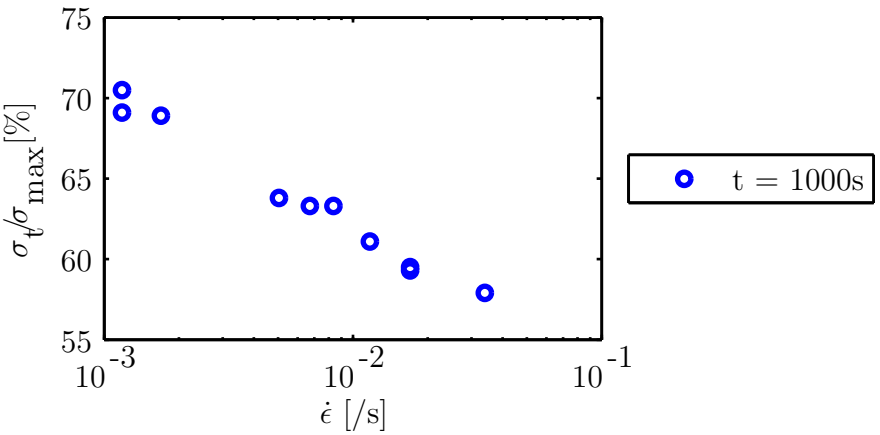

Figure 4.62: Ratio of stress after 1000s over maximum stress reached before relaxation as a function of strain rate for bi-HMHB

To compare the results to stress relaxation after creep, a linear curve is fitted through the strain rate dependency of $\sigma_{1000s}/\sigma_{max}$ for bi-HMHB (figure 4.62). This gives

$$\frac{\sigma_{1000s}}{\sigma_{max}} = -8.6log(\dot{\epsilon}) + 45. \tag{4.3}$$

Applying this empirical relation to the strain rates before creep relaxation for bi-HMHB (2.63 10^{-7}/s and 2.99 10^{-7}/s, as described in table 4.2) yields 101 ± 2 % in both cases. This corresponds to the 99 ± 3 % found experimentally. This indicates that the stress relaxation depends mainly on the strain rate, independently of whether it is reached by strain hardening or creep.

The stress relaxation behaviour of bi-HMLB after strain hardening to different stresses is studied. The results are shown in table 4.11. The stress before stress relaxation shows a correlation with the stress retained after 1000 and 10000s, though especially at high stress differences. This correlation is shown in figure 4.63. At higher draw ratios, bi-HMLB retains the stress better than at lower draw ratios.

σ_{max} [MPa]	λ_{max}	σ_{1000s} [MPa]	σ_{10000s} [MPa]	$\frac{\sigma_{1000s}}{\sigma_{max}}$ [%]	$\frac{\sigma_{10000s}}{\sigma_{max}}$ [%]
65 ± 1	6.7	44.9 ± 0.9	39.5 ± 0.9	69 ± 2	61 ± 2
81 ± 2	7.6	57 ± 1	50 ± 1	71 ± 2	61 ± 2
82 ± 2	6.9	56 ± 1	49 ± 1	68 ± 2	60 ± 2
91 ± 2	7.2	61 ± 1	54 ± 1	67 ± 2	60 ± 2
155 ± 3	9.6	101 ± 2	89 ± 2	65 ± 2	57 ± 2

Table 4.11: Parameters of the stress relaxation tests for bi-HMLB, at different stresses after strain hardening at around 1.6 $10^{-3}/s$. The error on the draw ratio is 0.2

4.2.7 Influence of temperature on strain hardening

The strain hardening behaviour is studied at different temperatures for the different bimodal materials, at a strain rate of 1.43 10^{-3}/s. It was measured around the testing temperature, and for bi-HMLB it was also measured at room temperature (25°C). The resulting strain hardening curves can be

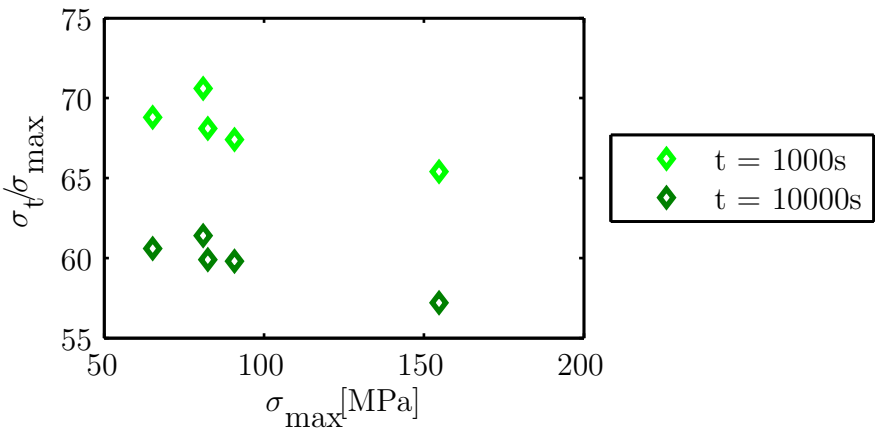

Figure 4.63: Ratio of stress after 1000s and 10000s over maximum stress reached before relaxation as a function of stress for bi-HMLB

found in figures 4.64, 4.65, 4.66 and 4.67 for bi-HMHB, bi-HMLB, bi-LMHB and bi-LMLB respectively.

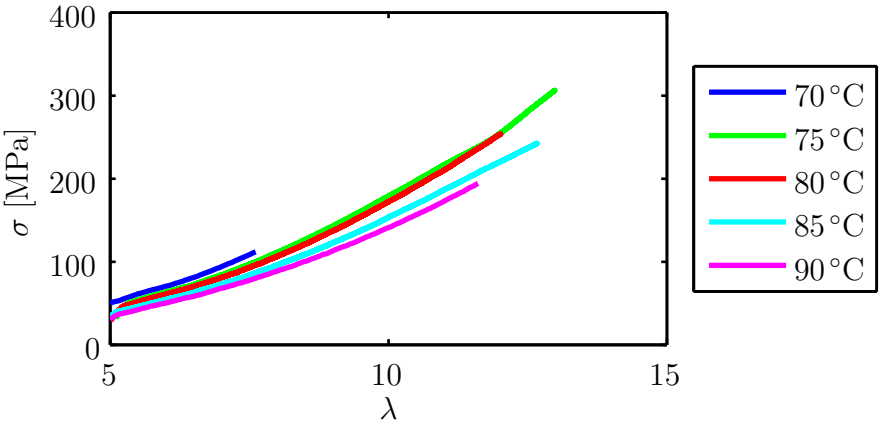

Figure 4.64: Stress as a function of draw ratio for bi-HMHB at different temperatures

In general, increasing the temperature decreases the resistance to strain hardening. For the high molecular mass materials, it is not possible to calculate the average strain hardening modulus between draw ratios 7 and 11 at every temperature. Therefore, it is calculated between draw ratios 6 and 7. Plotting this average strain hardening modulus as a function of temperature for these materials gives figure 4.68. It can be seen that the temperature sensitivity of the strain hardening modulus is similar for bi-HMHB and bi-HMLB.

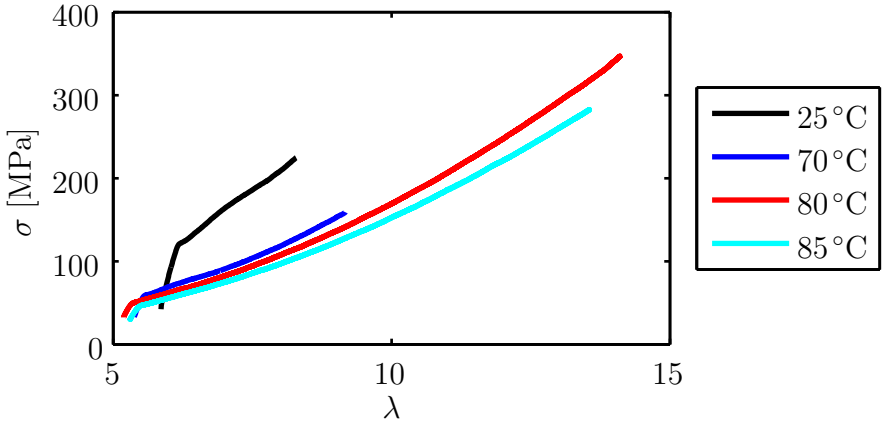

Figure 4.65: Stress as a function of draw ratio for bi-HMLB at different temperatures

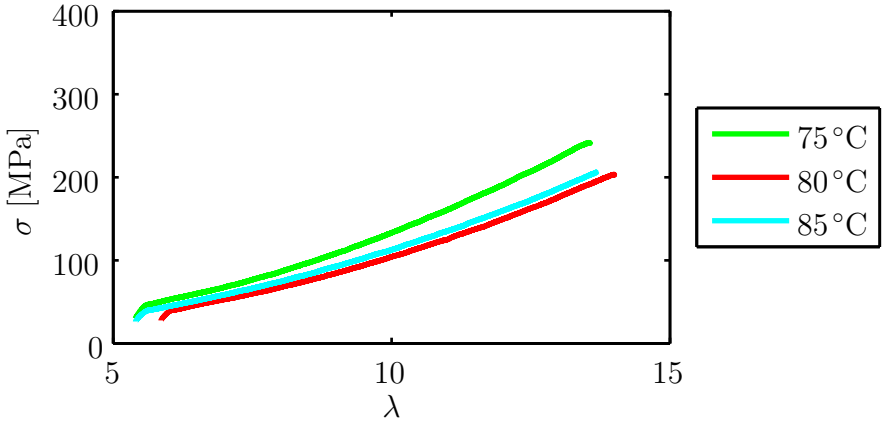

Figure 4.66: Stress as a function of draw ratio for bi-LMHB at different temperatures

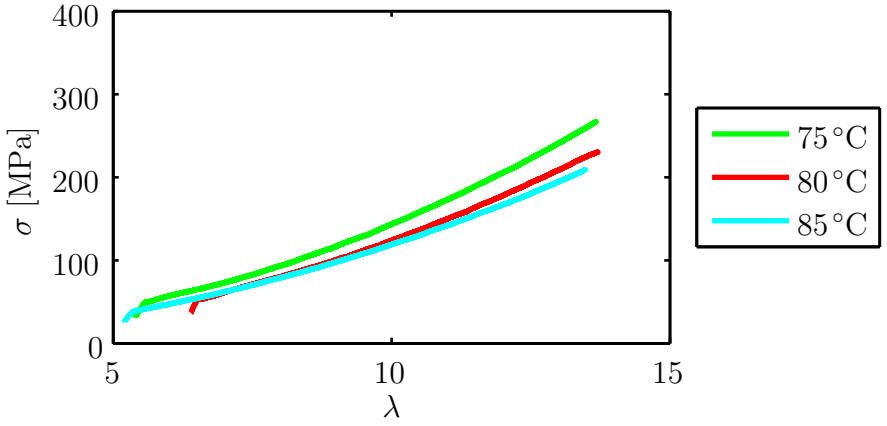

Figure 4.67: Stress as a function of draw ratio for bi-LMLB at different temperatures

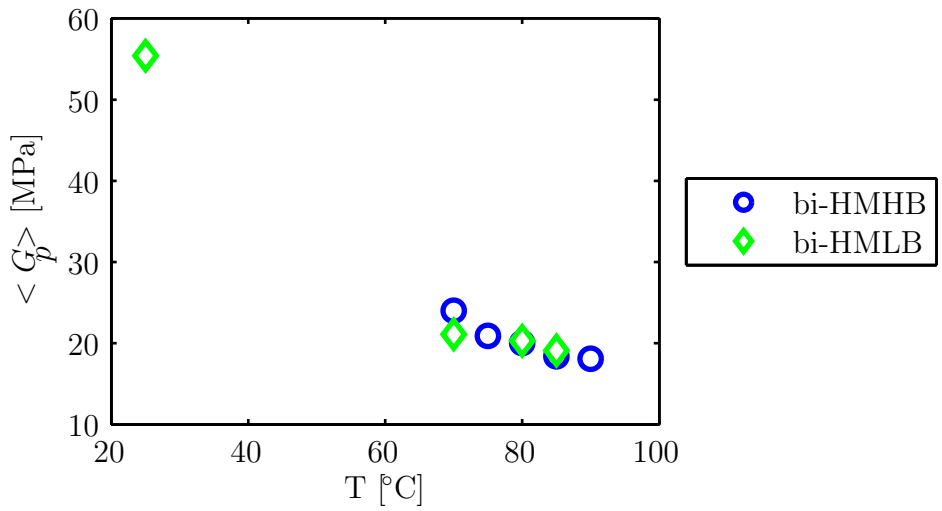

Figure 4.68: Average strain hardening modulus as a function of temperature for the highly branched bimodal materials

For the low molecular mass materials, the average strain hardening modulus, calculated between draw ratios 7 and 11, is given as a function of temperature in figure 4.69. Again, the strain hardening modulus decreases linearly with increasing temperature. So in the region studied, the temperature dependence of the strain hardening modulus is similar for all the bimodals.

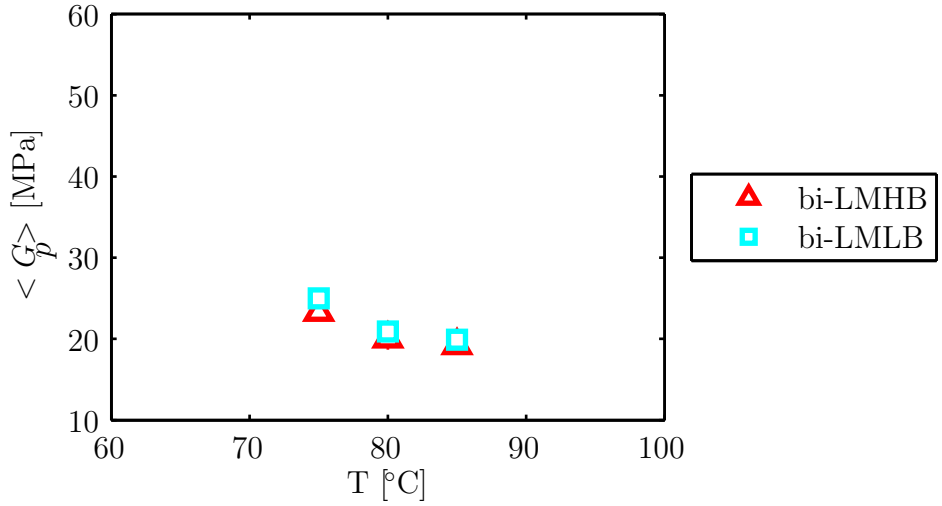

Figure 4.69: Average strain hardening modulus as a function of temperature for the low branched bimodal materials

The influence of temperature at high strain rates is studied for the low molecular mass bimodals. As can be seen on figure 4.70, the effect of branching on the strain hardening behaviour of the low molecular mass bimodals

is the same as for strain hardening at 80°C.

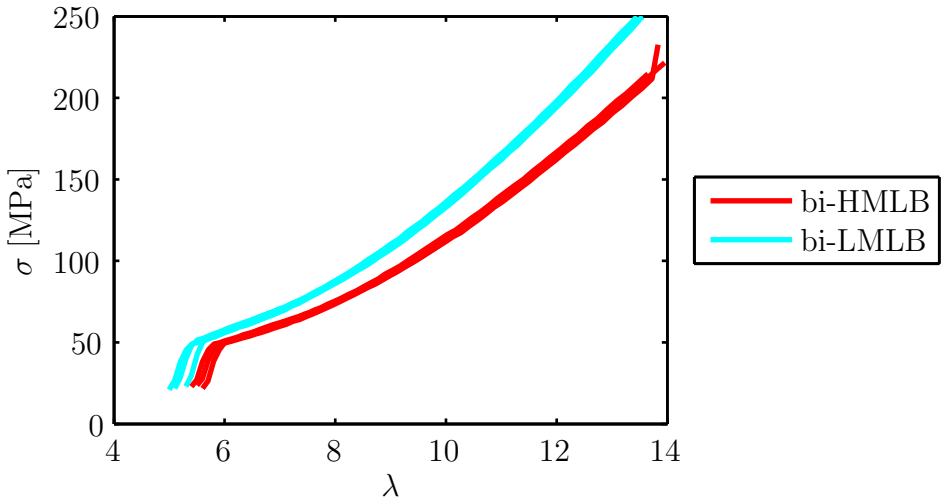

Figure 4.70: Strain hardening of bi-LMHB and bi-LMLB at 90°C, 1.6 10^{-1}/s

4.2.8 Discussion: influence of branch content and molecular mass on the strain hardening behaviour of bimodal polyethylene

Figures 4.46, 4.53 and 4.56 all confirm the same trends. For all bimodal materials, the strain hardening modulus increases with increasing strain rate and with decreasing temperature. If the strain hardening modulus would be caused by the extension of an entropic network only, there would be no strain rate sensitivity, and the strain hardening modulus would go up with increasing temperature. At low strain rates, the resistance to strain hardening ranks with molecular mass: a higher molecular mass yields a higher resistance to strain hardening. Hence, bi-LMLB and bi-LMHB display similar behaviour. Depending on how G_p is calculated, bi-HMLB and bi-HMHB display similar behaviour or bi-HMLB is slightly lower than bi-HMHB. At high strain rates, bi-LMLB has a higher strain hardening modulus than bi-LMHB. Again dependent on the calculation, bi-HMLB and bi-HMHB display similar behaviour or bi-HMLB performs better than bi-HMHB. In any case, the upswing in the stress - draw ratio curves at higher strain rates is more pronounced in the low branched materials. This can be seen both

from the error on the average slope and the deviation from Gaussian behaviour when applying the Neo-Hookean strain measure. The strain hardening modulus of the highly branched materials increases more or less linearly with increasing strain rate, while the strain hardening modulus of the low branched materials increases much more above a strain rate of 10^{-3}/s. So at low strain rates (between 10^{-6}/s and 10^{-3}/s), a high molecular mass yields a high strain hardening modulus, while at high strain rates (between 10^{-2}/s and 10^{-1}/s), a low branch content yields a high strain hardening modulus. The branch content has several effects on the molecular network that could cause this upswing. Firstly, it influences the α-relaxation temperature. Secondly, it influences the width of the molecular chain.

The first hypothesis, that the difference in α-relaxation temperature leads to different behaviour at high strain rates for low branched and high branched bimodals, is contradicted by the findings in section 4.2.7, where the influence of temperature on the strain hardening is discussed. The temperature sensitivity is similar in low branched and highly branched materials, and thus does not suggest that the α-relaxation affects those two sets of materials in a different way. Van Erp *et al.* studied the yield behaviour of polypropylene, and attributed the upswing of the yield stress above a certain strain rate to the onset of the α-relaxation [189]. Figure 4.71 shows the yield stress as a function of strain rate for the bimodal materials used in this work. The onset strain rate for the α-relaxation lays between 10^{-3} and 10^{-2}/s for all the materials. So the difference in behaviour between the low branched and the highly branched bimodal materials cannot be explained by a difference in the onset of strain rate evolution of the α-relaxation. However, the upswing in the yield stress reflects the upswing in strain hardening with strain rate, as will be explained in section 4.3.

The second hypothesis is based around the width of the molecular chain. The chain axis is on average more slender for materials with a lower branch content, hence they can be packed more closely together when stretched, which results in a higher resistance to stress. The failure behaviour after strain hardening seems to support this idea. The failure stress (and draw ratio) of bi-HMHB is lower than that of the rest of the materials. As ex-

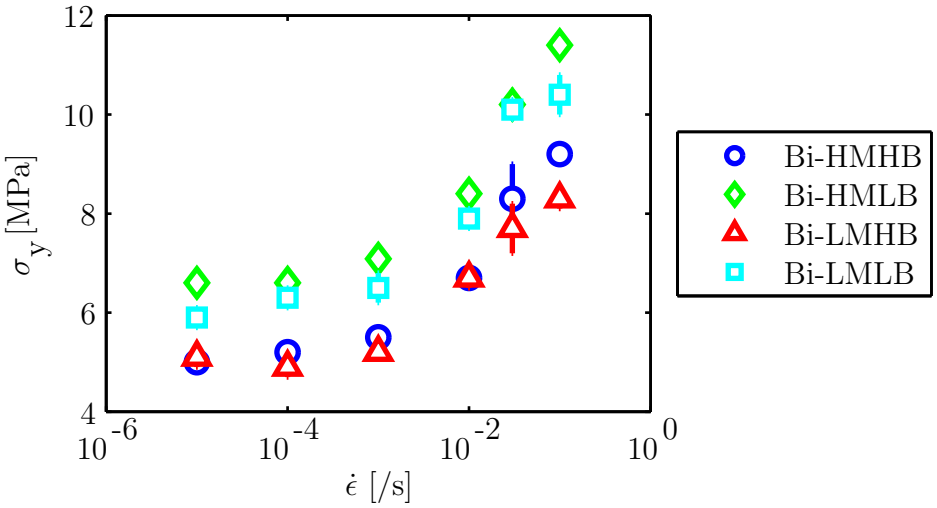

Figure 4.71: Yield stress as a function of strain rate at 80°C for the bimodal materials

plained in section 4.2.4, the failure stress is proportional to the chain axis density. It is lower for bi-HMHB, and decreases with strain rate. It seems to be more sensitive to strain rate at higher strain rates. No results for the failure behaviour of the other bimodal materials are available, but recalling equation 3.6 for the chain contour length per unit volume, for the same M_w, a lower average molecular mass per bond m_0 due to a lower branch content decreases the chain contour length and hence increases the effective crossing density, which could explain the difference in behaviour between low branched and highly branched bimodal materials at high strain rates [187]. Raman spectroscopy can be applied to determine the molecular stress from the band peak shift [164, 166], and a study of the influence of molecular mass and branch content on the band peak shift at different strain rates is suggested for future work.

4.3 Discussion: crystalline contribution to strain hardening

From figures 4.24 and 4.46, it can be seen that the ranking of the materials differs for creep and strain hardening: bi-HMHB is more resistant to creep, while in terms of strain hardening, bi-HMHB and bi-HMLB are more resis-

tant. A combination of high molecular mass and high branch content are required for an increased resistance against creep, while for strain hardening a high molecular mass is sufficient. This indicates that different processes dominate during creep and strain hardening. Deblieck *et al.* suggested that strain hardening includes a viscous contribution, originating from the crystals [11]. This suggestion is based on the evolution of the strain hardening modulus with strain rate and temperature, which is confirmed in this work (as discussed in section 4.2.8).

The evolution of the yield stress with strain rate suggest that this crystalline contribution originates in the α-relaxation. In polypropylene, the yield stress is used to estimate the crystalline contributions to the entanglement network [190]. The yield stress increases with strain rate (as seen from figure 4.71) and decreases with temperature, following the same trends as the strain hardening modulus [189]. Taking the yield stress as a measure for the crystalline contribution assumes that the evolution of the crystalline contribution with strain rate is the same in the strain hardening region as is it in the isotropic material. It should be kept in mind that this is probably not entirely correct. Dividing the (average) strain hardening modulus by the strain rate dependent yield stress results in figure 4.72. At strain rates below 10^{-3}/s, the ranking is now similar to that for the creep rate deceleration factor: the effective entanglement network of bi-HMHB has a higher resistance to deformation than that of the other bimodals.

If dividing by the yield stress eliminates all the crystalline contributions from the strain hardening, the curves on figure 4.72 would be expected to be flat. Especially in the case of bi-HMHB, they are not. It seems that at high strain rates, the crystalline contribution is overestimated by the yield stress. It could be imagined that at high strain rates, the long range order in the network is disrupted. For example, extended chain crystals can no longer be formed and will hence not be able to pin tie molecules. The evolution of stress recovery at constant draw ratio with strain rate (figure 4.62) supports this. After deformation at high strain rates, the stress relaxes more than after deformation at low strain rates. The stress is taken up by a less stable network and hence released more quickly. As the initial crystal structure

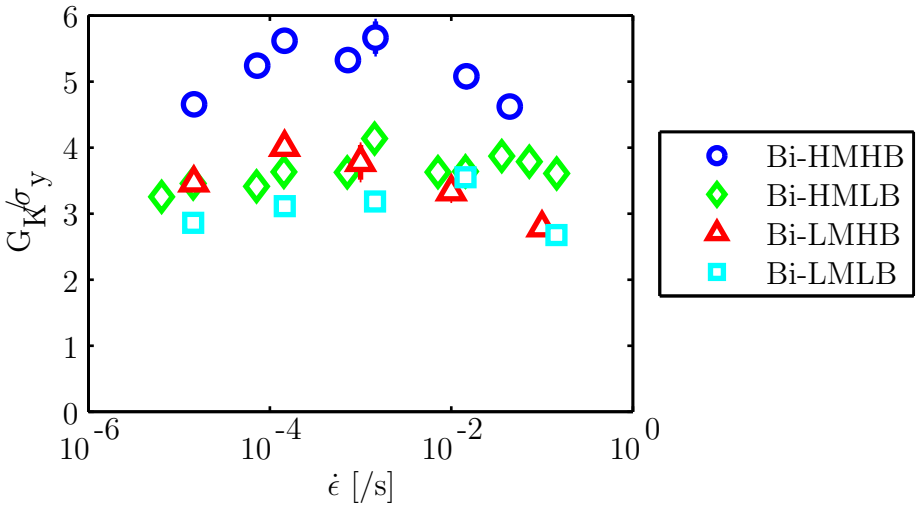

Figure 4.72: G_K divided by strain rate dependent yield stress as a function of strain rate

of the high branched materials is less perfect, the disrupting influence of the strain rate on the development of the crystals during strain hardening would be more severe.

4.4 Conclusions

This chapter discusses the deformation behaviour of bimodal polyethylenes. It is found that only a combination of high molecular mass and high branch content result in an increased resistance to creep. Varying these two features separately has no effect. We suggest that this can be explained in term of monomeric friction, which is higher in the melt for highly branched materials. This results in a higher effective network at a similar time scale for bi-HMHB than for the other bimodal materials. The materials rank differently in terms of resistance to creep than in terms of resistance to strain hardening. This can be attributed to a crystalline contribution to strain hardening, which we suggest can be estimated by the yield stress. Scaling the strain hardening modulus with yield stress results in a similar ranking for creep and strain hardening modulus at low strain rates. At high strain rates, the yield stress does not seem a good measure for the crystalline contribution. We suggest this could be because of a loss of long range order at high strain rates.

Chapter 5

Results II: Monomodal branched polyethylene

This chapter describes the deformation behaviour of the reactor 2 (R2) materials. These monomodal, branched polyethylenes represent the high molecular mass fraction of the bimodal materials. This fraction is responsible for the resistance to slow crack growth. In the bimodal materials, a low molecular mass (R1) fraction is added to decrease the melt viscosity and hence enhance processing capabilities. Firstly, the creep behaviour of the R2 materials is described. Secondly, their strain hardening behaviour is described. The results are compared to the results of the bimodal materials and the differences are discussed.

5.1 Creep behaviour

The R2 materials represent the fraction in the bimodal materials that is predominantly responsible for the resistance to slow crack growth. In the bimodal material, they are 'diluted' by a low molecular mass, linear fraction, present to enhance processing capabilities. The resistance to creep of the pure R2 materials is thus expected to be higher than for the bimodal materials. If no synergistic effects are present and the low molecular mass material simply 'dilutes' the properties of the R2 materials by the fraction of high molecular mass material, then resistance to deformation is expected to be double in the R2 materials compared to the bimodal materials.

5.1.1 Influence of stress on the shape of the creep curves

Figure 5.1 gives the load as a function of time during a creep test for R2-HMHB. The first part of the test is always the same, as the material is extended until the starting creep stress (given in the legend). When this stress is reached, the load is held constant by the Instron. Figure 5.2 shows the extension as a function of time. After the starting creep stress is reached, the material extends more for higher stresses. Compared to figure 4.2, extension as a function of time for bi-HMHB, it can already be seen that R2-HMHB extends less than its bimodal counterpart.

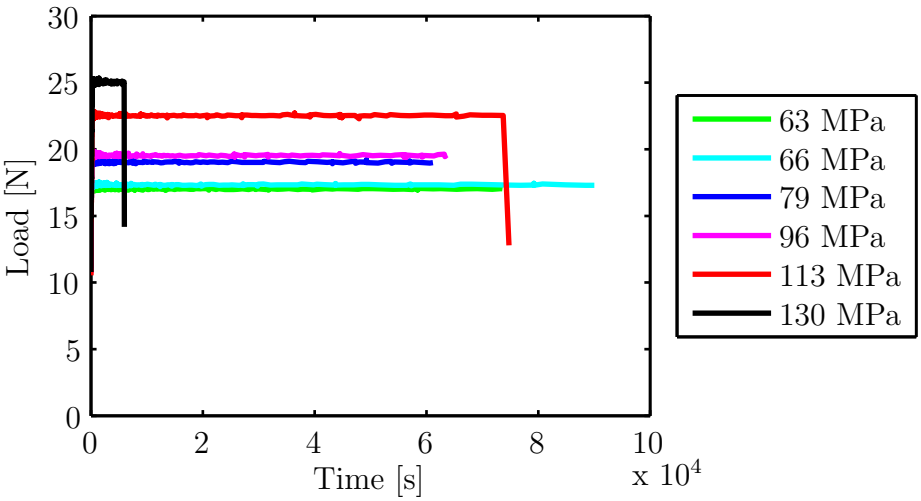

Figure 5.1: Load as a function of time during a creep test for R2-HMHB

Normalising the results to take into account sample dimensions results in figures 5.3 and 5.4. The draw ratio does not increase as much over time as it does for bi-HMHB (see figure 4.3), hence also the stress changes less over the course of a creep test (the stress depends on the applied load, which is constant, and the changing cross section which is influenced by the draw ratio). This indicates that the creep resistance is higher in R2-HMHB than in bi-HMHB. Figure 5.5 shows the strain rate decay as a function of time.

The Sherby-Dorn curves at different starting creep stresses are given in figures 5.6, 5.7, 5.8 and 5.9 for R2-HMHB, R2-HMLB, R2-LMHB and R2-LMLB respectively. The general shapes of the curves are similar to those

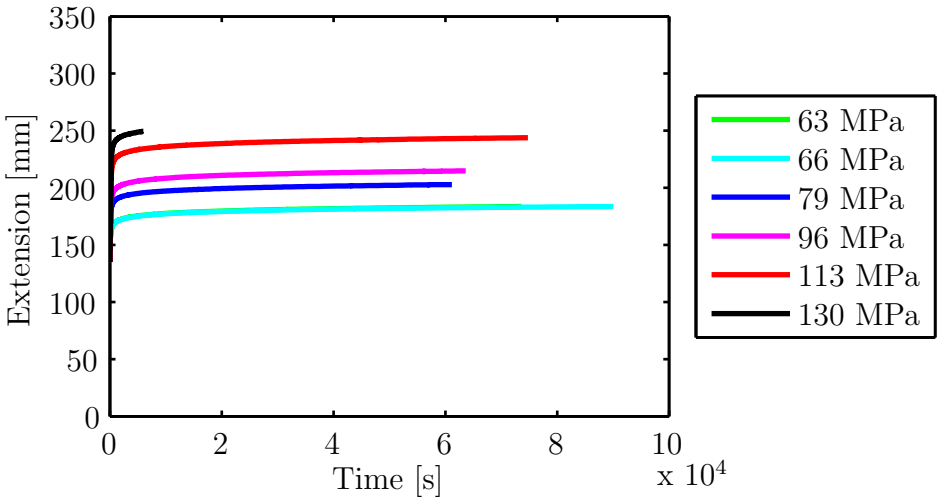

Figure 5.2: Extension as a function of time during a creep test for R2-HMHB

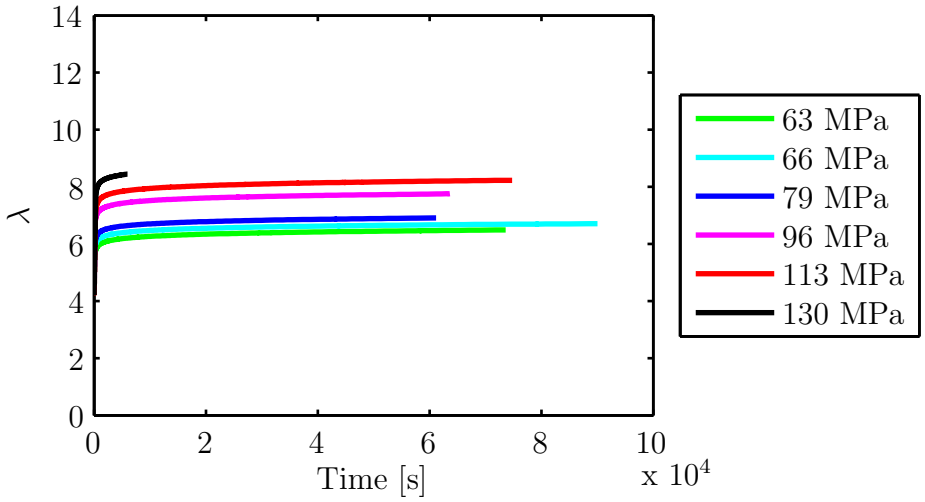

Figure 5.3: Draw ratio as a function of time during a creep test for R2-HMHB

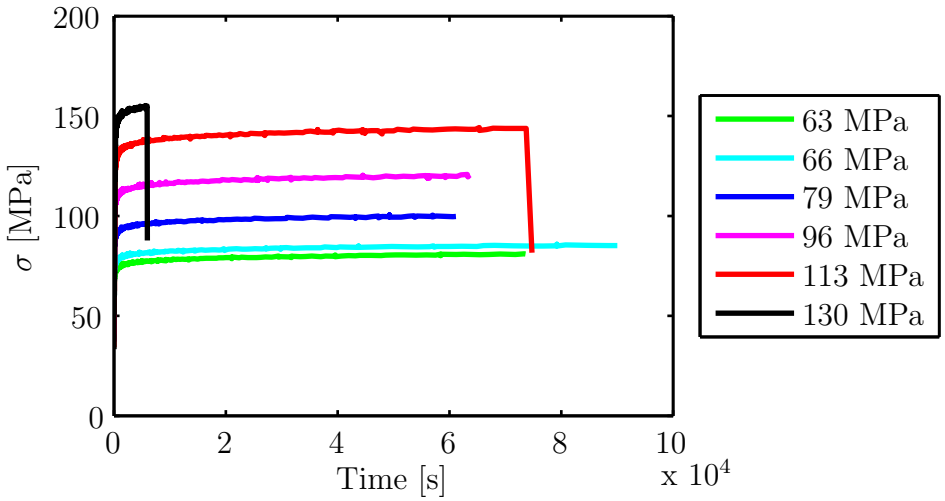

Figure 5.4: Stress as a function of time during a creep test for R2-HMHB

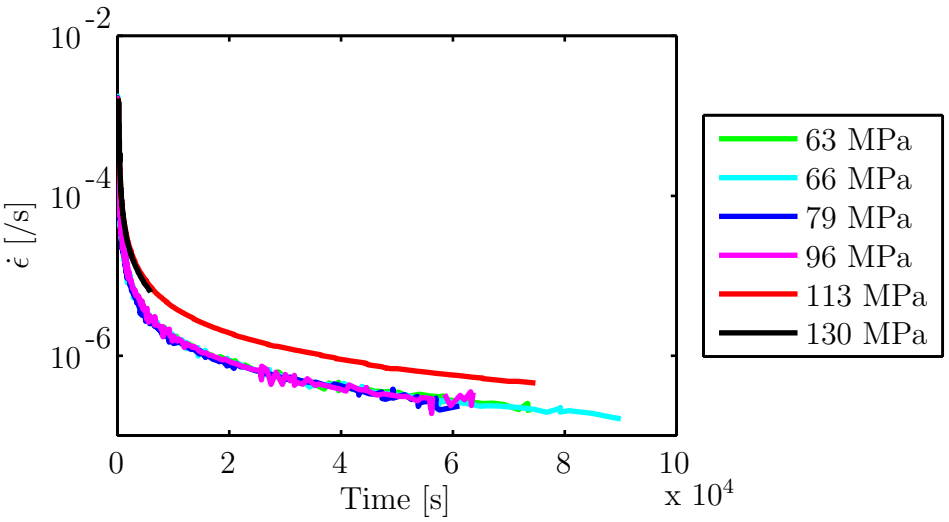

Figure 5.5: Strain rate as a function of time during a creep test for R2-HMHB

for the bimodal materials, but the starting draw ratios are lower, and the slopes are steeper. This indicates that the R2 materials have a steeper strain hardening (they reach the applied creep load at a lower draw ratio than their bimodal counterpart), and most likely a higher resistance to creep.

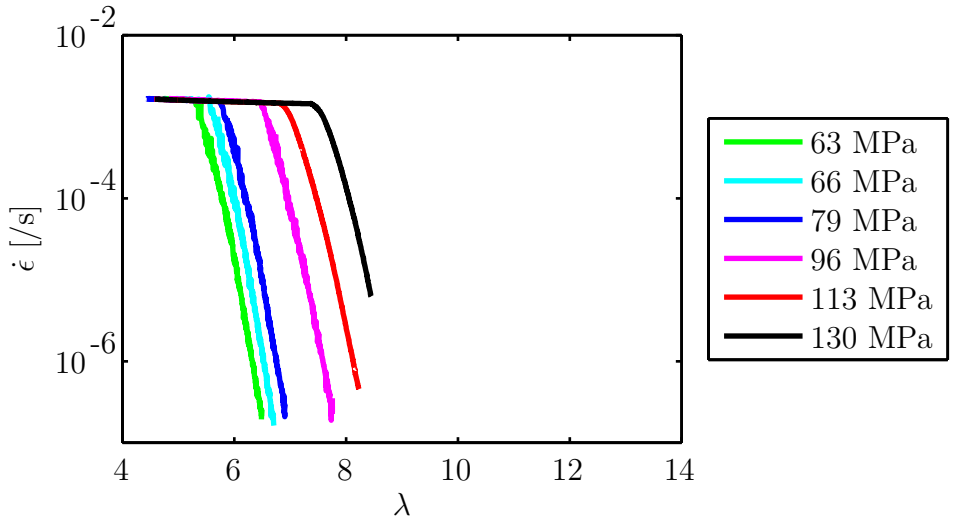

Figure 5.6: Strain rate as a function of draw ratio for R2-HMHB

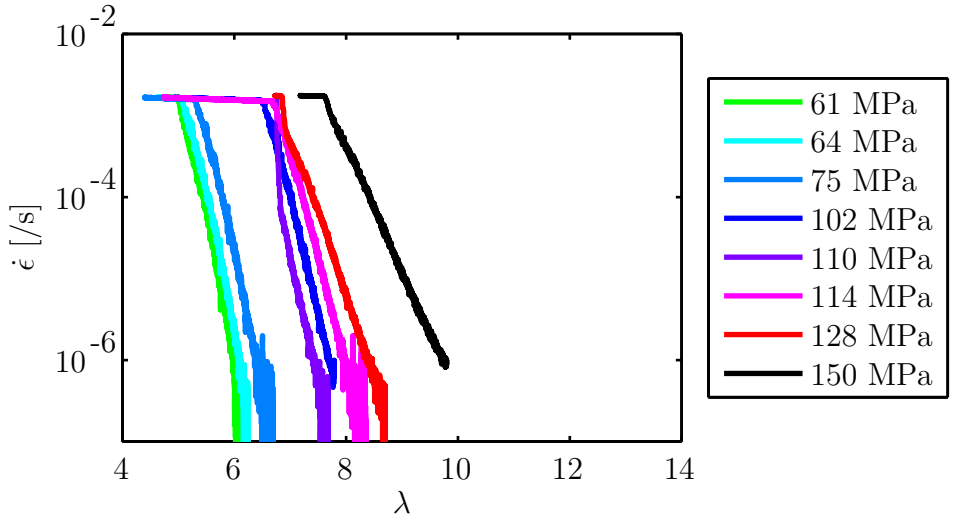

Figure 5.7: Strain rate as a function of draw ratio for R2-HMLB

5.1.2 Influence of stress on the creep rate deceleration factor

Plotting the creep rate deceleration factor as a function of starting creep stress results in figure 5.10. R2-HMHB has the lowest CRDF and hence

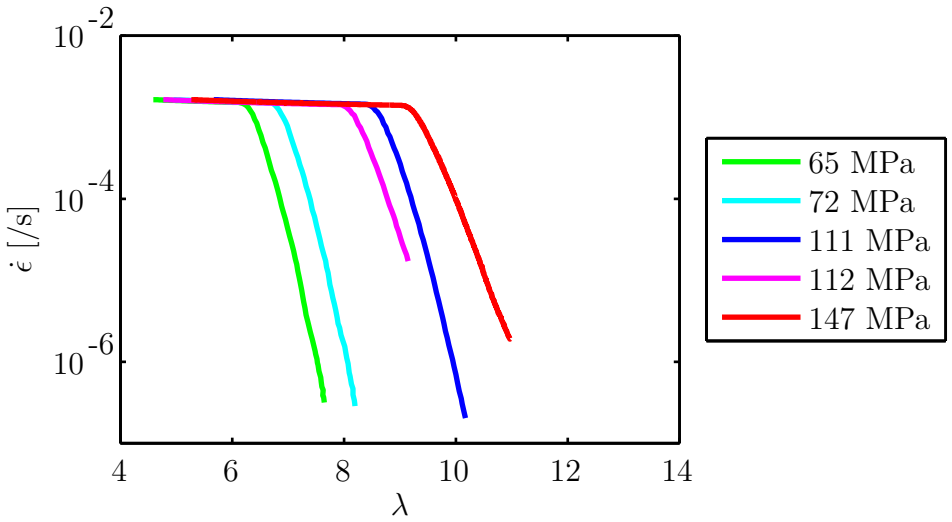

Figure 5.8: Strain rate as a function of draw ratio for R2-LMHB

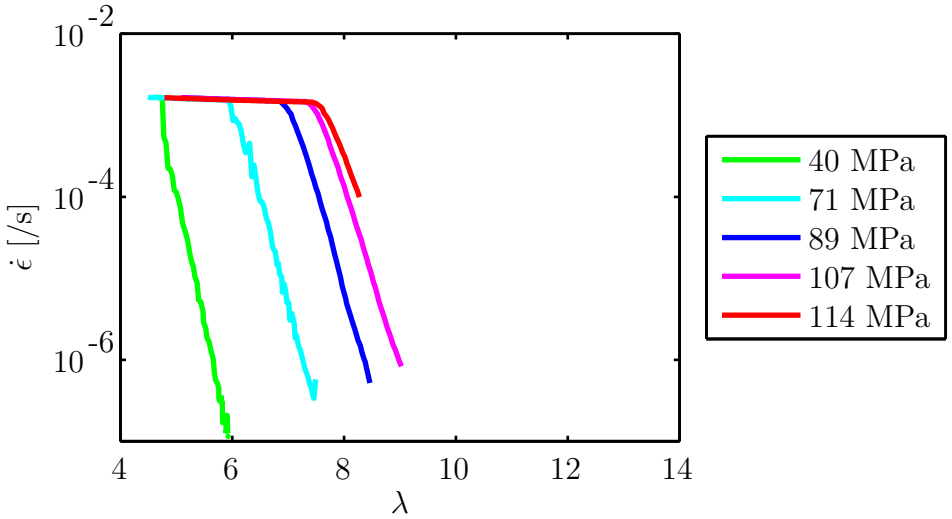

Figure 5.9: Strain rate as a function of draw ratio for R2-LMLB

the highest creep resistance over the range of stresses tested. R2-HMLB has a similar CRDF than R2-HMHB at low stresses, but on the high end of the stress range, it has a similar CRDF than R2-LMLB. R2-LMLB has the highest CRDF, and hence the lowest resistance to creep, over the stress range studied. There is some variation in the CRDF as a function of stress for R2-LMHB, but it generally lays between R2-HMLB and R2-LMLB at low stresses, and similar to those two materials at high stresses. The difference in slope between R2-HMLB and the other materials is significant: the CRDF increases more with increasing stress for this material.

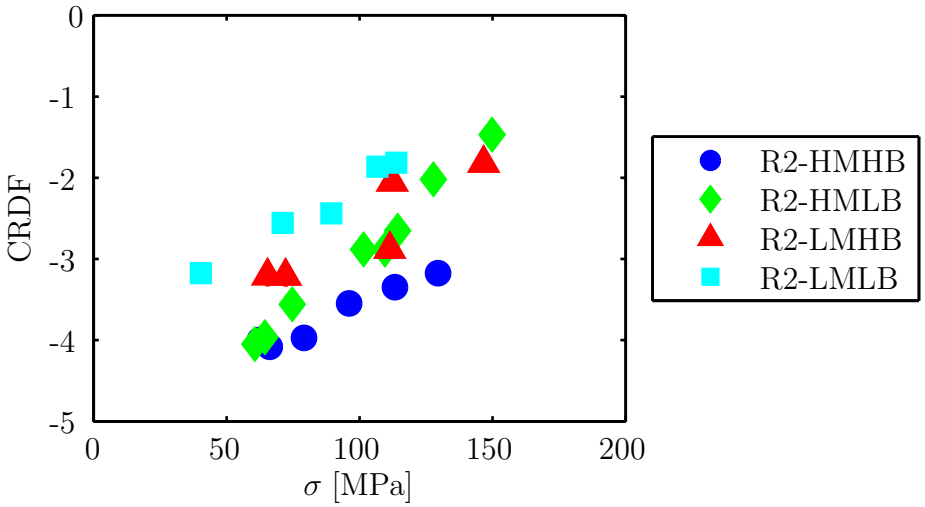

Figure 5.10: CRDF as a function of stress for the R2 materials

Failure after creep at high stress

Failure after creep occurs for R2-HMHB at an average stress of 150 ± 5 MPa and an average draw ratio of 8.3 ± 0.2. This is lower than its bimodal counterpart, bi-HMHB, where the failure stress is 223 ± 10 MPa and the failure draw ratio is 12.1 ± 0.2. The extensibility limit for the network is lower for R2-HMHB than for bi-HMHB. The available network density as calculated from solid state NMR is higher in the R2 materials than in the bimodal materials (see section 3.4), but the chain contour length is higher in these materials as there is no contribution of the slender, linear R1 chains.

5.1.3 Structure changes during creep

The structure of the R2 materials is measured after the creep tests. The evolution of the orientation and crystallinity is different for different materials. The structure is compared to the approximate structure before the creep test. For this, the materials are drawn at 10^{-3}/s until the approximate starting stress of the creep, and their birefringence, Raman orientation parameters and crystallinity are measured at that point. The parameters of the tests are given in table 5.1.

	Creep preparation parameters	Creep starting parameters	Creep final parameters
R2-HMHB	88 MPa, 6.1	66 MPa, 5.4	85 MPa, 6.2
R2-HMLB	99 MPa, 5.9	66 MPa, 5.0	82 MPa, 6.5
R2-LMHB	124 MPa, 7.4	111 MPa, 8.1	144 MPa, 8.3
R2-LMLB	118 MPa, 7.1	107 MPa, 7.1	133 MPa, 7.9

Table 5.1: Specimen parameters, samples mimicking structure before creep, actual starting creep parameters, and parameters at the end of the creep test. The standard error on the stress is ± 3%, and the standard error on the draw ratio is ± 0.02

Table 5.2 gives the birefringence before and after creep. This stays approximately constant for all the R2 materials, except for R2-LMLB, where it decreases slightly (despite a higher draw ratio). The crystallinity increases for this material, while it stays similar for the other R2 materials, as can be seen in table 5.3.

	Δn, before creep	Δn, after creep
R2-HMHB	0.044 ± 0.001	0.045 ± 0.001
R2-HMLB	0.043 ± 0.001	0.045 ± 0.001
R2-LMHB	0.047 ± 0.001	0.045 ± 0.001
R2-LMLB	0.046 ± 0.001	0.041 ± 0.001

Table 5.2: Birefringence before and after creep measurements

This can be compared to the structure after creep for bi-HMHB. The parameters for the tests are given in table 5.4. The birefringence and crys-

	$X_{c,d}$, before creep [%]	$X_{c,d}$, after creep [%]
R2-HMHB	47.1 ± 0.1	47.5 ± 0.1
R2-HMLB	50.8 ± 0.1	51.3 ± 0.2
R2-LMHB	52.2 ± 0.1	51.0 ± 0.3
R2-LMLB	52.1 ± 0.2	55.3 ± 0.4

Table 5.3: Crystallinity before and after creep measurements

tallinity before and after creep on bi-HMHB are shown in table 5.5. For bi-HMHB, the birefringence stays approximately constant. The crystallinity increases slightly, but not as significantly as for R2-LMLB. These results suggest that some recrystallisation can take place during the creep tests, but overall the crystal structure remains stable. The reason for the decrease in birefringence in the R2-LMLB material is unclear. From Raman measurements, no change in orientation is measured (see table 5.6).

	σ [MPa]	λ
Preparation	106 ± 2	7.4 ± 0.2
Start	82 ± 2	7.2 ± 0.2
Final	111 ± 2	8.3 ± 0.2

Table 5.4: Parameters at the end of the preparation test, the start of a creep test and the end of a creep test for bi-HMHB

	Preparation	Final
Δ n	0.045 ± 0.001	0.048 ± 0.001
$X_{c,d}$ [%]	62.0 ± 0.1	63.5 ± 0.2

Table 5.5: Structural parameters at the end of the preparation test and a the end of the creep test for bi-HMHB

5.1.4 Discussion: influence of the molecular mass and branch content on the creep behaviour of branched polyethylene

From figure 5.10, it can be seen that over the stress range studied, R2-HMHB has the highest creep resistance and R2-LMLB has the lowest creep

	$< P_{200} >$, before creep	$< P_{200} >$, after creep
R2-HMHB	0.5 ± 0.1	0.59 ± 0.034
R2-HMLB	0.53 ± 0.04	0.60 ± 0.04
R2-LMHB	0.63 ± 0.04	0.57 ± 0.04
R2-LMLB	0.59 ± 0.04	0.54 ± 0.04

Table 5.6: Raman orientation parameters for the reactor 2 materials at 1130 cm^{-1} before and after creep measurements

resistance. The creep resistance of R2-LMHB lies in between those two materials over the stress range studied. The stress sensitivity of the CRDF of R2-HMHB, R2-LMHB and R2-LMLB is similar. The stress sensitivity of R2-HMLB is higher, with the CRDF at low stresses being equal to that of R2-HMHB, and at high stresses increasing to the level of R2-LMLB. At low stress, the dominant contribution appears to be the molecular mass. At high stress, the ranking of the R2 materials is the same as for the bimodal materials. The creep tests take place at a strain rate of 10^{-3}/s and lower. In a tensile test, this is the strain rate at which α-relaxation sets in (as discussed in section 4.2.8). Below this strain rate, the crystals do not function as pinning points for the tie molecules [189]. While the onset strain rate for α-relaxation is not necessarily equal in a tensile test and a creep test due to the difference in stress and deformation mode, there is no step in the stress sensitivity of the CRDF to suggest that the critical strain rate is exceeded. We therefore assume that there is mobility inside the crystals during the creep tests, both at low and high stress. So the difference as a function of stress must depend on the total friction that needs to be overcome when pulling a chain into a crystal or over an entanglement. It is possible that at low stress, these processes are therefore less frequent than at high stress, and hence the branch content is of less importance. To make a difference at high stresses, the network must be well established, hence the advantage of the high molecular mass materials as they are expected to have a higher number of tie molecules.

5.2 Strain hardening behaviour

The strain hardening of the reactor 2 materials is studied to understand the effect of the possible dilution of the network by the addition of a low molecular mass, linear fraction in the bimodal materials.

5.2.1 Influence of strain rate on strain hardening behaviour of branched polyethylene

Figures 5.11 and 5.12 show the strain hardening for the R2 materials, as a function of draw ratio and NHSM respectively, for a strain rate around 10^{-3}/s. The strain hardening modulus as calculated using the Neo-Hookean strain measure is given in table 5.7. At this strain rate, the strain hardening modulus is similar for the high molecular mass R2 materials, R2-HMHB and R2-HMLB. It is lower for the low molecular mass materials, R2-LMHB and R2-LMLB. Of the low molecular mass materials, the low branched material has a higher strain hardening modulus. The yield stress has only been measured at a strain rate of 3 10^{-2}/s for these materials, and as the strain rate dependency of the yield stress depends on molecular architecture such as branch content, it is not known how different the yield stress at 3 10^{-2}/s and the yield stress at 10^{-3}/s are [189]. Therefore, the crystallinity was taken as a measure of the enthalpic contribution of the crystals. At low strain rates, the correction of the strain hardening using the crystallinity is more correct than at high strain rates, because of the disruption of long range crystal order at high strain rates.

	$\dot{\epsilon}$ [/s]	G_{NHSM} [MPa]
R2-HMHB	1.58 ± 0.01 10^{-3}	2.61 ± 0.03
R2-HMLB	1.60 ± 0.01 10^{-3}	2.63 ± 0.07
R2-LMHB	1.56 ± 0.01 10^{-3}	1.82 ± 0.05
R2-LMLB	1.58 ± 0.01 10^{-3}	2.08 ± 0.06

Table 5.7: Strain hardening modulus (calculated using the Neo-Hookean strain measure) calculated using the Neo-Hookean strain measure for the reactor 2 materials at a strain rate of around 10^{-3}/s

The results after dividing the strain hardening modulus by the crys-

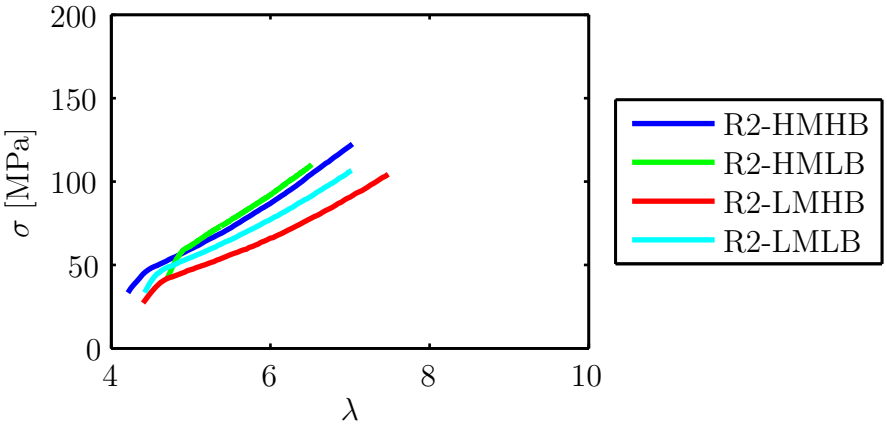

Figure 5.11: Stress as a function of draw ratio for R2 materials at an approximate strain rate of 10^{-3}/s

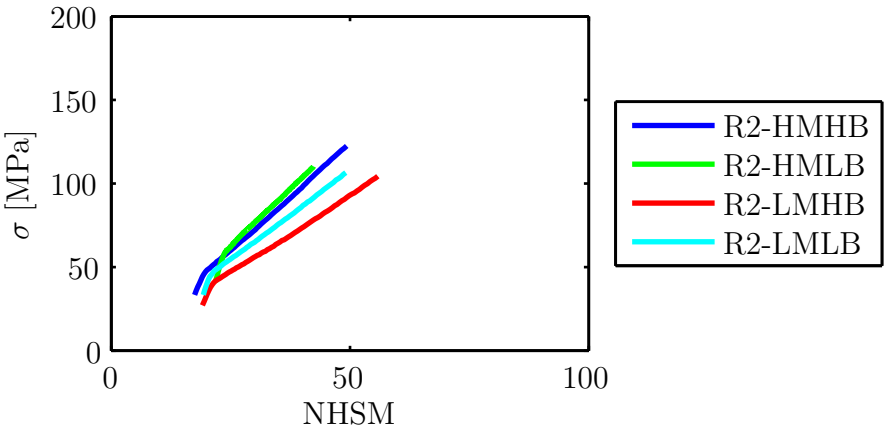

Figure 5.12: Stress as a function of NHSM for R2 materials at an approximate strain rate of 10^{-3}/s

tallinity are shown in table 5.8. When taking account of crystallinity, the strain hardening behaviour is similar for the low molecular mass materials, highest for R2-HMHB and in between for R2-HMLB. This will be further discussed in section 5.2.3.

	$\dot{\epsilon}$ [/s]	$G_{NHSM}/X_{c,d}$ [MPa]
R2-HMHB	$1.58 \pm 0.01\ 10^{-3}$	5.61 ± 0.09
R2-HMLB	$1.60 \pm 0.01\ 10^{-3}$	5.0 ± 0.1
R2-LMHB	$1.56 \pm 0.01\ 10^{-3}$	3.9 ± 0.1
R2-LMLB	$1.58 \pm 0.01\ 10^{-3}$	4.0 ± 0.1

Table 5.8: Strain hardening modulus (calculated using the Neo-Hookean strain measure) divided by crystallinity for the reactor 2 materials at a strain rate of around 10^{-3}/s

5.2.2 Structure changes during strain hardening

After strain hardening, the crystallinity of the R2 materials is, as usual, lower than that of the bimodal materials (see table 5.9 compared to table 4.4). Comparing the materials after strain hardening at 10^{-5}/s, when they all have a draw ratio of around 5.5, the influence of the branch content can be seen: materials with a low branch content have a high crystallinity, both for the R2 and the bimodal materials. The R2 materials increase slightly in crystallinity after strain hardening, compared to both the crystallinity of the pellet material and the sheet material, except for R2-HMLB. R2-HMLB stays at the same crystallinity as after compression moulding, lower than the pellet material.

The birefringence of the samples was measured after strain hardening. The results are given in table 5.10 and figure 5.13. The birefringence is measured on the sample under strain. Only a small range of draw ratios was measured, but in general, the birefringence goes up with draw ratio, as expected. The birefringence of the R2 materials is similar to that of the bimodal materials. R2-LMLB has a higher birefringence at draw ratio 7 than R2-LMHB, after strain hardening at 10^{-3}/s.

Table 5.11 shows the orientation in the amorphous phase after strain

	SH parameters	$X_{c,SH}$ [%]
R2-HMHB	10^{-3}/s, 6.1	47.1 ± 0.1
	10^{-5}/s, 5.5	47.2 ± 0.2
R2-HMLB	10^{-3}/s, 5.9	50.8 ± 0.1
	10^{-5}/s, 5.6	50.5 ± 0.3
R2-LMHB	10^{-3}/s, 7.4	52.2 ± 0.1
	10^{-5}/s, 5.9	48.8 ± 0.1
R2-LMLB	10^{-3}/s, 7.1	52.1 ± 0.2
	10^{-5}/s, 5.5	52.3 ± 0.1

Table 5.9: Crystallinity evolution with strain hardening for R2 materials. The standard error on the draw ratio after strain hardening varies between 0.2 and 0.3

	SH parameters	Δn_{SH}
R2-HMHB	10^{-3}/s, 6.1 ± 0.2	0.044 ± 0.001
R2-HMLB	10^{-3}/s, 5.9 ± 0.2	0.043 ± 0.001
	10^{-3}/s, 6.4 ± 0.3	0.044 ± 0.001
R2-LMHB	10^{-3}/s, 7.0 ± 0.2	0.044 ± 0.001
	10^{-3}/s, 7.4 ± 0.2	0.046 ± 0.001
R2-LMLB	10^{-3}/s, 7.1 ± 0.2	0.047 ± 0.001

Table 5.10: Birefringence evolution with strain hardening

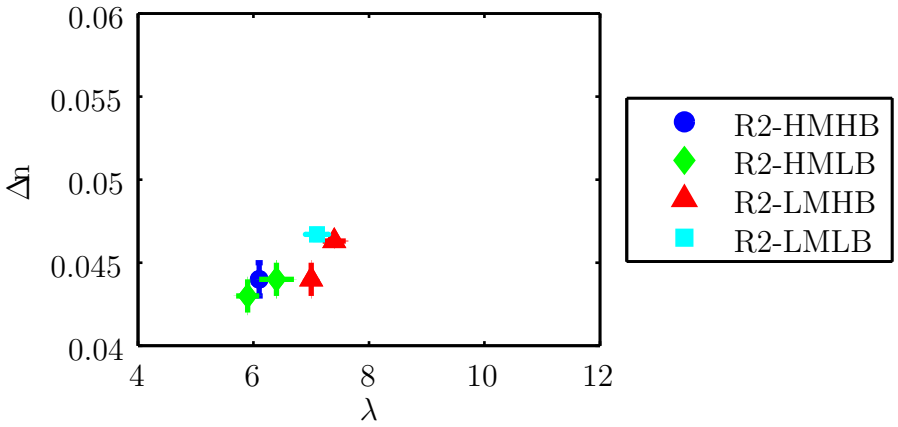

Figure 5.13: Birefringence as a function of draw ratio after strain hardening at 10^{-3}/s

hardening. When compared to table 3.9, the amorphous orientation in the isotropic material, it can be seen that the orientation has increased significantly. No significant difference can be seen between the materials after strain hardening.

	SH parameters	1-I_{yy}/I_{zz} $_{SH}$
R2-HMHB	10^{-3}/s, 6.1 ± 0.1	0.5 ± 0.1
	10^{-5}/s, 5.5 ± 0.3	0.6 ± 0.1
R2-HMLB	10^{-3}/s, 5.9 ± 0.2	0.6 ± 0.1
	10^{-5}/s, 5.6 ± 0.2	0.4 ± 0.1
R2-LMHB	10^{-3}/s, 7.4 ± 0.2	0.6 ± 0.1
	10^{-5}/s, 5.9 ± 0.2	0.4 ± 0.1
R2-LMLB	10^{-3}/s, 7.1 ± 0.2	0.6 ± 0.1
	10^{-5}/s, 5.5 ± 0.2	0.5 ± 0.1

Table 5.11: Qualitative orientation parameters at 1080 cm^{-1} from Raman after strain hardening

Table 5.12 shows the orientation in the crystalline phase after strain hardening. The $< P_{200} >$ order parameter increases in every material with draw ratio. The $< P_{200} >$ order parameter is slightly higher in the R2 materials than in the bimodal materials. For a draw ratio of around 5.7 after strain hardening at 10^{-5}/s, the orientation is similar for the R2 materials.

	SH parameters	$< P_{200} >$ $_{SH}$
R2-HMHB	10^{-3}/s, 6.1 ± 0.1	0.79 ± 0.06
	10^{-5}/s, 5.5 ± 0.3	0.71 ± 0.05
R2-HMLB	10^{-3}/s, 5.9 ± 0.2	0.70 ± 0.06
	10^{-5}/s, 5.6 ± 0.2	0.60 ± 0.09
R2-LMHB	10^{-3}/s, 7.4 ± 0.2	0.84 ± 0.06
	10^{-5}/s, 5.9 ± 0.2	0.74 ± 0.05
R2-LMLB	10^{-3}/s, 7.1 ± 0.2	0.83 ± 0.06
	10^{-5}/s, 5.5 ± 0.2	0.69 ± 0.05

Table 5.12: Order parameters at 1420 cm^{-1} from Raman after strain hardening

Table 5.13 shows the overall orientation after strain hardening. Comparing the R2 materials after strain hardening at 10^{-5}/s until a draw ratio

of around 5.7, the orientation is similar.

	SH parameters	$< P_{200} >_{SH}$
R2-HMHB	10^{-3}/s, 6.1 ± 0.1	0.5 ± 0.1
	10^{-5}/s, 5.5 ± 0.3	0.57 ± 0.04
R2-HMLB	10^{-3}/s, 5.9 ± 0.2	0.53 ± 0.04
	10^{-5}/s, 5.6 ± 0.2	0.48 ± 0.03
R2-LMHB	10^{-3}/s, 7.4 ± 0.2	0.60 ± 0.05
	10^{-5}/s, 5.9 ± 0.2	0.55 ± 0.04
R2-LMLB	10^{-3}/s, 7.1 ± 0.2	0.59 ± 0.04
	10^{-5}/s, 5.5 ± 0.2	0.53 ± 0.04

Table 5.13: Order parameters at 1130 cm^{-1} from Raman after strain hardening

5.2.3 Discussion: influence of the molecular mass and branch content on the strain hardening behaviour of branched polyethylene

The dominant factor in the strain hardening behaviour of R2 materials is, like for the bimodal materials, the molecular mass: a higher molecular mass yields a higher strain hardening modulus at a strain rate of around 10^{-3}/s. For the low molecular mass materials, the strain hardening modulus is slightly higher for the low branched material. In an effort to eliminate the crystalline contribution, the strain hardening modulus is divided by the crystallinity of the materials. This yields the same ranking as for the bimodal materials. For the low molecular mass materials, there is no influence of branching. For the high molecular mass materials, a higher branch content yields a higher strain hardening modulus. The yield stress of the R2 materials is lower than that of the bimodal materials (see table 3.10). So it can be expected that the friction contribution from crystals is smaller compared with the bimodal materials.

5.3 Discussion: comparison between the deformation behaviour of the bimodal and the reactor 2 materials

The deformation behaviour of the reactor 2 materials and the bimodal materials is summarised in figures 5.14 and 5.15. It can be seen that both in terms of creep and strain hardening, the resistance of the reactor 2 materials is higher than that of the bimodal materials. A comparison of the strain hardening moduli at 10^{-3}/s is given in table 5.14. The creep resistance of the bimodal materials is less sensitive to stress than that of the R2 materials, especially R2-HMLB. The failure stress and draw ratio after strain hardening at 10^{-3}/s are lower for the reactor 2 materials than for the bimodal materials, but the stress at a fixed draw ratio is approximately twice as high in the reactor 2 materials. The crystallinity is lower in the reactor 2 materials than in the bimodal materials, but follows the same trend (low crystallinity for a high branch content). Dividing the strain hardening modulus by the crystallinity results in the same ranking for the reactor 2 materials as for the bimodal materials, as can be seen in table 5.15. For the low molecular mass materials, there is no influence of the branch content on the strain hardening of the network. For the high molecular mass materials, a higher branch content leads to higher strain hardening of the network. From solid state NMR, it was found that the network density is almost three times higher in the reactor 2 materials than in the bimodal materials.

	R2		Bimodal	
	$\dot{\epsilon}$ [/s]	G_{NHSM} [MPa]	$\dot{\epsilon}$ [/s]	G_{NHSM} [MPa]
HMHB	$1.58 \pm 0.01\ 10^{-3}$	2.61 ± 0.03	$1.46 \pm 0.01\ 10^{-3}$	1.77 ± 0.06
HMLB	$1.60 \pm 0.01\ 10^{-3}$	2.63 ± 0.07	$1.43 \pm 0.01\ 10^{-3}$	1.69 ± 0.02
LMHB	$1.56 \pm 0.01\ 10^{-3}$	1.82 ± 0.05	$1.00 \pm 0.01\ 10^{-3}$	1.10 ± 0.06
LMLB	$1.58 \pm 0.01\ 10^{-3}$	2.08 ± 0.06	$1.44 \pm 0.01\ 10^{-3}$	1.17 ± 0.03

Table 5.14: Comparison of the strain hardening moduli (calculated using the Neo-Hookean strain measure) for R2 and bimodal materials at a strain rate of around 10^{-3}/s

5.3 Discussion: comparison between the deformation behaviour of the bimodal and the reactor 2 materials

	R2 $\dot{\epsilon}$ [/s]	$G_{NHSM}/X_{c,d}$ [MPa]	Bimodal $\dot{\epsilon}$ [/s]	$G_{NHSM}/X_{c,d}$ [MPa]
HMHB	1.58 ± 0.01 10^{-3}	5.61 ± 0.09	1.46 ± 0.01 10^{-3}	2.8 ± 0.1
HMLB	1.60 ± 0.01 10^{-3}	5.0 ± 0.1	1.43 ± 0.01 10^{-3}	2.48 ± 0.04
LMHB	1.56 ± 0.01 10^{-3}	3.9 ± 0.1	1.00 ± 0.01 10^{-3}	1.7 ± 0.1
LMLB	1.58 ± 0.01 10^{-3}	4.0 ± 0.1	1.44 ± 0.01 10^{-3}	1.73 ± 0.05

Table 5.15: Comparison of the strain hardening moduli (calculated using the Neo-Hookean strain measure) corrected for the crystalline contribution for R2 and bimodal materials at a strain rate of around 10^{-3}/s

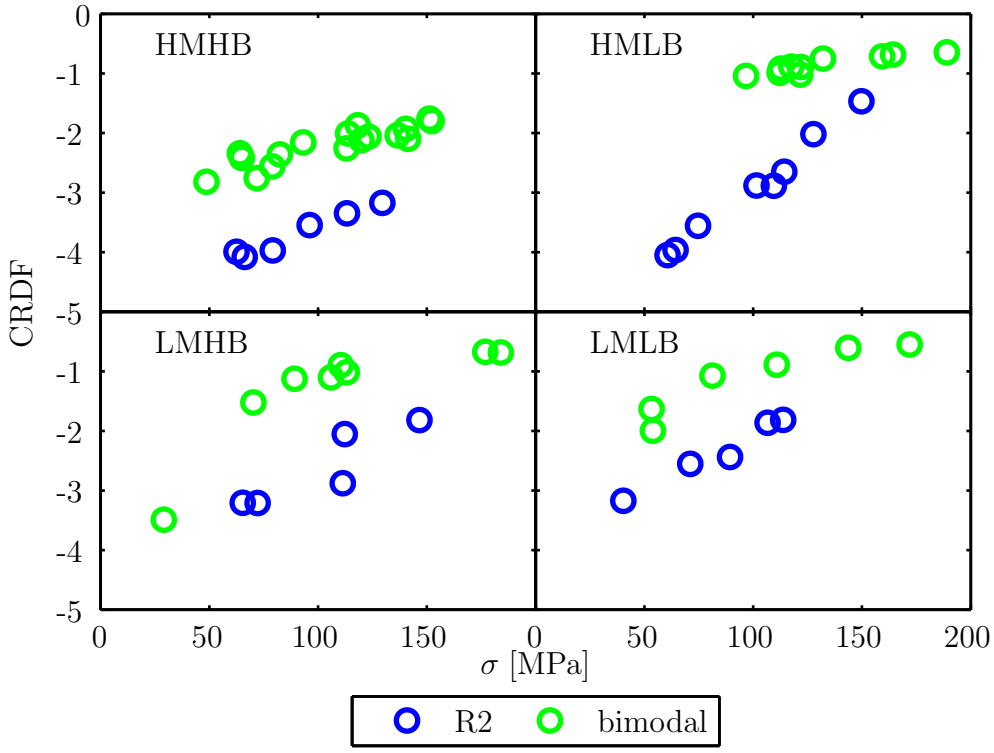

Figure 5.14: CRDF as a function of stress, comparison of all materials

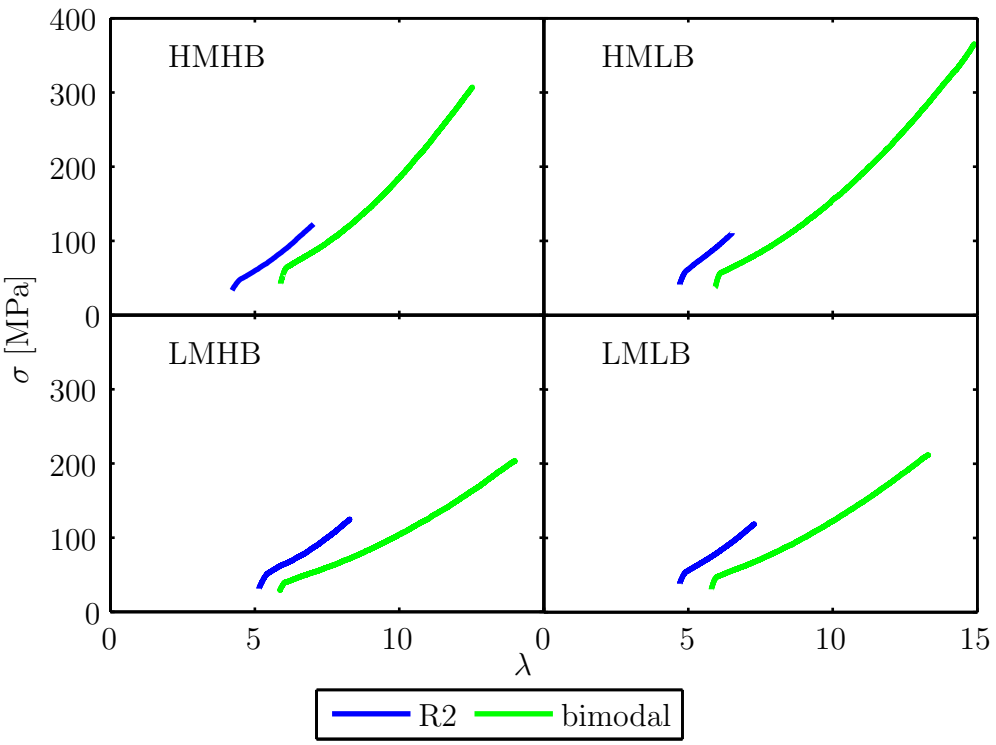

Figure 5.15: Comparison of strain hardening of R2 and bimodal materials at an approximate strain rate of 10^{-3}/s

We will now use these experimental observations to hypothesise the physical mechanisms acting during the deformation of the reactor 2 and the bimodal materials. The high available network density in the reactor 2 materials compared to the bimodal materials is a clear indication that the low molecular mass, linear fraction has a negligible contribution to the network. This implies that when a certain stress is applied to the network, this stress is divided over more chains in the reactor 2 materials than in the bimodal materials. In other words, the effective force per chain is lower in the reactor 2 materials. This explains why the reactor 2 materials have a higher resistance to deformation both during creep and during strain hardening. From the strain rate sensitivity of the strain hardening modulus of the bimodal materials, it was concluded that the α-relaxation causes an upswing in the strain hardening of these materials (especially those with a high crystallinity) from a strain rate of 10^{-3}/s. The strain rate sensitivity of the strain hardening (and the yield stress) of the reactor 2 materials was not studied, but it would be expected that this effect is smaller for these materials due to their lower crystallinity. When taking into account

crystallinity, the ranking of the reactor 2 materials is the same as for the bimodal materials in terms of strain hardening (though the strain hardening is higher for the reactor 2 materials). This indicates that correcting for the crystallinity indeed eliminates crystalline friction contributions. This ranking also agrees with the results from solid state NMR, but further work needs to be done to see whether the differences in network density from NMR within one family of materials are significant, and how the available network density translates to the effective network density as a function of time. From figure 5.14, it can be seen that at all stresses measured, the creep rate deceleration factor is lower for the reactor 2 materials than for the bimodal materials. However, the difference decreases with increasing stress, especially for the HMLB materials. Due to the lower force per tie chain in the reactor 2 materials, a higher applied stress is needed to pull a branch into a crystal or over an entanglement. The friction contribution is therefore lower at low stresses than at high stresses for the reactor 2 materials, while it could be that for the bimodal materials, this friction process is already fully active at lower stresses, hence the low sensitivity to stress. This effect can be expected to be larger in the R2-HMLB material. Its high molecular mass in combination with a high crystallinity results in stable crystals, well connected by tie chains at low stress. At high stress, the crystals have a much lower effect because it is easier to pull branches into crystals, and now the low branch content results in a lower resistance to creep compared to R2-HMHB.

In terms of stress during strain hardening, it can be seen from figure 5.15 that at the same draw ratio, the reactor 2 material can roughly take double the stress at the bimodal material. From table 5.15, it can be calculated that $G_{NHSM}/X_{c,d}$ is 2.00 ± 0.04 for the high molecular mass materials, and 2.30 ± 0.03 for the low molecular mass materials. The low molecular mass, linear fraction in the bimodal material is 49%. Hence no major synergistic effect is seen. The doubling in stress is combined with a significant reduction in failure stress and draw ratio. So while the reactor 2 materials would be ideal materials to resist creep up until 150 MPa, they will break at a higher applied stress. Furthermore, the R2 materials are difficult to process. Hence of the eight materials studied in this work, bi-HMHB performs best overall

in terms of resistance to creep and strain hardening, failure stress and draw ratio and processability.

5.4 Conclusions

In conclusion, the monomodal, branched polyethylenes have a higher resistance to creep and strain hardening than the bimodal polyethylenes. This indicates the importance of the available network density. A higher number of effective network chains reduces the effective force per chain. The creep resistance of the reactor 2 materials is more sensitive to starting creep stress than in the bimodal materials, especially for R2-HMLB. We suggest that this is caused by the friction needed to be overcome to pull a chain branch into a crystal or over an entanglement. If the effective force per chain is higher, like in the bimodal materials, this process will be activated at lower stresses. Overall, materials with a combination of high molecular mass and high branch content perform the best out of the eight materials studied in this work. The combination of a high number of tie chains with a high monomeric friction increases the friction to be overcome by the material to deform, whether it originates from pulling a branch over an entanglement or into a crystal.

Chapter 6

Conclusions

The conclusions of this work are summarised in this chapter and suggestions for future work are given.

6.1 Overall conclusions

The most common failure mode for polyolefin pressure pipes is brittle failure caused by slow crack growth. A crack is preceded by a craze, a voided wedge of material bridged by highly deformed fibrils. Upon failure of the fibrils, the crack propagates. Both the tendency of the material to form voids and the strength of the fibril at the craze - crack interface are governed by the effective entanglement network. The effective entanglement network comprises all the intermolecular junctions in the material that can effectively transfer load at the time scale of the experiment, whether originating from entanglements in the amorphous phase or intercrystalline tie molecules. In this work, the effective entanglement network of bimodal polyethylene is probed through tensile and creep measurements. Bimodal polyethylene is the industrial standard material for polyethylene pressure pipes, and consists of a high molecular mass, branched fraction and a low molecular mass, linear fraction. The former is responsible for the resistance to slow crack growth, the latter for enabling processing.

For the first part of the work, four materials are produced. They are all bimodal polyethylenes, of which the high molecular mass fraction is varied in terms of molecular architecture:

- low molecular mass and low branch content,
- low molecular mass and high branch content,
- high molecular mass and low branch content and
- high molecular mass and high branch content.

The creep and strain hardening behaviour of these four materials is studied. It is found that only a combination of high molecular mass and high branch content increases the resistance to creep, independent of the starting creep stress. The resistance to strain hardening increases with strain rate, but the strain rate sensitivity is different for the different bimodal materials. Over the strain rate range studied, molecular mass is the dominant factor, with a higher strain hardening for the high molecular mass materials. At low strain rates, branch content has no effect on strain hardening. At high strain rates, a low branch content results in an improved strain hardening compared to high branch content. The strain rate sensitivity of the strain hardening is ascribed to a crystalline contribution caused by the α-relaxation. Assuming that the crystalline contribution is dominant and the long range order parameters are similar in the isotropic material and the strain hardening region, the strain rate dependent yield stress can be taken as a measure for the friction contribution during strain hardening. When scaling the strain hardening modulus by the yield stress, the ranking of the materials at low strain rates now agrees with the ranking in creep. At high strain rates, however, the resistance to strain hardening now decreases with strain rate, suggesting that scaling by the yield stress overestimates the crystalline contribution at high strain rates. This is ascribed to a loss of long range order during strain hardening at these strain rates.

For the second part of this work, four other materials are produced. They are all monomodal polyethylenes, representing the high molecular mass fraction of the bimodal polyethylenes described above. The purpose for studying these materials is to establish whether the same mechanisms for increasing the resistance of a polyethylene against strain hardening and creep are present in the bimodal materials and the monomodal materials. In other words, does optimising the branched fraction of a bimodal polyethylene result in an optimisation of the bimodal polyethylene as a whole? The

monomodal, branched polyethylenes have a higher resistance to creep and strain hardening than the bimodal polyethylenes. This indicates the importance of the available network density. A higher number of effective network chains reduces the effective force per chain. The creep resistance of the reactor 2 materials is more sensitive to starting creep stress than in the bimodal materials, especially for R2-HMLB. We suggest that this is caused by the friction needed to be overcome to pull a chain branch into a crystal or over an entanglement. If the effective force per chain is higher, like in the bimodal materials, this process will be activated at lower stresses. Overall, materials with a combination of high molecular mass and high branch content performs the best out of the eight materials studied in this work. The combination of a high number of tie chains with a high monomeric friction increases the friction to be overcome by the material to deform, whether it originates from pulling a branch over an entanglement or into a crystal.

Of the eight materials studied in this work, bi-HMHB performs best overall in terms of resistance to creep and strain hardening, failure stress and draw ratio and processability.

6.2 Future work

This work studied the mechanical behaviour of bimodal and monomodal branched polyethylene and used the results to hypothesise on the physical mechanisms behind the differences in behaviour. Further work is needed to substantiate these hypotheses further. In this work, it is suggested that the mechanical behaviour can be interpreted as a combination of available network density and monomeric friction, irrespective of the nature of the morphological components causing this friction. To substantiate this claim, the melt friction of these materials should be measured and compared to their mechanical behaviour. The time dependency of the available network density measured in solid state NMR should be assessed. A first step for doing is would be dynamical mechanical analysis, comparing the plateau modulus at different frequencies with the NMR results. To assess the chain axis density of the different materials at different strain rates, a detailed

study of the fracture stress as a function of strain rate should be performed. It would be interesting to do Raman measurements at different stages during the strain hardening at different strain rates, to see if peak splitting can be observed. Peak splitting indicates chains of the same morphology being stressed in different amounts, and can be used to calculated molecular stress. However, the feasibility of such a study at high strain rates is low. The strain hardening and yield behaviour at different strain rates for the R2 materials should be explored, to see if our conclusions hold. To assess if the idea of a general friction contribution is adequate, material with a set branch content can be annealed to obtain different crystallinities. In this way, the other aspects of the morphology of the material are less critically altered than for the materials used in this work. A study similar to the one in this work could then be performed. This type of mechanical studies on well characterised materials is crucial in the understanding of creep and strain hardening and their relation to slow crack growth, as morphological and structural studies at high strain rates and high deformation can be very challenging.

References

[1] R. Deblieck, L. Havermans, K. Remerie, M. Bonner, and I. Ward, "The importance of network response for polymer properties." October 2012. 3, 27

[2] M. J. Kanters, "Assessing long-term performance of solid polymers based on short-term testing," Master's thesis, Eindhoven University of Technology, 2011. 3

[3] U. W. Gedde, J. Viebke, H. Leijström, and M. Ifwarson, "Long-term properties of hot-water polyolefin pipes: a review," *Polymer Engineering & Science*, vol. 34, no. 24, pp. 1773–1787, 1994.

[4] R. W. Lang, A. Stern, and G. Doerner, "Applicability and limitations of current lifetime prediction models for thermoplastic pipes under internal pressure," *Die Angewandte Makromolekulare Chemie*, vol. 247, no. 1, pp. 131–145, 1997. 3

[5] S. K. Bhattacharya and N. Brown, "Micromechanisms of crack initiation in thin films and thick sections of polyethylene," *Journal of Materials Science*, vol. 19, pp. 2519 – 2532, 1984. 3, 11

[6] N. Brown and S. Bhattacharya, "The initiation of slow crack growth in linear polyethylene under single edge notch tension and plane strain," *Journal of Materials Science*, vol. 20, no. 12, pp. 4553–4560, 1985.

[7] X. Lu, X. Wang, and N. Brown, "Slow fracture in a homopolymer and copolymer of polyethylene," *Journal of Materials Science*, vol. 23, no. 2, pp. 643–648, 1988. 25, 26

[8] N. Brown and X. Lu, "A fundamental theory for slow crack growth in polyethylene," *Polymer*, vol. 36, no. 3, pp. 543–548, 1995.

[9] N. Brown and X. Lu, "The fracture mechanics of slow crack growth in polyethylene," *International Journal of Fracture*, vol. 69, no. 4, pp. 371–377, 1995. 3

[10] A. Lustiger and R. Corneliussen, "The role of crazes in the crack growth of polyethylene," *Journal of Materials Science*, vol. 22, no. 7, pp. 2470–2476, 1987. xiii, 4, 11

[11] R. A. Deblieck, D. J. van Beek, K. Remerie, and I. M. Ward, "Failure mechanisms in polyolefines: The role of crazing, shear yielding and the entanglement network," *Polymer*, vol. 52, pp. 2979 – 2990, 2011. xiii, xiv, 4, 19, 21, 24, 29, 32, 33, 94, 153

[12] V. authors, *100+ Years of plastics. Leo Baekeland and beyond*, vol. 1080 of *ACS Symposium series*. American Chemical Society, 2011. 5, 10

[13] J. M. Cowie and V. Arrighi, *Polymers: chemistry and physics of modern materials*. CRC Press, 3 ed., 2008. 5, 6, 8, 10, 86

[14] W. Guenther, "Fifty years of Ziegler Catalysts: consequences and development of an invention," *Angewandte Chemie International Edition*, vol. 42, no. 41, pp. 5000–5008, 2003. 5

[15] R. S. Porter and J. F. Johnson, "The entanglement concept in polymer systems," *Chemical Reviews*, vol. 66, no. 1, pp. 1–27, 1966. 6

[16] L. J. Fetters, D. J. Lohse, S. T. Milner, and W. W. Graessley, "Packing length influence in linear polymer melts on the entanglement, critical, and reptation molecular weights," *Macromolecules*, vol. 32, no. 20, pp. 6847–6851, 1999. 6

[17] H. Bromstrup, ed., *PE 100 Pipe Systems*. Vulkan-Verkag GmbH, 2 ed., 2004. 7, 29

[18] K. Cho, B. H. Lee, K.-M. Hwang, H. Lee, and S. Choe, "Rheological and mechanical properties in polyethylene blends," *Polymer Engineering & Science*, vol. 38, no. 12, pp. 1969–1975, 1998. 7

[19] P. M. Wood-Adams, J. M. Dealy, A. W. Degroot, and O. D. Redwine, "Effect of molecular structure on the linear viscoelastic behavior of polyethylene," *Macromolecules*, vol. 33, no. 20, pp. 7489–7499, 2000. 7

[20] C. A. García-Franco, B. A. Harrington, and D. J. Lohse, "Effect of short-chain branching on the rheology of polyolefins," *Macromolecules*, vol. 39, no. 7, pp. 2710–2717, 2006. 7, 96

[21] R. Alamo, R. Domszy, and L. Mandelkern, "Thermodynamic and structural properties of copolymers of ethylene," *The Journal of Physical Chemistry*, vol. 88, no. 26, pp. 6587–6595, 1984. 8

[22] C. France, P. Hendra, W. Maddams, and H. Willis, "A study of linear low-density polyethylenes: branch content, branch distribution and crystallinity," *Polymer*, vol. 28, no. 5, pp. 710–712, 1987.

[23] R. Séguéla and F. Rietsch, "Tensile drawing behaviour of ethylene/α-olefin copolymers: influence of the co-unit concentration," *Polymer*, vol. 27, no. 5, pp. 703–708, 1986. 9

[24] S. Hosoda, H. Nomura, Y. Gotoh, and H. Kihara, "Degree of branch inclusion into the lamellar crystal for various ethylene/α-olefin copolymers," *Polymer*, vol. 31, no. 10, pp. 1999–2005, 1990. 26

[25] Z. Zhou, X. Lu, and N. Brown, "The effect of blending high-density and linear low-density polyethylenes on slow crack growth," *Polymer*, vol. 34, no. 12, pp. 2520–2523, 1993. 8, 25, 28

[26] J. Fatou and L. Mandelkern, "The effect of molecular weight on the melting temperature and fusion of polyethylene," *The Journal of Physical Chemistry*, vol. 69, no. 2, pp. 417–428, 1965. 8

[27] G. Capaccio and I. Ward, "Preparation of ultra-high modulus linear polyethylenes; effect of molecular weight and molecular weight distribution on drawing behaviour and mechanical properties," *Polymer*, vol. 15, no. 4, pp. 233–238, 1974. 10

[28] R. K. Krishnaswamy, Q. Yang, L. Fernandez-Ballester, and J. A. Kornfield, "Effect of the distribution of short-chain branches on crystallization kinetics and mechanical properties of high-density polyethylene," *Macromolecules*, vol. 41, pp. 1693 – 1704, 2008. 8, 27, 29, 37

[29] I. M. Ward and J. Sweeney, *Mechanical properties of solid polymers*. John Wiley & Sons, 2013. 8, 20, 31, 35, 38, 46, 138

[30] G. Capaccio and I. Ward, "Effect of molecular weight on the morphology and drawing behaviour of melt crystallized linear polyethylene," *Polymer*, vol. 16, no. 4, pp. 239–243, 1975. 10

[31] P. Coates and I. Ward, "Drawing of polymers through a conical die," *Polymer*, vol. 20, no. 12, pp. 1553–1560, 1979. 10

[32] A. Peacock, *Handbook of polyethylene: structures: properties, and applications*. CRC Press, 2000. 10

[33] P. Moldenaers, *Kunststoffen*. KU Leuven, 2009. 10

[34] A. Toda and A. Keller, "Growth of polyethylene single crystals from the melt: morphology," *Colloid and Polymer Science*, vol. 271, pp. 328–342, 1993. xiii, 11, 12

[35] L. Lin and A. Argon, "Structure and plastic deformation of polyethylene," *Journal of Materials Science*, vol. 29, pp. 294–323, 1994. 11, 14

[36] P. Geil, "Small angle x-ray scattering from bulk crystalline polymers," *Journal of Polymer Science Part C: Polymer Symposia*, vol. 13, pp. 149–163, 1966. 11

[37] I. L. Hay and A. Keller, "A study on orientation effects in polyethylene in the light of crystalline texture," *Journal of Materials Science*, vol. 2, pp. 538 – 558, 1967. 11

[38] A. Keller, "A note on single crystals in polymers: evidence for a folded chain configuration," *Philosophical Magazine*, vol. 2, no. 21, pp. 1171–1175, 1957.

[39] A. Keller and S. Sawada, "On the interior morphology of bulk polyethylene," *Die Makromolekulare Chemie*, vol. 74, pp. 190–221, 1964. 11

[40] H. R. Brown and T. P. Russell, "Entanglements at polymer surfaces and interfaces," *Macromolecules*, vol. 29, no. 2, pp. 798–800, 1996. 11

[41] R. Oslanec and H. R. Brown, "Entanglement density at the interface between two immiscible polymers," *Macromolecules*, vol. 36, no. 15, pp. 5839–5844, 2003. 11

[42] H. D. Keith, F. J. Padden, and R. G. Vadimsky, "Intercrystalline links in polyethylene crystallized from the melt," *Journal of Polymer Science Part A-2: Polymer Physics*, vol. 4, no. 2, pp. 267–281, 1966. 11, 27

[43] H. Keith, F. Padden Jr, and R. Vadimsky, "Further studies of intercrystalline links in polyethylene," *Journal of Applied Physics*, vol. 37, no. 11, pp. 4027–4034, 1966.

[44] H. Keith, F. Padden Jr, and R. Vadimsky, "Intercrystalline links: critical evaluation," *Journal of Applied Physics*, vol. 42, no. 12, pp. 4585–4592, 1971.

[45] H. D. Keith, F. J. Padden, and R. G. Vadimsky, "Origin of intercrystalline links," *Journal of Polymer Science: Polymer Physics Edition*, vol. 18, no. 11, pp. 2307–2309, 1980.

[46] K. Friedrich, "Crazes and shear bands in semi-crystalline thermoplastics," vol. 52-53 of *Advances in Polymer Science*, pp. 225–274, Springer Berlin Heidelberg, 1983.

[47] A. Lustiger and N. Ishikawa, "An analytical technique for measuring relative tie-molecule concentration in polyethylene," *Journal of Polymer Science Part B: Polymer Physics*, vol. 29, no. 9, pp. 1047–1055, 1991.

[48] C. J. Plummer and H.-H. Kausch, "Deformation and entanglement in semi-crystalline polymers," *Journal of Macromolecular Science, Part B: Physics*, vol. 35, no. 3-4, pp. 637–657, 1996. 24

[49] H. H. Kausch, R. Gensler, C. Grein, C. J. Plummer, and P. Scaramuzzino, "Crazing in semi-crystalline thermoplastics," *Journal of Macromolecular Science*, vol. 38, pp. 803–815, 1999. 11

[50] R. Séguéla, "Critical review of the molecular topology of semi-crystalline polymers: the origin and assessment of intercrystalline tie molecules and chain entanglements," *Journal of Polymer Science Part B: Polymer Physics*, vol. 43, pp. 1729 – 1748, 2005. xiii, 13, 23, 24

[51] A. Peterlin, "Plastic deformation of crystalline polymers," *Polymer Engineering & Science*, vol. 17, no. 3, pp. 183–193, 1977. 11, 16

[52] R. Séguéla and F. Rietsch, "Molecular topology in ethylene copolymers studied by means of mechanical testing," *Journal of Materials Science*, vol. 23, pp. 415–421, 1988. xiii, 11, 15

[53] S. Patlazhan and Y. Remond, "Structural mechanics of semi-crystalline polymers prior to the yield point: a review," *Materials Science*, vol. 47, pp. 6749 – 6767, 2012. 14

[54] A. Rozanski and A. Galeski, "Controlling cavitation of semi-crystalline polymers during tensile drawing," *Macromolecules*, vol. 44, pp. 7273–7287, 2011. 14

[55] S. Humbert, O. Lame, J. M. Chenal, C. Rochas, and G. Vigier, "New insight on initiation of cavitation in semi-crystalline polymers: in-situ SAXS measurements," *Macromolecules*, vol. 43, pp. 7212–7221, 2010. 14

[56] L. Farge, S. Andre, F. Meneau, J. Dillet, and C. Cunat, "A common multiscale feature of the deformation mechanisms of a semi-crystalline polymer," *Macromolecules*, vol. 46, pp. 9659–9668, 2013. 14, 16

[57] Y. Men and G. Strobl, "Critical strains determining the yield behavior of s-PP," *Journal of Macromolecular Science, Part B*, vol. 40, pp. 775–796, 2001. 14

[58] R. Young, "A dislocation model for yield in polyethylene," *Philosophical Magazine*, vol. 30, no. 1, pp. 85–94, 1974. xiv, 14, 15

[59] R. Young, "Screw dislocation model for yield in polyethylene," vol. 11, pp. 210–216, Institute of Metals and Materials Australasia, 1988. 14

[60] Z. Bartczak, "Effect of chain entanglements on plastic deformation behavior of ultra-high molecular weight polyethylene," *Journal of Polymer Science Part B: Polymer Physics*, vol. 48, no. 3, pp. 276–285, 2010. 14

[61] A. S. Argon, *The Physics of Deformation and Fracture of Polymers*. Cambridge University Press, 2013. 14, 20

[62] K. Yamada and M. Takayanagi, "Superstructural description of deformation process in uniaxial extension of preoriented isotactic polypropylene," *Journal of Applied Polymer Science*, vol. 24, no. 3, pp. 781–799, 1979. 14, 86

[63] P. B. Bowden and R. J. Young, "Deformation mechanisms in crystalline polymers," *Journal of Materials Science*, vol. 9, pp. 2034–2051, 1974. xiv, 14, 16

[64] R. Hiss, S. Hobeika, C. Lynn, and G. Strobl, "Network stretching, slip processes, and fragmentation of crystallites during uniaxial drawing of polyethylene and related copolymers: a comparative study," *Macromolecules*, vol. 32, pp. 4390 – 4403, 1999. 14, 17, 86

[65] G. Meinel and A. Peterlin, "Plastic deformation of polyethylene II. Change of mechanical properties during drawing," *Journal of Polymer Science Part A-2: Polymer Physics*, vol. 9, no. 1, pp. 67–83, 1971. 16

[66] A. Peterlin, "Molecular model of drawing polyethylene and polypropylene," *Materials Science*, vol. 6, pp. 490 – 508, 1971. xiv, 16, 17, 37

[67] S. Magonov, S. Sheiko, R. Deblieck, and M. Moller, "Atomic-force microscopy of gel-drawn ultrahigh-molecular-weight polyethylene," *Macromolecules*, vol. 26, no. 6, pp. 1380–1386, 1993.

[68] Y. Tang, Z. Jiang, Y. Men, L. An, H. Enderle, D. Lilge, S. Roth, R. Gehrke, and J. Rieger, "Uniaxial deformation of overstretched polyethylene," *Polymer*, vol. 48, pp. 5125–5132, 2007. 16, 17

[69] Z. Bartczak, A. Galeski, A. S. Argon, and R. E. Cohen, "On the plastic deformation of the amorphous component in semi-crystalline polymers," *Polymer*, vol. 37, pp. 2113–2123, 1996. 16, 17

[70] A. Peterlin, "Plastic deformation of polymers with fibrous structure," *Colloid and Polymer Science*, vol. 253, no. 10, pp. 809–823, 1975. 16

[71] A. Peterlin, "Drawing and extrusion of semi-crystalline polymers," *Colloid and Polymer Science*, vol. 265, no. 5, pp. 357–382, 1987. 16

[72] T. Amornsakchai, A. Unwin, I. Ward, and D. Batchelder, "Strain inhomogeneities in highly oriented gel-spun polyethylene," *Macromolecules*, vol. 30, pp. 5034–5044, 1997. 17

[73] E. J. Kramer, "Microscopic and molecular fundamentals of crazing," pp. 1–56, Springer, 1983. 18, 19

[74] E. J. Kramer and L. L. Berger, "Fundamental processes of craze growth and fracture," pp. 1–68, Springer, 1990. 19, 20, 21

[75] R. Séguéla, "On the natural draw ratio of semi-crystalline polymers: review of the mechanical, physical and molecular aspects," *Macromolecular Materials and Engineering*, vol. 292, pp. 235–244, 2007. 18, 37, 89

[76] C. Thomas, R. Séguéla, F. Detrez, V. Miri, and C. Vanmansart, "Plastic deformation of spherulitic semi-crystalline polymers - an in situ AFM study of polybutene under tensile drawing," *Polymer*, vol. 50, pp. 3714 – 3723, 2009. 19

[77] S. I. Krishnamachari, *Applied stress analysis of plastics: a mechanical engineering approach*. Chapman and Hall, 1993. 19

[78] H. B. Hamouda, M. Simoes-Betbeder, F. Grillon, P. Blouet, N. Billon, and R. Piques, "Creep damage mechanisms in polyethylene gas pipes," *Polymer*, vol. 42, no. 12, pp. 5425–5437, 2001.

[79] Y. Men, J. Rieger, H. Enderle, and D. Lilge, "The mobility of the amorphous phase in polyethylene as a determining factor for slow crack growth," *European Physics Journal Part E: Soft Matter*, vol. 15, pp. 421 – 425, 2004. 24

[80] C. Thomas, V. Ferreiro, G. Coulon, and R. Séguéla, "In situ AFM investigation of crazing in polybutene spherulites under tensile drawing," *Polymer*, vol. 48, no. 20, pp. 6041–6048, 2007. 19, 20

[81] E. Nezbedová, P. Hutař, M. Zouhar, Z. Knésl, J. Sadílek, and L. Náhlík, "The applicability of the Pennsylvania notch test for a new generation of PE pipe grades," *Polymer Testing*, vol. 32, pp. 106–114, 2013. 19

[82] A. Argon, "Physical basis of distortional and dilational plastic flow in glassy polymers," *Journal of Macromolecular Science, Part B: Physics*, vol. 8, no. 3-4, pp. 573–596, 1973. 19

[83] A. S. Argon and M. Salama, "Growth of crazes in glassy polymers," *Philosophical Magazine*, vol. 36, no. 5, pp. 1217–1234, 1977. 19, 20

[84] P. O'Connell, M. Bonner, R. Duckett, and I. Ward, "The relationship between slow crack propagation and tensile creep behaviour in polyethylene," *Polymer*, vol. 36, pp. 2355–2362, 1995. 20, 36, 37

[85] A. Argon, J. Im, and R. Safoglu, "Cavity formation from inclusions in ductile fracture," *Metallurgical Transactions A*, vol. 6, no. 4, pp. 825–837, 1975. 20

[86] L. Rose, A. Channell, C. Frye, and G. Capaccio, "Slow crack growth in polyethylene: a novel predictive model based on the creep of craze fibrils," *Journal of Applied Polymer Science*, vol. 54, pp. 2119 – 2124, 1994. xv, 20, 36, 38, 99

[87] J. M. Lagarón, N. M. Dixon, D. L. Gerrard, W. Reed, and B. J. Kip, "Cold-drawn material as model material for the environmental stress cracking (ESC) phenomenon in polyethylene. A Raman spectroscopy study of molecular stress induced by macroscopic strain in drawn polyethylenes and their relation to environmental stress cracking," *Macromolecules*, vol. 31, no. 17, pp. 5845–5852, 1998. 20, 23, 29

[88] L. L. Berger, "Relationship between craze microstructure and molecular entanglements in glassy polymers. 1," *Macromolecules*, vol. 22, no. 7, pp. 3162–3167, 1989. 20

[89] C. J. Plummer, A. Goldberg, and A. Ghanem, "Micromechanisms of slow crack growth in polyethylene under constant tensile loading," *Polymer*, vol. 42, no. 23, pp. 9551–9564, 2001. xiv, 22

[90] H. Brown, "A molecular interpretation of the toughness of glassy polymers," *Macromolecules*, vol. 24, no. 10, pp. 2752–2756, 1991. xiv, 21, 22

[91] C. Hui, A. Ruina, C. Creton, and E. Kramer, "Micromechanics of crack growth into a craze in a polymer glass," *Macromolecules*, vol. 25, no. 15, pp. 3948–3955, 1992. 21

[92] H. G. Van Melick, L. E. Govaert, and H. E. Meijer, "On the origin of strain hardening in glassy polymers," *Polymer*, vol. 44, pp. 2493–2502, 2003. 23, 32

[93] K. Prasad and D. T. Grubb, "Direct observation of taut tie molecules in high-strength polyethylene fibers by Raman spectroscopy," *Journal of Polymer Science Part B: Polymer Physics*, vol. 27, no. 2, pp. 381–403, 1989. 23

[94] W. Wong and R. Young, "Analysis of the deformation of gel-spun polyethylene fibres using Raman spectroscopy," *Journal of Materials science*, vol. 29, no. 2, pp. 510–519, 1994.

[95] R. J. Meier and H. Vansweefelt, "Some comments on the analysis of vibrational bands in strained polymers: polyethylene," *Polymer*, vol. 36, no. 20, pp. 3825–3829, 1995. 23

[96] Y.-L. Huang and N. Brown, "Dependence of slow crack growth in polyethylene on butyl branch density: morphology and theory," *Journal of Polymer Science Part B: Polymer Physics*, vol. 29, no. 1, pp. 129–137, 1991. 23, 26, 27

[97] Z. Zhou and N. Brown, "Slow crack growth of blends of high density and linear low density polyethylenes as influenced by morphology," *Polymer*, vol. 35, no. 17, pp. 3619–3623, 1994. xiv, 23, 24, 25, 28

[98] L. L. Bohm, H. F. Enderle, and M. Fleißner, "High-density polyethylene pipe resins," *Advanced Materials*, vol. 4, no. 3, pp. 234–238, 1992.

[99] R. A. García, A. Carrero, M. Aroca, O. Prieto, and C. Dominguez, "Slow crack growth resistance in resin blends of chromium and metallocene catalyzed ethylene-hexene copolymers for pipe applications," *Polymer Engineering & Science*, vol. 48, no. 5, pp. 925–933, 2008.

[100] J. J. Cheng, M. A. Polak, and A. Penlidis, "Polymer network mobility and environmental stress cracking resistance of high density polyethylene," *Polymer-Plastics Technology and Engineering*, vol. 48, no. 12, pp. 1252–1261, 2009. 25

[101] J. J. Cheng, M. A. Polak, and A. Penlidis, "Influence of micromolecular structure on environmental stress cracking resistance of high density polyethylene," *Tunnelling and Underground Space Technology*, vol. 26, no. 4, pp. 582–593, 2011. 31

[102] A. Adib, C. Domínguez, J. Rodríguez, C. Martín, and R. A. García, "The effect of microstructure on the slow crack growth resistance in polyethylene resins," *Polymer Engineering & Science*, vol. 55, no. 5, pp. 1018–1023, 2015. 24, 25, 31

[103] V. Litvinov, W. Barendswaard, and M. Van Duin, "The density of chemical crosslinks and chain entanglements in unfilled EPDM vulcanizates as studied with low resolution, solid state ^{1}H NMR," *Rubber Chemistry and Technology*, vol. 71, no. 1, pp. 105–118, 1998. 25

[104] V. Litvinov and P. Steeman, "EPDM-carbon black interactions and the reinforcement mechanisms, as studied by low-resolution ^{1}H NMR," *Macromolecules*, vol. 32, no. 25, pp. 8476–8490, 1999.

[105] V. Litvinov, "EPDM/PP thermoplastic vulcanizates as studied by proton NMR relaxation: phase composition, molecular mobility, network structure in the rubbery phase, and network heterogeneity," *Macromolecules*, vol. 39, no. 25, pp. 8727–8741, 2006. 25

[106] V. M. Litvinov and L. Kurelec, "Remarkably high mobility of some chain segments in the amorphous phase of strained HDPE," *Polymer*, vol. 55, pp. 1–6, 2013. 25, 94, 95

[107] X. Lu and N. Brown, "A test for slow crack growth failure in polyethylene under a constant load," *Polymer Testing*, vol. 11, no. 4, pp. 309–319, 1992. 25

[108] A. Ward, X. Lu, Y. Huang, and N. Brown, "The mechanism of slow crack growth in polyethylene by an environmental stress cracking agent," *Polymer*, vol. 32, no. 12, pp. 2172–2178, 1991. 25

[109] Y.-L. Huang and N. Brown, "The dependence of butyl branch density on slow crack growth in polyethylene: kinetics," *Journal of Polymer Science Part B: Polymer Physics*, vol. 28, no. 11, pp. 2007–2021, 1990. 25, 26

[110] X. Lu, Z. Zhou, and N. Brown, "A sensitive mechanical test for slow crack growth in polyethylene," *Polymer Engineering & Science*, vol. 37, no. 11, pp. 1896–1900, 1997. 25, 26

[111] S. Humbert, O. Lame, and G. Vigier, "Polyethylene yielding behaviour: What is behind the correlation between yield stress and crystallinity?," *Polymer*, vol. 50, no. 15, pp. 3755 – 3761, 2009. 26

[112] R. Bubeck and H. Baker, "The influence of branch length on the deformation and microstructure of polyethylene," *Polymer*, vol. 23, no. 11, pp. 1680–1684, 1982. 26

[113] J. Yeh, J.-H. Chen, and H.-S. Hong, "Environmental stress cracking behavior of short-chain branch polyethylenes in Igepal solution under a constant load," *Journal of Applied Polymer Science*, vol. 54, no. 13, pp. 2171–2186, 1994. 26

[114] Y.-L. Huang and N. Brown, "The effect of molecular weight on slow crack growth in linear polyethylene homopolymers," *Journal of Materials Science*, vol. 23, no. 10, pp. 3648–3655, 1988. 26, 27

[115] J. B. Soares, R. Abbott, and J. Kim, "Environmental stress cracking resistance of polyethylene: The use of CRYSTAF and SEC to establish structure–property relationships," *Journal of Polymer Science Part B: Polymer Physics*, vol. 38, no. 10, pp. 1267–1275, 2000. 26, 28

[116] J. D. Hoffman and R. L. Miller, "Kinetics of crystallization from the melt and chain folding in polyethylene fractions revisited: theory and experiment," *Polymer*, vol. 38, no. 13, pp. 3151–3212, 1997. 27

[117] T. Bremner, A. Rudin, and D. Cook, "Melt flow index values and molecular weight distributions of commercial thermoplastics," *Journal of Applied Polymer Science*, vol. 41, pp. 1617 – 1627, 1990. 27

[118] Y.-L. Huang and N. Brown, "Slow crack growth in blends of HDPE and UHMWPE," *Polymer*, vol. 33, no. 14, pp. 2989–2997, 1992. 27

[119] J. Cazenave, B. Sixou, and R. Séguéla, "Structural approaches of polyethylene environmental stress-crack resistance," *Oil & Gas Science and Technology-Revue de l'IFP*, vol. 61, no. 6, pp. 735–742, 2006. 28, 37, 38, 89

[120] L. Hubert, L. David, R. Séguéla, G. Vigier, C. Degoulet, and Y. Germain, "Physical and mechanical properties of polyethylene for pipes in relation to molecular architecture. I. Microsctructure and crystallisation kinetics," *Polymer*, vol. 42, pp. 8425–8434, 2001. 29

[121] L. Hubert, L. David, R. Séguéla, G. Vigier, C. Corfias-Zuccalli, and Y. Germain, "Physical and mechanical properties of polyethylene for pipes in relation to molecular architecture. II. Short-term creep of isotropic and drawn materials," *Journal of Applied Polymer Science*, vol. 84, pp. 2308 – 2317, 2002. 29

[122] L. Kurelec, M. Teeuwen, H. Schoffeleers, and R. Deblieck, "Strain hardening modulus as a measure of environmental stress crack resistance of high density polyethylene," *Polymer*, vol. 46, pp. 6369–6379, 2005. xiv, 31, 34, 121

[123] M. McCarthy, R. A. Deblieck, P. Mindermann, R. Kloth, L. Kurelec, and H. Martens, "New accelerated method to determine slow crack growth behaviour of polyethylene pipe materials," *Plastics Pipes XIV, Budapest*, 2008. 31, 35, 121

[124] J. M. Lagarón, G. Capaccio, L. J. Rose, and B. J. Kip, "Craze morphology and molecular orientation in the slow crack growth failure of

polyethylene," *Journal of Applied Polymer Science*, vol. 77, pp. 283–296, 2000. 31, 39

[125] E. J. Kramer, "Open questions in the physics of deformation of polymer glasses," *Journal of Polymer Science Part B: Polymer Physics*, vol. 43, pp. 3369–3371, 2005. 32

[126] R. H. Boyd, "Relaxation processes in crystalline polymers: experimental behavioura review," *Polymer*, vol. 26, no. 3, pp. 323–347, 1985. 32

[127] M. Mansfield and R. H. Boyd, "Molecular motions, the α relaxation, and chain transport in polyethylene crystals," *Journal of Polymer Science Part B: Polymer Physics*, vol. 16, pp. 1227 – 1252, 1978. 32

[128] Y. P. Khanna, E. Turi, T. Taylor, V. Vickroy, and R. Abbott, "Dynamic mechanical relaxations in polyethylene," *Macromolecules*, vol. 18, pp. 1302–1309, 1985. 32

[129] R. Popli, M. Glotin, L. Mandelkern, and R. S. Benson, "Dynamic mechanical studies of α and β relaxations of polyethylenes," *Journal of Polymer Science: Polymer Physics Edition*, vol. 22, pp. 407–448, 1984. 32

[130] F. Chen, R. A. Shanks, and G. Amarasinghe, "Structural and mechanical properties changes of ethylene-α-olefin copolymer blends induced by thermal treatments and composition," *Macromolecular Materials and Engineering*, vol. 289, no. 6, pp. 552–561, 2004. 32

[131] B. Coussens, F. Oosterlinck, and H. van de Werff, "Molecular modeling of chain pull-out and scission for oriented polyethylene," 2012. 33

[132] D. Fotheringham and B. Cherry, "The role of recovery forces in the deformation of linear polyethylene," *Journal of Materials Science*, vol. 13, pp. 951–964, 1978. 33

[133] M. J. Bonner, H. M. de Oca, M. Brown, and I. M. Ward, "A novel approach to predict the recovery time of shape memory polymers," *Polymer*, vol. 51, pp. 1432 – 1436, 2010. xv, 33, 34

[134] T. Tervoort and L. Govaert, "Strain-hardening behavior of polycarbonate in the glassy state," *Journal of Rheology*, vol. 44, no. 6, pp. 1263–1277, 2000. 35

[135] R. Haward, "Strain hardening of thermoplastics," *Macromolecules*, vol. 26, no. 22, pp. 5860–5869, 1993.

[136] R. Haward, "Strain hardening of high density polyethylene," *Journal of Polymer Science Part B: Polymer Physics*, vol. 45, no. 9, pp. 1090–1099, 2007. 35

[137] L. R. G. Treloar, *The physics of rubber elasticity*. Oxford University Press, USA, 1975.

[138] A. Cohen, "A Padé approximant to the inverse Langevin function," *Rheologica Acta*, vol. 30, no. 3, pp. 270–273, 1991. 35

[139] M. J. Cawood, A. D. Channell, and G. Capaccio, "Crack initiation and fibre creep in polyethylene," *Polymer*, vol. 34, pp. 423–425, 1993. 36, 37

[140] O. D. Sherby and J. E. Dorn, "Anelastic creep of polymethyl methylacrylate," *Journal of the Mechanics and Physics of Solids*, vol. 6, pp. 145 –162, 1958. 36

[141] P. D. Coates, *The plastic deformation and hydrostatic extrusion of crystalline polymers*. PhD thesis, University of Leeds, 1976. 36

[142] M. J. Bonner, *The creep behaviour of isotropic and oriented polyethylene*. PhD thesis, University of Leeds, 1995.

[143] P. A. O'Connell, M. J. Bonner, R. A. Duckett, and I. M. Ward, "Effect of molecular weight and branch content on the creep behavior of oriented polyethylene," *Journal of Applied Polymer Science*, vol. 89, pp. 1663 – 1670, 2003. 36

[144] P. Tarin and E. Thomas, "The role of inter-and intra-links in the transformation of folded chain lamellae into microfibrils," *Polymer Engineering & Science*, vol. 19, no. 14, pp. 1017–1022, 1979. 37, 89

[145] R. Duckett, B. Escaig, and C. G'sell, "Plastic deformation of amorphous and semi-crystalline materials," *Les Editions de Physique*, vol. B, pp. 253–264, 1982. 37

[146] J. Cazenave, R. Séguéla, B. Sixou, and Y. Germain, "Short-term mechanical and structural approaches for the evaluation," xv, 37, 38, 39

[147] A. Sukhadia, M. Lamborn, P. Deslauriers, R. Garcia, and C. Dominguez, "Plastic pipes XV," September 2010. 37

[148] T. G. Scholte, N. Meijerink, H. Schoffeleers, and A. Brands, "Mark–Houwink equation and GPC calibration for linear short-chain branched polyolefines, including polypropylene and ethylene–propylene copolymers," *Journal of Applied Polymer Science*, vol. 29, no. 12, pp. 3763–3782, 1984. 43, 68

[149] B. Wunderlich and G. Czornyj, "A study of equilibrium melting of polyethylene," *Macromolecules*, vol. 10, no. 5, pp. 906–913, 1977. 44

[150] H. Zhou and G. L. Wilkes, "Comparison of lamellar thickness and its distribution determined from DSC, SAXS, TEM and AFM for high-density polyethylene films having a stacked lamellar morphology," *Polymer*, vol. 38, pp. 5735–5747, 1997. 44

[151] F. M. Mirabella and A. Bafna, "Determination of the crystallinity of polyethylene/α-olefin copolymers by thermal analysis: Relationship of the heat of fusion of 100% polyethylene crystal and the density," *Journal of Polymer Science Part B: Polymer Physics*, vol. 40, no. 15, pp. 1637–1643, 2002. 44

[152] S. Abbas, R. Mukherjee, S. De, and S. Ganguly, "Real-time inferencing of solid–liquid phase equilibria in solution polymerization of polyethylene," *Chemical Engineering and Processing: Process Intensification*, vol. 43, no. 12, pp. 1449–1458, 2004. 45

[153] A. Ehringhaus, "Drehkompensatoren mit besonders großem Meßbereich," *Zeitschrift für Kristallographie-Crystalline Materials*, vol. 102, no. 1-6, pp. 85–111, 1940. 45

[154] Y. Dirix, T. Tervoort, C. Bastiaansen, and P. Lemstra, "Solid-state drawing of polyethylenes: the pseudo-affine deformation scheme and aggregate models revisited," *Journal of The Textile Institute*, vol. 86, pp. 314–321, 1995. 46

[155] I. M. Ward, "Optical and mechanical anisotropy in crystalline polymers," *Proceedings of the Physical Society*, vol. 80, p. 1176, 1962. 46

[156] S. Crawford and H. Kolsky, "Stress birefringence in polyethylene," *Proceedings of the Physical Society. Section B*, vol. 64, no. 2, p. 119, 1951. 46

[157] J. Rossignol, R. Séguéla, F. Rietsch, and J. Dupuis-Lallemand, "Intrinsic amorphous birefringence of semi-crystalline polyethylene from combined birefringence and infrared dichroism measurements," *Journal of Polymer Science Part C: Polymer Letters*, vol. 27, no. 13, pp. 527–532, 1989. 46

[158] P. Vandenabeele, *Practical Raman spectroscopy: an introduction*. Wiley, 2013. xv, 47, 48

[159] Z. Zhang, *Research into order parameters and graphene dispersions in liquid crystal systems using Raman spectroscopy*. PhD thesis, University of Manchester, 2014. 48, 49

[160] A. Cao, A. K. Pandya, G. K. Serhatkulu, R. E. Weber, H. Dai, J. S. Thakur, V. M. Naik, R. Naik, G. W. Auner, R. Rabah, *et al.*, "A robust method for automated background subtraction of tissue fluorescence," *Journal of Raman Spectroscopy*, vol. 38, no. 9, pp. 1199–1205, 2007. 49

[161] L. A. Reisner, A. Cao, and A. K. Pandya, "An integrated software system for processing, analyzing, and classifying Raman spectra," *Chemometrics and Intelligent Laboratory Systems*, vol. 105, no. 1, pp. 83–90, 2011. 49

[162] M. Pigeon, R. E. Prud'Homme, and M. Pezolet, "Characterization of molecular orientation in polyethylene by Raman spectroscopy," *Macromolecules*, vol. 24, no. 20, pp. 5687–5694, 1991. 50, 52

[163] B. J. Kip, M. C. Van Eijk, and R. J. Meier, "Molecular deformation of high-modulus polyethylene fibers studied by micro-raman spectroscopy," *Journal of Polymer Science Part B: Polymer Physics*, vol. 29, no. 1, pp. 99–108, 1991.

[164] J. A. Moonen, W. A. Roovers, R. J. Meier, and B. J. Kip, "Crystal and molecular deformation in strained high-performance polyethylene fibers studied by wide-angle X-ray scattering and Raman spectroscopy," *Journal of Polymer Science Part B: Polymer Physics*, vol. 30, no. 4, pp. 361–372, 1992. 152

[165] B. J. Kip, M. van Gurp, S. P. van Heel, and R. J. Meier, "Orientational order in polyethylene foils: a polarized Raman spectroscopic study," *Journal of Raman spectroscopy*, vol. 24, no. 8, pp. 501–510, 1993.

[166] T. Kida, Y. Hiejima, and N. Koh-hei, "Raman spectroscopic study of high-density polyethylene during tensile deformation," *International Journal of Experimental Spectroscopic Techniques*, vol. 1, no. 001, p. 001, 2016. 50, 52, 152

[167] L. Mandelkern and J. Maxfield, "Morphology and properties of low-density (branched) polyethylene," *Journal of Polymer Science: Polymer Physics Edition*, vol. 17, no. 11, pp. 1913–1927, 1979. 72

[168] J. M. Brady and E. L. Thomas, "Effect of short-chain branching on the morphology of LLDPE-oriented thin films," *Journal of Polymer Science Part B: Polymer Physics*, vol. 26, no. 12, pp. 2385–2398, 1988. 72

[169] F. J. Stadler, J. Kaschta, and H. Münstedt, "Dynamic-mechanical behavior of polyethylenes and ethene-α-olefin-copolymers. Part I. α'-Relaxation," *Polymer*, vol. 46, no. 23, pp. 10311–10320, 2005. 72

[170] L. Mandelkern, R. Alamo, and M. Kennedy, "The interphase thickness of linear polyethylene," *Macromolecules*, vol. 23, no. 21, pp. 4721–4723, 1990. 73

[171] R. Kitamaru, F. Horii, and K. Murayama, "Phase structure of lamellar crystalline polyethylene by solid-state high-resolution carbon-13

NMR detection of the crystalline-amorphous interphase," *Macromolecules*, vol. 19, no. 3, pp. 636–643, 1986. 73

[172] A. A. Bondi *et al.*, "Physical properties of molecular crystals liquids, and glasses," 1968. 80

[173] K. T. N. D.W. Van Krevelen, *Properties of polymers*. Elsevier, 2009. 80

[174] J. Penning, J. Van Ruiten, R. Brouwer, and W. Gabriëlse, "Orientation and structure development in melt-spun nylon-6 fibres," *Polymer*, vol. 44, no. 19, pp. 5869–5876, 2003. 83

[175] N. W. Brooks, R. A. Duckett, and I. M. Ward, "Investigation into double yield points in polyethylene," *Polymer*, vol. 33, pp. 1872–1880, 1992. 86

[176] V. Gupta and S. Rana, "Double yield in tensile deformation of high-density polyethylene fiber," *Journal of Macromolecular Science, Part B: Physics*, vol. 37, no. 6, pp. 783–804, 1998. 86

[177] R. Séguéla and F. Rietsch, "Double yield point in polyethylene under tensile loading," *Journal of Materials Science Letters*, vol. 9, no. 1, pp. 46–47, 1990. 86

[178] R. Séguéla and O. Darras, "Phenomenological aspects of the double yield of polyethylene and related copolymers under tensile loading," *Journal of Materials Science*, vol. 29, no. 20, pp. 5342–5352, 1994. xviii, 86, 88

[179] V. Gaucher-Miri and R. Séguéla, "Tensile yield of polyethylene and related copolymers: mechanical and structural evidences of two thermally activated processes," *Macromolecules*, vol. 30, no. 4, pp. 1158–1167, 1997. 86

[180] N. Brooks, R. Duckett, and I. Ward, "Temperature and strain-rate dependence of yield stress of polyethylene," *Journal of Polymer Science Part B: Polymer Physics*, vol. 36, no. 12, pp. 2177–2189, 1998. 86

[181] S. Hobeika, Y. Men, and G. Strobl, "Temperature and strain rate independence of critical strains in polyethylene and poly (ethylene-co-vinyl acetate)," *Macromolecules*, vol. 33, no. 5, pp. 1827–1833, 2000. 86

[182] L. J. Fetters, D. J. Lohse, C. A. García-Franco, P. Brant, and D. Richter, "Prediction of melt state poly (α-olefin) rheological properties: the unsuspected role of the average molecular weight per backbone bond," *Macromolecules*, vol. 35, no. 27, pp. 10096–10101, 2002. 93

[183] F. J. Stadler and H. Münstedt, "Terminal viscous and elastic properties of linear ethene/ α-olefin copolymers," *Journal of Rheology (1978-present)*, vol. 52, no. 3, pp. 697–712, 2008.

[184] X. Chen, F. J. Stadler, H. Münstedt, and R. G. Larson, "Method for obtaining tube model parameters for commercial ethene/α-olefin," 93, 94

[185] M. Doi and S. Edwards, *The theory of polymer dynamics*. Clarendon Press, 2013. 94

[186] V. Raju, G. Smith, G. Marin, J. Knox, and W. Graessley, "Properties of amorphous and crystallizable hydrocarbon polymers. i. melt rheology of fractions of linear polyethylene," *Journal of Polymer Science: Polymer Physics Edition*, vol. 17, no. 7, pp. 1183–1195, 1979. 94

[187] D. Richter, B. Farago, R. Butera, L. Fetters, J. Huang, and B. Ewen, "On the origins of entanglement constraints," *Macromolecules*, vol. 26, no. 4, pp. 795–804, 1993. 94, 152

[188] V. Litvinov, "NMR on Elastomers," *Encyclopedia of Polymeric Nanomaterials*, pp. 1392–1397, 2014. 95

[189] T. B. van Erp, D. Cavallo, G. W. Peters, and L. E. Govaert, "Rate-, temperature-, and structure-dependent yield kinetics of isotactic polypropylene," *Journal of Polymer Science Part B: Polymer Physics*, vol. 50, pp. 1438 – 1451, 2012. 151, 153, 165, 166

[190] R. Steenbakkers, L. Havermans, V. P., R. Jonathan, and R. A. Deblieck, "Strain hardening modulus: a measure for ranking time to failure of random polypropylene pipe materials." Proceedings of the 18th Plastic Pipes Conference PPXVIII September 12-14, 2016, Berlin, Germany, September 2016. 153